An Optical Study of Dwarf Galaxies with Narrow HI linewidths:

Dark Matter and the Tully–Fisher Relation at the Faint End

Richard Joseph Patterson
Charlottesville, Virginia

B. A., University of Virginia, 1984
M. A., University of Virginia, 1989

A Dissertation Presented to the Graduate Faculty of the University of Virginia
in Candidacy for the Degree of Doctor of Philosophy

Department of Astronomy
University of Virginia
May, 1995

David C. Brydges

Robert W. O'Connell

Mercedes T. Richards

Morton S. Roberts

Lawrence E. Thomas

D. Mark Whittle

Trinh X. Thuan

Contents

List of Figures

List of Tables

Abstract

CCD $B-$ and $I-$band surface photometry is presented for a sample of 51 dwarf and low surface brightness galaxies. The main selection criterion was their extremely narrow HI linewidths ($\Delta V_{20} < 100$ km s^{-1}), chosen in order to examine the Tully–Fisher (TF) relation between linewidth and absolute magnitude at the low–luminosity end. In this regime, a substantial fraction of the linewidth is attributable to turbulent rather than rotational motion. Therefore, it is not surprising that the original TF relation, an expression of the scaling relation between mass (from the linewidth due to rotation) and luminosity, does not hold in this regime.

If we assume the linewidth is due to both turbulent *and* rotational motion, we obtain a mass for the dwarfs which *does* correlate with luminosity. However, the relation is distinct from the TF relation for spirals, and indicates the presence of an increasing amount of dark matter at low luminosities. We find that the locus of dwarf galaxies in the mass/luminosity plane is well fit by the theoretical prediction of Dekel & Silk [1986, ApJ, 303, 39], $M/L \propto L^{-0.37}$, where M/L decreases with increasing L, while the spirals follow a relation in which M/L *increases* with increasing L ($M/L \propto L^{0.2}$), which corresponds to the observed slope (~ 7) of the TF relation for spirals. For dwarfs fainter than $L_B/L_\odot \sim 10^7$, the observed M/L is ~ 20, while it drops to unity for $L_B/L_\odot \sim 10^{9.5}$.

The Dekel–Silk relation arises in low mass systems with massive dark halos which undergo extensive mass loss due to supernova–driven winds. The halo allows the galaxy to remain bound even as most of the gas is removed, drastically reducing the rate of star formation. The trend towards higher M/L at lower L is the result of the lower escape velocity of the less massive systems, allowing the gas to be removed more efficiently.

The same relation has previously been seen to hold for dwarf Spheroidal galaxies, providing further evidence for a common evolutionary history of these two types of dwarf systems, radically different from "normal" early– and late–type galaxies.

Chapter 1

General Introduction

1.1 Dwarf Galaxies

Dwarf Galaxies are the most common type of galaxy in the Universe. However, "normal" galaxies dominate galaxy catalogs except in the few distance–limited catalogs (e.g. Kraan Korteweg 1986; Tully 1988; Schmidt & Boller 1992) where their intrinsic faintness (absolute B magnitude, $M_B \lesssim -16$) is not a factor. The growing realization of the astrophysical importance of dwarfs has led recently to increased numbers of studies of these objects.

This interest is based in part on the observed excess of faint blue galaxies at intermediate redshift as compared to the local luminosity function (cf. Tyson 1988; Broadhurst, Ellis, & Shanks 1988; Ferguson 1992, Babul & Rees 1992). This can be interpreted as evidence for a large population of star forming dwarfs which have now

faded away. In addition, there is increasing evidence that accretion and mergers of dwarf galaxies may play a large role in galaxy formation (Schweizer 1992).

Dwarf galaxies are found in all environments although there does appear to be some segregation based on type (Binggeli, Tarenghi, & Sandage 1990). Gas–rich dwarf irregulars (dIs) are more likely to be found outside of clusters, often in loose groups. The most extreme star–forming dwarfs are the blue compact dwarfs (BCDs).

Dwarf Ellipticals (dEs), on the other hand, tend to be found in clusters of galaxies or as close companions to massive galaxies; dEs comprise $\sim 75\%$ of the members of the Virgo cluster. In this work, we shall limit our scope to the gas rich dwarf irregulars.

In the remainder of this introduction, we discuss the following areas in which dwarf galaxies are of significant astrophysical interest. Dwarf irregulars present a simplified setting within which to study *star formation*. They often appear optically as little more than intergalactic H II regions, where star formation can be studied in isolation, without complicating factors such as spiral density waves. Similarly, the primordial (low metallicity and high gas content) state of dwarfs makes them suitable to studies of *galaxy formation*.

The low (baryonic) masses of dwarfs allow strong constraints to be placed on the nature of the *dark matter* in the halos of galaxies (Tremaine & Gunn 1978). The large numbers of dwarfs makes them useful as test particles for *cosmological studies*.

Finally, due to the smaller masses and lower rotation velocities of dIs as compared to spirals, the *Tully Fisher (TF) relation* can be tested in the extreme case of

turbulence–dominated motion. Investigation of the TF relation in this regime should help to shed light on the exact origin of the relation.

1.2 Star formation

A simple phenomenological model of star formation, called stochastic self–propagating star formation (SSPSF) has been developed and applied to the dIs (Gerola, Seiden & Schulman 1980). This model appears to fit observations fairly well in a qualitative way (Hunter & Gallagher 1985), while the physical processes which drive star formation remain poorly understood. In low mass dIs the SSPSF model predicts distinct bursts of star formation. This is consistent with the picture of BCDs as dIs in the middle of a burst (Thuan 1986).

Due to their extreme physical characteristics, dIs can also be used to directly study the conditions which lead to star formation. For example, is there a "universal" minimum H I density required before star formation can occur, similar to the relation found by Kennicutt (1989) for spirals? Studies show that the III content of dIs appears to increase with respect to the total mass as the mass decreases (Staveley–Smith, Davies, & Kinman 1993). However, below $M_{\rm B} \sim -12$ there appears to be a dramatic rise in the mass to light ratios for dIs (Freeman 1987; Lo, Sargent & Young 1993), which corresponds to the H I mass, $M_{\rm HI}$, just dropping below $10^7 M_\odot$. Further study is needed before it will be known if the onset of star formation corresponds to a minimum gas density. Moreover, it is not presently understood how such low mass systems which lack rotational support can *avoid* collapsing and forming stars

for periods $\gtrsim 10^9$ years, which is the time interval between bursts in a BCD (Thuan 1991).

The current star formation rate (SFR) in a galaxy can be estimated from observations of the Hα luminosity, $L(\mathrm{H}\alpha)$, since most of the stars providing the ionizing radiation are massive and therefore short lived. In addition, ultraviolet spectra from IUE observations allow the massive star population to be directly investigated (Fanelli, O'Connell, & Thuan 1988). Broadband colors, on the other hand, are dependent on both age and metallicity, and it is therefore difficult to obtain more than an estimate of the star formation history of a galaxy from such data. These broadband colors can be combined with the evolutionary models of Larson & Tinsley (1978) or, more recently, Bruzual & Charlot (1993) to provide an estimate of the age of the most recent burst of star formation, as well as the age of the underlying old stellar population.

Kennicutt (1989) has found a star formation law in disk galaxies in which star formation was found to occur in gas very close to a threshold surface density. It would be interesting to compare the gas densities in regions of star formation in dwarf galaxies to see if similar conditions are found to apply. Lo *et al.* (1993) find that the HI surface densities in a sample of nine faint, largely non-rotating dwarfs significantly exceed the Kennicutt critical threshold density. The intrinsic faintness and paucity of Hα emission in these dwarfs, indicates little star formation in these systems, perhaps due to the lack of some sort of "trigger" such as differential rotation.

Van der Hulst *et al.* (1993), on the other hand, have found that in a sample of LSB disk galaxies, only small areas of the HI disk exceed the critical HI threshold,

which agrees at least quantitatively with the Kennicutt model, in which the marked lack of star formation in LSB galaxies is interpreted as being due to the low HI surface density in the disk. These two results, one for turbulence–supported, faint dwarf galaxies, and the other for rotationally–supported LSB galaxies, point to the critical role played by differential rotation versus stochastic cloud collisions in the process of star formation.

Any episode of massive star formation in such low mass objects would very likely lead to the neutral gas being blown out from the stellar disk because of their low escape velocity. Ionizing photons from OB associations and winds from supernovae would give rise to holes in the HI distribution observed in the dIs Holmberg II (Puche *et al.* 1992), as well as Holmberg I and M81dwA (Westpfahl & Puche 1994). Broadline components of Hα ($\Delta v \sim$ 1000 $-$ 3000 km s^{-1}) seen in several BCDs observed by Thuan *et al.* 1994, as well as the elongated X–ray emitting structure around VII Zw 403 (Papaderos *et al.* 1994), provide additional evidence for mass outflow in dwarfs. This may lead to a self–regulation of the star formation rate in the entire galaxy; no further episode of star formation can occur until the massive stars have died and the the neutral gas is allowed to cool and collapse into the center of the gravitational potential (Hunter, Hawley & Gallagher 1993). If the gas is entirely lost by the galaxy, star formation will be essentially quenched (Dekel & Silk 1986).

Any detailed determination of the stellar populations of the individual galaxies requires the application of the techniques of population synthesis. This involves comparing the combined galaxian spectral energy distribution to a stellar library, in order to determine the approximate composition of the galaxy by stellar type.

Hunter & Gallagher (1985) find evidence of low but steady star formation rates when modeling brighter dwarf irregulars. More detailed synthesis techniques, drawing on a stellar spectral library in the UV, have been employed by Fanelli, O'Connell & Thuan (1988) for modeling the star formation histories of several BCDs. They find clear evidence of episodic bursts of intense star formation activity in these objects.

1.3   Galaxy Formation

Because of the high gas content, low star formation rate, the low metallicity and the lack of spiral structure, present day dIs may closely approximate conditions which existed in larger galaxies while they were forming. Of course, the free fall collapse leading to the formation of the bulge in spirals does not occur in dwarfs; (Sandage 1986). In spite of this difference, the presence of a large number of dwarfs in various stages of evolution that are within easy observational reach make them objects worthy of detailed study.

The low metallicity of the II II regions in dIs also lend themselves to a study of the chemical evolution of galaxies (Peimbert 1985). In BCDs, a primordial helium abundance, Y, can be obtained by extrapolating the Y vs O/H relation to zero metallicity (Pagel et $al.$ 1992; Izotov et $al.$ 1994).

1.4 Dark Matter

The missing–mass problem first pointed out by Zwicky (1933), has remained a problem in that we are still uncertain of the nature of the dark matter which leaves its dynamical signature in the rotation curves of spirals and in the motions of clusters of galaxies. Because the number density of dwarf galaxies increases so steeply at low luminosity, it is very important to determine how much, if any, dark matter is present in dwarfs. It is possible that while dwarfs contribute a negligible amount to the total luminosity, they may contribute significantly, or even dominate in the mass distribution in the universe.

Observations to detect dark matter in dIs have been undertaken by several groups (Carignan, Beaulieu & Freeman 1990; Lo *et al.* 1993). They combine VLA 21cm observations with optical data to construct models of the HI distribution in the dwarfs and the overall mass–to–light ratios. They find that the extreme dIs with $M_B \sim -10$ and $M_{virial} \sim 10^7 M_\odot$ seem to be embedded in a dark matter halo. Values for M/L as high as ~ 25 were reported in the extremely low luminosity dwarf LGS 3 ($M_B \sim -9.2$). This low limit on the presence of a dark halo, along with similar work for dEs (Mateo 1993), effectively rules out massive neutrinos or other dynamically "hot" low–mass particles as the source of the dark matter.

1.5 Cosmology

Biased galaxy formation (Rees 1985), in which "normal" galaxies arise from 2-3 σ peaks in the density fluctuations in the early universe, explains voids as regions in which the mean density was slightly below the average and no peaks large enough to form normal galaxies occurred. It is expected that dwarf galaxies would have formed from much smaller fluctuations ($\sim 1\sigma$), and they should therefore populate the voids observed in redshift surveys (Dekel & Silk 1986).

Several H I surveys of dwarf galaxies were carried out in order to test just this hypothesis (Thuan *et al.* 1991, and references therein). Although a few faint galaxies have been found to lie within voids (Salzer, Hanson, & Gavazzi 1990), nearly all of these surveys found that the dIs follow the void boundaries in the same way as the larger galaxies. These observations place restrictions on the biased galaxy formation theory. Interestingly, Salzer (1989) and Salzer & Rosenberg (1994) find that active, emission line galaxies (ELGs) are sometimes found in voids. Recently, Pustil'nik *et al.* (1994*a* and *b*) find that $\sim$ 20% of the BCDs in the Second Byurkan Survey are found in voids.

1.6 The Tully–Fisher Relation

It has long been known that there is a strong correlation between the rotational velocity and the luminosity of spiral/irregular galaxies. However, it was not until the work of Tully & Fisher (1977) that the usefulness of this correlation for the determination

of extragalactic distances was fully appreciated. Therefore, this luminosity–linewidth relation is often referred to as the Tully–Fisher (TF) relation.

The rotational velocity of a disk galaxy can be obtained from observations of the global H I line profile for the galaxy. This velocity implies a value for the luminosity of the galaxy through the TF relation; therefore by measuring the apparent magnitude of the galaxy, one can determine the distance modulus. The line width must be corrected for the effects of inclination, and the galactic magnitude must be corrected for internal and galactic extinction. This leads to a relation of the form,

$$B_T^O = a \log(\Delta V_{20}^0) + b, \tag{1.1}$$

where B_T^O is the total absolute B magnitude corrected for internal and external extinction, ΔV_{20}^0 is the H I 21 cm linewidth at 20% of peak flux corrected for the inclination of the galaxy and a and b are constants, determined through observations of a large group of calibrator galaxies with reliable distances determined by other means (e.g., the Cepheid period–luminosity relation).

Most of the early calibration and application of the TF relation was carried out using B magnitudes, as these were the most commonly available magnitudes. However, a strong Hubble type dependence was found to exist for the B Tully–Fisher relation (Roberts 1978; Rubin *et al.* 1985), because the B–band is a strong tracer of the young stellar population in a galaxy and this varies with type at a constant galaxian mass. The uncertainty in the (large) correction due to internal extinction in B further increased the dispersion of the TF relation, which is observed to be ~ 0.35 mag (Pierce & Tully 1988).

This difficulty was remedied by using infrared H–band magnitudes (Aaronson, Huchra & Mould 1979). Since the infrared luminosity is dominated by late–type giants, it is less subject to young star formation than the B magnitude. The extinction in H is only 10% of that in B, so the correction for internal extinction introduces less uncertainty in the infrared TF relation. This was reflected in a significantly reduced dispersion in the infrared TF relation. The dispersion in the H (as well as the R and I) band relation is ~ 0.25 mag (Pierce & Tully 1992).

Pierce and Tully (1988) determined TF relations for three different bands, B, V, and I, and found that the dispersion for the I band was $\sim 25\%$ smaller than that in the B–band (most of the remaining dispersion may have been due to depth effects in the clusters they were using). The I–band has since become one of the most important bands for TF–type studies (e.g. Lu 1993) for several reasons. First, the limits in the sensitivity of infrared arrays and the brightness of the infrared sky make it exceedingly difficult to obtain accurate H–band magnitudes for faint, extended galaxies. Second, the I–band CCD data also has the advantage over the B band of allowing smaller corrections for the (uncertain) Galactic and internal extinction. Finally, the I band traces the older stellar population, and therefore the mass, of the galaxy better than the B band, which contributes to the tighter relationship found by Pierce & Tully. This sensitivity to the older stellar population also leads to a better estimate of the inclination from surface photometry.

While the TF relation is essentially an empirical relation (which must therefore be carefully calibrated in each wavelength in which it is employed), there is some physical basis for the relation, at least for spiral galaxies. The following justification

is outlined in Aaronson, Huchra & Mould (1979).

For a spherically symmetric rotating galaxy, the balance of gravitational and centrifugal force implies that the total mass $M_T(r)$ contained within r is $M_T(r) \sim rV^2(r)$, while constant surface brightness implies $L \sim r^2$. Assuming a constant mass–to–light ratio (M/L), the combination of the two previous relations gives $L \sim V_{max}^4$ (which is equivalent to the Faber–Jackson relation for elliptical galaxies). This yields a slope of 10 for the TF relation ($a = 10$ in equation 1.1) which is roughly the slope found for the H band relation.

A major problem with this simple picture is the fact that the mass to light ratio is observed to increase dramatically for low luminosity systems (Pierce 1991; Lo *et al.* 1993), yet with the scarce existing data, these galaxies appear to obey the same TF relation as the more massive galaxies which have a nearly constant M/L. These dwarfs appear to be dark matter dominated; however, the visible matter must be tightly coupled to the dynamical mass, if the TF relation is to hold. A similar situation is seen in the disk–halo "conspiracy" in spiral galaxies (Sancisi & van Albada 1987).

Very few galaxies at the low–luminosity end have sufficiently accurate magnitude data to constrain the TF relation in this regime. The major motivation for this thesis was to obtain observations for a sample of such dwarfs, in order to investigate the precise character of the TF relation at very low luminosities.

1.7   Outline of the Thesis

In order to investigate the optical properties and Tully–Fisher relation for extreme dwarf galaxies, a sample of 50 dwarf irregular galaxies with very narrow HI linewidths (dominated by turbulent rather than rotational motion), was observed in both the B and I bands. From these observations we shall investigate the I band Tully Fisher relation (as well as the less reliable, but more widely used B band relation) in the low luminosity regime.

The thesis is organized in the following way. In Chapter 2, the observations and reductions are detailed and the surface photometry is presented. In Chapter 3, the corrections to absolute magnitude, from our surface photometry and HI linewidth, from the literature, for reddening, dust and inclination are discussed. These results are used in Chapter 4 to derive a Tully–Fisher relation for small ΔV_{20}^0 and the scatter in the relation is analyzed. A modified version of the Tully–Fisher relation is suggested for dwarf galaxies. In Chapter 5, the structural parameters and global properties of the dwarfs are examined and compared with LSB and normal spirals. Finally, a summary of the results is presented.

Chapter 2

CCD Surface Photometry of Dwarf Galaxies

2.1 Sample Selection

The galaxies in this sample are very low luminosity dwarf galaxies selected by their III line width, Δv_{20}, III velocity, and magnitude. They are drawn almost exclusively from the sample of 1557 Uppsala General Catalogue (UGC; Nilson, 1973) dwarf and low surface brightness galaxies which were detected in III by Schneider *et al.* (1990, 1992). Their sample included all galaxies in the UGC classified with a Hubble type of Sc Irr or later (or a de Vaucouleurs class of Sd dm or later), with the majority chosen for our subsample classified as dwarfs, which Nilson categorized as "objects with (1) very low surface brightness and (2) little or no central concentration of light on the red prints".

Galaxies were chosen which had a $\Delta v_{20} < 100$ km s^{-1} and a $v_0 < 1500$ km s^{-1}, with a sufficiently faint m_{pg} (from Zwicky *et al.* 1960 1968, or from Nilson's own very uncertain visual estimates) to qualify as a dwarf under the definition of Tammann (1980): $M_B \gtrsim -16$. For galaxies not observed by Schneider *et al.* (1990; 1992), HI data was taken from Huchtmeier & Richter (1989).

The major and minor axis (a and b from Nilson) and the Hubble classification from Nilson were used in an attempt to exclude face–on spirals from the sample. Finally, the Palomar Observatory Sky Survey (POSS) prints were visually inspected in order to include only dwarfs in this sample. These were usually found to be galaxies of low surface brightness with superimposed irregular patches of star formation. The III profile shape was used to select a large number of galaxies with Gaussian profiles. This should restrict the sample to galaxies which lack rotational support (after excluding the face on spirals).

In addition to the low redshift, narrow width dwarfs in the sample, several low surface brightness (LSB) galaxies at larger redshift, and/or with larger line widths were included in the sample, in order to allow overlap and comparison with other Tully–Fisher relation studies.

In Table 1, the basic data for the sample are presented. The UGC number (or other name) is listed (marked by a c if it is an LSB galaxy), followed by the coordinates, the heliocentric velocity $v_\odot$, the III line full widths at half power and at 20% maximum, and the III flux corrected for beam size, all from Schneider *et al.*. The profile shape is then classified as a Gaussian (G), probable Gaussian (G?),

probable double–horned (D?), or double–horned (D). Galaxies for which the signal–to–noise of the HI observations was too poor to allow an accurate classification were all placed in the two intermediate categories (D? and G?). The results discussed in Chapters 4 and 5 are based *only* on the galaxies which could be definitively classified as either D or G. Finally, the optical blue dimensions, Hubble Type and photographic magnitude taken from the UGC are listed.

In Figure 0 (immediately after Table 1) a histogram of the linewidth distribution is shown for the narrow-lined dwarfs in (a), as well as for the sample as a whole in (b).

Five of the seven galaxies for which B and R images had been obtained on the May85 run (before the present project was fully conceived) were included for $I-$band observations, although they did not strictly satisfy the above selection criteria. All seven of these galaxies are marked by an r in Table 1.

Finally, several galaxies were included because of their scientific interest. UGC 8091 (=GR8, DDO 155) was included to allow comparison with the surface photometry of Carignan, Beaulieu & Freeman (1990). M81dwA was included because of the earlier work of Sargent, Sancisi & Lo (1983) which indicates that this dwarf is probably not supported by rotation. Kara 10 and 37 were chosen from the list of dwarf galaxies of Karachentseva (1968) which had single dish observations from Schneider & Thuan (1989). K10 qualifies as a narrow lined dwarf as described above, but K37 has a large, single–peaked Δv_{20}, and was thought to be of interest. Subsequent VLA observations which we made of 10 galaxies in the sample, show that the unusual HI profile of K37 is actually caused by two galaxies, K37 and IC342dw6

Table 1

Data for Sample of Dwarf Irregulars

| Galaxy	RA	Dec	v_o	Δv_{50}	Δv_{20}	Flux	Profile	axb	Hubble	m_{pg}
	(1950.0)		(km/s)	(km/s)	(km/s)	(Jy·km/s)	Shape	(′)	Type	(Zw)
U00031	00 02 18.2	+16 54 50	1239	44	68	1.97	G	1.4x1.1	IRR	15.3
U00063	00 05 16.0	+35 41 18	687	39	59	3.52	G	1.0x0.7	IRR	15.6
U00300	00 27 29.7	+03 14 03	1489	27	41	4.10	G	1.4x1.4	DWARF	18.
U00772	01 11 06.0	+00 36 42	1263	43	66	5.10	G	1.6x1.4	DWRF IR	17.
U01171	01 37 02.4	+15 38 51	874	29	51	1.53	G	1.4x1.3	DWARF	17.
KARA10	01 40 54.3	+15 26 27	921	35	52	3.64	G	...	...	...
U01981	02 27 43.1	+00 43 06	1546	31	47	1.06	G	1.7x1.5	DWARF	17.
U02017	02 29 54.0	+28 37 00	1123	...	104	14.10	G	2.5x2.0	DWRF IR	17.
U02034	02 30 34.0	+40 18 26	752	44	66	31.40	D?	3.5x3.0	DWRF IR	15.0
U02053	02 31 31.0	+29 31 47	1174	55	64	29.00	G	2.3x1.3	DWRF IR	15.7
U02162	02 37 49.0	+01 00 47	1218	51	65	5.20	G?	2.0x2.0	DWRF IR	18.
KARA37	03 29 00.1	+67 55 02	1578	146	208	22.38	G	...	...	...
U03212	04 55 17.9	+71 06 09	1398	49	72	1.33	G	1.2x0.4	DWRF SP	18.
U03384	05 55 25.2	+73 07 00	1262	78	100	22.76	D	1.9x1.9	DWRF SP	16.0
U03817	07 19 06.6	+45 12 00	471	...	52	10.20	G?	2.0x1.0	DWARF	17.
U03860	07 24 50.2	+40 52 13	365	40	55	16.90	G?	1.8x1.2	DWRF IR	15.5
U03966	07 38 01.1	+40 13 47	368	71	91	25.10	D	2.2x2.0	DWRF IR	16.0
U04173	07 58 36.0	+80 16 00	1054	...	89	29.50	D?	3.3x0.7	IRR	15.7
c U04204	08 01 25.2	+56 05 33	3053	130	179	3.50	D	1.2x0.9	DWARF	17.
M81dwA	08 18 42.0	+71 11 36	262	19	37	4.20	G	...	...	...
U05423	10 01 25.3	+70 36 27	466	47	67	3.39	G?	1.3x1.0	IRR	15.3
U05706	10 28 19.2	+34 45 35	1466	33	48	3.99	G	1.5x1.2	DWRF IR	18.
c U05709	10 28 33.3	+19 38 30	6103	242	277	2.82	D	1.3x0.8	...	15.7
U06151	11 03 16.0	+20 05 40	1241	27	41	6.40	G?	1.8x1.8	DWRF SP	17.
U06248	11 10 15.9	+10 28 21	1156	30	48	1.94	G	1.6x1.3	DWRF IR	18.
c U06596	11 35 08.1	+56 25 13	2379	154	177	10.88	D	1.2x0.7	IRR	15.5
U06628	11 37 24.0	+46 12 00	901	41	56	24.70	G?	3.5x3.5	...	14.6
c U07295	12 14 03.8	+33 43 34	6687	232	265	2.43	D	1.0x0.25	...	16.5
U07548	12 24 18.2	+13 27 08	−86	30	44	2.37	G?	1.3x0.5	IRR	15.2
U07596	12 26 01.0	+08 54 54	465	25	42	0.28	D?	1.9x0.7	DWARF	15.3
U07608	12 26 18.0	+43 30 00	601	60	74	29.95	G?	4.0x3.5	DWRF IR	16.0
×U07636	12 27 28.3	+08 12 15	178	25	57	0.28	G	1.2x0.8	DWRF IR	15.4
U07684	12 29 48.4	+18 31 14	767	26	48	0.28	G	1.1x0.7	...	15.4
c U07882	12 40 21.8	+33 33 34	6834	356	370	3.71	D	1.5x0.2	Sc-IRR	15.7
U08091	12 56 09.8	+14 29 12	163	31	47	8.40	G	1.1x0.9	IRR	15.3
U08201	13 04 39.4	+67 58 16	202	42	68	36.00	G?	3.7x2.5	DWRF IR	14.1
U08683	13 40 23.0	+39 54 26	747	32	44	7.50	G	2.3x2.3	DWRF IR	15.7
U08760	13 48 40.2	+38 15 48	273	38	45	9.60	G	2.3x0.6	DWRF IR	15.4
U08833	13 52 42.0	+36 05 00	303	...	38	5.30	G	1.1x0.9	IRR	16.5
U09128	14 13 37.9	+23 17 06	197	34	54	12.80	G	1.8x1.6	DWRF IR	15.3
c U09391	14 33 13.0	+59 33 20	2090	119	134	7.94	D	1.8x1.1	...	15.5
r U10031	15 44 54.6	+61 42 36	1099	...	71	7.00	D	1.7x1.5	DWRF SP	17.
r U10058	15 48 17.4	+26 04 12	2276	117	135	5.83	D	1.2x0.9	DWRF SP	17.
r U10290	16 11 59.4	+00 56 42	1995	119	138	9.94	D	2.0x1.9	DWRF SP	15.0
r U10376	16 22 29.4	+65 33 00	3474	41	69	2.30	G	1.5x1.4	DWRF SP	16.5
r U10669	17 00 52.8	+70 21 36	681	...	52	3.00	G	1.4x1.4	DWARF	17.
r U11764	21 30 45.0	+07 46 42	3717	73	107	3.76	D?	1.0x1.0	DWRF SP	18.0
U12082	22 31 52.7	+32 36 06	1081	67	83	31.60	D?	3.5x3.0	DWRF SP	15.6
r U12151	22 38 59.4	+00 08 24	1939	167	193	5.00	D?	3.0x2.0	DWARF	16.0
U12894	23 57 48.0	+39 12 54	592	34	57	6.75	G	1.0x1.0	DWRF IR	17.
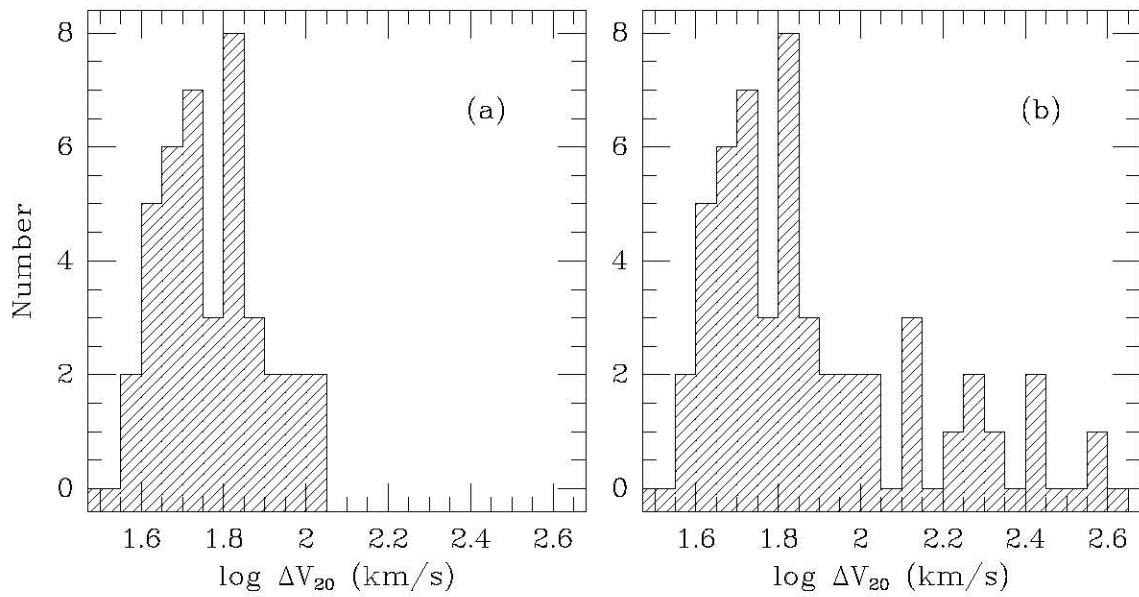
Figure 0: Histogram of Linewidths for the sample. (a) shows the distribution of linewidths for the narrow–lined galaxies ($\Delta V_{20} \lesssim 100$ km s^{-1}). (b) shows the distribution for all the galaxies in the sample, listed in Table 1.

(Börngen & Karachentseva 1985), which appear from the VLA data to be spirals in the background of the IC 342 complex.

The HI data for UGC 7636 (marked by an asterisk in Table 1) actually applies to a cloud of III which has been removed from the dwarf by ram–pressure stripping by the hot X–ray emitting gas around the giant elliptical NGC 4472 in the Virgo Cluster (Patterson & Thuan 1992; McNamara *et al.* 1994). The data for UGC 7636 are presented, but are excluded from the analysis in Chapters 4 and 5.

2.2   Observations

The B, R and I photometric observations of 51 dwarf and LSB galaxies were obtained during several observing runs from 1985 to 1993 with different CCD chips and telescope combinations. Specific details about the observing runs are given in Tables 2 and 3. For each observing run, Table 2 details the number of galaxies observed and the filters used, as well as listing the telescope aperture and focal ratio, the CCD type, size and pixel scale, the field of view (FOV), the gain and read noise of the chip.

Table 3 gives the galaxy name, filters used, date of observations, filters used, number and length of exposures, seeing, airmass and sky conditions (photometric or some cirrus present).

Most of the these galaxies (38) were observed in the B– and I–bands in October 1990 and April 1991 at the $f/7.5$ focus of the 2.1m telescope at Kitt Peak National

Observatory[1] (KPNO). The CCD camera used for these observations consisted of a Tektronix (TEK2/T5HA) chip. In addition, 7 of the galaxies were observed in B– and R–bands in May 1985 with the 4m telescope by Trinh Thuan and Ken Mitchell (Thuan *et al.*, 1992). In Sept. 1991, January 1993 and April 1993, 13 of the galaxies with the largest angular size (as well as those galaxies with images suffering from fringing problems, marked by an f in Table 3; see §2.3) were reobserved with a larger CCD chip at the 2.1m or 0.9m telescopes in order to image the entire galaxy and to include a sufficiently large area around the galaxy for proper sky subtraction. These subsequent observations were made by John Spitzak and Steve Schneider (Sep91); Rich Gelderman and Patterson (Jan93); and Trinh Thuan and Valentin Lipovetsky (Apr93).

During the Oct 90 and Apr 91 runs the galaxies were imaged through the B ($\lambda_o = 4400$Å, FWHM=1152Å) and I ($\lambda_o = 8205$Å, FWHM=1851Å) filters in the KPNO Mould filter system. Each observation was broken up into three separate exposures of 10 minutes in B and 7 minutes in I and displaced from each other by $\sim 10''$ in Right Ascension or Declination, for a total of 30 minutes in the B and 21 minutes in the I filter. These slight displacements are useful in the subsequent processing for removing bad pixels and cosmic ray events.

During the May85 4m run, the Mould B and Mould R ($\lambda_o = 6467$Å FWHM=1108Å) filters were used, and the Mould B filter was used for the Apr93 run. The Harris

Figure 1: Transmission curves, with λ_0 and FWHM, for the CCD Filters used in this work. From KPNO manuals.

Table 2
Observing Run Information

Date	#	Band	Telescope & CCD	Size	Scale	FOV	Gain	RN
(Galaxies Observed)			(KPNO)	(pixels)	$(\frac{arcsec}{pixel})$	(arcmin)	$(\frac{e^-}{ADU})$	(e^-)
1985 May 22–23	7	BR	4m, f/2.8	RCA1	320×512	0.60	3.2×5.1	11.5	79.0
1990 Oct 19–22	16	BI	2.1m, f/7.5	T5HA	512^2	0.34	2.9×2.9	3.25	7.5
1991 Apr 17–21	29	BI	2.1m, f/7.5	T5HA	512^2	0.34	2.9×2.9	3.25	7.5
1991 Sep 13–16	3	BI	0.9m, f/7.5	ST1K	1024^2	0.59	10.0×10.0	2.7	2.8
1993 Jan 23–24	8	BI	2.1m, f/7.5	T1KA	1024^2	0.30	5.1×5.1	1.7	3.5
1993 Apr 18–20	3	B	0.9m, f/7.5	T2KA	1024^2	0.68	11.6×11.6	7.0	4.0

Table 3
Observing Log

Galaxy	band	run	night	exp. time (#×sec)	seeing arcsec	airmass	sky conditions
U31	B	Oct90	22	3×420.0	1.7	1.08	Photo
	I f	Oct90	22	3×420.0	1.4	1.05	Photo
U63	B	Oct90	21	3×600.0	1.9	1.02	Photo
	I f	Oct90	21	3×420.0	1.4	1.01	Photo
U300	B	Oct90	20	1×1800.0	2.0	1.25	Photo
	I	Oct90	20	3×1200.0	2.9	1.49	Photo
U772	B	Oct90	22	6×510.0	2.0	1.18	Photo
U1171	B	Oct90	22	6×420.0	1.9	1.10	Photo
K10	B	Oct90	22	3×600.0	2.7	1.15	Photo
	I f	Oct90	22	3×420.0	1.0	1.07	Photo
	B	Jan93	23	1×600.0	1.2	1.16	Cirrus
	I	Jan93	23	3×420.0	1.2	1.23	Cirrus
U1981	B	Oct90	21	3×600.0	1.4	1.34	Photo
	I f	Oct90	21	2×420.0	1.0	1.24	Photo
	B	Jan93	24	1×600.0	1.8	1.90	Cirrus
	I	Jan93	24	3×420.0	1.5	1.74	Cirrus
U2017	B	Oct90	21	3×600.0	1.4	1.05	Photo
	I f	Oct90	21	3×420.0	1.0	1.11	Photo
	B	Jan93	24	3×600.0	1.5	1.05	Cirrus
	I	Jan93	24	3×420.0	1.2	1.02	Cirrus
U2034	B	Oct90	22	1×180.0	1.4	1.29	Photo
	I f	Oct90	22	9×180.0	0.7	1.30	Photo
	B	Jan93	23	3×600.0	1.7	1.13	Cirrus
	I	Jan93	23	3×420.0	1.2	1.19	Cirrus
U2053	B	Oct90	20	3×600.0	2.2	1.17	Photo
	I	Oct90	20	2×1200.0	1.9	1.08	Photo
U2162	B	Oct90	22	3×600.0	1.2	1.27	Photo
	I f	Oct90	22	3×420.0	0.9	1.35	Photo
	B	Jan93	24	3×600.0	1.5	1.33	Cirrus
	I	Jan93	24	3×420.0	1.2	1.44	Cirrus
K37	B	Oct90	21	3×600.0	1.4	1.28	Photo
	I	Oct90	21	3×600.0	1.0	1.25	Photo
	B	Sep91	16	1×300.0	1.8	1.24	Photo
	I f	Sep91	15	2×450.0	2.4	1.25	Photo
K37C	B	Sep91	16	2×300.0	1.8	1.25	Photo
	I	Sep91	15	1×600.0	2.4	1.25	Photo
U3212	B	Oct90	21	3×600.0	1.2	1.29	Photo
	I f	Oct90	21	3×420.0	1.2	1.30	Photo
U3384	B	Apr91	17	3×600.0	1.7	1.69	Photo
	I f	Apr91	17	3×420.0	1.4	1.61	Photo
U3817	B	Oct90	21	3×600.0	1.4	1.04	Photo
	I f	Oct90	21	3×420.0	1.0	1.03	Photo
U3860	B	Oct90	22	3×583.0	1.4	1.04	Photo
U3966	B	Apr91	18	3×600.0	1.7	1.23	Cirrus
	I	Apr91	18	3×420.0	1.4	1.14	Cirrus
U4204	B	Apr91	19	3×600.0	2.0	1.21	Cirrus
	I	Apr91	19	2×420.0	1.4	1.17	Cirrus
U4173	B	Apr91	18	3×600.0	2.7	1.65	Cirrus
	I	Apr91	18	3×420.0	2.7	1.61	Cirrus
	B	Jan93	23	2×600.0	1.2	1.51	Photo
	I	Jan93	23	2×420.0	1.2	1.50	Photo
M81dwA	B	Apr91	17	3×600.0	1.7	1.52	Photo
	I	Apr91	17	3×420.0	1.4	1.46	Photo
	B	Jan93	23	3×600.0	1.2	1.34	Photo
	I	Jan93	23	3×420.0	1.4	1.37	Photo
M81dwB	B	Jan93	24	3×600.0	1.8	1.34	Cirrus
	I	Jan93	24	3×420.0	1.5	1.30	Cirrus
U5706	B	Apr91	21	3×600.0	17.1	00	Photo
	I	Apr91	21	3×420.0	1.4	1.00	Photo

Table 3 continued

Galaxy	band	run	night	exp. time (#×sec)	seeing arcsec	airmass	sky conditions
U5709	B	Apr91	17	3×600.0	3.4	1.36	Photo
	I	Apr91	17	4×465.0	1.4	1.21	Photo
U6151	B	Apr91	20	3×600.0	2.0	1.05	Photo
	I	Apr91	20	3×420.0	1.7	1.03	Photo
U6248	B	Apr91	21	3×600.0	1.7	1.09	Photo
	I	Apr91	21	3×420.0	1.4	1.08	Photo
U6596	B	Apr91	19	3×600.0	1.4	1.10	Cirrus
	I	Apr91	19	3×420.0	1.4	1.10	Cirrus
U6628	B	Apr91	17	3×300.0	2.4	1.35	Photo
	I	Apr91	17	3×300.0	2.0	1.26	Photo
	B	Apr93	20	2×600.0	1.7	1.06	Cirrus
U7295	B	Apr91	20	3×600.0	3.1	1.01	Photo
	I	Apr91	20	3×240.0	1.7	1.00	Photo
U7548	B	Apr91	19	3×600.0	2.0	1.10	Cirrus
	I	Apr91	19	3×420.0	2.0	1.07	Cirrus
U7596	B	Apr91	19	3×600.0	1.4	1.36	Photo
	I	Apr91	19	3×420.0	1.7	1.26	Photo
U7608	B	Apr91	18	3×600.0	1.4	1.04	Cirrus
	I	Apr91	18	3×420.0	1.2	1.03	Cirrus
	B	Apr93	18	3×600.0	1.7	1.03	Cirrus
U7636	B	Apr91	21	3×600.0	1.4	1.11	Photo
	I	Apr91	21	3×420.0	1.4	1.10	Photo
U7684	B	Apr91	21	3×600.0	1.7	1.13	Photo
	I	Apr91	21	3×420.0	1.4	1.08	Photo
U7882	B	Apr91	19	3×600.0	2.0	1.00	Cirrus
	I	Apr91	19	3×420.0	1.5	1.01	Cirrus
U8091	B	Apr91	21	2×600.0	1.4	1.34	Cirrus
	I	Apr91	21	2×420.0	1.4	1.23	Cirrus
U8201	B	Apr93	19	2×600.0	2.0	1.32	Cirrus
U8683	B	Apr91	21	3×600.0	1.4	1.29	Photo
	I	Apr91	21	3×420.0	1.4	1.20	Photo
U8760	B	Apr91	19	3×600.0	1.4	1.23	Cirrus
	I	Apr91	19	4×465.0	1.5	1.14	Cirrus
U8833	B	Apr91	19	4×570.0	1.7	1.58	Photo
	I	Apr91	19	6×390.0	1.0	1.48	Photo
U9128	B	Apr91	21	2×600.0	1.9	1.56	Photo
	I	Apr91	21	3×420.0	1.5	1.42	Photo
U9391	B	Apr91	17	3×600.0	2.0	1.21	Cirrus
	I	Apr91	17	3×420.0	2.2	1.18	Cirrus
U10031	B	May85	23	1×600.0	2.4	1.44	Photo
	R	May85	23	1×600.0	2.1	1.41	Photo
	I	Apr91	20	3×420.0	1.4	1.18	Photo
U10058	B	May85	23	1×600.0	1.8	1.28	Photo
	R	May85	23	1×600.0	1.8	1.33	Photo
	I	Apr91	17	3×420.0	1.7	1.08	Cirrus
U10290	B	May85	22	1×900.0	1.8	1.39	Photo
	R	May85	22	2×300.0	1.8	1.34	Photo
	I	Apr91	17	3×300.0	1.7	1.29	Cirrus
U10376	B	May85	23	1×900.0	1.5	1.27	Photo
	R	May85	23	2×450.0	1.5	1.25	Photo
	I	Apr91	20	3×420.0	1.4	1.22	Photo
U10669	B	May85	22	1×900.0	1.8	1.33	Photo
	R	May85	22	2×300.0	1.5	1.35	Photo
	I	Apr91	20	3×420.0	1.4	1.30	Photo
U11764	B	May85	22	1×900.0	2.1	1.21	Photo
	R	May85	22	1×600.0	1.8	1.26	Photo
U12082	B	Sep91	13	3×300.0	1.8	1.27	Photo
	I	Sep91	13	2×300.0	1.8	1.04	Photo
U12151	B	May85	23	1×600.0	1.5	1.61	Photo
	R	May85	23	1×600.0	1.5	1.53	Photo
U12894	B	Oct90	21	3×600.0	1.4	1.14	Photo
	I f	Oct90	21	3×420.0	1.4	1.09	Photo

B ($\lambda_o = 4320$Å, FWHM=1064Å) and Mould I filters were used for the remaining runs (Sep91 and Jan93). The different filters had the effect of changing the transformation coefficients for the different runs (see §2.3). The transmission curves for the Harris and Mould filters are shown in Figure 1.

The photometry was calibrated by making repeated observations of several standard stars from Landolt (1983) throughout the night. Fainter standards from the new list of Landolt (1992) were used during the Apr 91 and Jan 93 runs. During the May 85 run, additional observations were made of a standard field in Selected Area 57 which contained fainter stars, with a moderate range in color, and photometry provided by Sandage (1985). Observations of the globular clusters identified by Christian *et al.* (1985), with photometry from Davis (1991), were made during the Apr 91, Jan 93, and Apr 93 runs. In addition, M67 (Schild, 1983) was observed during the Apr 93 run.

Dome flats using the standard color corrected lamps and a white reflective spot on the inside of the dome were taken at the beginning and end of each night. A sequence of ∼ 20 bias frames were also taken at this time. In addition, twilight flats of the sky were obtained each night in each filter, usually in the evening. A "blank" field, containing few bright stars, from Christian *et al.* (1985) was imaged several times with slight offsets between exposures during each run (except for May 85 and Jan 93). Since the May 85 and Jan 93 runs were made up mostly of observations of point sources (Thuan *et al.* 1992, and Gelderman 1994), these object frames were combined to form equivalent blank dark sky and fringe frames (see following section).

2.3   Data Reduction

The CCD data were reduced by using the IRAF[2] software package CCDRED. The
following description applies in particular to the TEK2/T5HA 512×512 chip which
was used to obtain the majority of the data, but all the data were reduced using the
same basic procedure (see Massey & Jacoby 1992).

First, a bias offset, equal to the mean of 32 columns in the overscan region
from each row, was subtracted from each frame. The resulting images were then
trimmed to a 508×508 format. A composite zero frame, the average of 20 in-
dividual bias frames (with the overscan already subtracted), was constructed with
the ZEROCOMBINE task and then subtracted from all frames to compensate for
pixel-to-pixel variations in the bias level. This bias pattern was found to be very
stable throughout the night and from night to night.

High signal–to–noise level dome flats for each night were combined with FLAT-
COMBINE, which scales the individual flats by the median to create a master dome
flat, for the removal of the pixel to pixel variation in the detector sensitivity. The
twilight sky flats and/or the blank dark sky flats where then combined with the dome
flats using MKILLUMCOR, which heavily smooths the lower signal to noise sky
flats so that they can be used to remove the large scale variation of the detector.
The dome flats may not illuminate the CCD in the same way as the night sky does

---

[2]IRAF is distributed by National Optical Astronomy Observatories, which is operated by the
Association of Universities for Research in Astronomy, Inc., under cooperative agreement with the
National Science Foundation

because of light leaks, uneven illumination of the white spot on the dome, or incorrect color balance of the lamps. As a result, the large scale variation of the detector can only be removed with sky flats, preferably blank dark sky flats, to achieve the best color match with the object frames.

The blank dark sky exposures in the $I-$ and $R-$bands were used to remove the interference fringe pattern produced by night sky emission lines. In this case the blank dark sky frames were not smoothed as described above. Instead they were processed using CCDRED in which the overscan is removed, the master zero frame is subtracted, the image is trimmed, and finally the master flat for the night is scaled and divided into the blank dark sky exposure. The individual frames from the same night and in the same filter are combined using COMBINE. The median value of the resultant frame is determined and subtracted from the frame, leaving a fringe frame with a median of zero. This fringe frame is then scaled by factors of 0.1 to 2.0 and subtracted from the fringed galaxy images which had previously been processed through the flat fielding stage.

At this point, the images were inspected to see which subtraction had produced the most complete removal of the fringes. In this way, the fringes were removed without changing the average value across the frame. This trial and error process is necessary because the fringe levels change throughout the night depending on the relative position of the sun with respect to the upper atmosphere where the night sky emission lines are produced.

The blank dark sky exposures for the Oct 90 run were obtained on the first clear night of the run, after which the secondary of the 2.1m telescope shifted notice-

ably (throwing the focus off by a very large amount, among other things). It was later discovered that the optical path had changed enough to render the resulting frames useless for removing fringes from data taken after the secondary shift. The frames were still found to be sufficient for the removal of large scale variations as flat field frames. Therefore, the I–band frames of eleven galaxies were contaminated by fringes; six of these objects were subsequently reobserved leaving just five galaxies with some fringes. These objects are indicated by an f next to the I in the band column of Table 3. The fringes cause a $\sim$ 2% systematic variation on a fairly small ($\sim$ 20 pixel) spatial scale.

After the individual object frames were processed through the flat fielding stage using CCDRED (and fringes removed as described above from the I– and R–band frames), the separate exposures were aligned using IMALIGN. This routine determines the centroids of the stars in the frame and then shifts and trims the images. The COMBINE task was then used to combine the images by filter, using average sigma clipping to remove most of the cosmic rays and bad pixels. Of course, in the few cases in which there were only two images taken in a filter, the images could only be averaged (which will not remove the cosmic rays). The COSMICRAYS task was then used to remove nearly all of the remaining radiation events in the combined frames, after which IMEDIT was used to remove any remaining blemishes. At this point, the systematic variation across the frame was $\sim$ 2%.

2.3.1 Sky Subtraction

A low order polynomial, usually a tilted plane, was fit to the sky surrounding the galaxy on each frame, using IMSURFIT. Great care was taken to avoid including in the fit any of the outer regions of the galaxy itself or the halos of bright stars. The sky subtraction proved to be particularly critical because of the large angular size and low surface brightness of many of these nearby galaxies and the relatively small field of view of most of the observations.

It was found empirically that the *shape* of the sky could be best fit by setting sigma rejection to 3 sigma for both the lower and upper rejection ($3\sigma_L, 3\sigma_U$), while the *median* value for the sky intensity was best determined with 3 sigma lower rejection and 0 sigma upper rejection ($3\sigma_L, 0\sigma_U$). This was possibly due to the presence of numerous background stars which contribute only in a positive sense to the sky intensity. Therefore the ($3\sigma_L, 3\sigma_U$) frame was scaled to the level of the ($3\sigma_L, 0\sigma_U$) frame. The scaling of the sky frame in this way did not introduce much additional error since the difference between the medians of the two frames was less than $\sim 1\%$, which is the approximate error in the sky level determination itself. This resulting sky frame was then subtracted from the image, and this sky–subtracted frame was then divided by the sky frame to produce a normalized sky–subtracted frame. This technique of normalizing the object frames serves to remove most of the residual local errors (Pence 1978; Carignan 1983 and 1985; Ichikawa, Wakamatsu, & Okamura 1986). The pixel to pixel variation across the frame at the end of the reduction was less than $\sim 1\%$.

The effective exposure time, or the mean of the exposure times for all of the images that were combined, the effective airmass determined with the SETAIRMASS task, and the sky level in ADU obtained from the median of the $(3\sigma_L, 0\sigma_U)$ frame, were then added to the header using HEDIT. Finally the images were reoriented so that North was at the top and East at the left using IMTRANSPOSE and/or ROTATE, depending on the original orientation.

2.4   Photometric Calibration

Aperture photometry was performed on the standard star observations using the PHOT task in IRAF. An aperture, usually 30 pixels in radius (at least $5 \times$ FWHM), was automatically centered on the standard to be measured, then a radial profile was extracted and examined to determine whether the standard was saturated or contaminated by fainter stars. The most frequently occurring value, or mode, of the pixel values in a sky annulus was determined (after sigma rejection) and this sky level was subtracted. The resulting counts within the aperture were summed up and converted to a PHOT instrumental magnitude using

$$\mathrm{m}_{phot} = -2.5 \log \left[\sum^{aperture} \frac{\mathrm{ADU}}{t} \right] + \mathrm{zmag}, \tag{2.1}$$

where ADU is the number of counts in Analog to Digital Units, t, is the exposure time in seconds and zmag is an arbitrary, but fixed, zero point selected so that the magnitudes come out to reasonable numbers. In this work, zmag was always set equal to 26.

For crowded fields typical of the globular cluster fields of Davis (1991), it is necessary to use a much smaller aperture to avoid contamination from neighboring stars. In these cases, several bright and relatively isolated stars in the frame are selected and measured using both this smaller aperture and the larger (~ 30 pixel) aperture, while the remaining stars are measured using only the smaller aperture (typically ~ 5 pixels). Again, the radial profiles are useful for detecting faint nearby stars. Aperture corrections are then determined for each frame by averaging the corrections for each of the bright, uncontaminated stars selected.

The PHOTCAL package was then used to determine the transformation equations for photometric calibration. Transformation equations of the form

$$B - I = \alpha_{(B-I)} \left[(b_{phot} - k_B * X_B) - (i_{phot} - k_I * X_I) \right] + \zeta_{(B-I)} \qquad (2.2)$$

$$B = \alpha_B \left[B - I \right] + (b_{phot} - k_B * X_B) + \zeta_B \qquad (2.3)$$

$$I = \alpha_I \left[B - I \right] + (i_{phot} - k_I * X_I) + \zeta_I, \qquad (2.4)$$

were set up and verified with the MKCONFIG and CHKCONFIG tasks. Here α is the slope and ζ the zero point of the color and magnitude equations, k is the extinction coefficient and X the airmass, and b_{phot} and i_{phot} are the instrumental B and I magnitudes from equation 2.1.

The parameter fitting procedure requires that certain information be prepared for input into the PHOTCAL fitting routine, FITPARAMS, using the routines MKIMSETS and MKNOBSFILE. These include the instrumental magnitude of the standards, the image header files for each observation, the aperture corrections for each image, and a catalog of standard star magnitudes and colors.

Table 4a
2.1m Photometric Calibration

Run Night	# of stds	Extinction Coefficients			Transformation Slopes			Transformation Zero Points		
		k_B (σ)	k_I (σ)	k_{B-I} (σ)	α_B (σ)	α_I (σ)	α_{B-I} (σ)	ζ_B (σ) [RMS]	ζ_I (σ) [RMS]	ζ_{B-I} (σ) [RMS]
Oct 1990	26	0.1619 (0.0369)	0.0576 (0.0183)	0.1120 (0.0375)	0.0811 (0.0037)	0.0047 (0.0016)	1.0784 (0.0037)	....	....	....
20	10	....	....	....	....	....	....	−2.0504 (0.0049) [0.085]	−2.8864 (0.0031) [0.027]	0.9074 (0.0043) [0.062]
21	9	....	....	....	....	....	....	−2.0250 (0.0043) [0.081]	−2.8798 (0.0023) [0.026]	0.9252 (0.0045) [0.060]
22	7	....	....	....	....	....	....	−2.0215 (0.0039) [0.091]	−2.8957 (0.0064) [0.054]	0.9495 (0.0164) [0.063]
Apr 1991	64	0.1935 (0.0393)	0.0412 (0.0205)	0.1699 (0.0154)	0.0711 (0.0043)	−0.0103 (0.0039)	1.0926 (0.0041)	....	....	....
17	28	....	....	....	....	....	....	−2.0254 (0.0066) [0.446]	−2.9208 (0.0073) [0.076]	0.9741 (0.0019) [0.495]
18	59	....	....	....	....	....	....	−2.0795 (0.0218) [1.828]	−2.9901 (0.0092) [0.917]	0.8450 (0.0726) [0.962]
19	17	....	....	....	....	....	....	−2.0794 (0.0073) [0.461]	−2.9264 (0.0039) [0.049]	0.9536 (0.0102) [0.554]
20	50	....	....	....	....	....	....	−2.0315 (0.0034) [0.331]	−2.8977 (0.0033) [0.044]	0.9431 (0.0079) [0.377]
21	31	....	....	....	....	....	....	−2.0224 (0.0042) [0.035]	−2.8984 (0.0025) [0.038]	0.9627 (0.0047) [0.065]
Jan 1993	118	0.3079 (0.0282)	0.0999 (0.0289)	0.2887 (0.0307)	0.0509 (0.0051)	0.0023 (0.0075)	1.0460 (0.0071)	....	....	....
23	50	....	....	....	....	....	....	−1.7061 (0.0052) [0.060]	−2.2658 (0.0085) [0.113]	0.6227 (0.0103) [0.098]
24	68	....	....	....	....	....	....	−1.7762 (0.0067) [0.053]	−2.3066 (0.0070) [0.076]	0.5789 (0.0071) [0.058]

Table 4b
0.9m Photometric Calibration

Run / Night	# of stds	Extinction Coefficients			Transformation Slopes			Transformation Zero Points		
		k_B (σ)	k_I (σ)	k_{B-I} (σ)	α_B (σ)	α_I (σ)	α_{B-I} (σ)	ζ_B (σ) [RMS]	ζ_I (σ) [RMS]	ζ_{B-I} (σ) [RMS]
Sep 1991	66	0.3359 (0.0276)	0.0885 (0.0439)	0.2183 (0.05787)	0.0321 (0.0054)	−0.00799 (0.0043)	1.0572 (0.0064)	....	....	....
13	12	....	....	....	....	....	....	−4.0854 (0.0075) [0.024]	−4.6846 (0.0103) [0.025]	0.5639 (0.0180) [0.044]
14	11	....	....	....	....	....	....	−4.0371 (0.0103) [0.033]	−4.6662 (0.0061) [0.016]	0.5965 (0.0092) [0.024]
15	17	....	....	....	....	....	....	−4.0295 (0.0044) [0.018]	−4.6689 (0.0058) [0.022]	0.6151 (0.0073) [0.028]
16	10	....	....	....	....	....	....	−4.0141 (0.0056) [0.017]	−4.6651 (0.0056) [0.016]	0.6092 (0.0066) [0.019]
Apr 1993		0.1935 (Jan93)	....	....	....	....	....	....	....	....
18	39	....	....	....	....	....	....	−4.7897 (0.0137) [0.120]	....	....
19	57	....	....	....	....	....	....	−4.8285 (0.0089) [0.098]	....	....
20	57	....	....	....	....	....	....	−4.8212 (0.0102) [0.241]	....	....

4m Photometric Calibration

Run	# of stds	Extinction Coefficients			Transformation Slopes			Transformation Zero Points		
		k_B	k_R	k_{B-R}	α_B (σ)	α_R (σ)	α_{B-R} (σ)	ζ_B (σ)	ζ_R (σ)	ζ_{B-R} (σ)
May 1985	51	0.23	0.10	0.13	0.0747 (0.1727)	−0.0022 (0.0245)	1.0829 (0.0105)	−2.3307 (0.0196)	−2.6612 (0.0277)	0.3581 (0.0094)
		(canonical KPNO values)								

The FITPARAMS task was used to perform an interactive linear least squares fit, which allows bad observations to be flagged and rejected. The fit was performed three times for each observing run. On the first iteration, the best estimate of the extinction was found by fitting the entire data set (all standards observed on a given run) and allowing k, α, and ζ to vary. The extinction was then set to this value and the slope and zero point were fit again, to obtain the value of the slope for the entire run. The final fit was performed holding both the extinction coefficient and the slope constant while determining the zero points for each night of the run.

For the May 85 run, a common solution was determined for all 3 nights as there were too few observations of standard stars to allow an accurate nightly zero point determination. Also, equations 2.2 to 2.4 were changed by replacing I with R. In Apr 93, once again there were an insufficient number of standard star observations. In this case the Jan 93 observing run extinction coefficient, k_B, was adopted. Since only B observations were made during the Apr 93 run, the equations simplify to

$$B = b_{phot} - k_B * X_B + \zeta_B, \tag{2.5}$$

which unfortunately removes all color dependence from the fit.

The extinction coefficients, slopes and zero points for all the runs are listed in Table 4a and 4b. The standard deviation of the fit, as well as the r.m.s. of the standards from the fit for zero point are listed.

2.4.1   Flux Calibration of Galaxy Images

The normalized sky-subtracted galaxy images were converted into flux calibrated images with the aid of IMFORT, a FORTRAN programming environment designed to interface with IRAF. This program, CALIB, accesses the relevant header information, namely the run and night of observation, filter, effective airmass, exposure time and sky level from the B and I or R-band image. The appropriate pixel scale, extinction and transformation coefficients and photometric zero points are selected automatically based on this header information. The $(B - I)$ sky color in mag arcsec^{-2} was calculated from

$$(B - I)_{sky} = \alpha_{(B-I)}(b - i)_{0,sky} + \zeta_{(B-I)}, \tag{2.6}$$

where the B-band instrumental magnitude is given by

$$b_{0,sky} = -2.5 \log \left[\frac{C_{Bsky}}{S^2 t_B} \right] - k_B * X_B + 26, \tag{2.7}$$

with a similar equation for $i_{0,sky}$. C_{Bsky} is the sky level in ADU (Analog to Digital Units) for the B image, and t_B and X_B are the effective exposure time and airmass for the B image. These parameters were read directly from the image header. The plate scale, S, in arcsec pixel^{-1}, and the extinction coefficient, k_B, were selected based on the run and night information in the header. The zero point shift of 26 is chosen to keep magnitudes consistent with the standards measured with PHOT (see equation 2.1).

The sky brightness in each filter was calculated using equation (2.6)

$$B_{sky} = \alpha_B(B - I)_{sky} + b_{0,sky} + \zeta_B, \tag{2.8}$$

with a similar equation for I_{sky}.

Since the images are in the form

$$C_{rel}(B) \;=\; \frac{C_{gal+sky}(B) - C_{sky}(B)}{C_{sky}(B)}, \qquad (2.9)$$

all of the zero point, pixel scale, and extinction terms are contained in the B_{sky} term and flux calibrated images can simply be obtained by including the slopes, α, in the following way:

$$F(B) = C_{rel}(B-I)^{\alpha_B \alpha (B-I)} \; C_{rel}(B)10^{-B_{sky}/2.5}, \qquad (2.10)$$

with a similar equation for $F(I)$, and

$$F(B-I) = C_{rel}(B-I)^{\alpha (B-I)} \; 10^{-(B-I)_{sky}/2.5}. \qquad (2.11)$$

The flux calibrated images were calculated in units of $\mathrm{ergs/s/cm^2/\mathring{A}} \times 10^{10}$ to avoid roundoff errors due to small numbers. Magnitudes calibrated on the standard system were then calculated using

$$B = -2.5 \log\left[F(B) \times 10^{10} \right] \;+\; 25, \qquad (2.12)$$

with similar equations for I and $B-I$. The additive constant of $25 = 2.5 \log 10^{10}$ is present simply because the flux has been multiplied by a factor of 10^{10}.

2.5 Ellipse Fitting and Radial Profile Extraction

The one–dimensional, azimuthally averaged radial profiles of the surface brightness of the galaxies, $\mu(r)$, can be obtained by fitting ellipses to the galaxy isophotes. Two

fitting algorithms were tested. The first, the ISOPHOTE package in STSDAS, is based on an iterative least squares fit to a Fourier expansion, implemented in GASP (GAlaxy Surface Photometry package) by M. Cawson (Carter 1978; Davis et al., 1985) and described in some detail by Jedrzejewski (1987). This method is widely used in fitting the surface brightness distributions of elliptical galaxies. The contributions of the various terms in the Fourier series indicate the nature and extent of any deviation from ellipticity. However, it is necessary to use a modified technique when fitting the light of spiral and irregular galaxies (which have even less uniform profiles), because the ISOPHOTE algorithm often produces an unstable fit (Freudling 1992).

This latter technique involves a fully two–dimensional linear fit of the harmonics to the image. The intensity in this case is parameterized by

$$I(r, \phi) = \sum_{n=0}^{k} I_n(r) \cos \left\{ n \left[\phi - \phi_n(r) \right] \right\}, \tag{2.13}$$

which yields a direct (non–iterative) linear determination of the fit. This fit is then used as the initial value for the usual Fourier series expansion fit as in ISOPHOTE, in order to obtain the ellipticity directly. This procedure is implemented in GALPHOT which was written by Marijn Franx with some modifications by Inger Jørgensen (Franx, Illingworth & Heckman 1989; Jørgensen, Franx & Kjærgaard 1992).

Stars and cosmic rays were masked out using DAOPHOT (Stetson 1987) based routines called GALFIND and CLASSIFY, which generate several lists of pixels to be avoided in the subsequent fit. The harmonic fit was done using the routine HARMFIT, and a residual image was inspected for any remaining stars or cosmic rays which may have been previously masked by the galaxy image. Most of these are

automatically marked and masked by the DEVIATE task, which masks any pixel which deviates by more than $5 \times r.m.s.$ from zero in this residual image.

The results from the harmonic fit are then used as the initial values for the ellipse–fitting routine, ELLIPFIT. The ellipses were generally allowed to vary in center, position angle, and ellipticity out to about 100 pixels, and ellipses were fit out to a radius where only 60% of the points on the ellipse lay within the image. This had the advantage of incorporating the sky dominated regions of the image into the profile, allowing the sky level to be checked using the task SKYCALC as described in Jørgensen *et al.* (1992). The sky subtraction detailed in §2.2.1 was found to be adequate and no changes were made to the sky level at this point.

In order to fit galaxies as irregular as the ones in this sample, the allowed errors in the shape and position of the ellipse had to be increased from 2% to 10%; the remaining values for all the tasks were set to their default values.

Most of the irregularity in these galaxies is actually intrinsic to the galaxy (i.e. HII regions, not foreground stars) and contributes to the total light, but must be considered excess to the underlying stellar component that is being fit. Therefore, some modifications were made to the GALPHOT package. The HII regions and stars within the galaxy were excluded from the image along with the foreground stars and cosmic rays during the fitting process. An additional task, GETMU, was written to allow the profiles to be calculated from the actual galaxy image rather than from the model image produced by ELLIPFIT. This is described below.

After the ellipses had been fit and the resulting residual image inspected for any

remaining deviant pixels (and refitting performed as needed), the task MODMAGS was used to calculate the surface brightness and total magnitudes as a function of the effective radius, $r_{eff} = \sqrt{ab}$, where a and b are the semi–major and semi–minor axis lengths, respectively. The task was run three times. First, it used the model intensity calculated from ELLIPFIT (the original version of MODMAGS). These are the profiles to which the exponentials were fitted as described in Chapter 3 and plotted in Figures 3–64. Next, profiles were calculated with the actual intensity including any HII regions and stars in the galaxy, masked during the fitting, but here included through GETMU. These are the profiles which are plotted as points in Figures 3–64. Finally, all foreground stars were included as well (again through GETMU), in order to more easily illustrate which parts of the profile were being distorted by the stars which had not been completely masked out.

The profiles were magnitude calibrated by adding a zero point of 25.0 (since the flux calibrated images have been multiplied by 10^{10}; see equation 2.12) and the radius was converted from units of pixels to arcseconds in MODMAGS. The resulting profiles were written to STSDAS TABLES format tables, which simplifies subsequent manipulation of the data.

2.6 Comparison with Previous Data

Surface photometry exists for several of the galaxies in this sample, from either photographic or CCD images. The photographic data include observations of UGC 5423 (Schmidt, Richter & Karachentseva 1985); UGC 7548, UGC 7596 and UGC
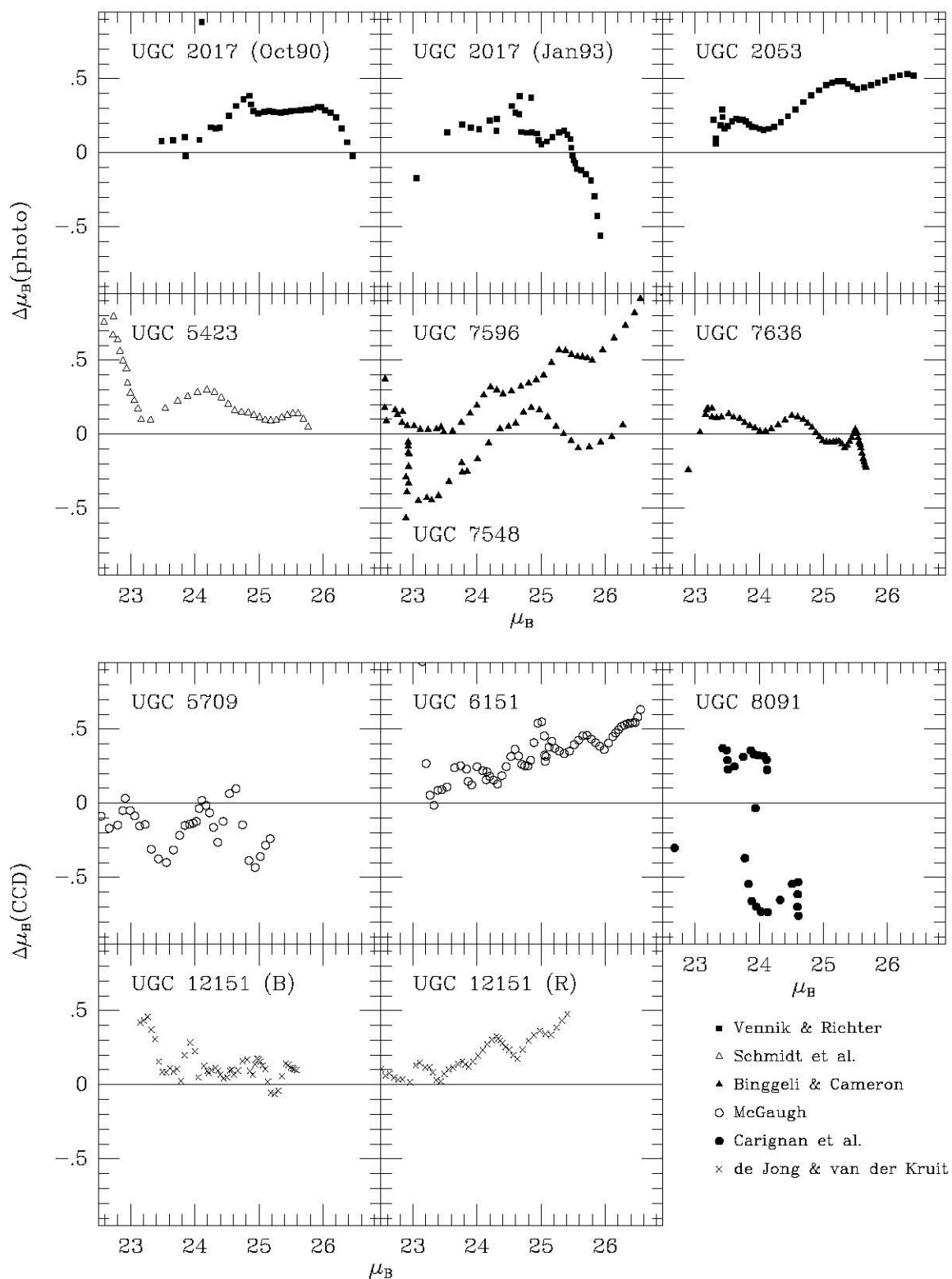
Figure 2: Comparison with other Photographic and CCD Surface Photometry. $\Delta\mu_B = \mu_B(\text{This work}) - \mu_B(\text{Literature})$.

7636 by Binggeli & Cameron (1993); and UGC 2017 and UGC 2053 by Vennik & Richter (1994). The comparison with our data, in the sense $\Delta\mu_B = \mu_B(CCD) - \mu_{photo}$, is shown in the upper half of Figure 2. The deviation at extremely low surface brightness levels is attributable to small uncertainties in the sky level, color gradients (since the passbands do not match) and the fact that the profiles are dependent on the reduction technique (choice of "center" of the galaxy). The proximity of NGC 4472 to UGC 7636 surely contributes to the small difference between the Binggeli & Cameron data and our data (see Patterson & Thuan 1992, for details of the sky subtraction in the case of UGC 7636).

The surface brightness profiles obtained from CCD $B-$band data is compared with our own data in the lower half of Figure 2. The UGC 5709 and UGC 6151 data are from McGaugh & Bothun (1993); the UGC 8091 data are from Carignan, Beaulieu & Freeman (1990); and the UGC 12151 data are from de Jong & van der Kruit (1994). The intrinsic irregularity of the galaxies (especially UGC 8091) makes it difficult to directly compare fits made using different algorithms. In particular, the choice of which stars to exclude from the fit obviously has a great impact on the final profile. Under these limitations, it was felt that the agreement with the previous data (typically, $\Delta\mu_B < 0.5$mag arcsec^{-2}), as illustrated in Figure 2, was satisfactory.

2.7 Presentation of the Data

Immediately following this section is a series of figures which present the imaging data, as well as the results of the ellipse fitting for each galaxy. In Figures 3–63 a greyscale image along with a contour plot are shown for each galaxy for each band in which it was observed. The center of the galaxy from the ellipse fitting, and the scale in arcseconds, is indicated on the contour plot. Below these, the surface brightness profile from the ellipse fitting is given both with (open circles) and without (closed circles) the HII regions and stars in the galaxy included in the total light. The actual fit was made to the $I-$band image with the "HII regions" excluded. This isophotal fit was then used to obtain the profile fit including these "HII regions". The B profile was also obtained using the $I-$band isophotal fit. The line shown is a fit to the indicated region *without* "IIII regions"

In Figures 64–71, the ellipticity and $\cos(4\theta)$ term, from the ellipse fitting, and the color profile are shown. The ellipticity ($e = 1 - b/a$) varies a great deal for small radii, but usual becomes stable at large r_{eff}. The adopted value of the ellipticity (the average value of the ellipticity at large radii), used to derive the inclination in Chapter 3, is marked. The variation of the $\cos(4\theta)$ term indicates to some extent how well the galaxies light is fit by an ellipse at a given isophote level. Deviations of this term from 0 are used to determine whether an elliptical galaxy has "peanut–shaped" or "pointy" isophotes. In the present application we use this deviation as a measure of the applicability of elliptical isophotes to these galaxies. If there is a large deviation from 0 at a large r_{eff}, the assumption of an underlying disk is suspect.

Corrections to the magnitude and HI linewidth (discussed in Chapter 3) based on an assumed inclination are questionable under these circumstances, and these galaxies are excluded from the Tully–Fisher analysis in Chapter 4.

The color profiles were formed from the difference of the average surface brightness (*excluding* "HII regions"; actually HII regions as well as stars present in the galaxy and masked for the ellipse fitting) within an elliptical annulus in each filter. The ellipses are identical in each filter, having been determined from the I–band image.

Histograms of the size distribution of the "HII regions" are shown in Figures 72 74. The clumpiness of the distribution is caused by the finite pixel size. The radial and azimuthal distribution of these regions are presented in Figures 75–80. The data are presented in this way to give a feel for the distribution of the regions which were excluded from the fit. Because the objects are not restricted to HII regions, it would be misleading to compare these data with that of authors such as van den Bergh (1981) and Strobel, Hodge & Kennicutt (1991), who investigate the size distribution of HII regions with respect to the global properties of the parent galaxies.

Figures 3–63: Images, Contour Plots and Surface Brightness Profiles of all Galaxies in the Sample. The first 53 (Figures 3–56) figures are of B and I pairs of images of galaxies in the sample, with the remainder being R data and B data with no corresponding I data. All of the images (upper panel) are oriented with North at the top and East to the left.

The contour plots (middle panel) are plotted in steps of 0.5 mag arcsec^{-2}, starting at a contour level of 27.0 for B and R and 25.5 for I, unless specifically noted on the figure. The highest contour level shown, usually corresponding to the peak surface brightness within the galaxy, is listed. The arrows in the contour plot indicate the center that was used for fitting ellipses, determined from the $I-$band image. The scale for both the images and contour plots is indicated by the scale bar in the contour plot. Also, each of the small tickmarks around the contour and the image plots represent $20''$.

The surface brightness profiles panels (at the bottom) show the profiles ($\bullet$), obtained from GALPHOT, excluding the HII regions and stars and the exponential fit (described in Chapter 3) over the indicated interval of radius. In addition, the points including the HII regions and stars within the galaxy, but excluding foreground stars, are plotted (o) for comparison. In nearly every case, the $I-$band image was used in the ellipse fitting. In the few cases where no I data was taken, they were fit to either the $R-$ (if available) or $B-$band images.

B **I**

$\mu_{\rm top}=22.0$

$\mu_{\rm top}=21.0$

15"

fit

fit

μ_B

μ_I

r (arcsec)

r (arcsec)
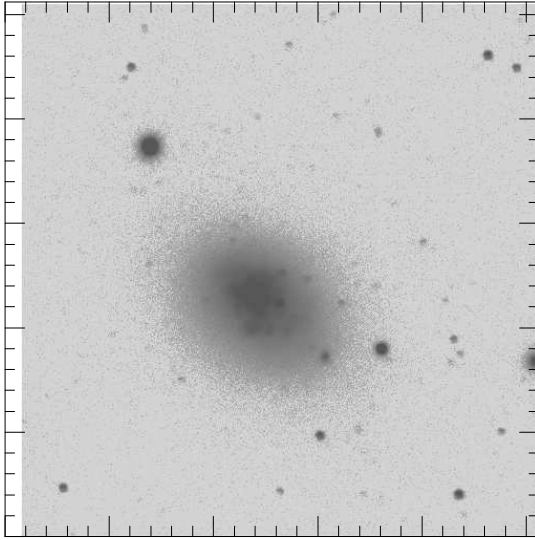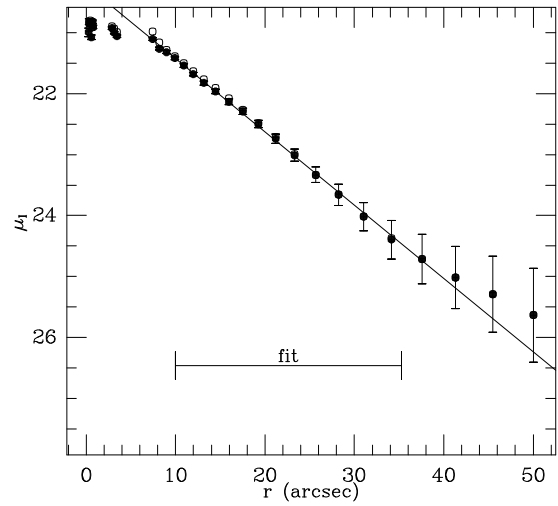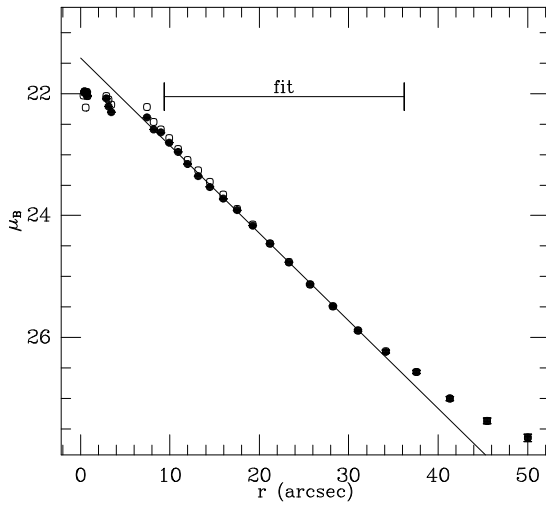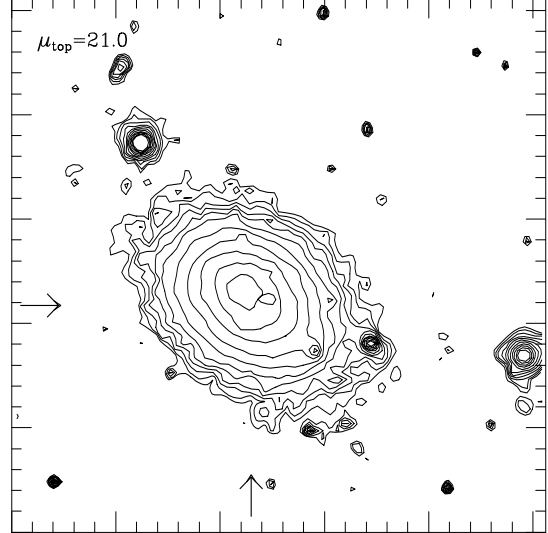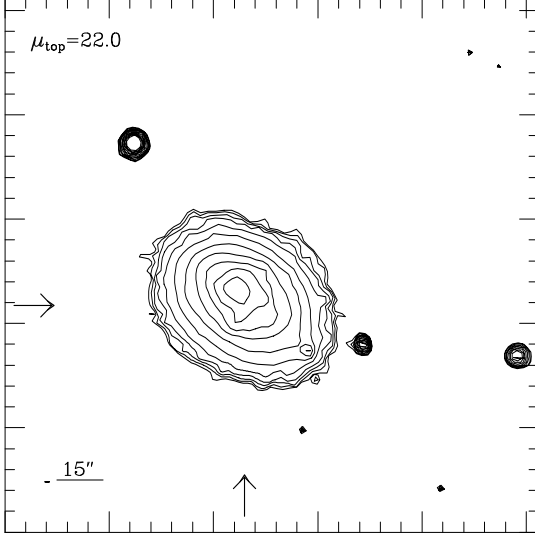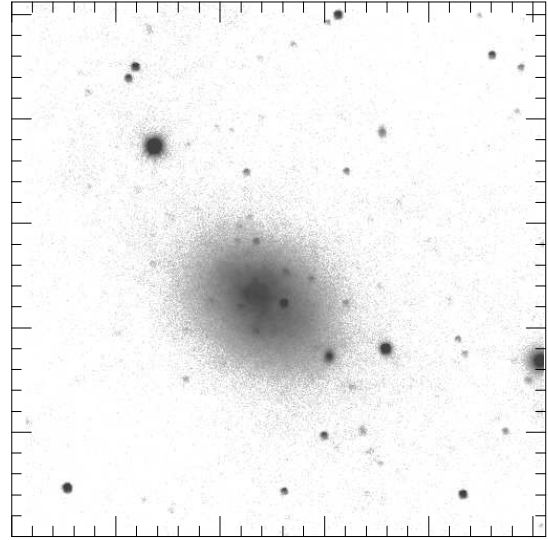
Figure 3: UGC 00031
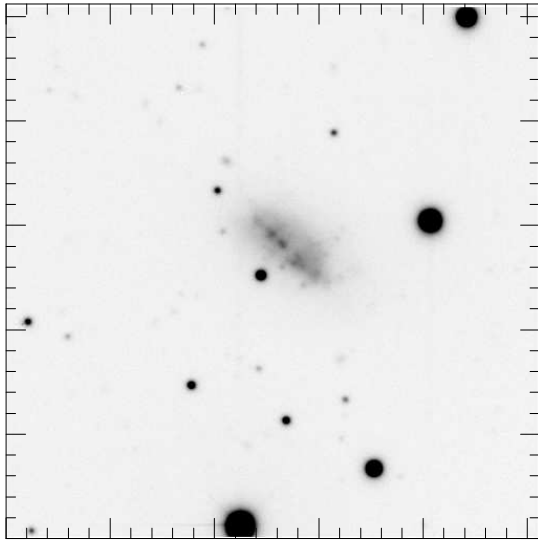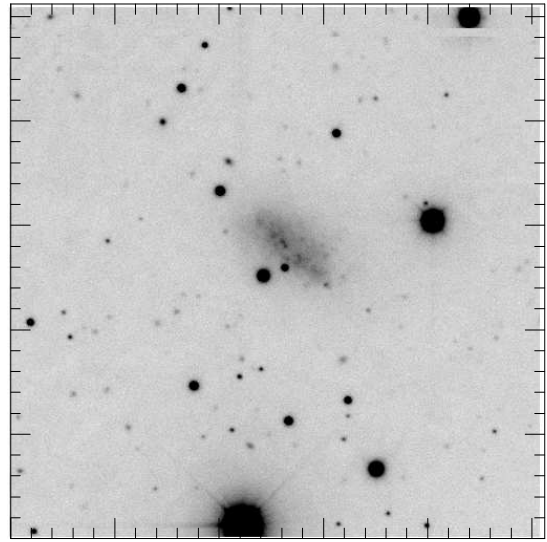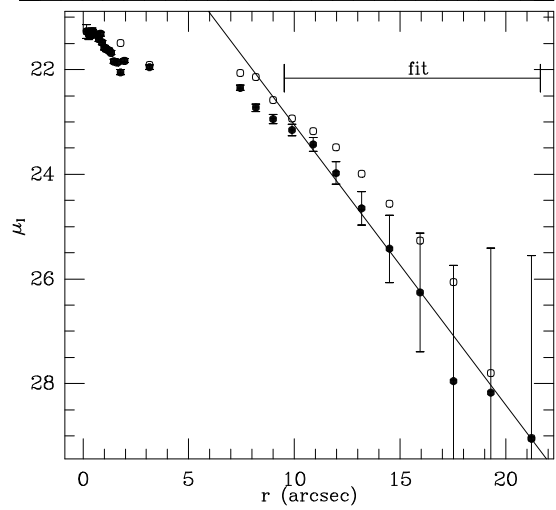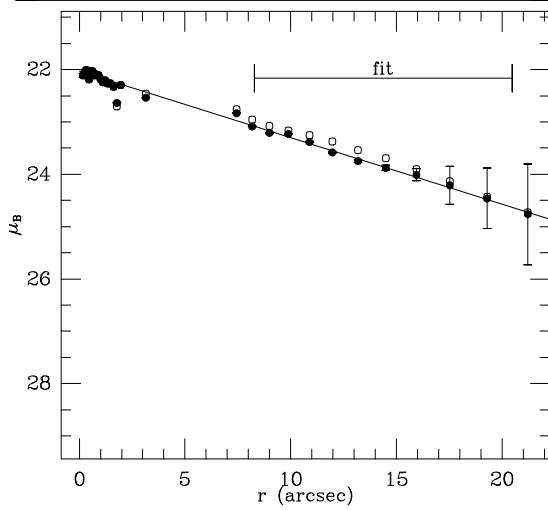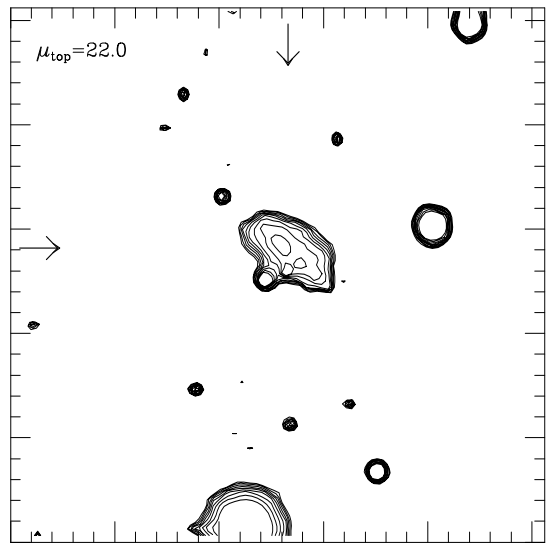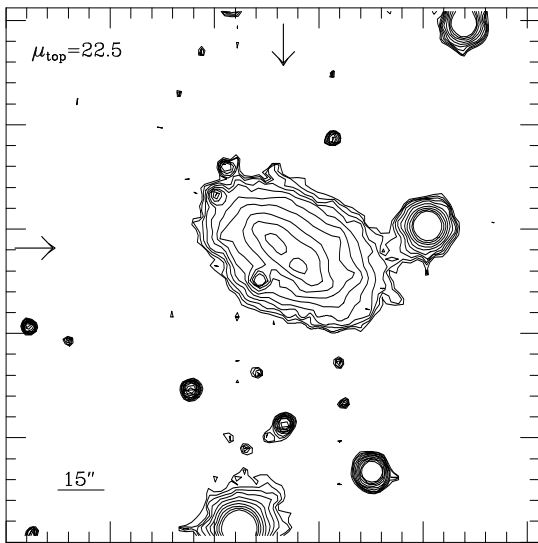
Figure 4: UGC 00063
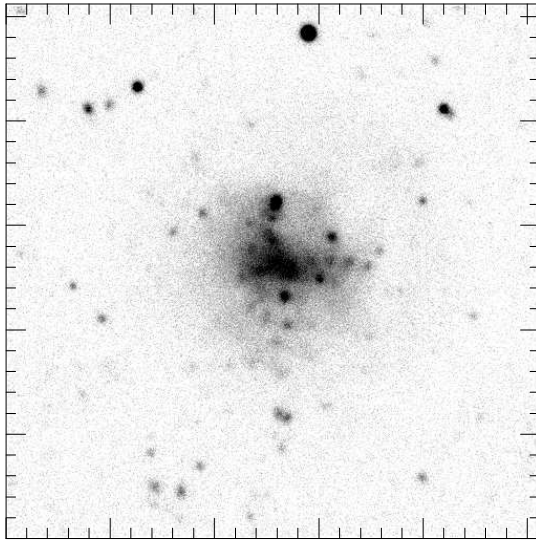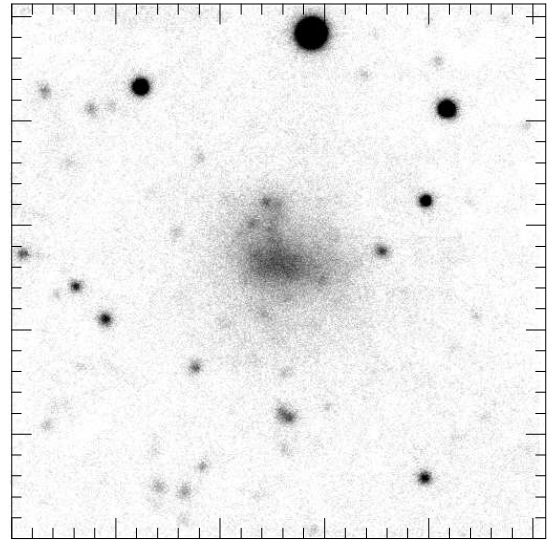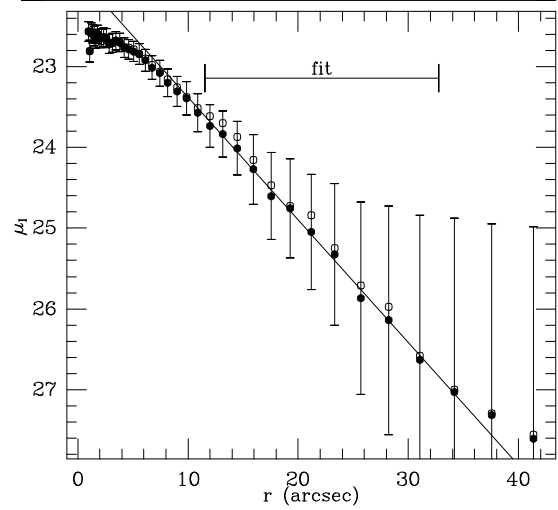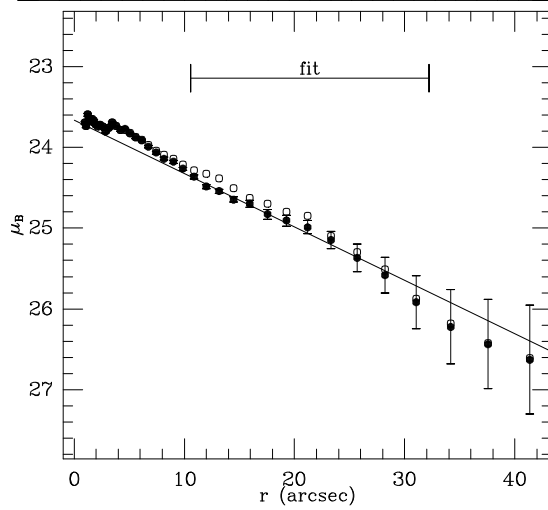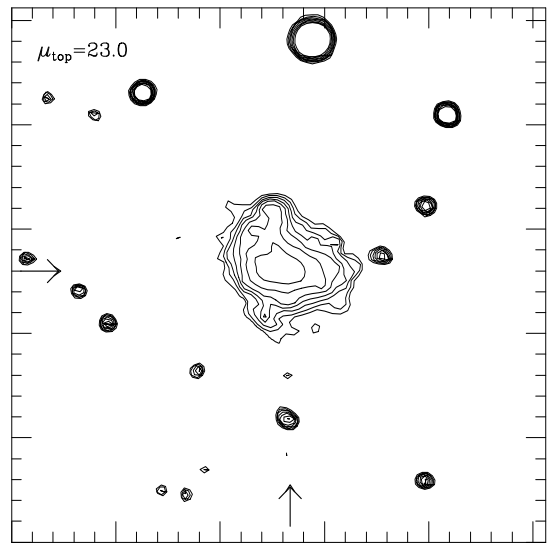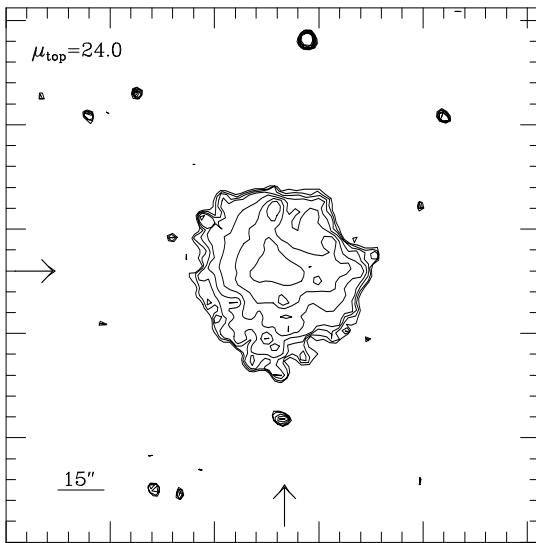
Figure 5: UGC 00300
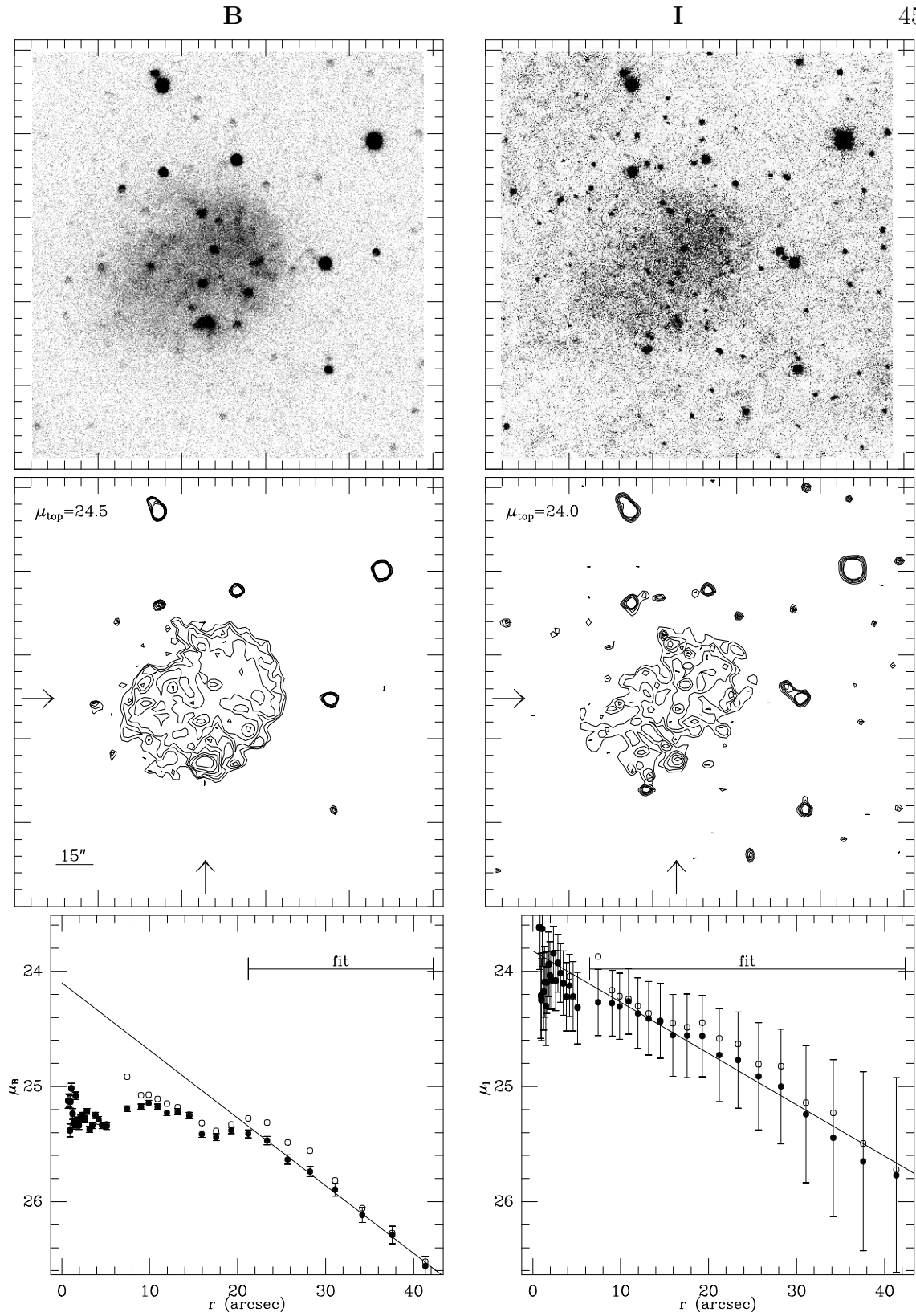
Figure 6: Karachentsev 10

$\mu_{top}=25.0$
$\mu_{bottom}=29.0$

$\mu_{top}=23.0$
$\mu_{bottom}=26.5$

15"

fit

fit

μ_B

μ_I

r (arcsec)

r (arcsec)
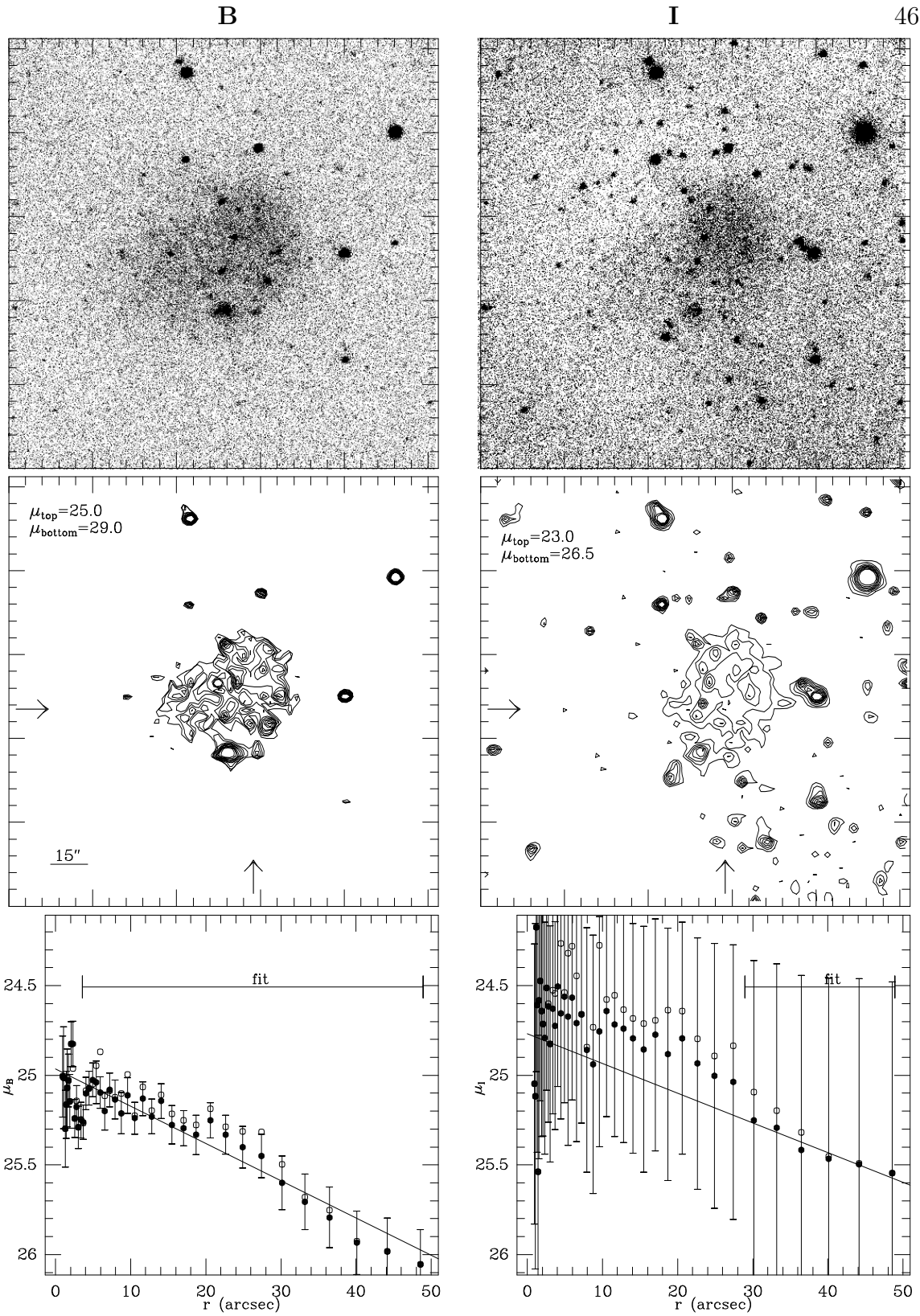
Figure 7: Karachentsev 10 (Jan93)
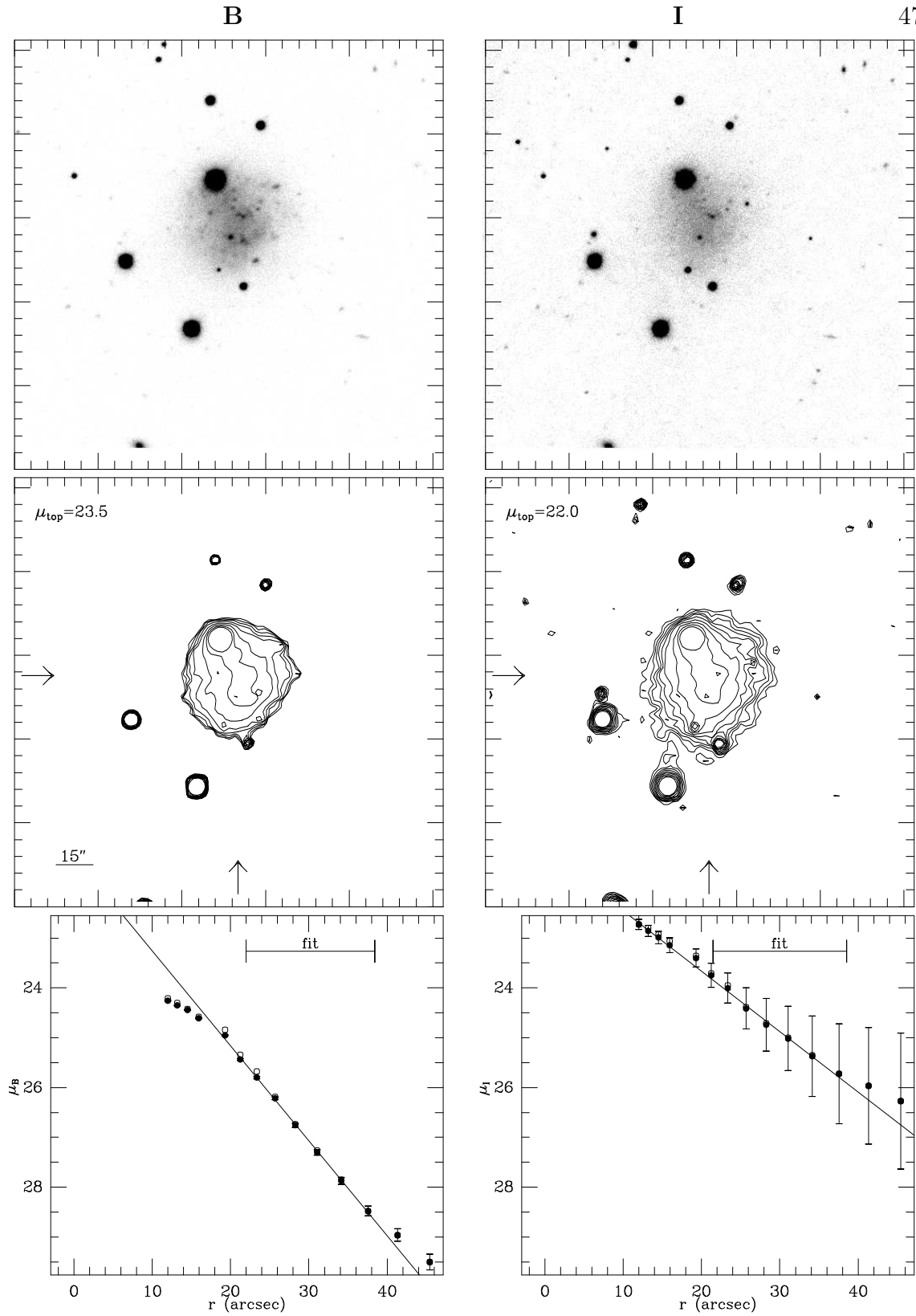
Figure 8: UGC 01981
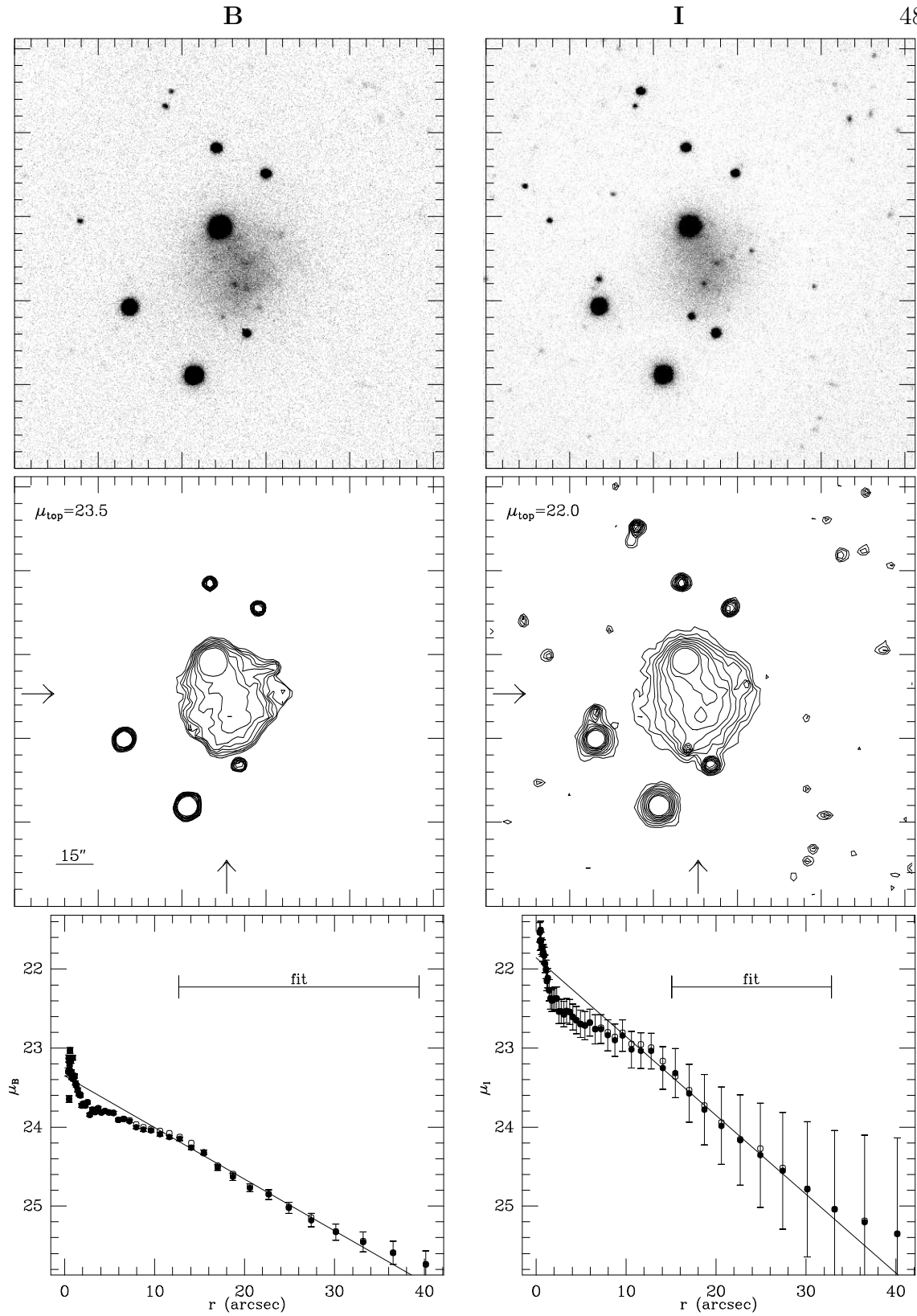
Figure 9: UGC 01981 (Jan93)
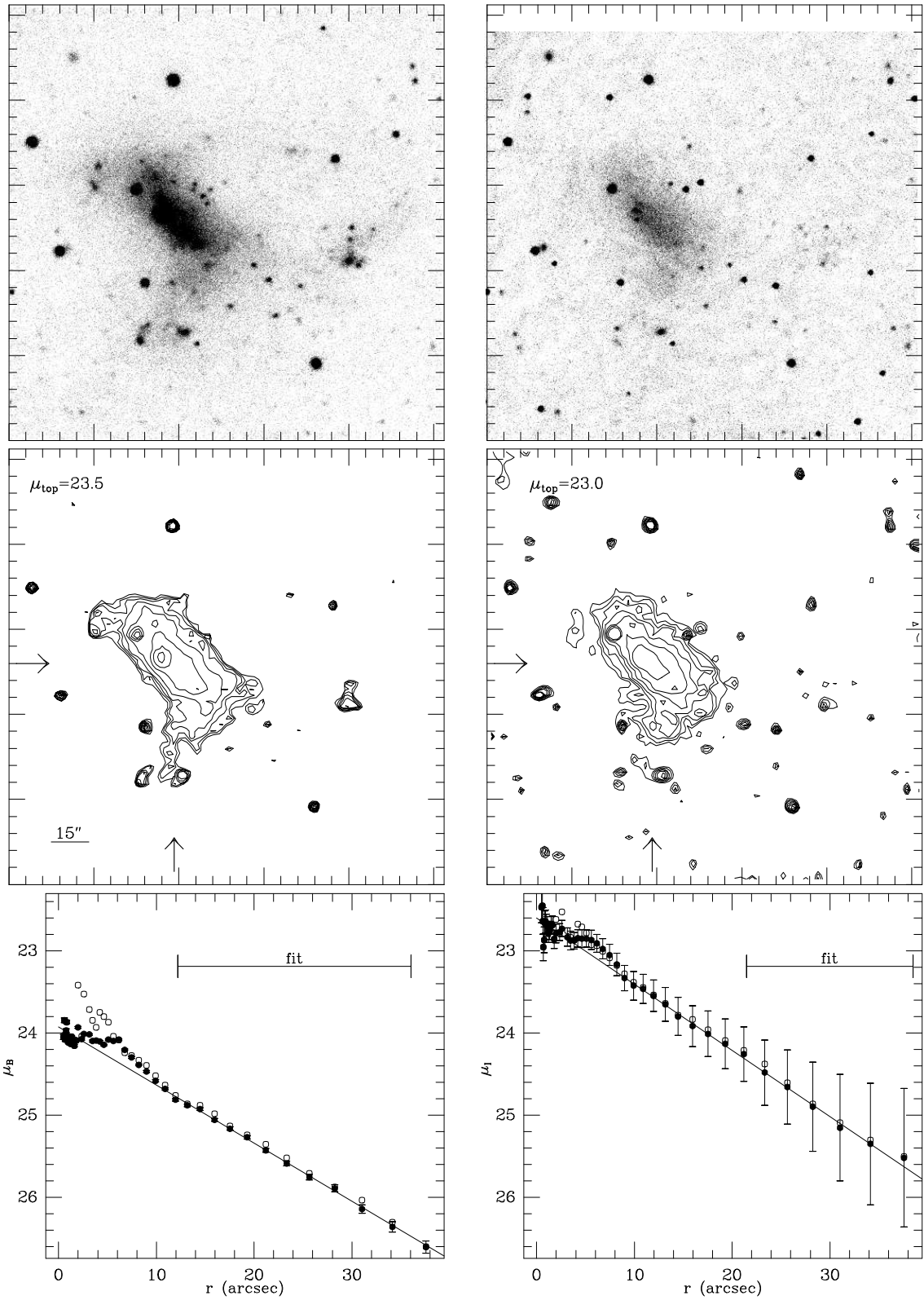
Figure 10: UGC 02017
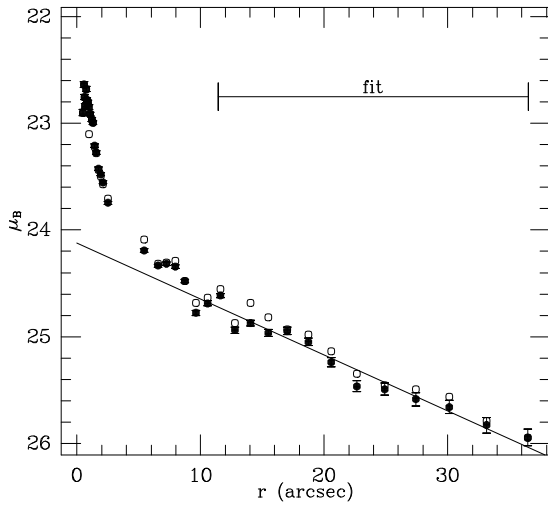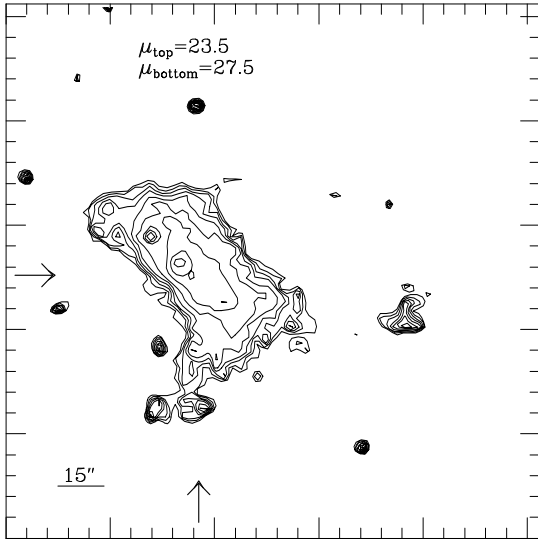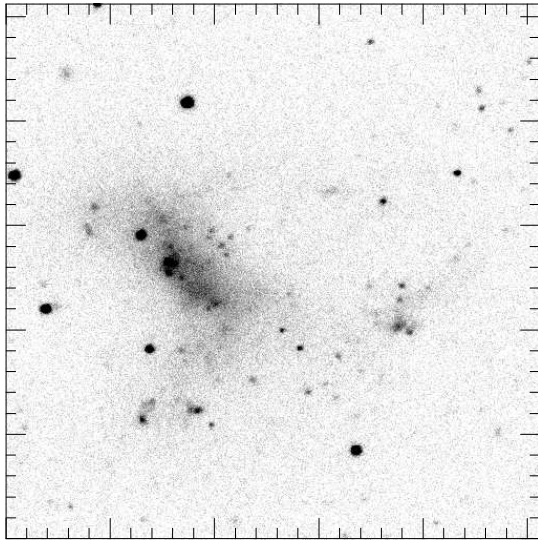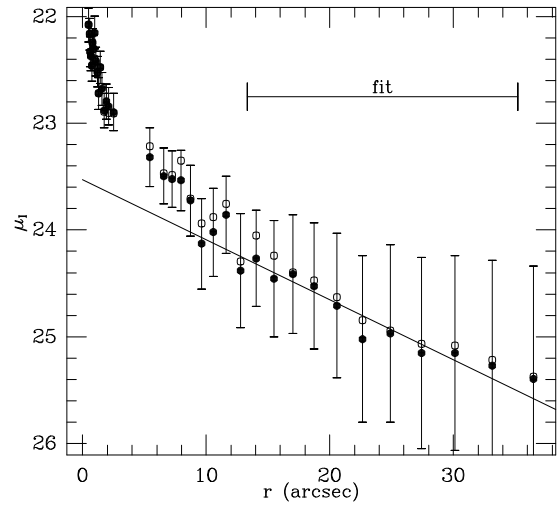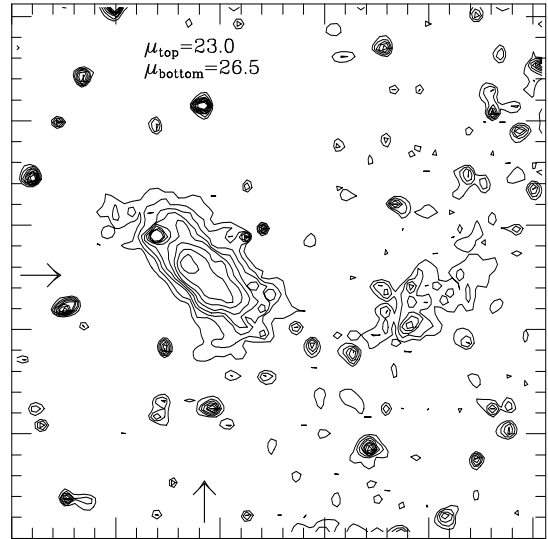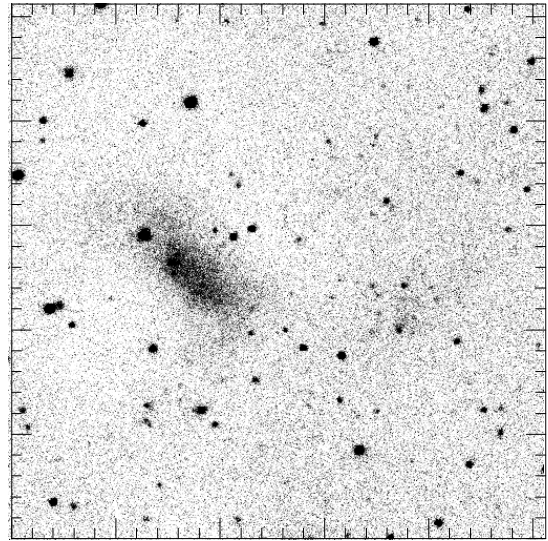
Figure 11: UGC 02017 (Jan93)

Figure 12: UGC 02034

$\mu_{top}=23.0$

$\mu_{top}=21.5$

15″

μ_B

fit

μ_I

fit

r (arcsec)

r (arcsec)
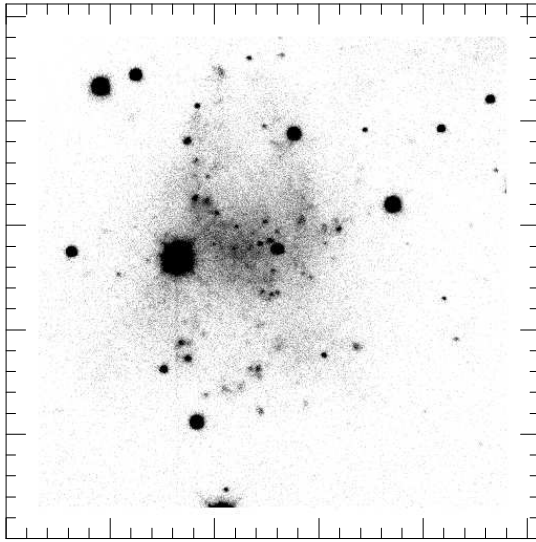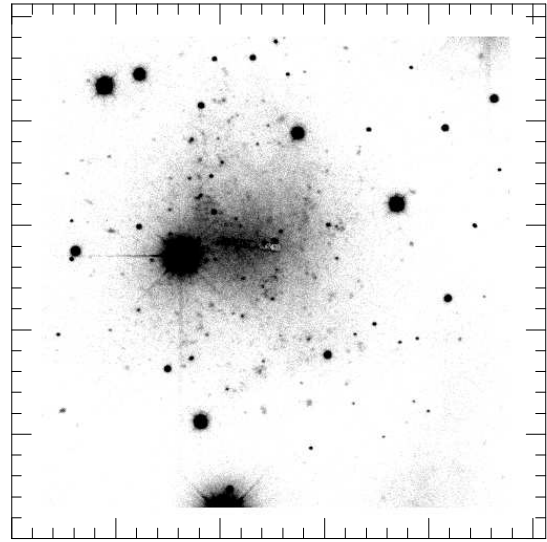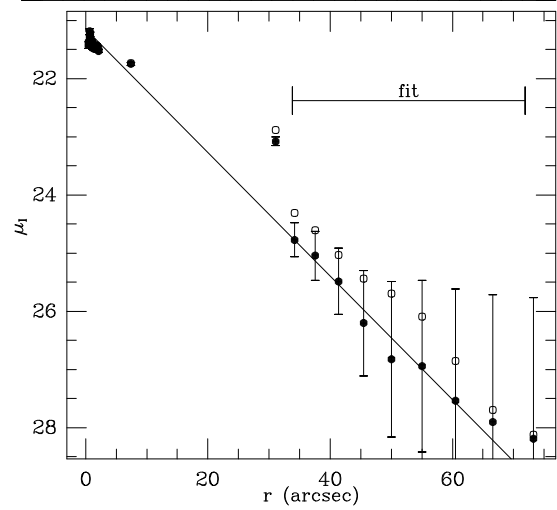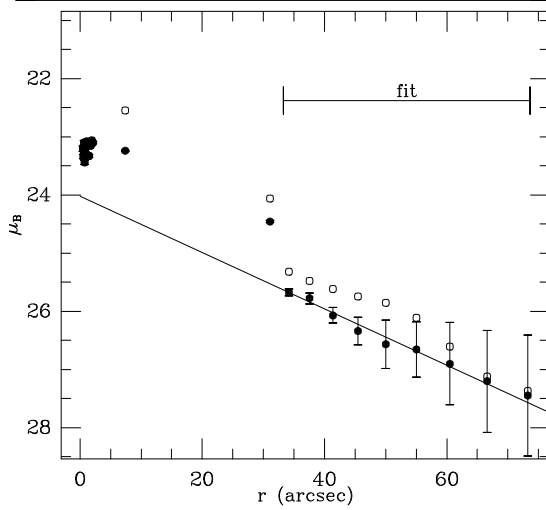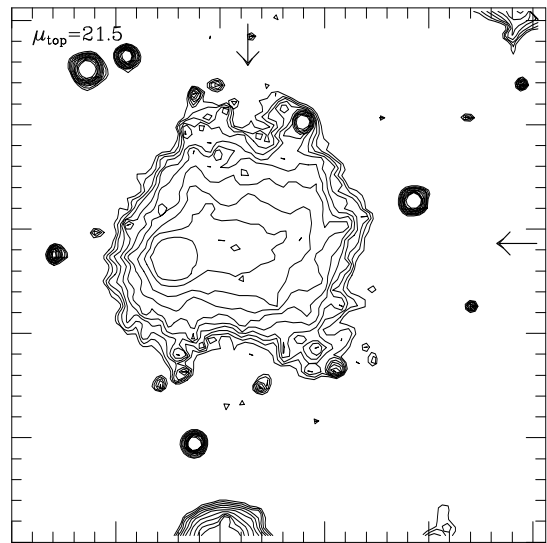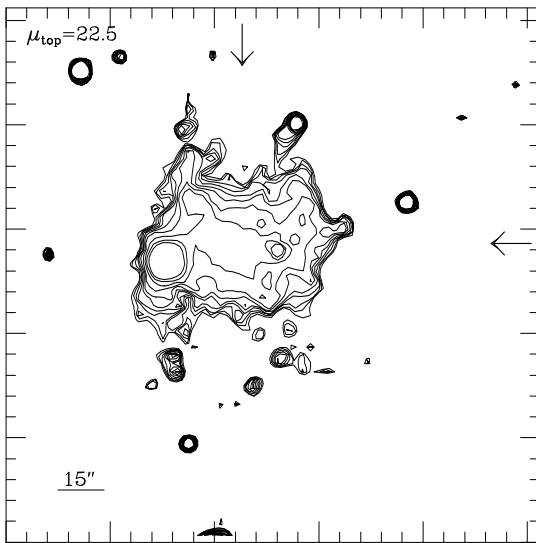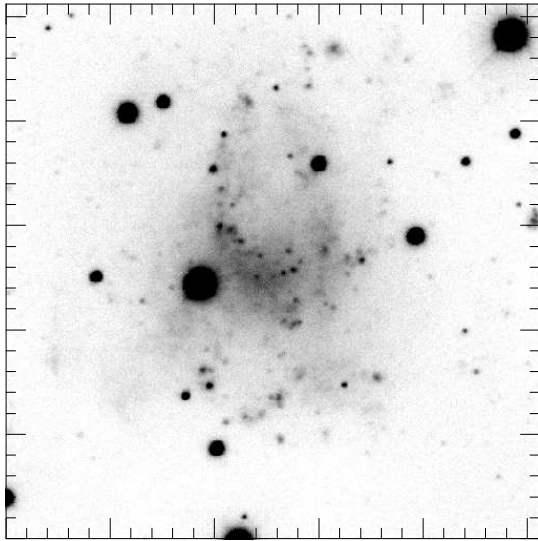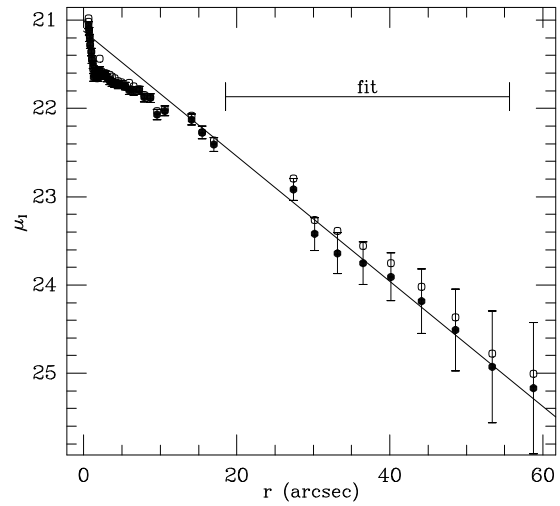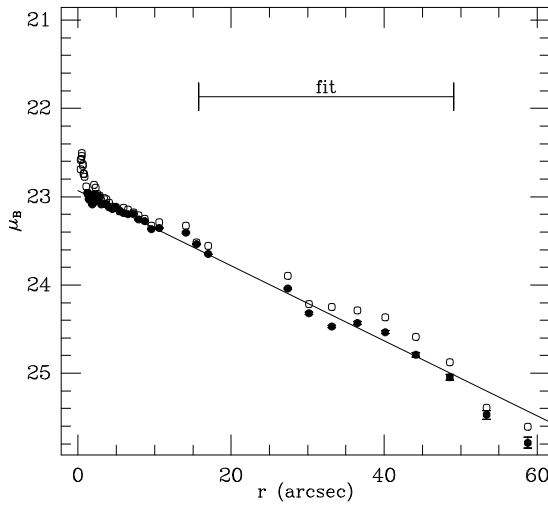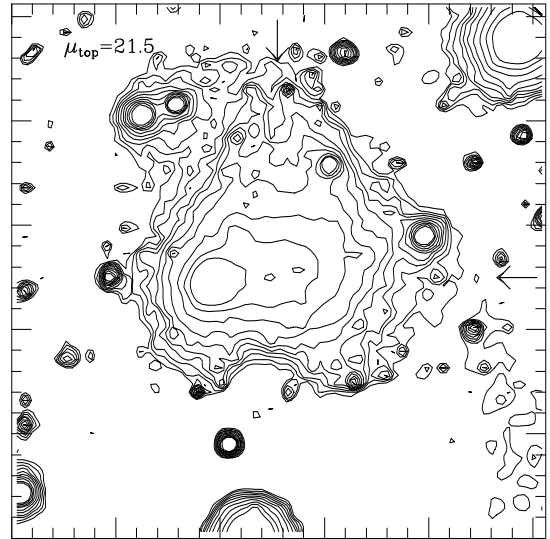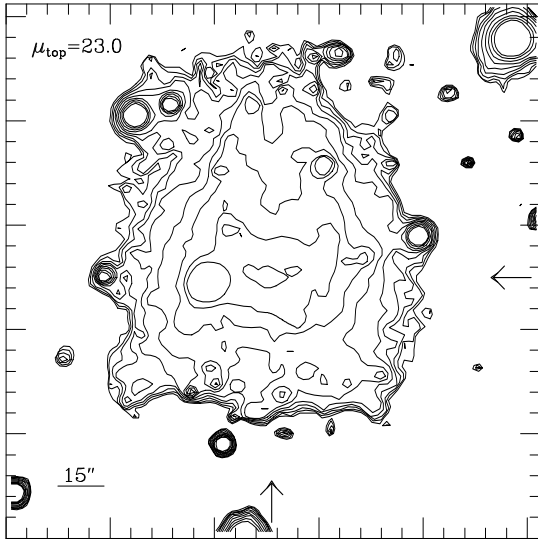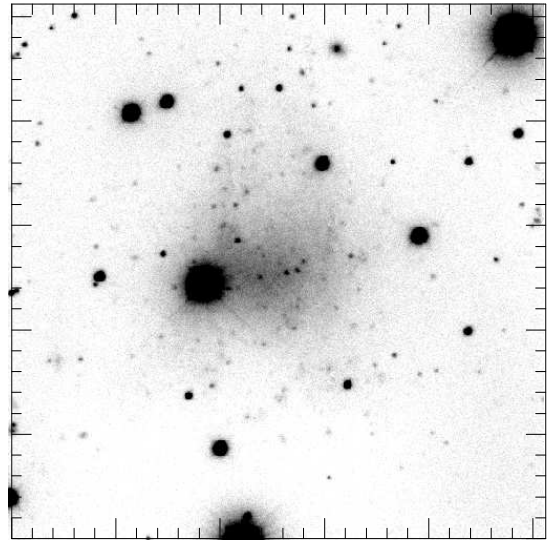
Figure 13: UGC 02034 (Jan93)

$\mu_{top}=23.5$

$\mu_{top}=22.5$

15″

fit

fit

μ_B

μ_I

r (arcsec)

r (arcsec)
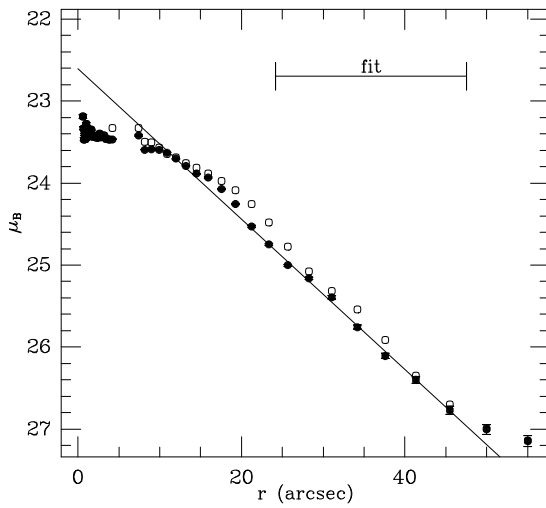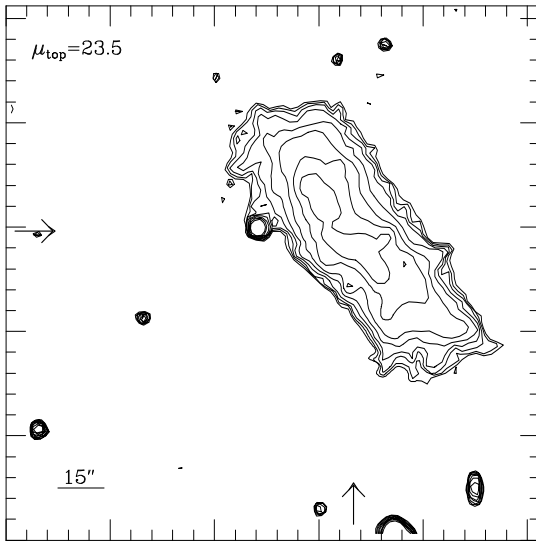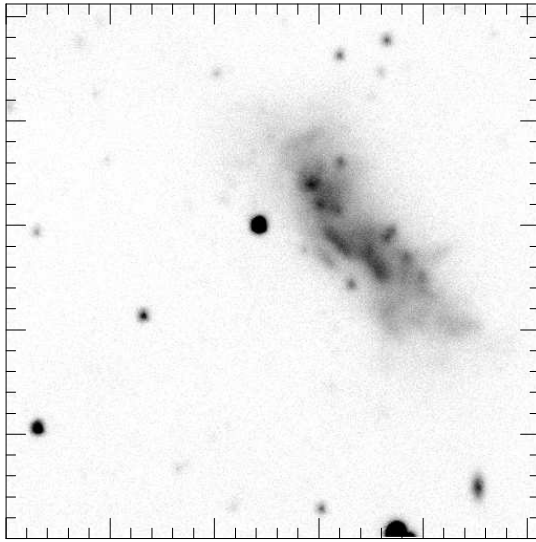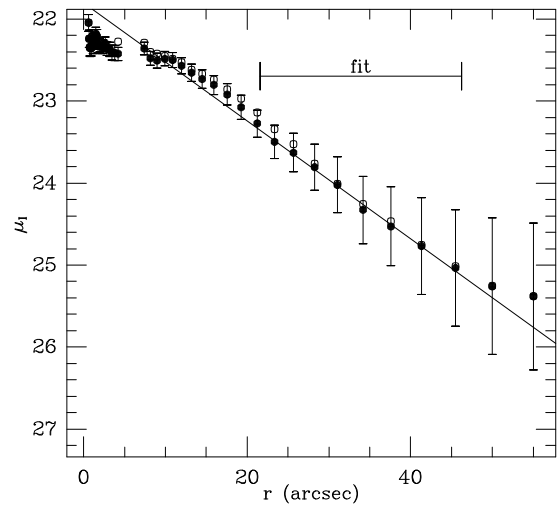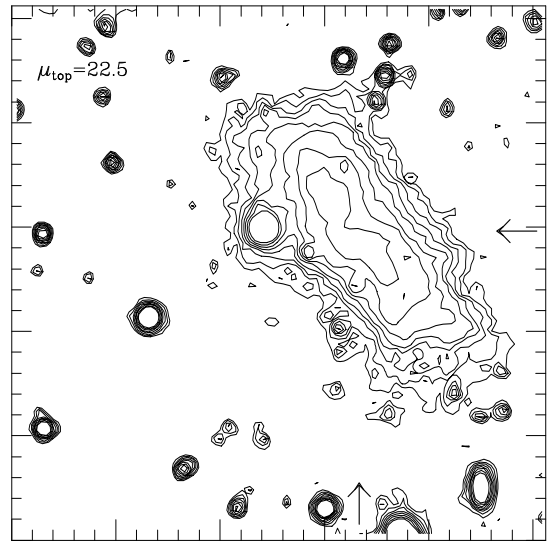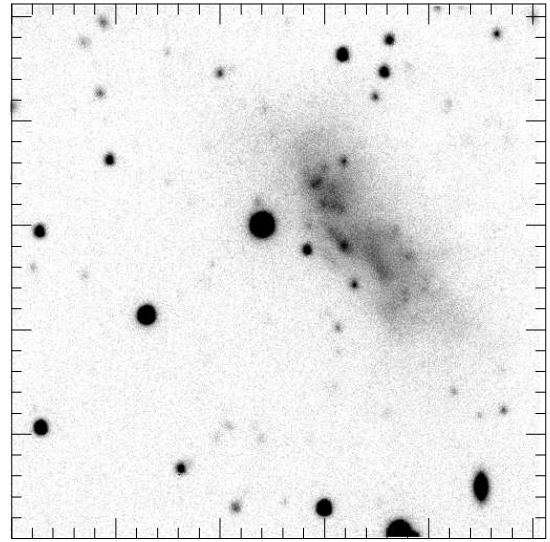
Figure 14: UGC 02053
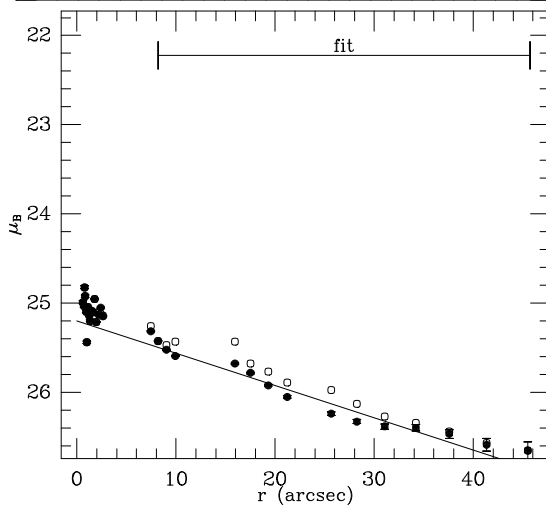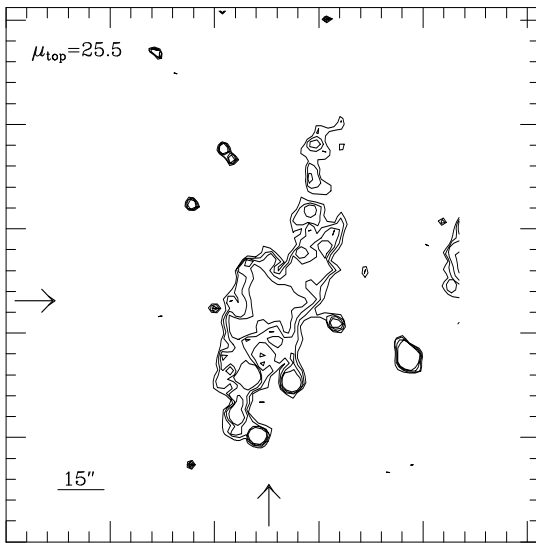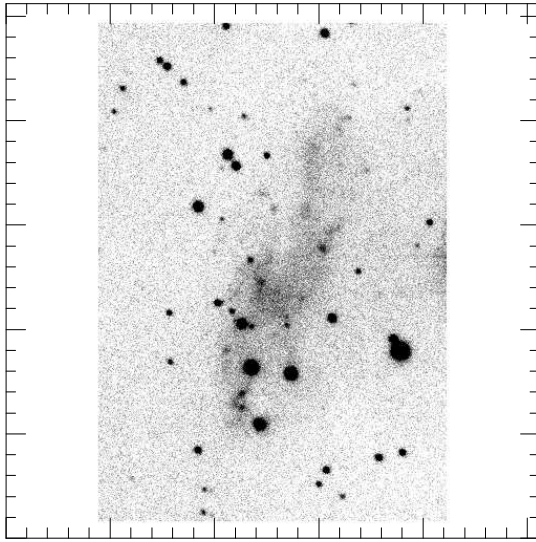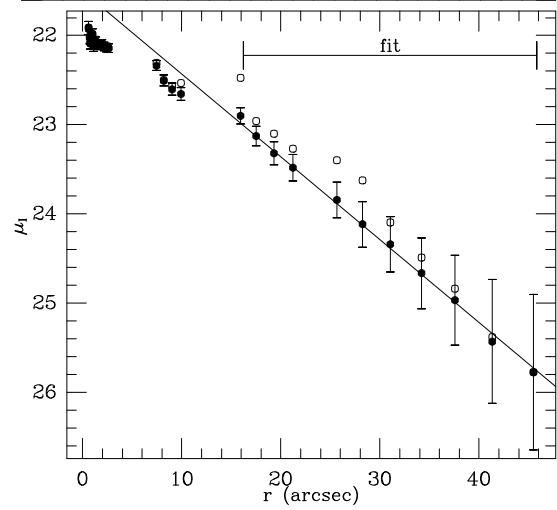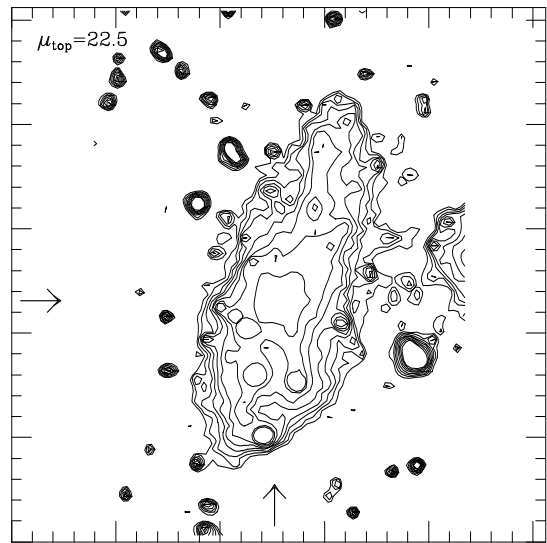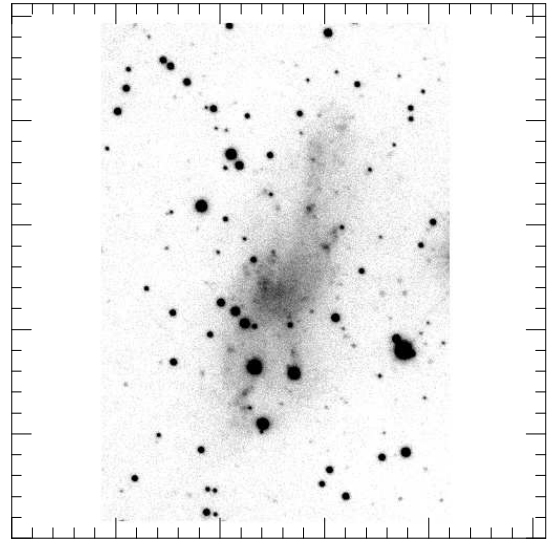
Figure 15: Karachentsev 37
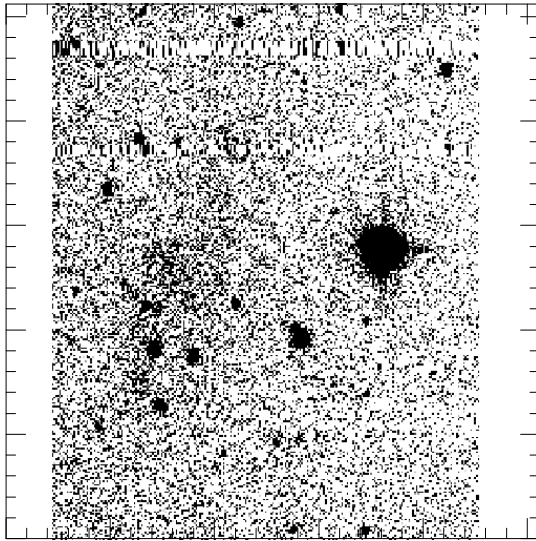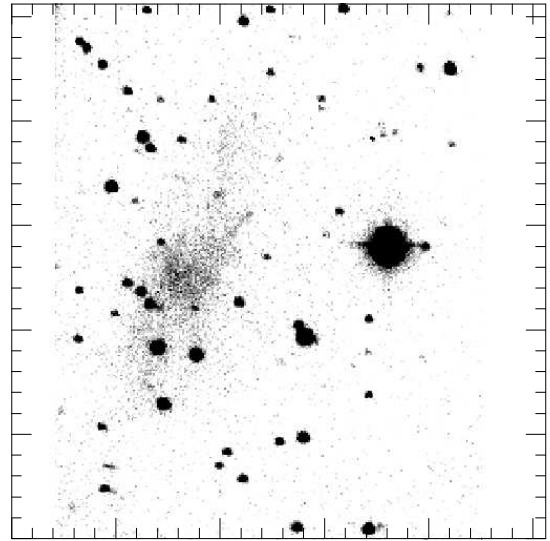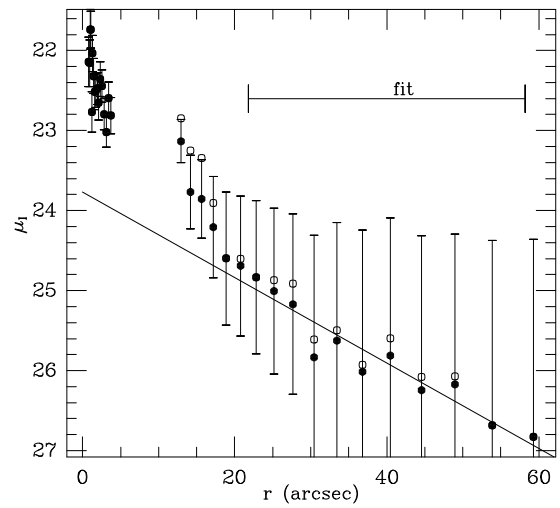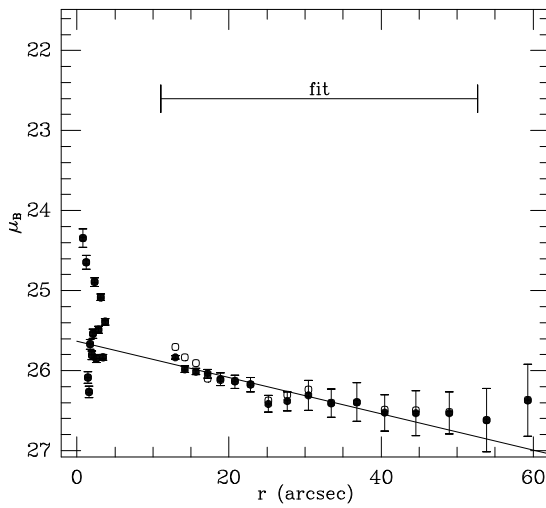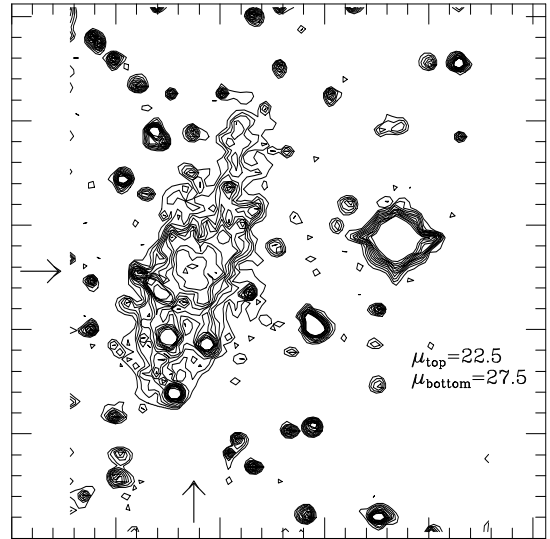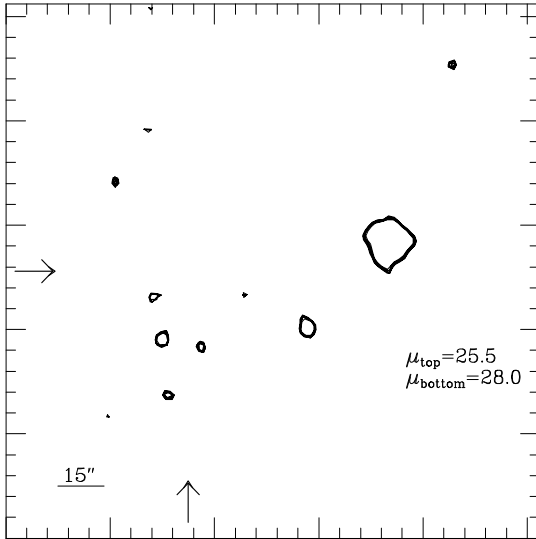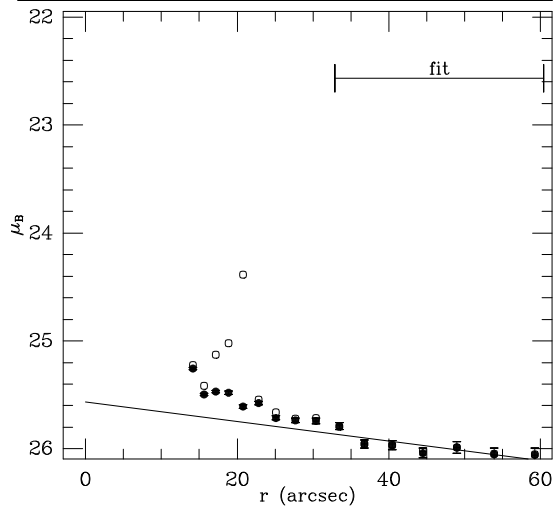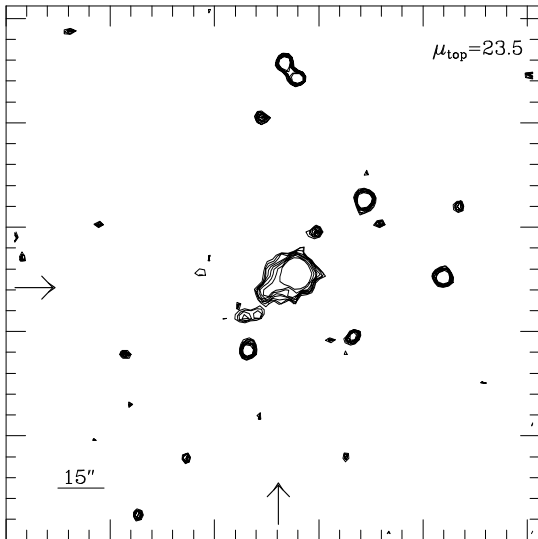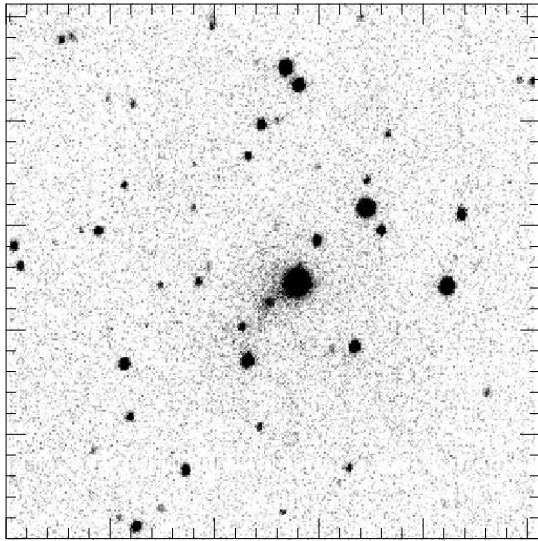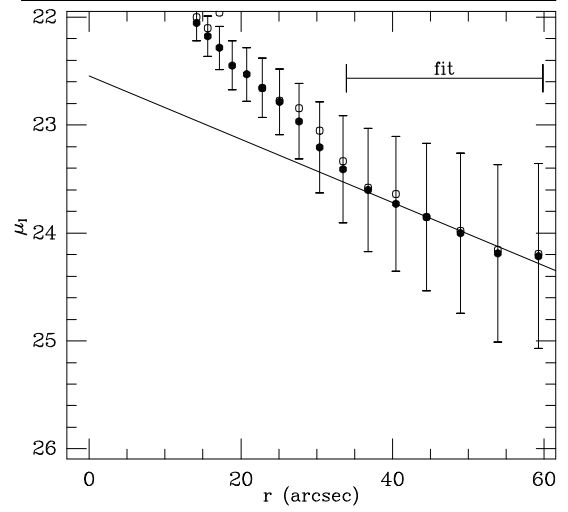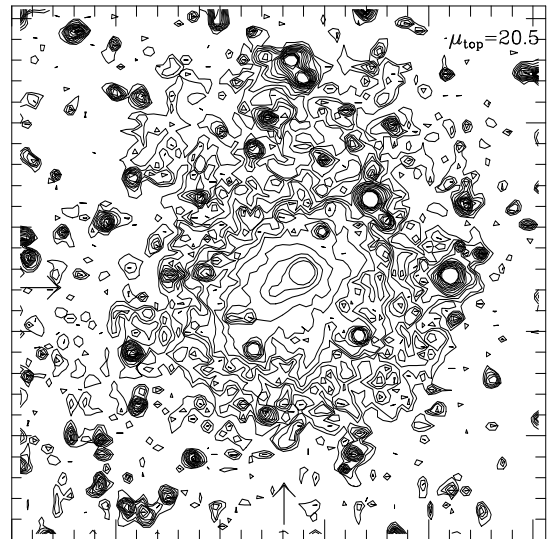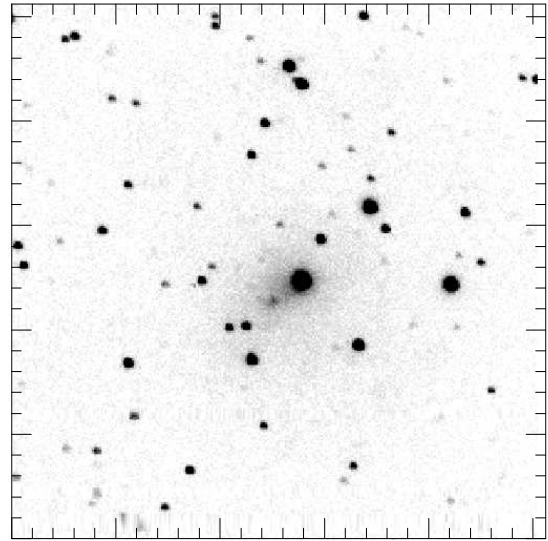
Figure 17: Karachentsev 37C (Sep91)
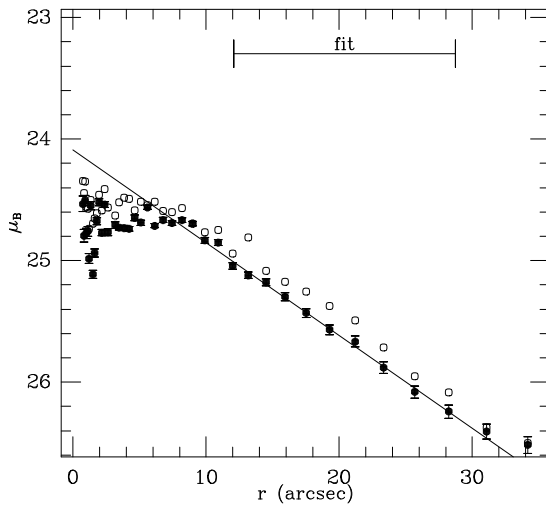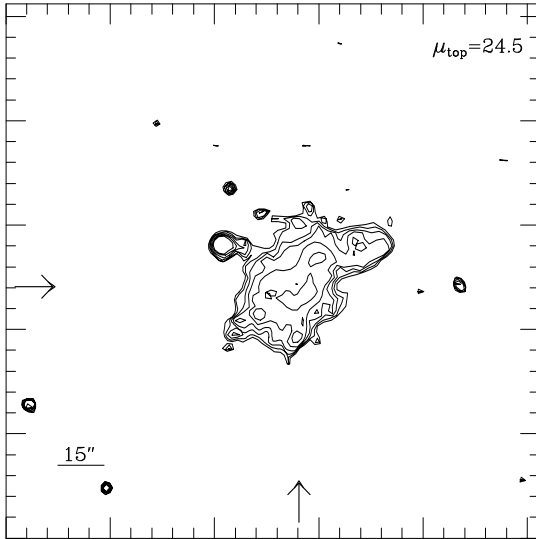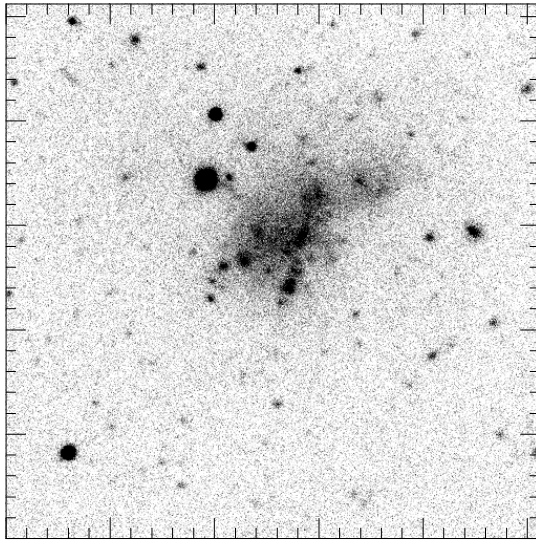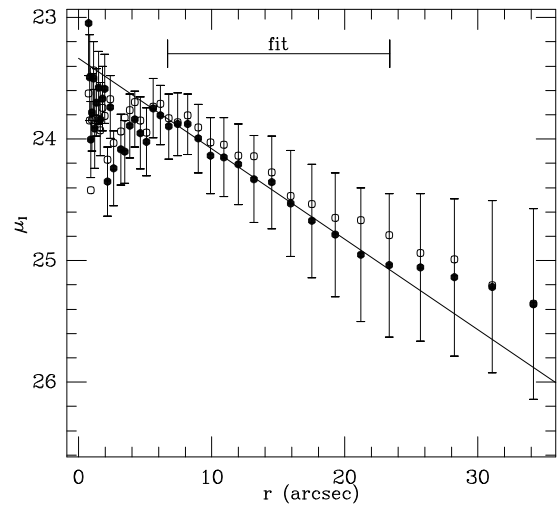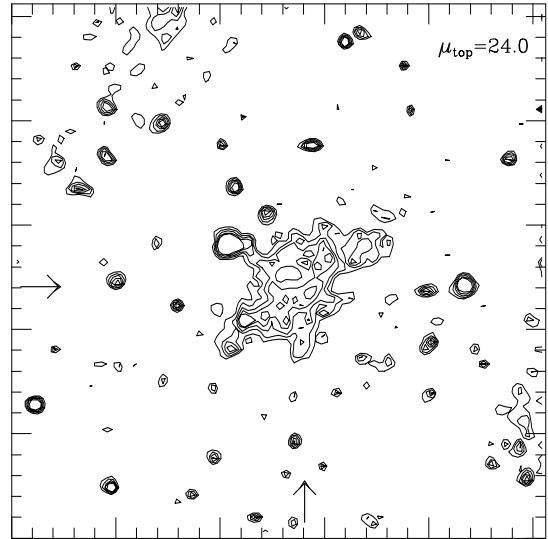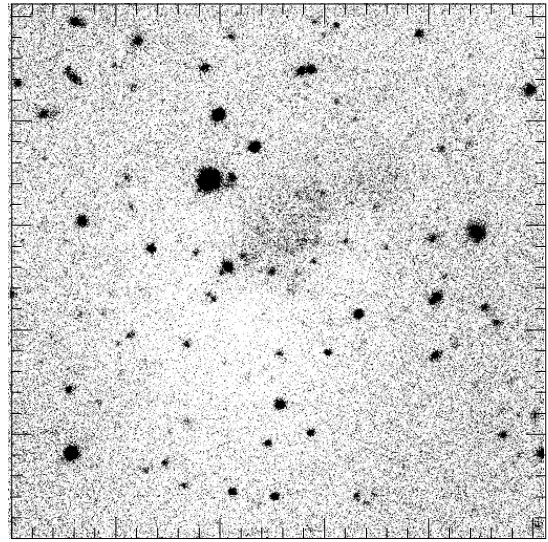
Figure 18: UGC 02162
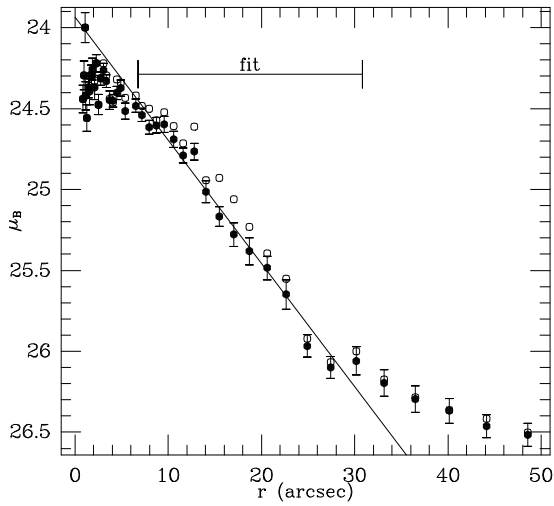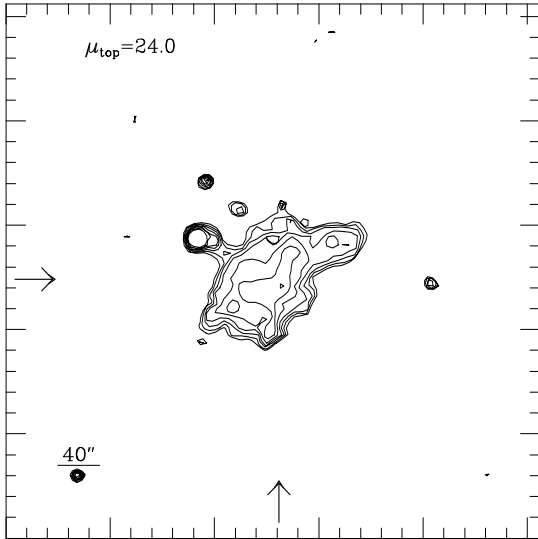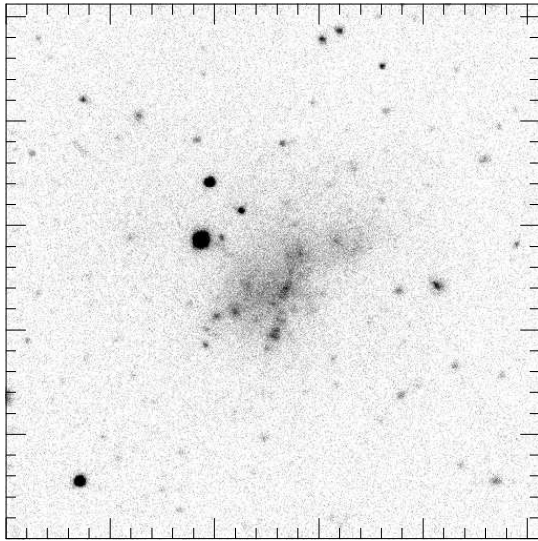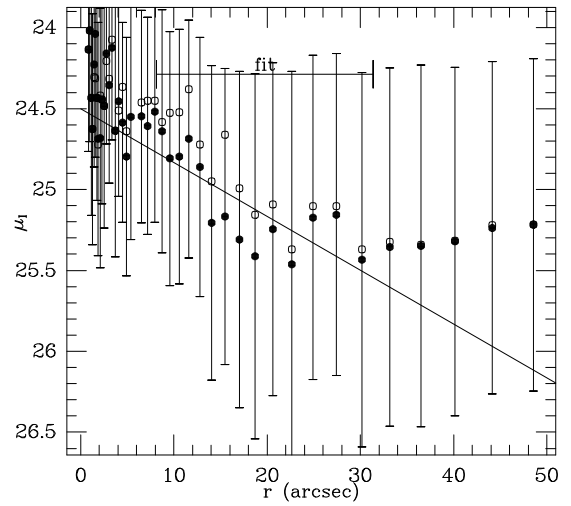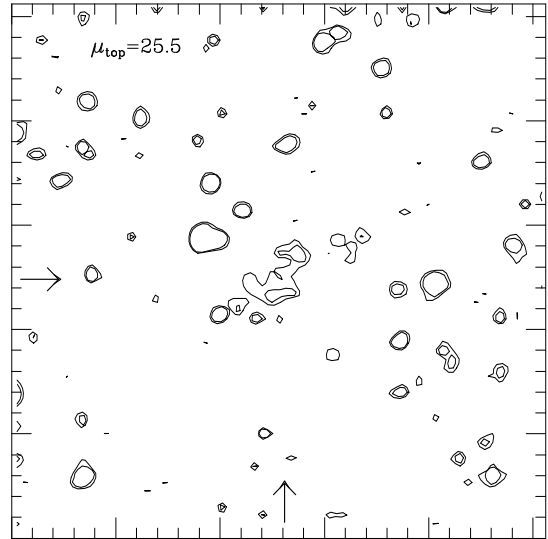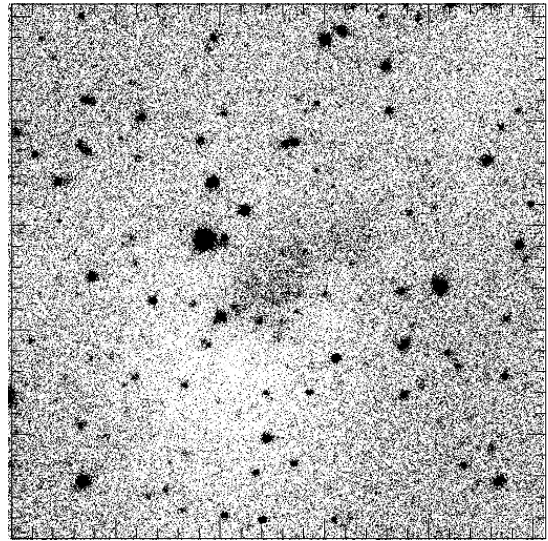
Figure 19: UGC 02162 (Jan93)
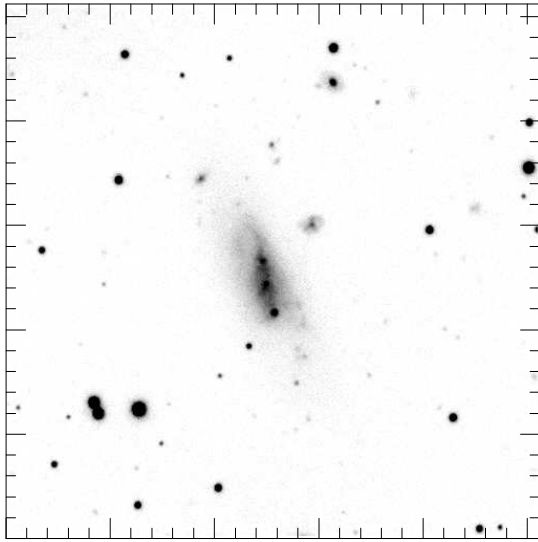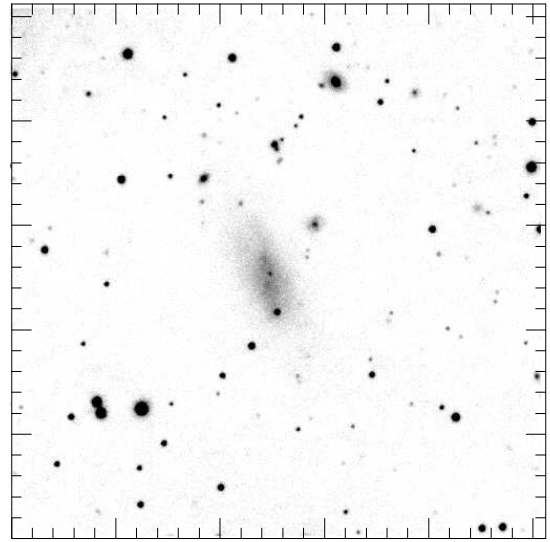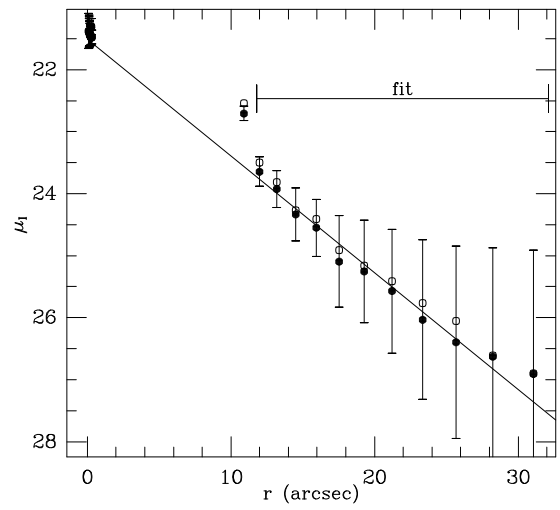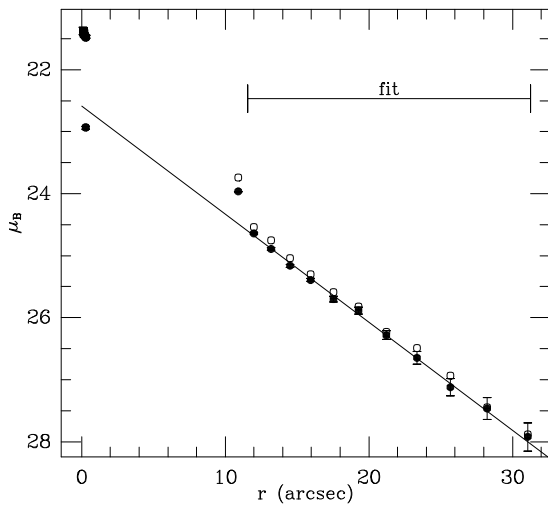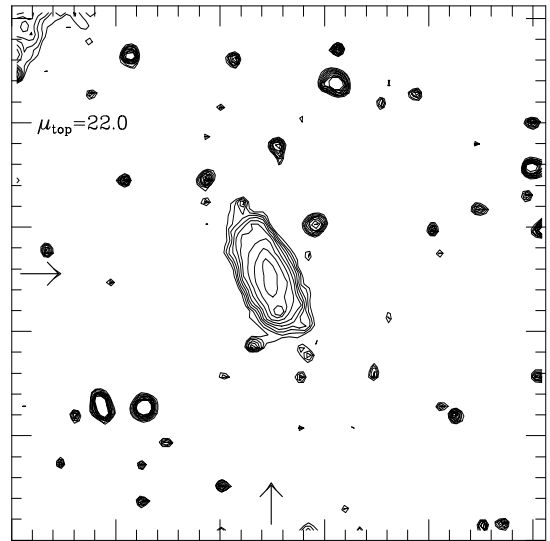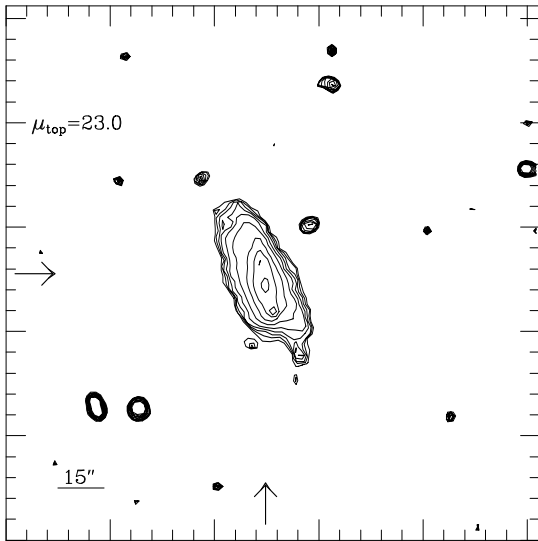
Figure 20: UGC 03212
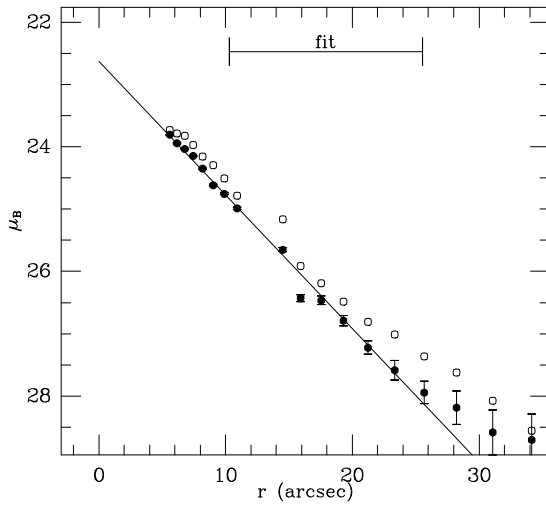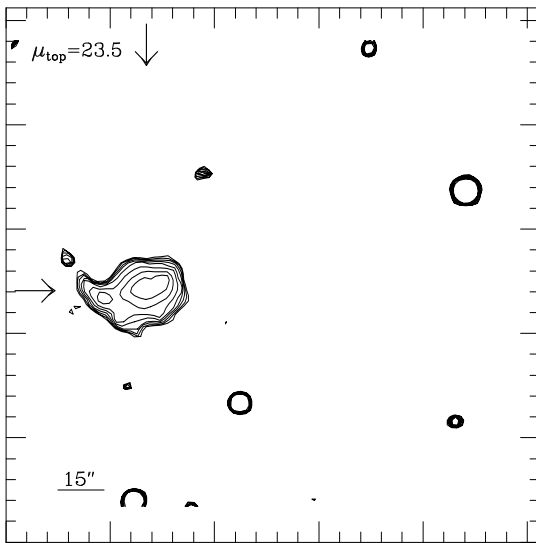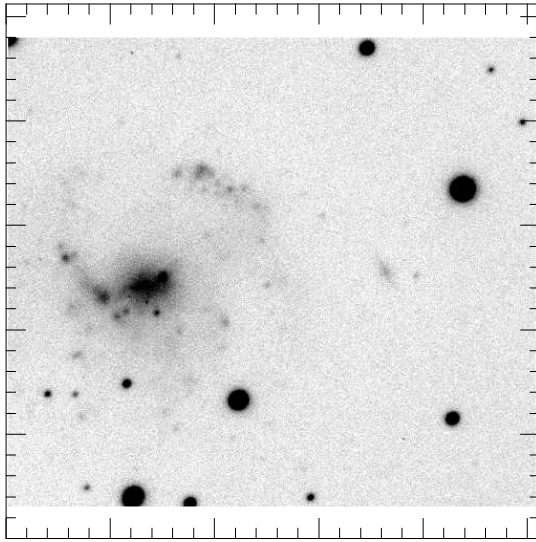
Figure 21: UGC 03384

Figure 22: UGC 03817

Figure 23: UGC 03966

$\mu_{top}=24.0$
$\mu_{bottom}=27.5$

$\mu_{top}=22.5$
$\mu_{bottom}=26.5$

15″

fit

fit

μ_B

μ_I

r (arcsec)

r (arcsec)
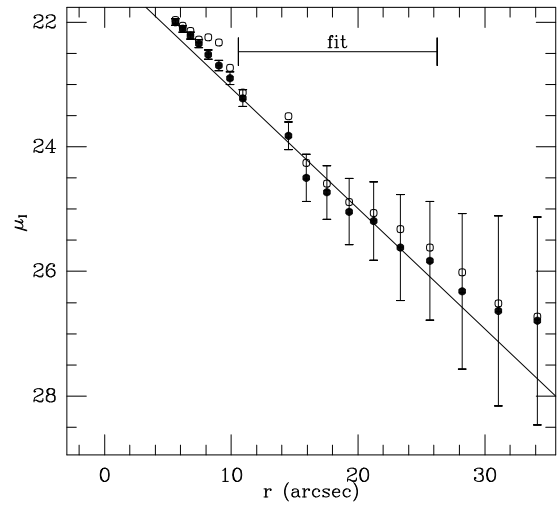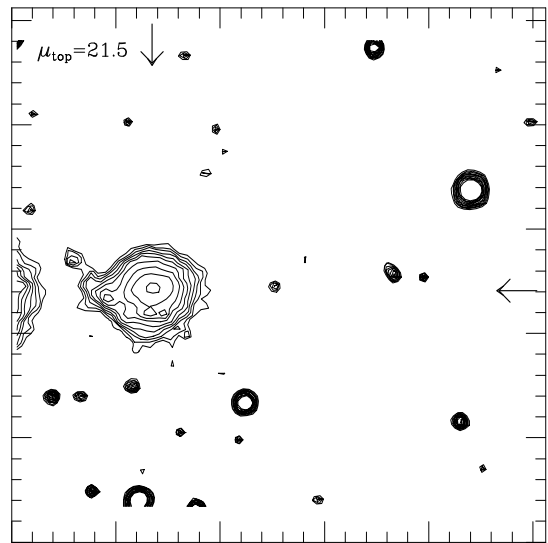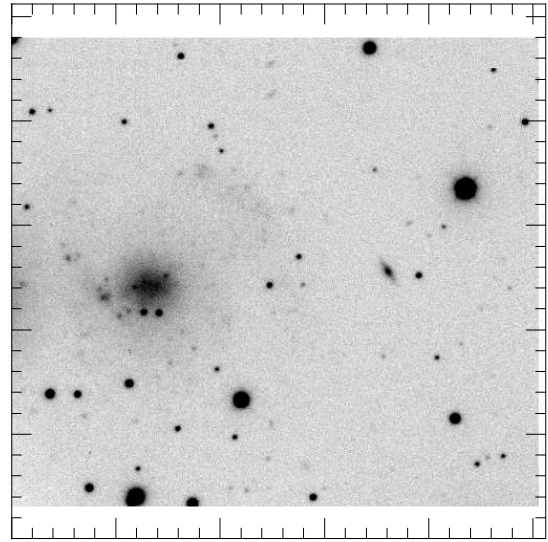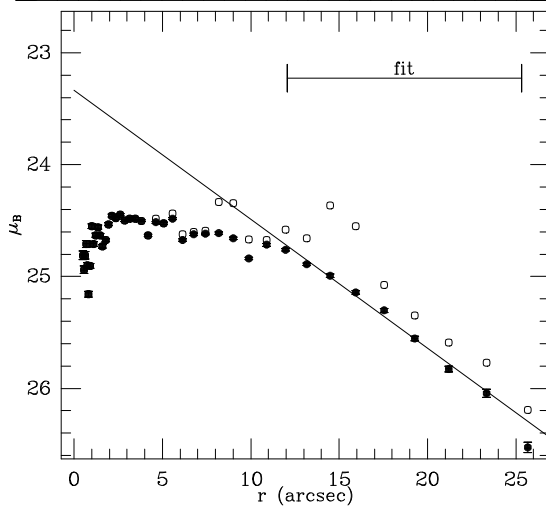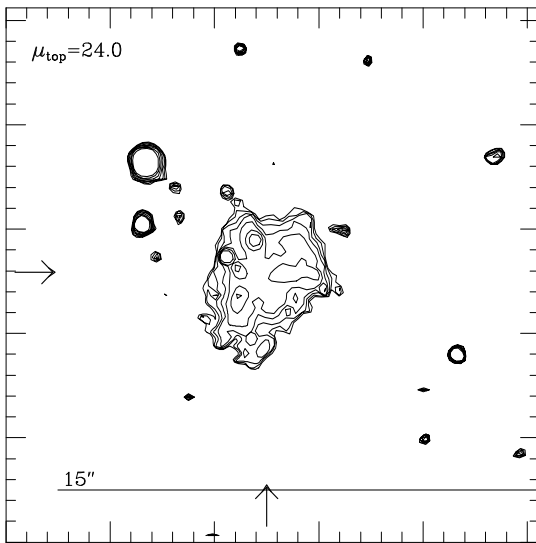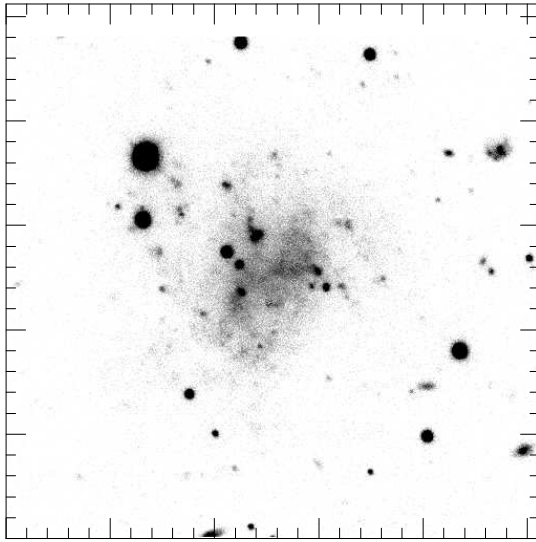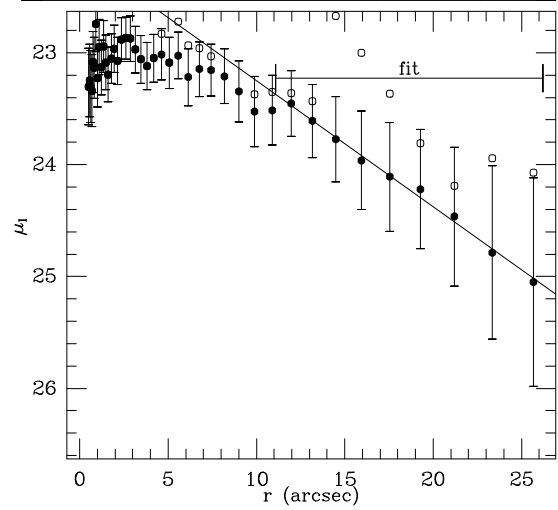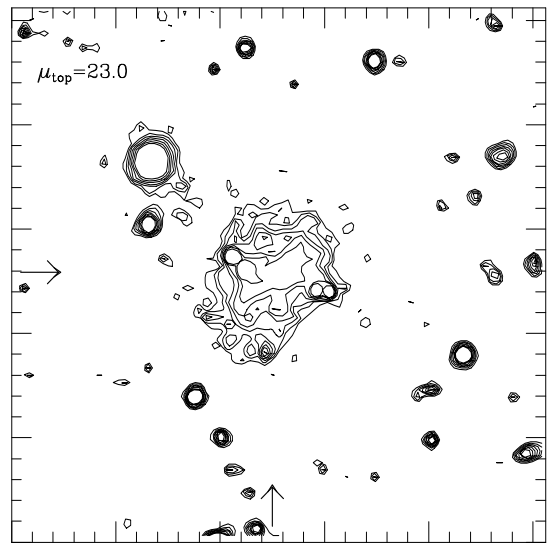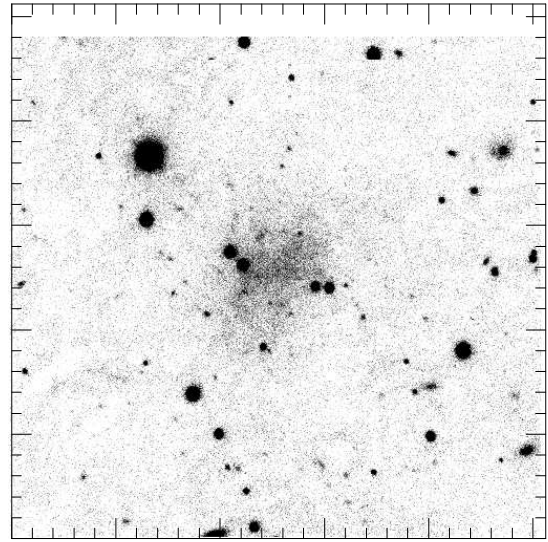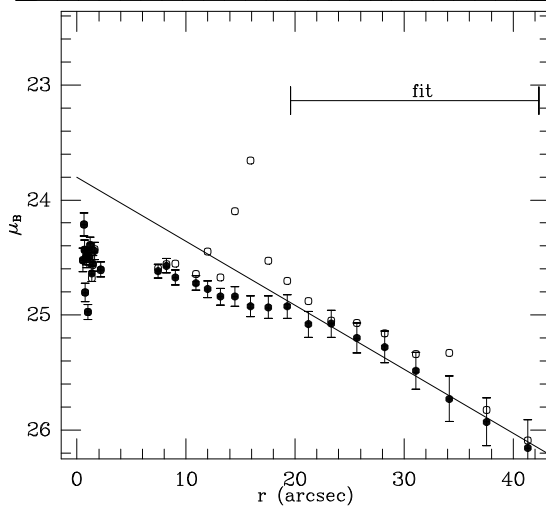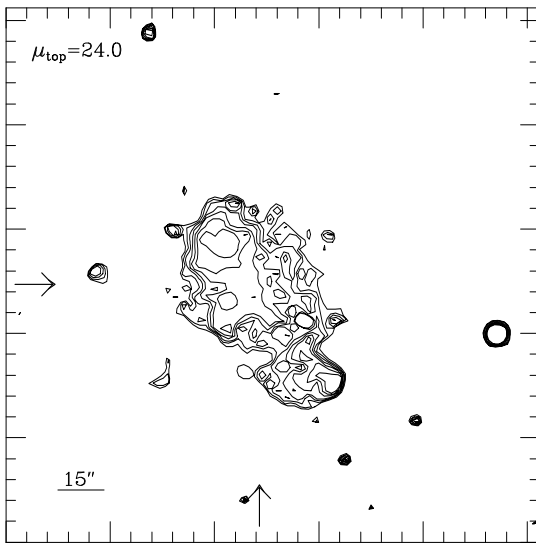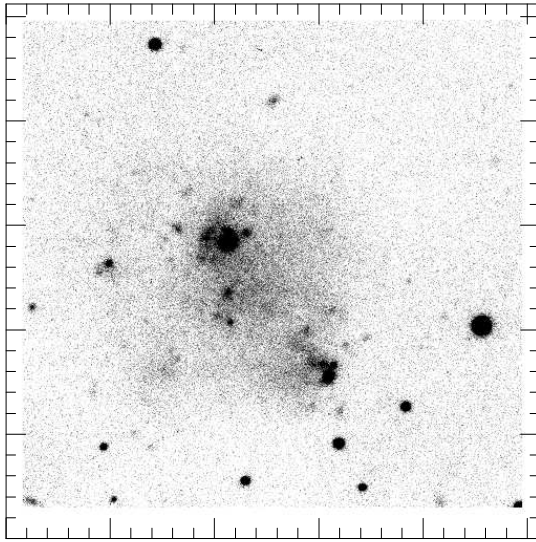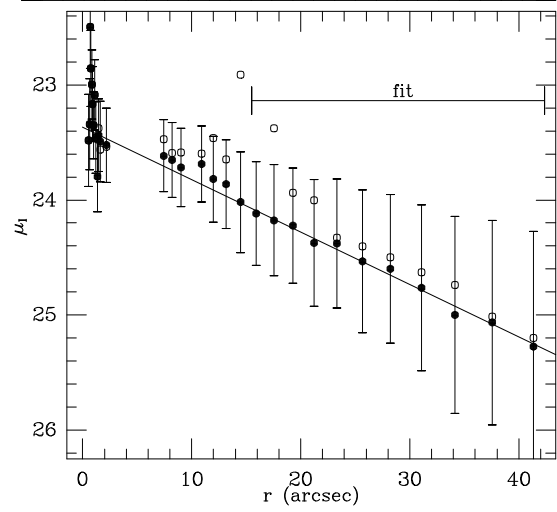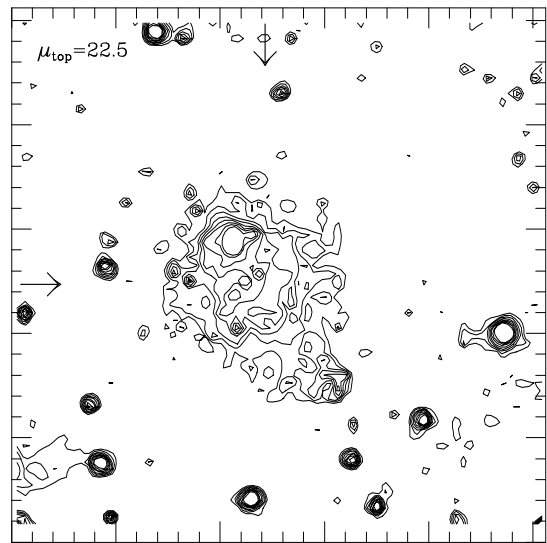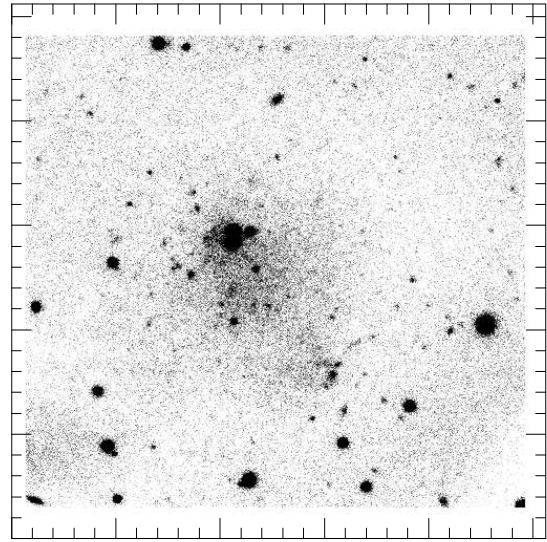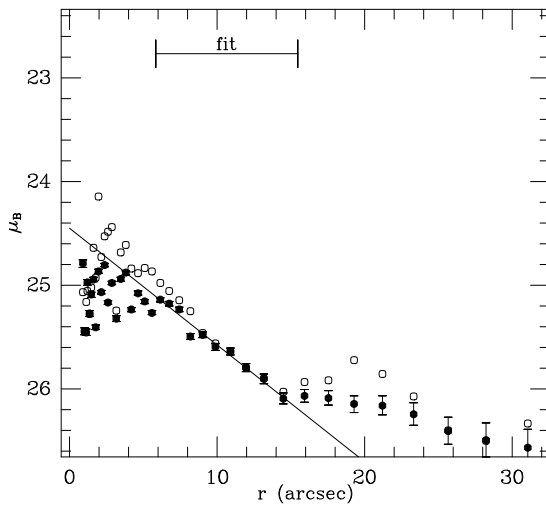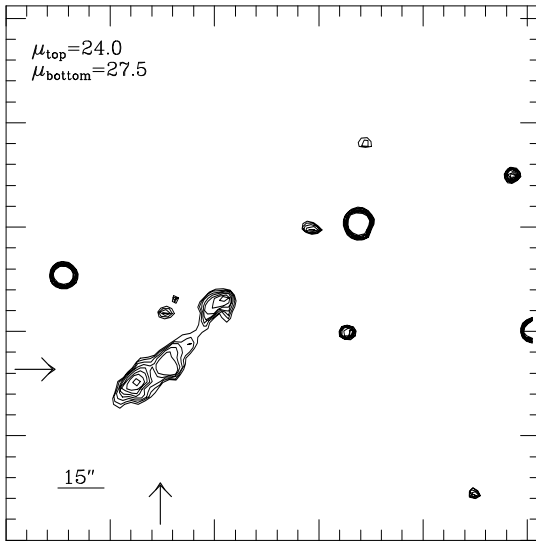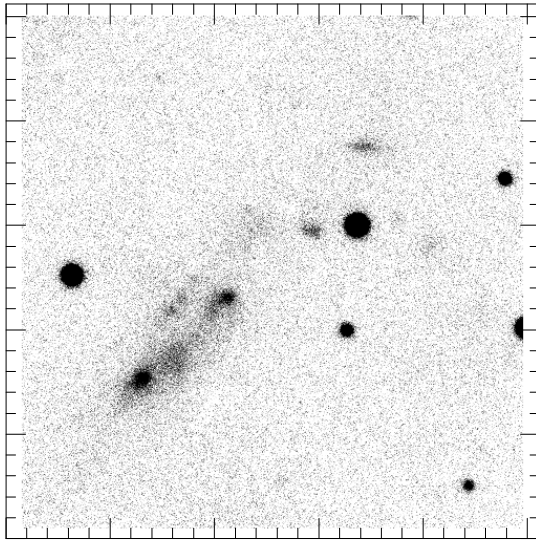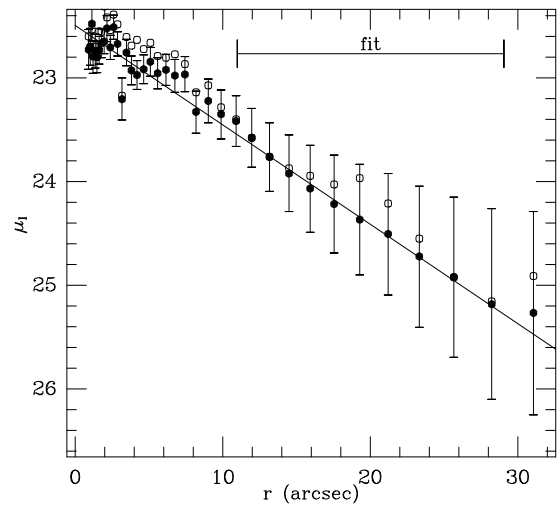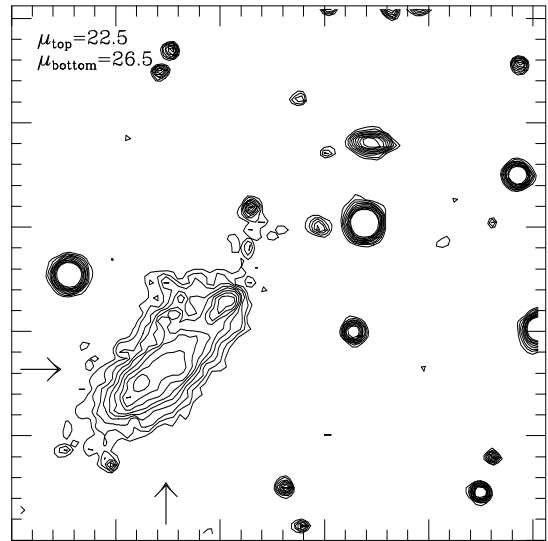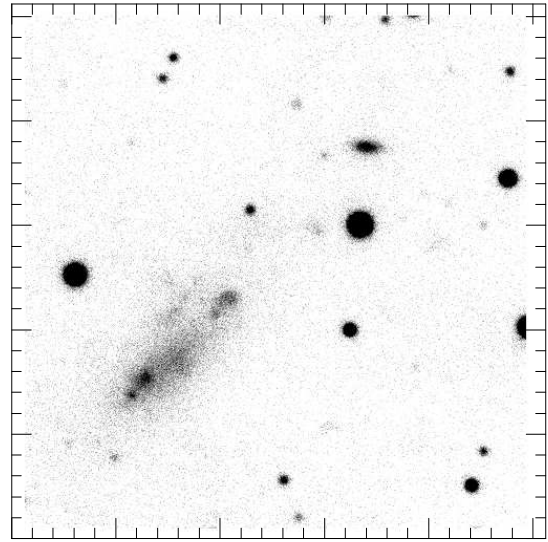
Figure 24: UGC 04173
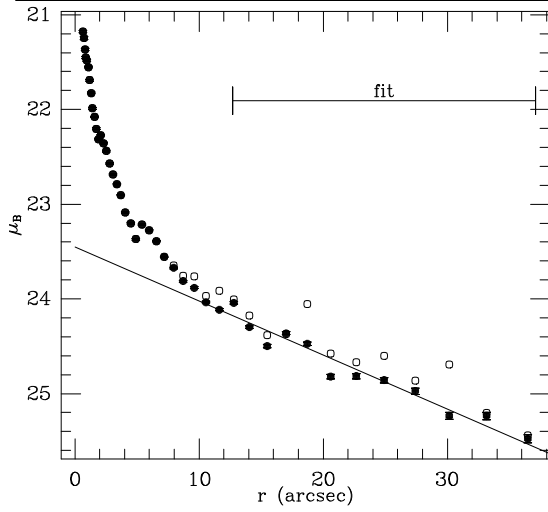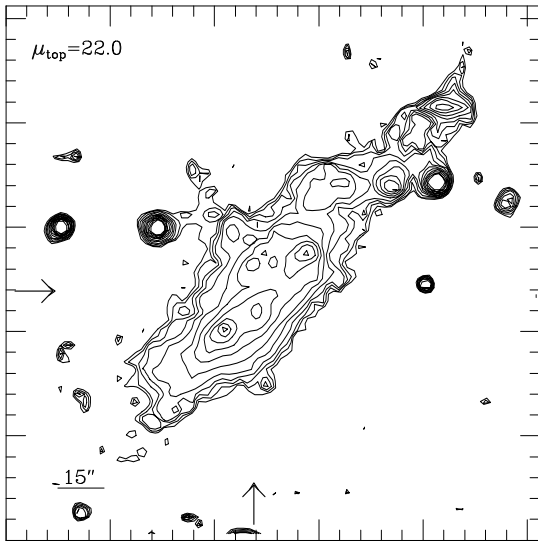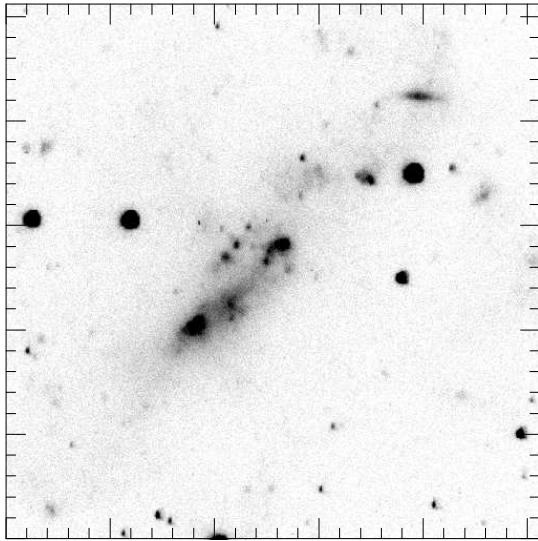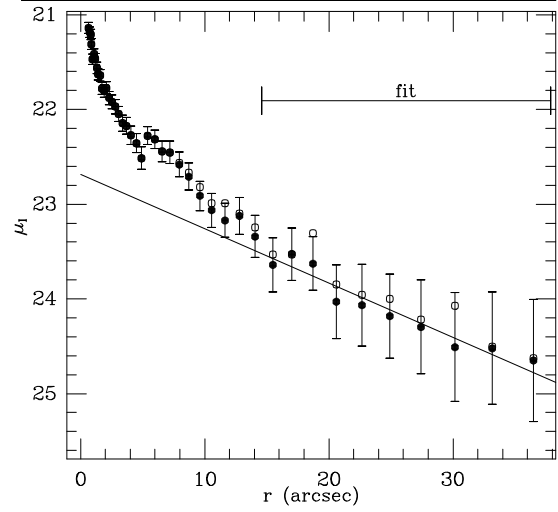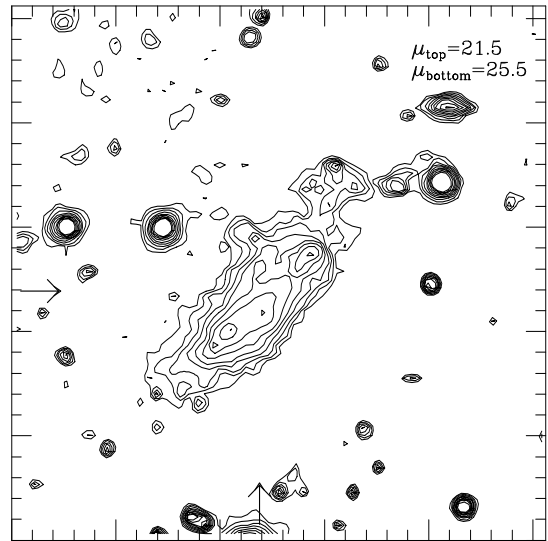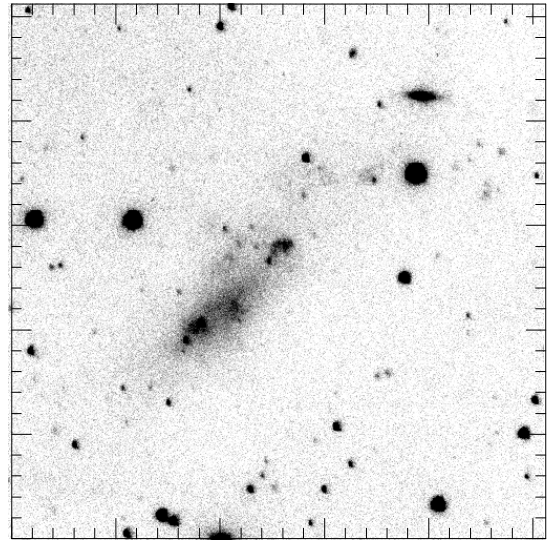
Figure 25: UGC 04173 (Jan93)

$\mu_{\rm top}=23.0$

$\mu_{\rm top}=21.5$

15″

μ_B

μ_I

fit

fit

r (arcsec)

r (arcsec)
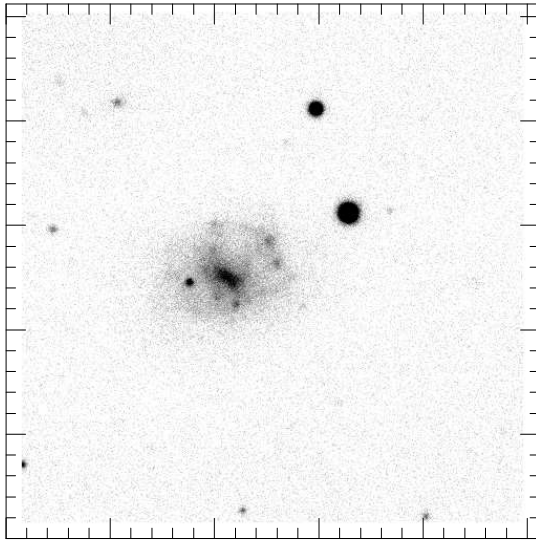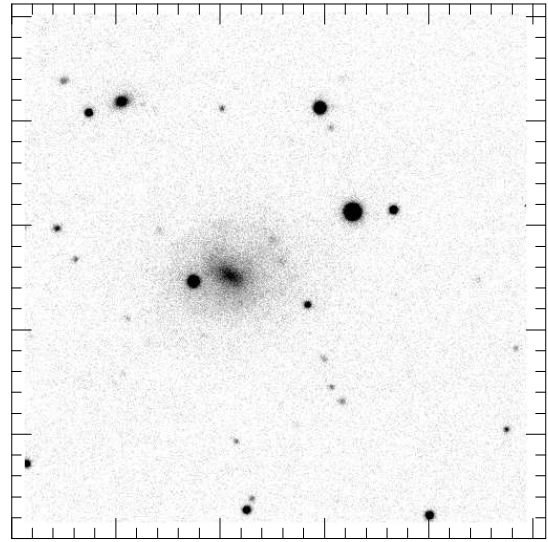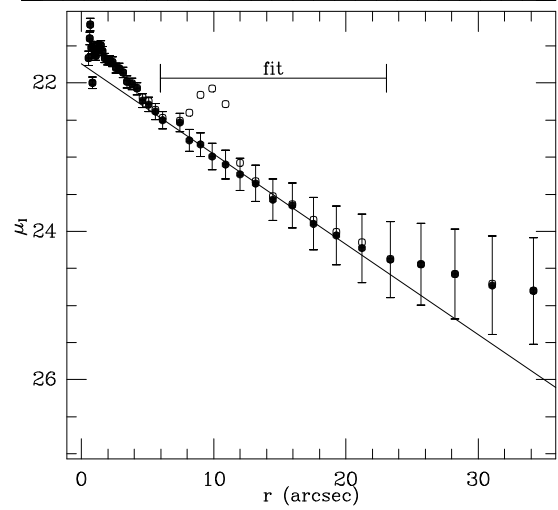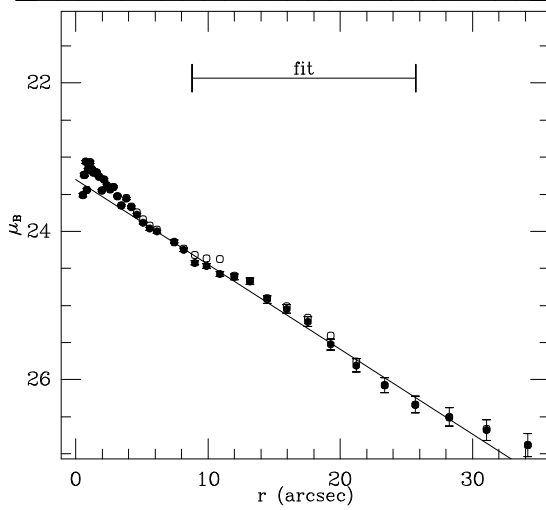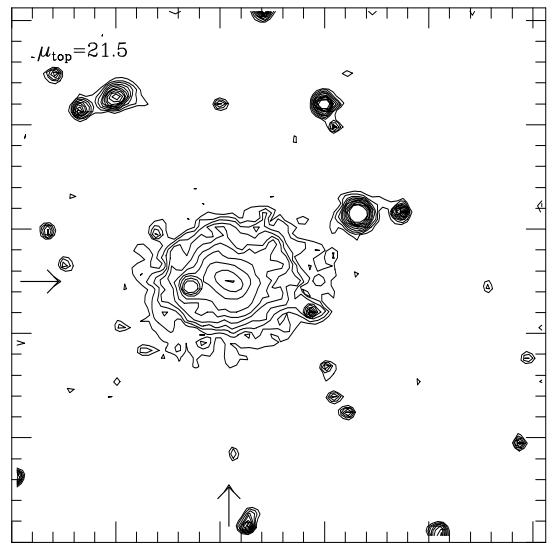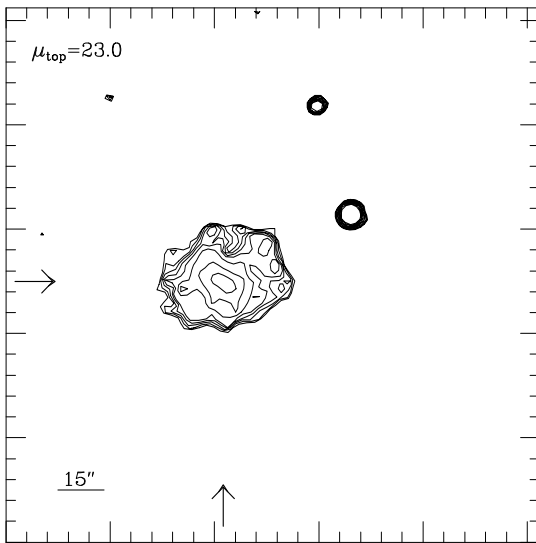
Figure 26: UGC 04204
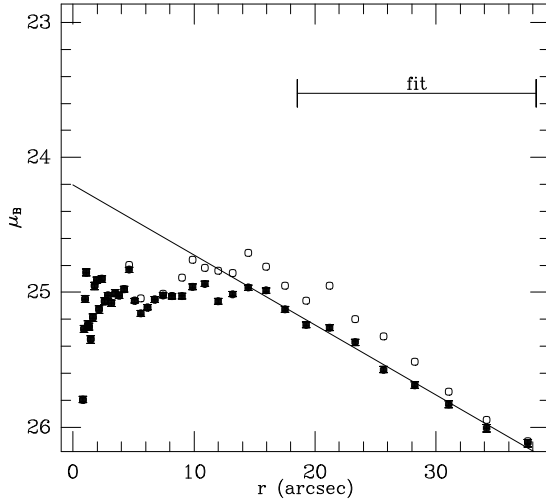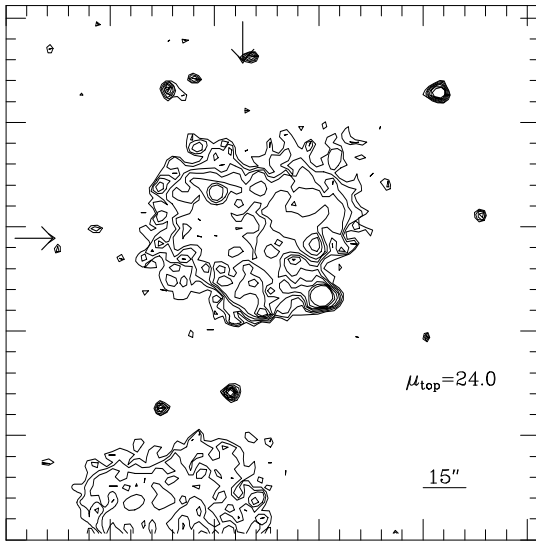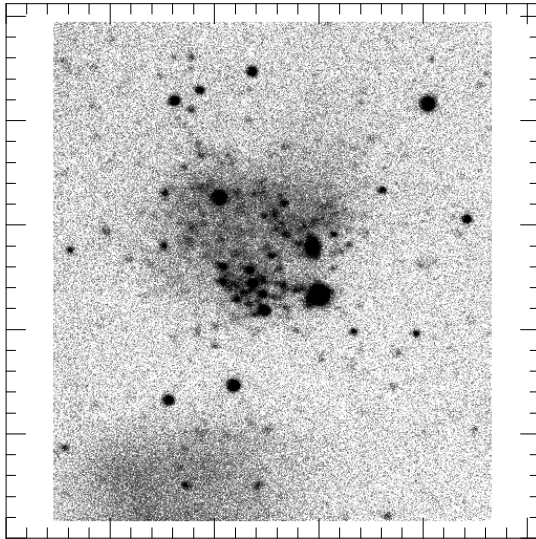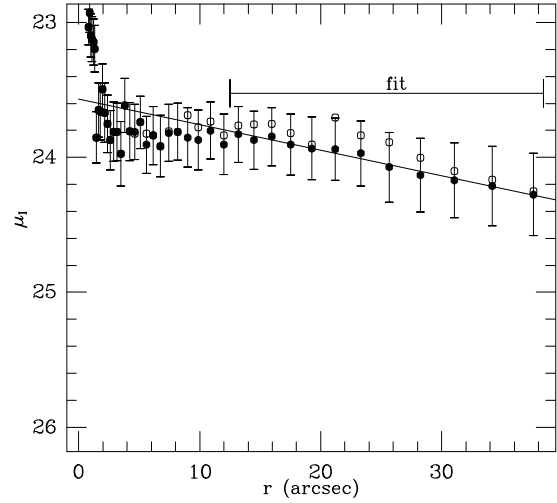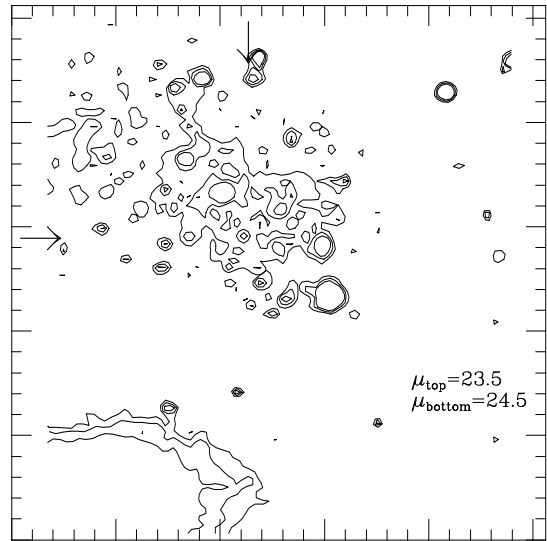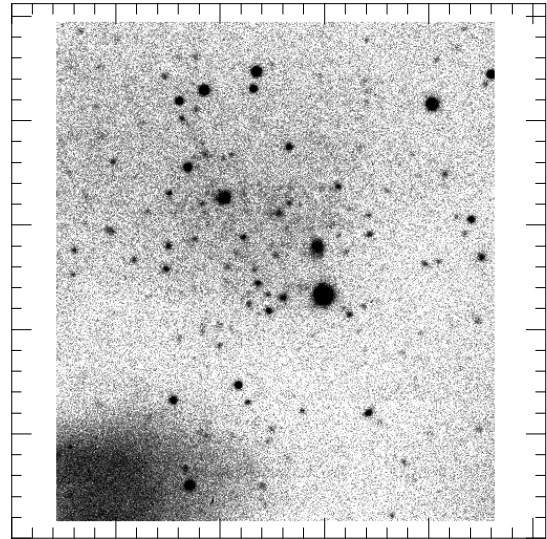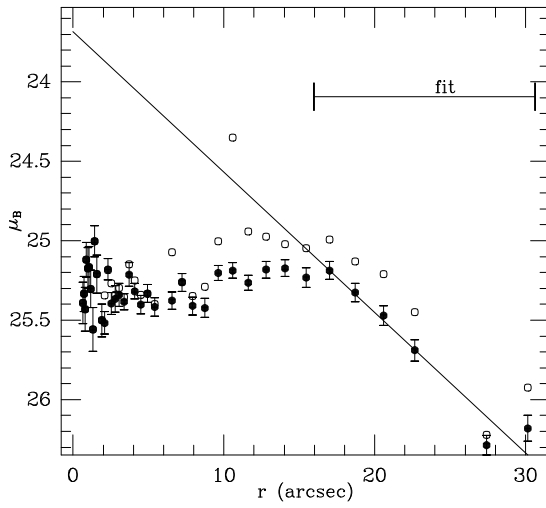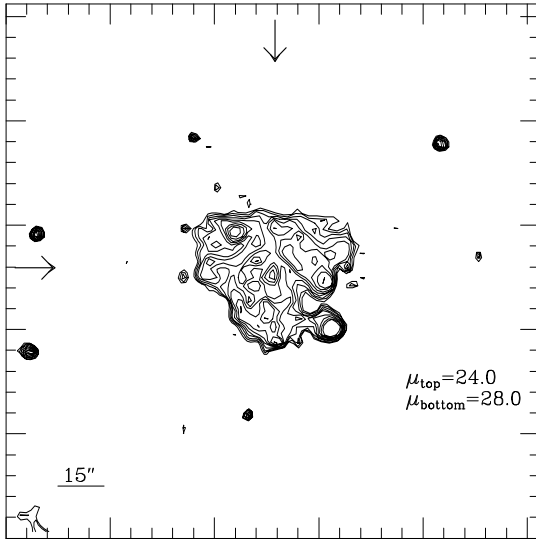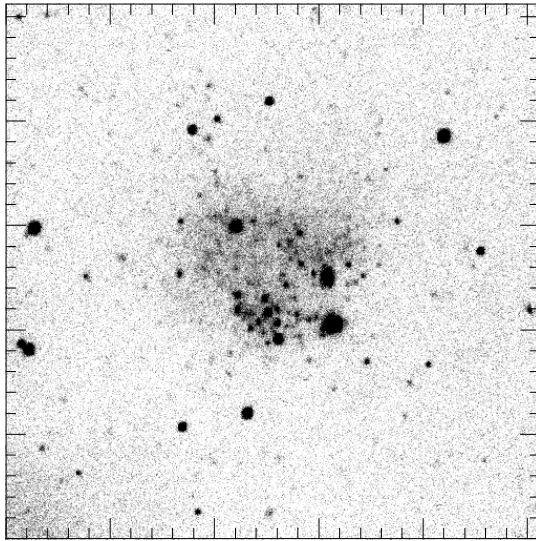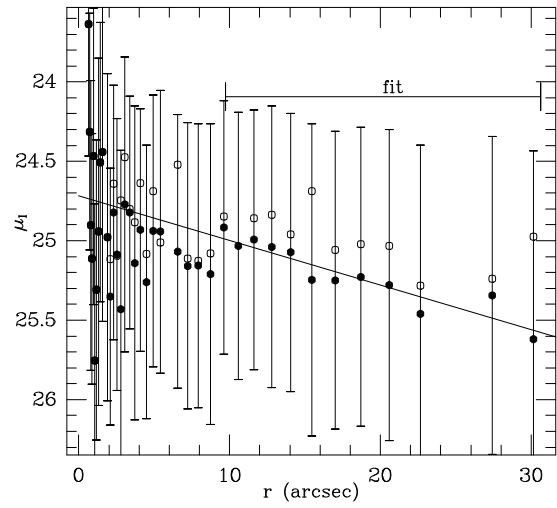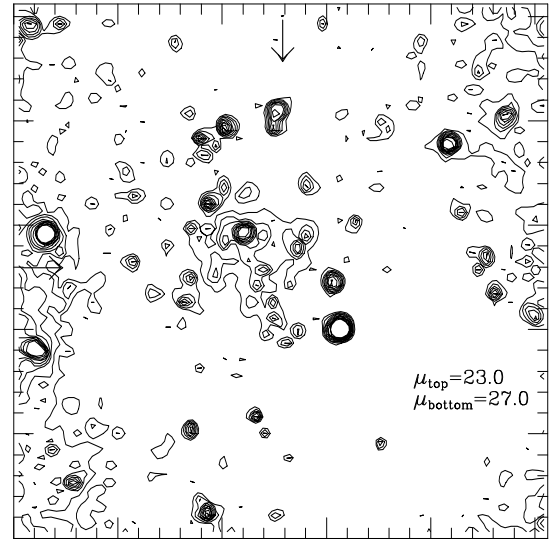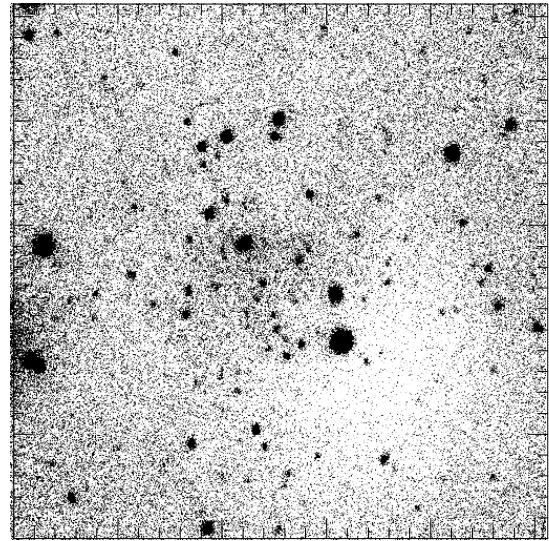
Figure 27: M81dwA

Figure 28: M81dwA (Jan93)
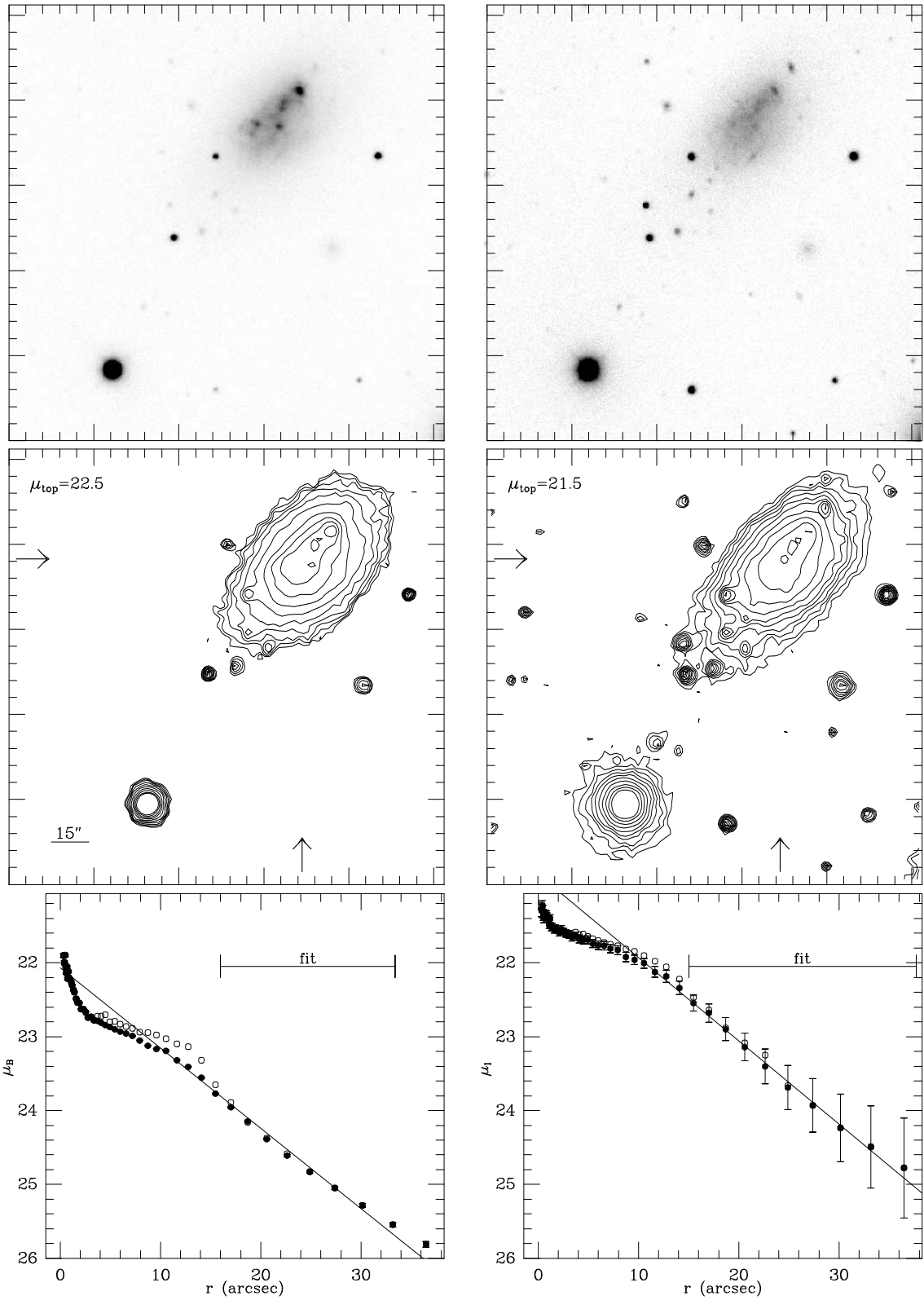
Figure 29: UGC 05423 (M81dwB; Jan93)
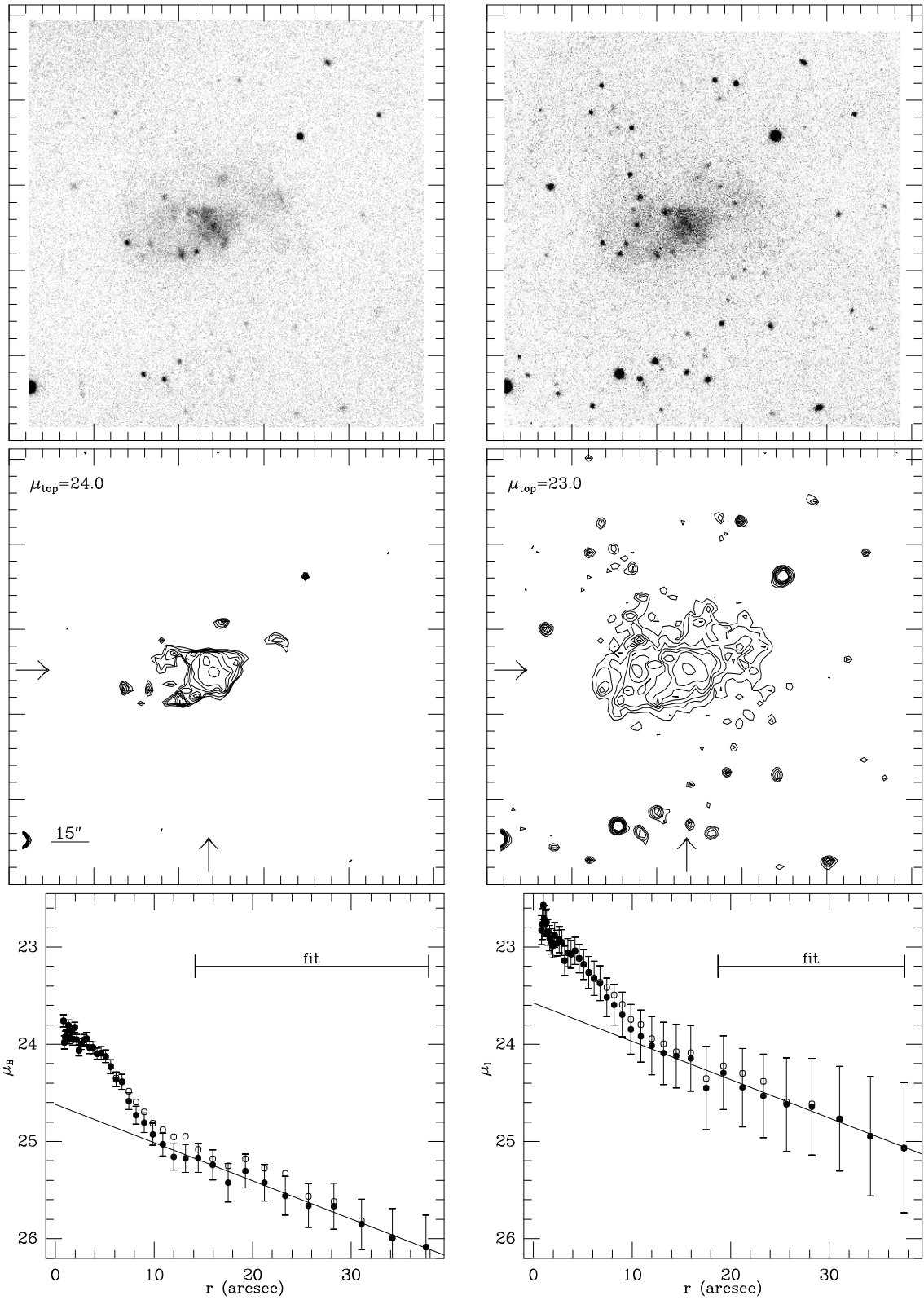
Figure 30: UGC 05706
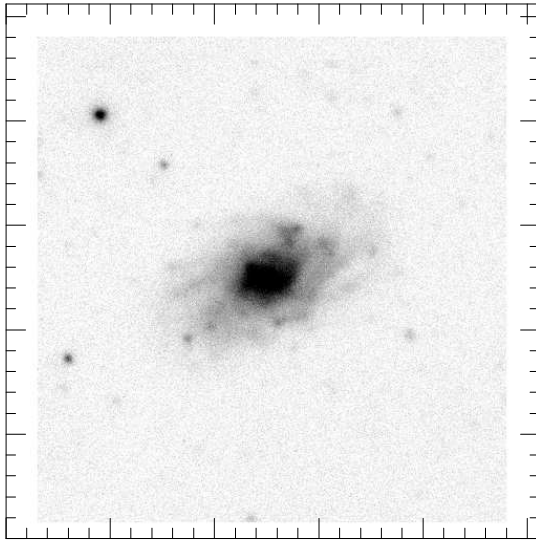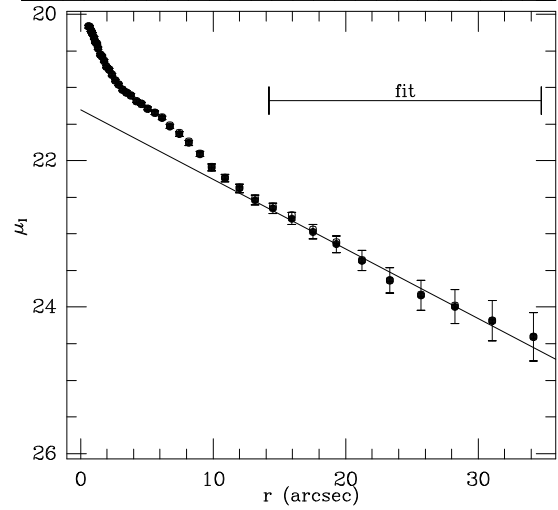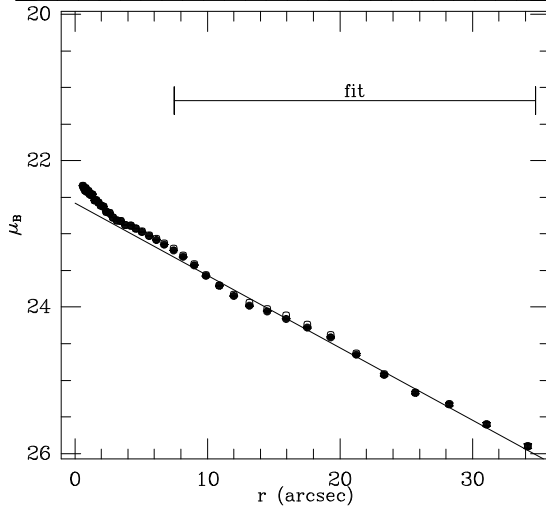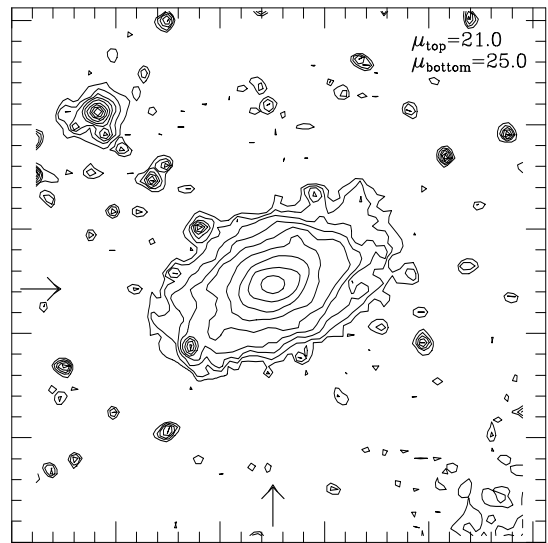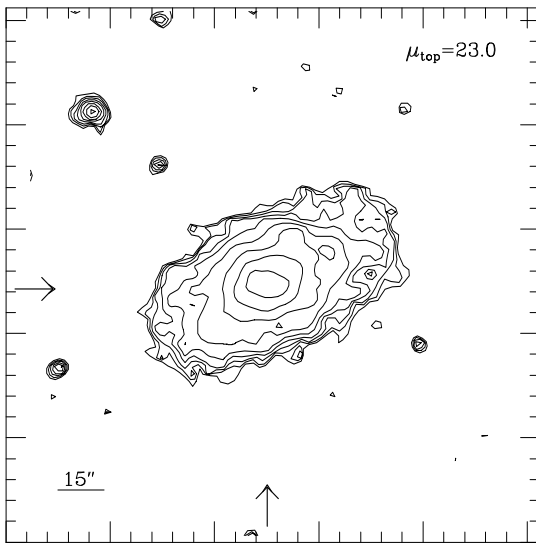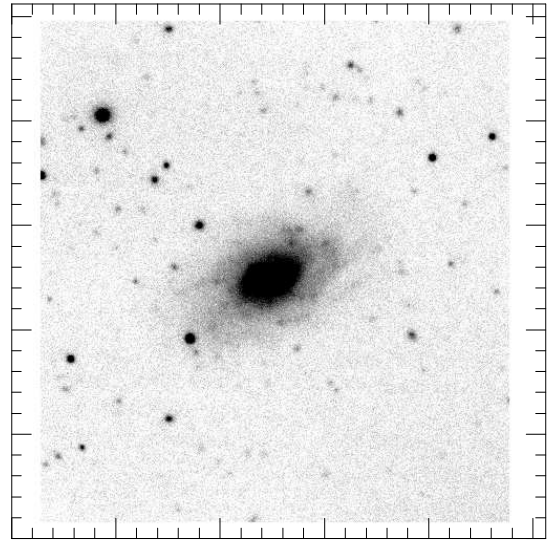
Figure 31: UGC 05709

$\mu_{top}=23.0$

$\mu_{top}=21.5$

15″
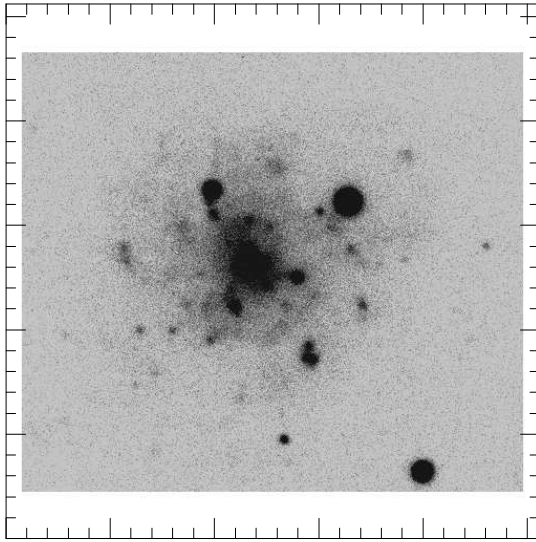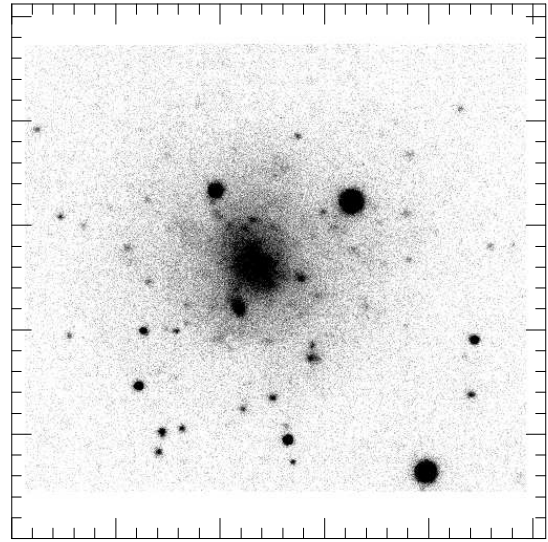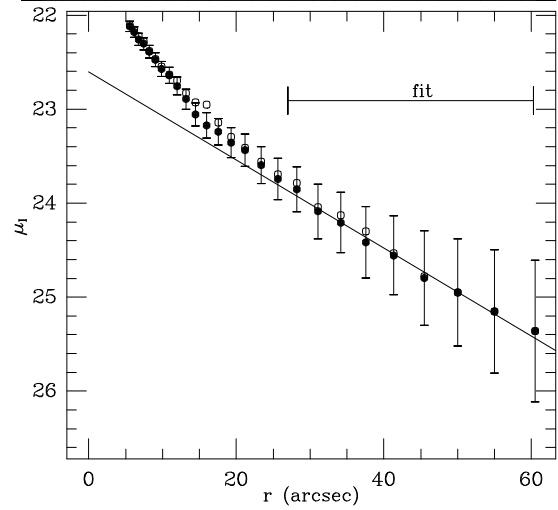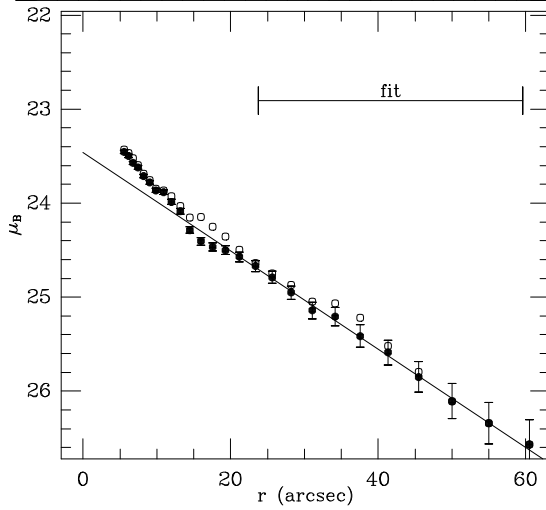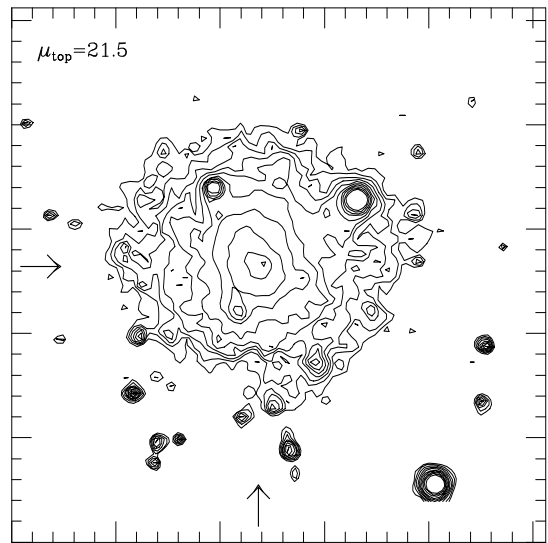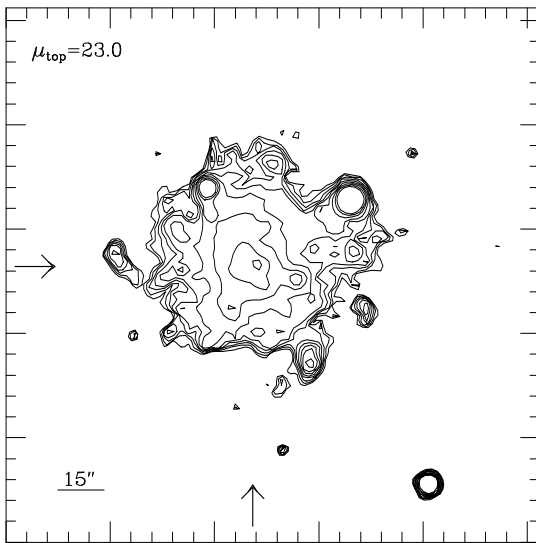
Figure 32: UGC 06151
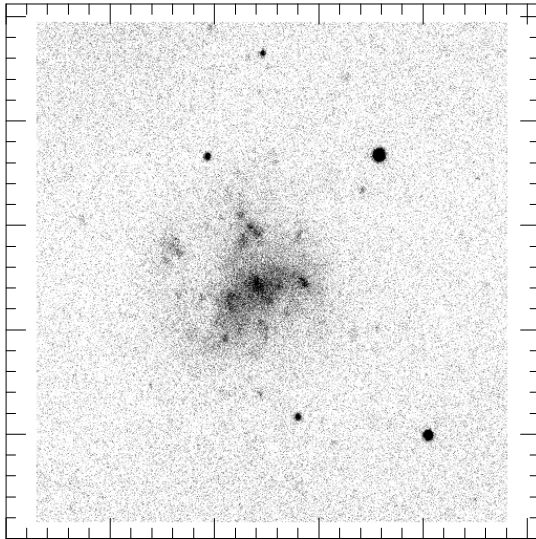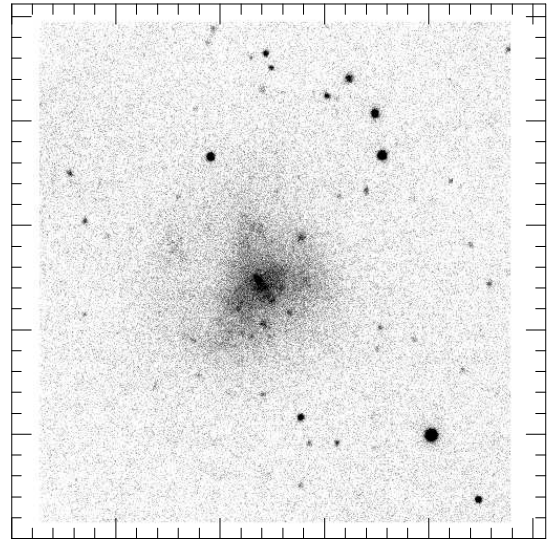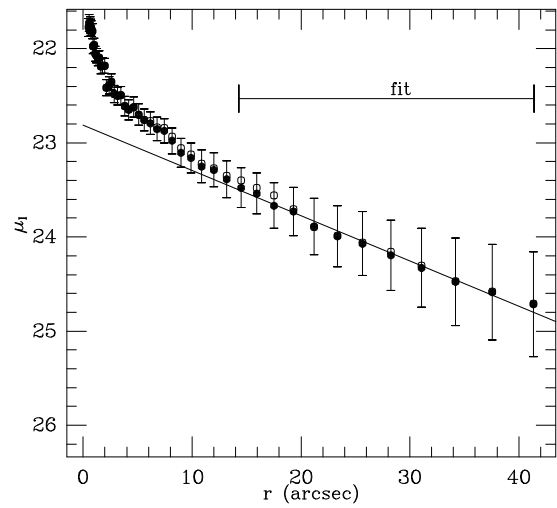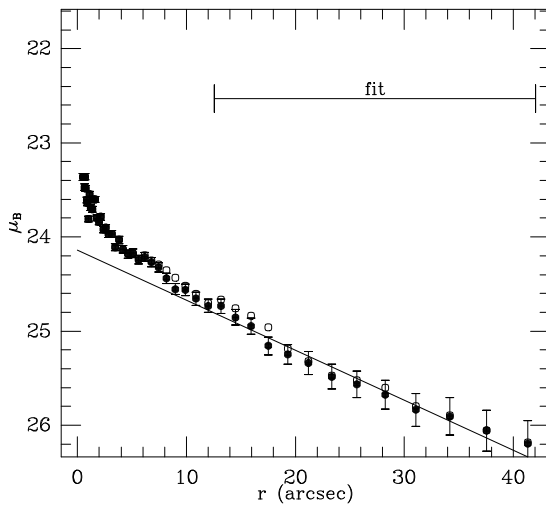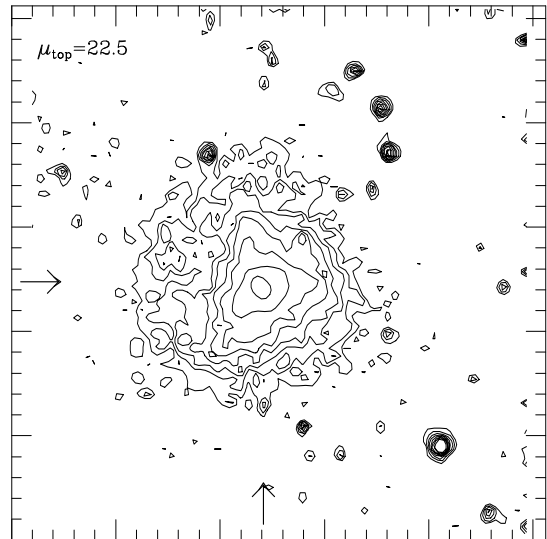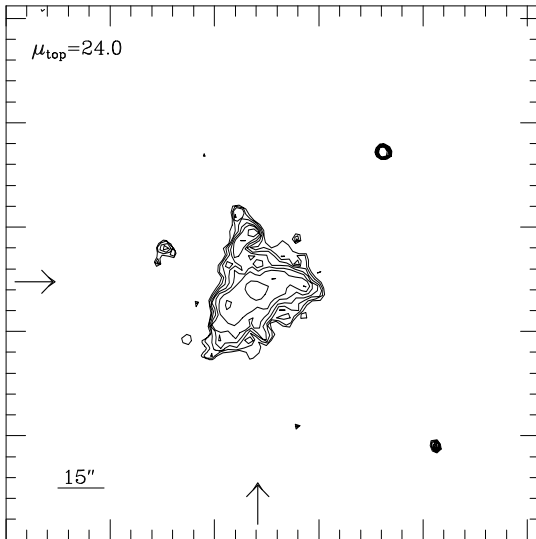
Figure 33: UGC 06248
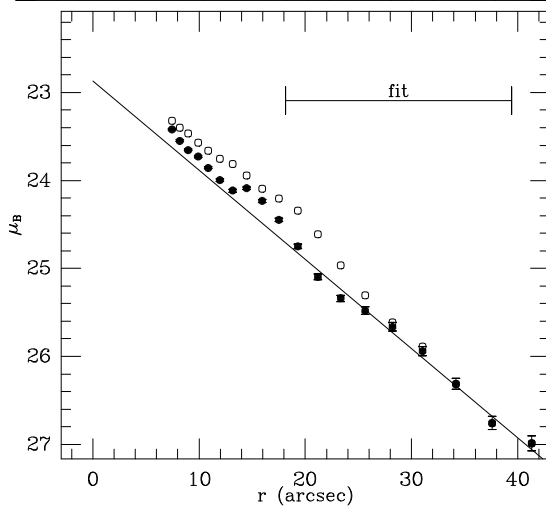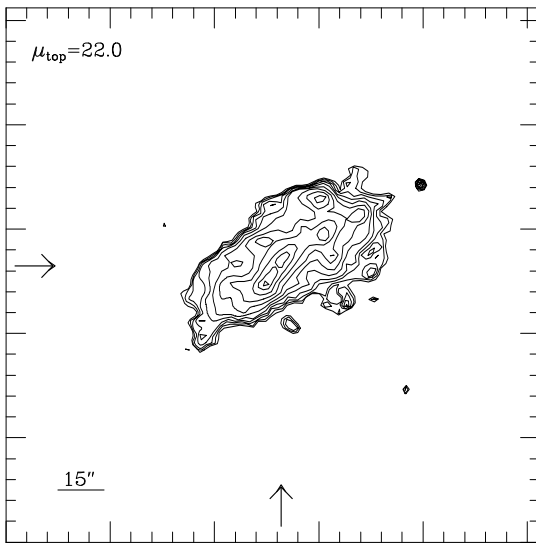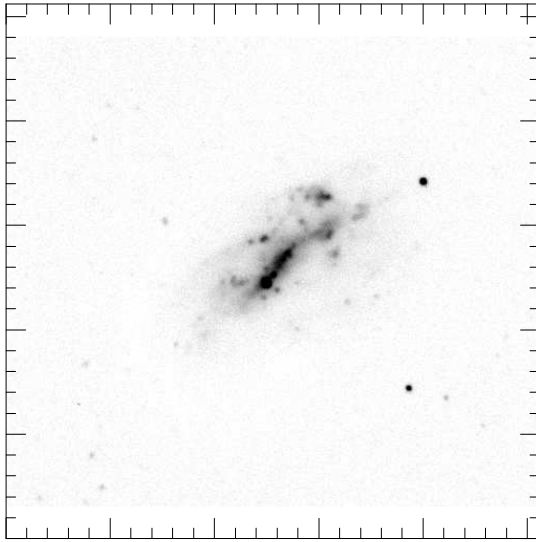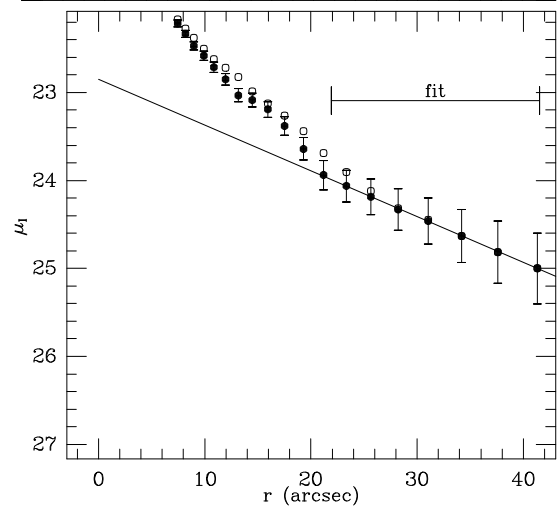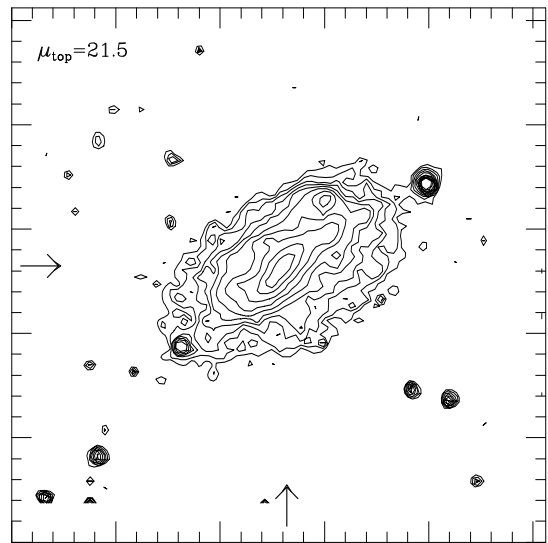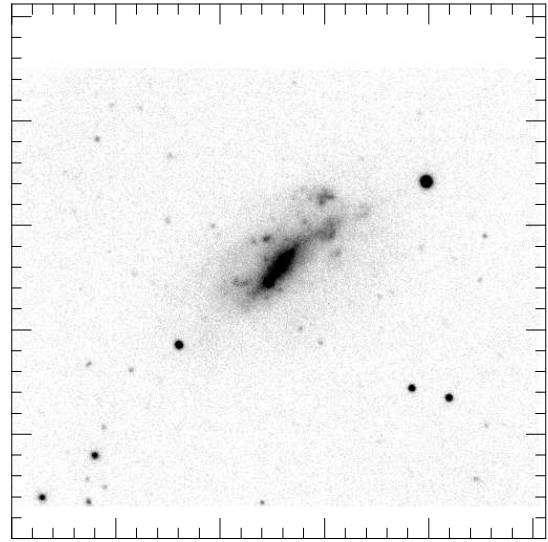
Figure 34: UGC 06596

$\mu_{top}=23.0$

$\mu_{top}=20.5$

15″

fit

fit

μ_B

μ_I

r (arcsec)

r (arcsec)
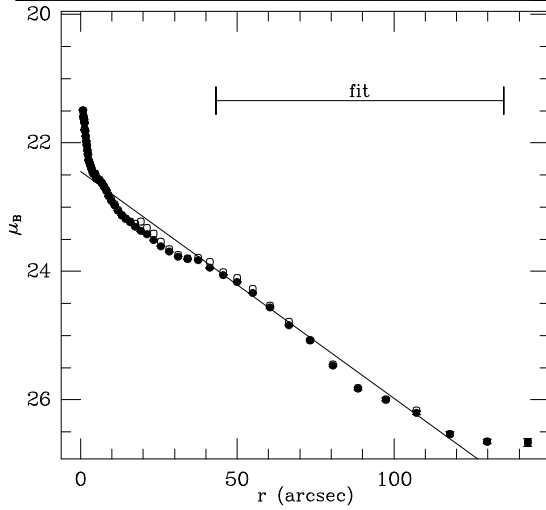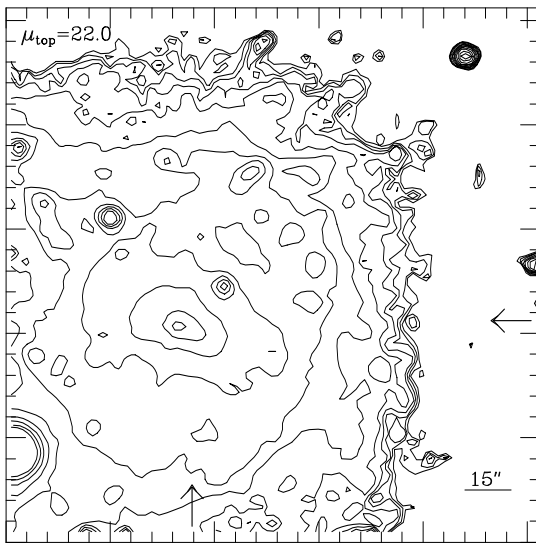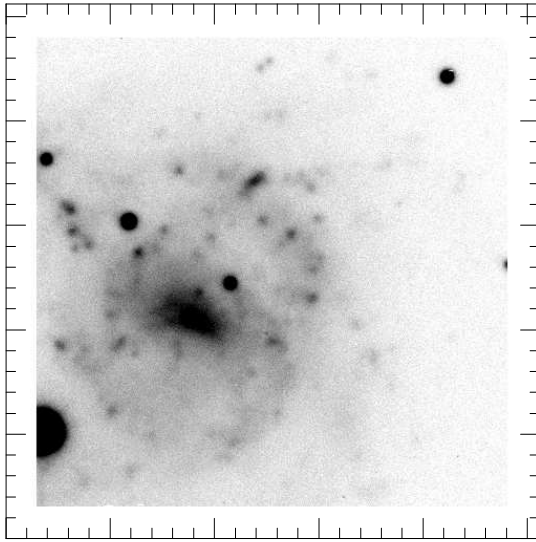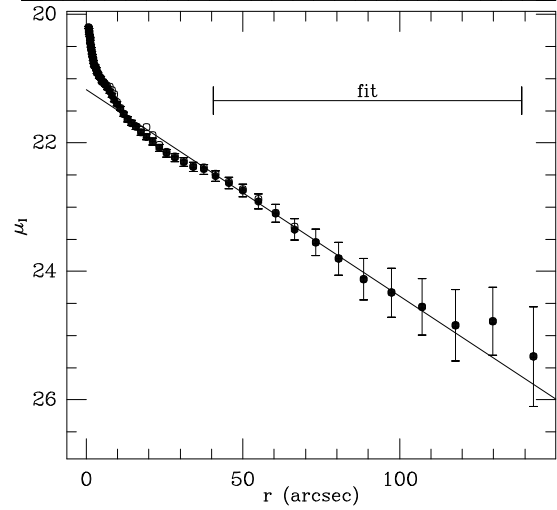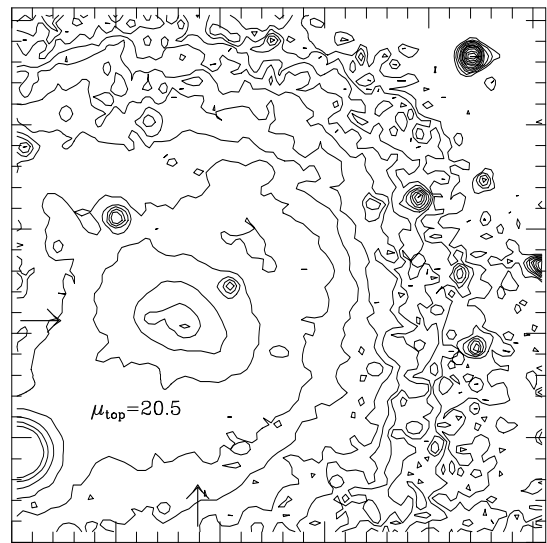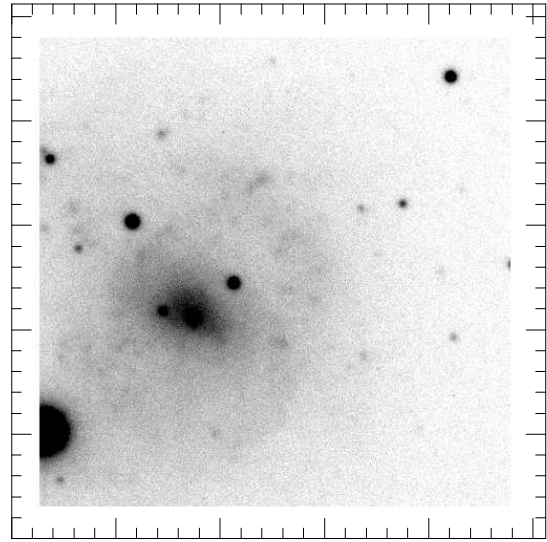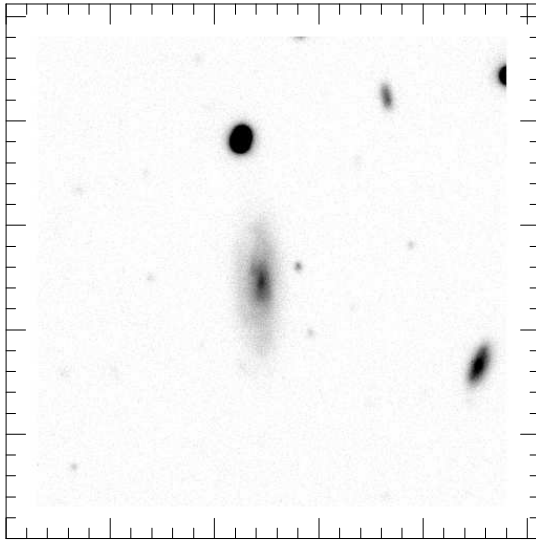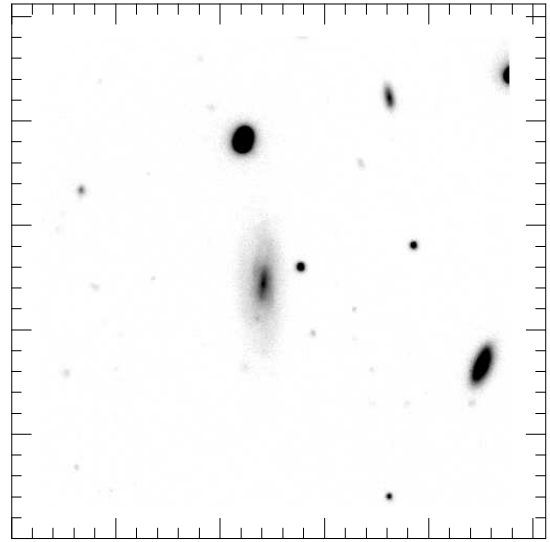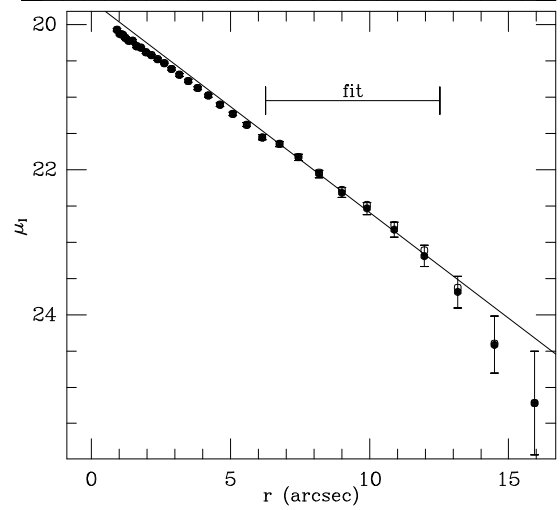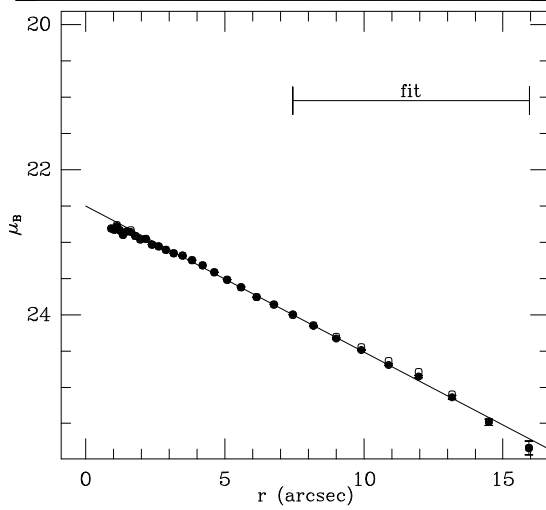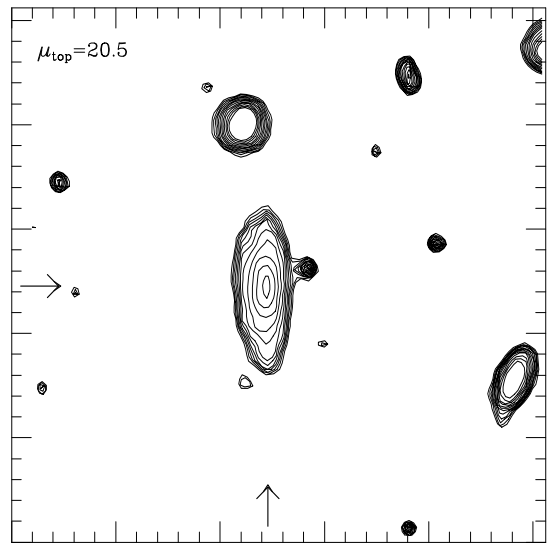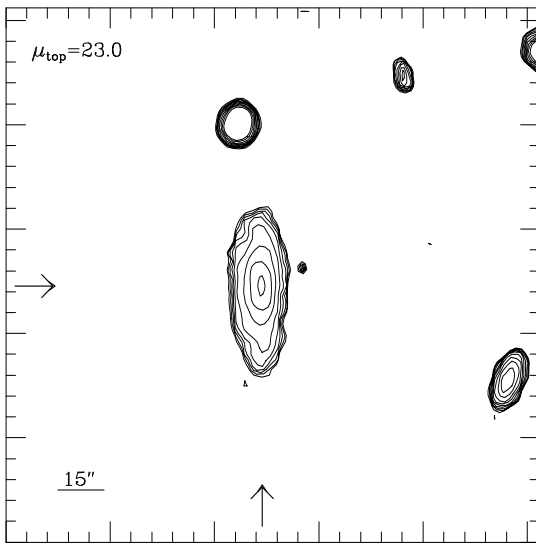
Figure 36: UGC 07295

$\mu_{top}=22.5$

$\mu_{top}=22.0$

15″
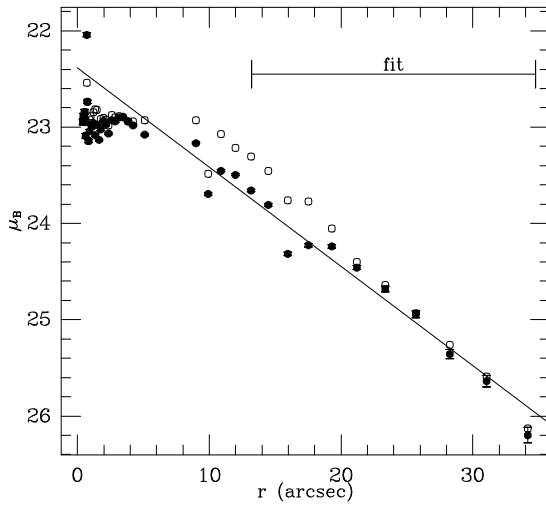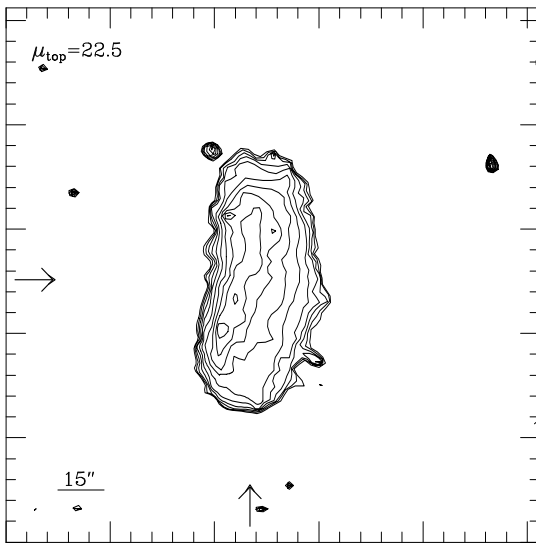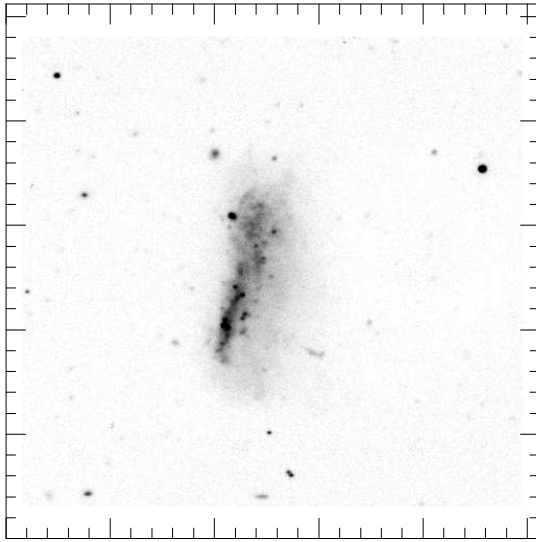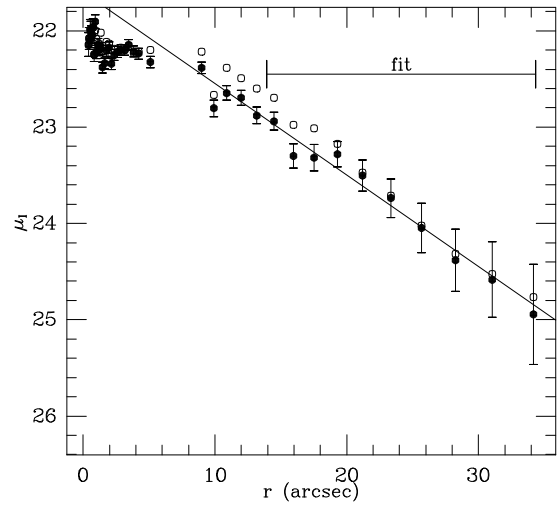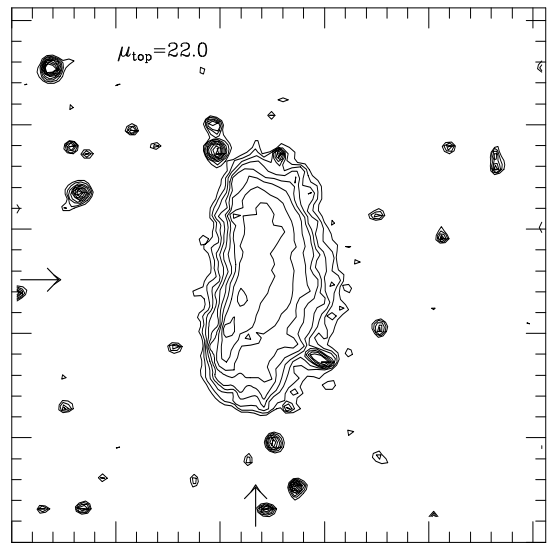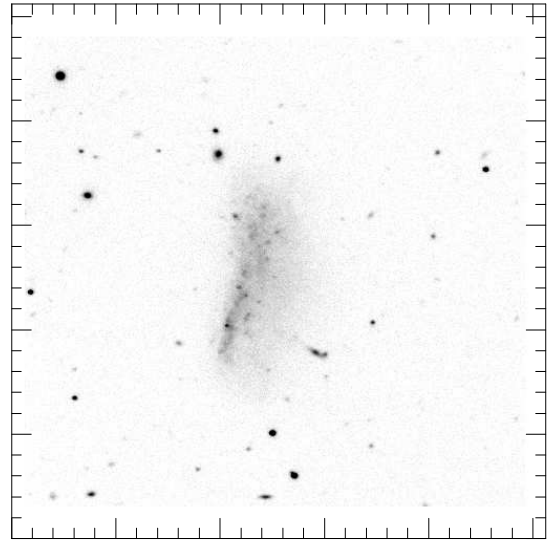
Figure 37: UGC 07548
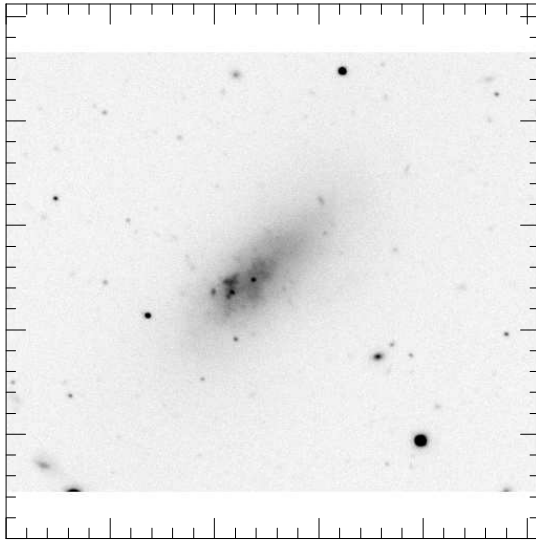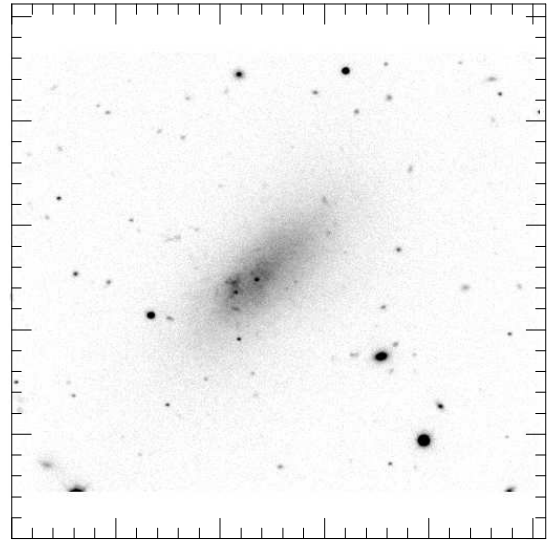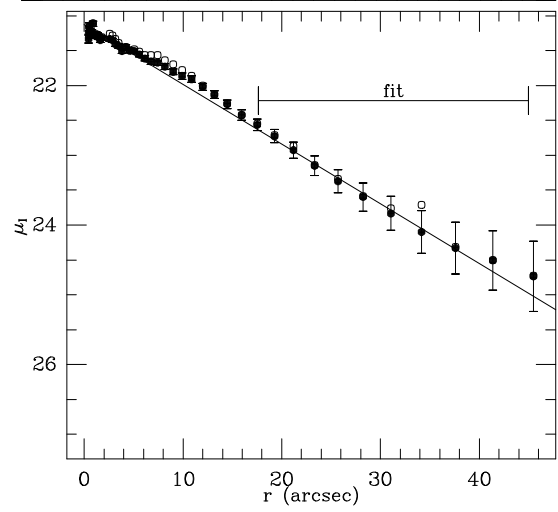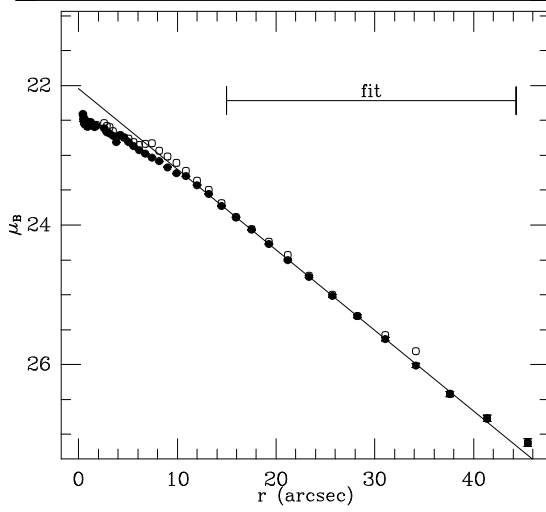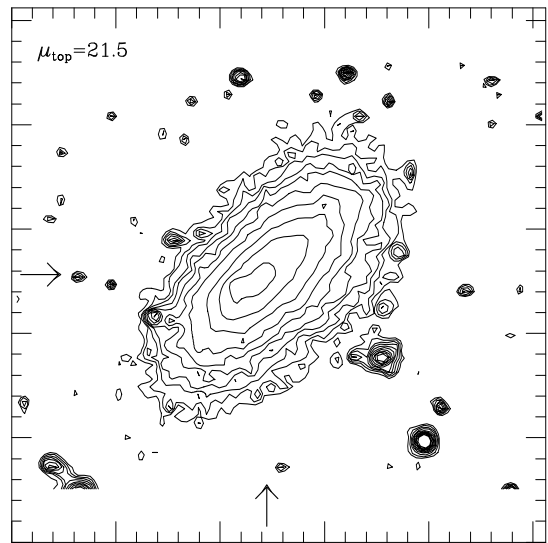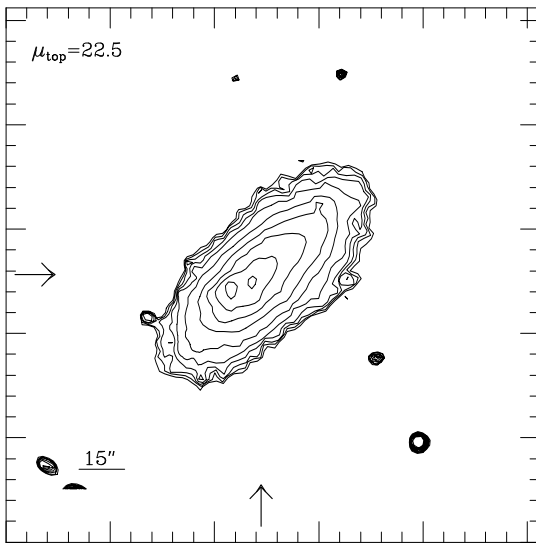
Figure 38: UGC 07596
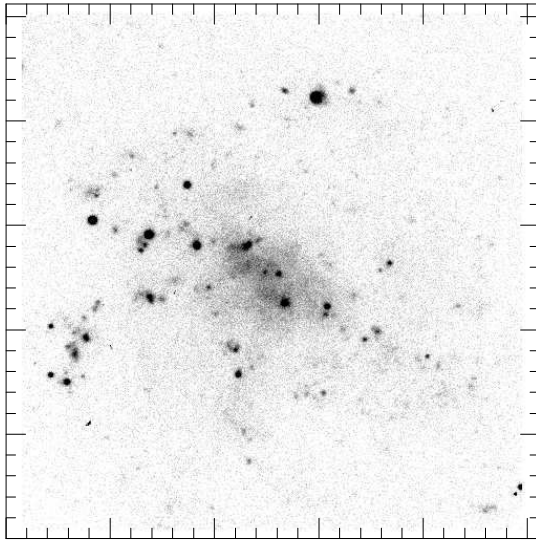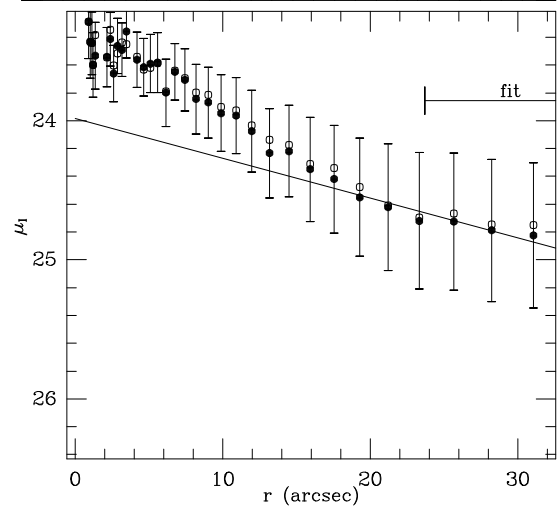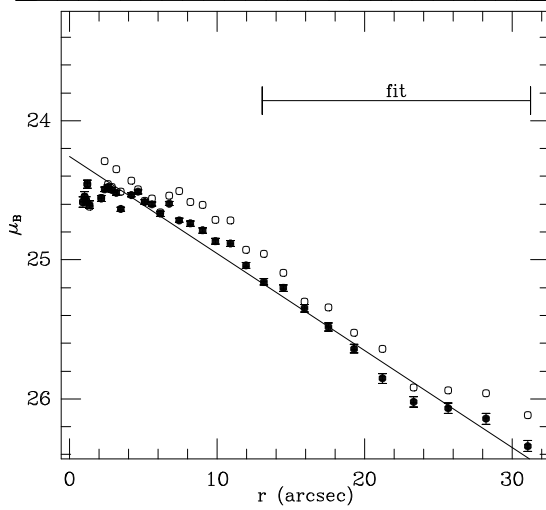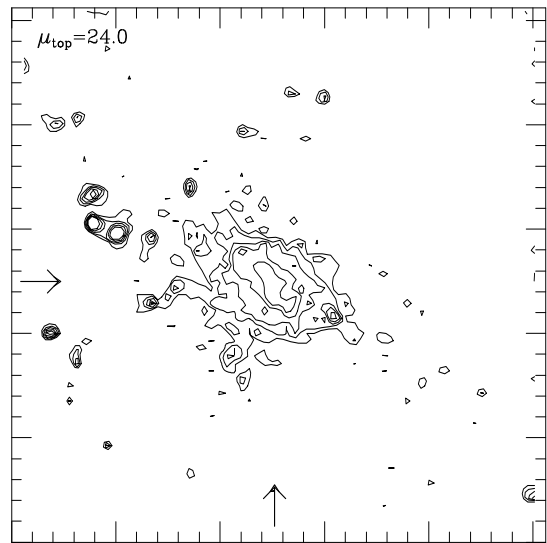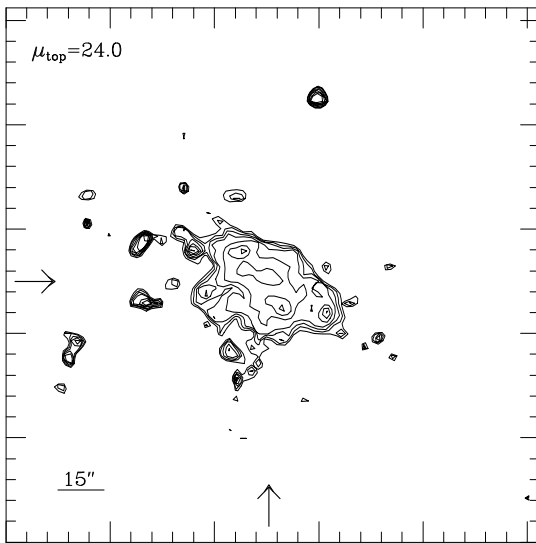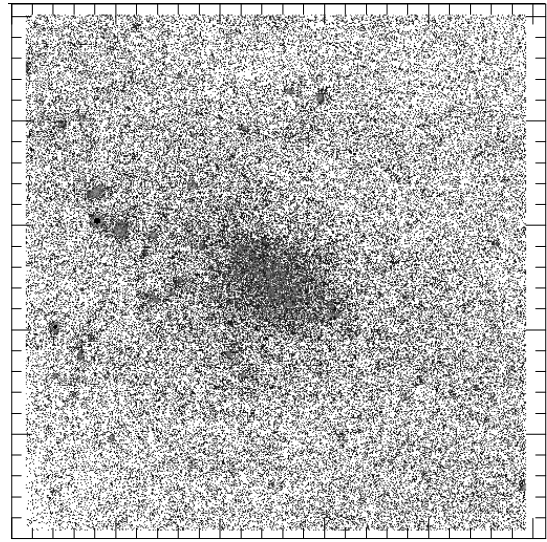
Figure 39: UGC 07608
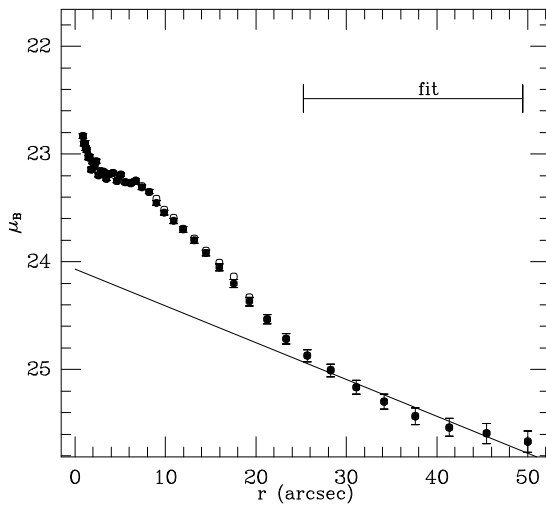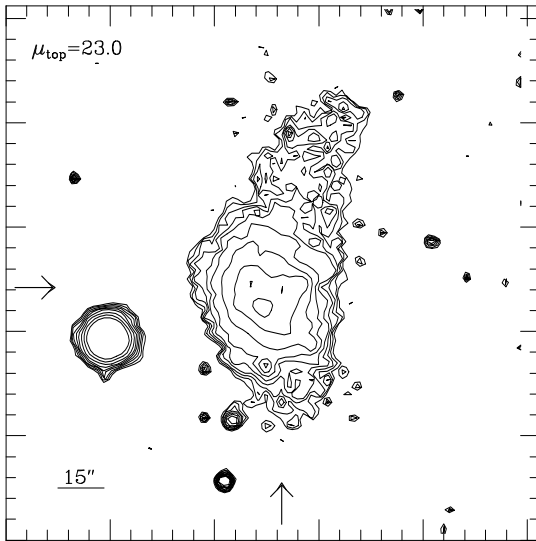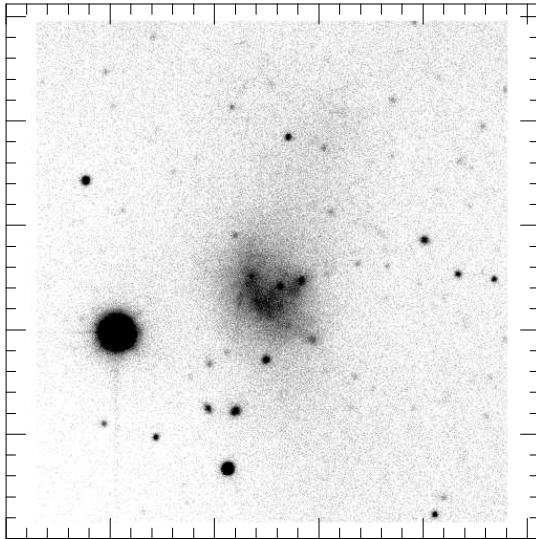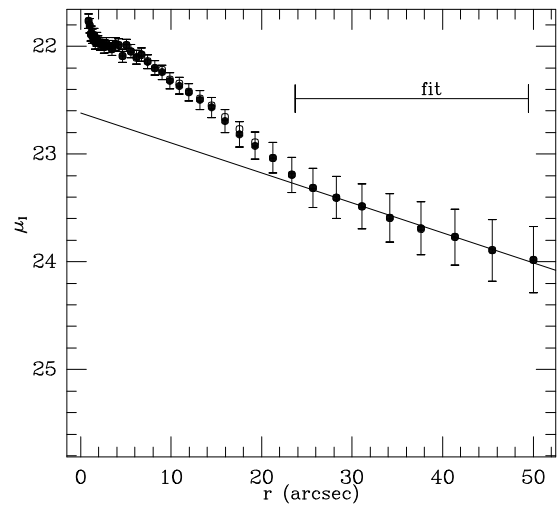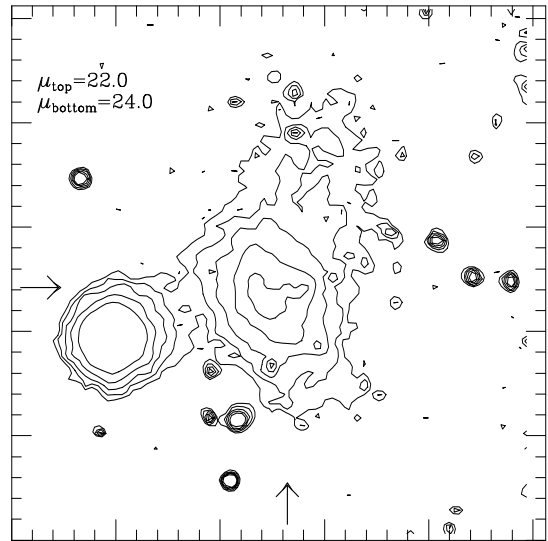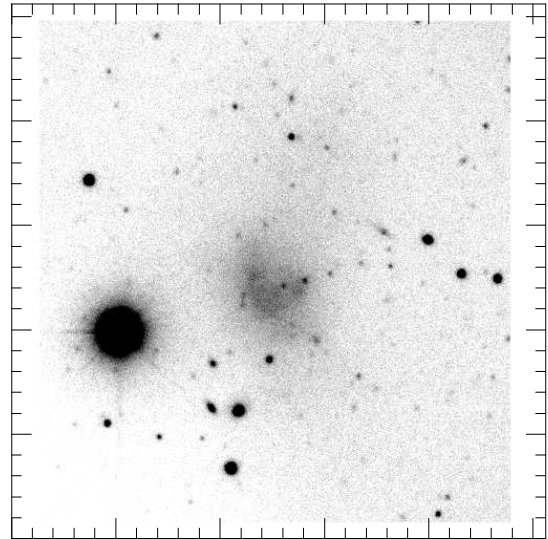
Figure 40: UGC 07636
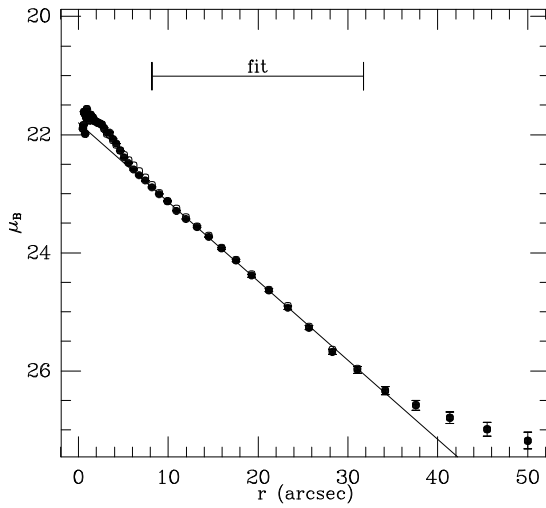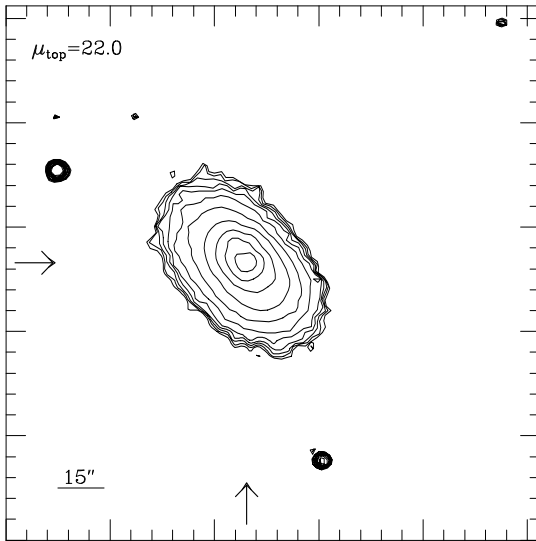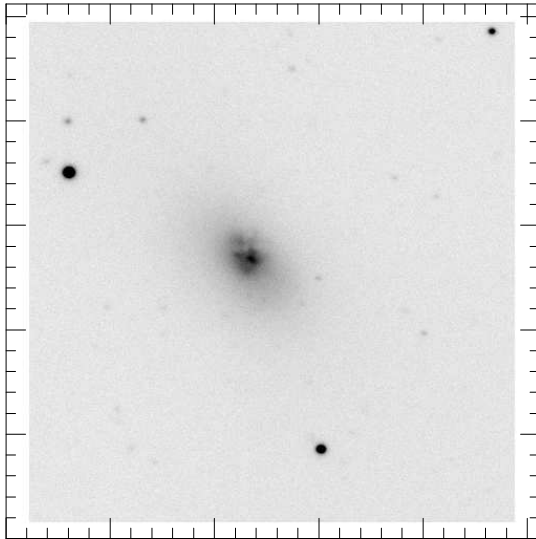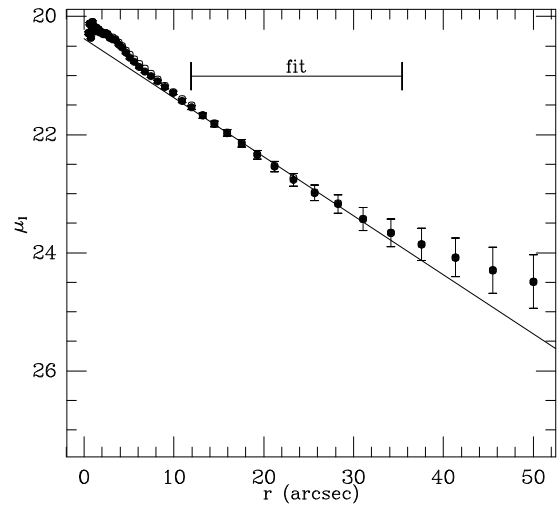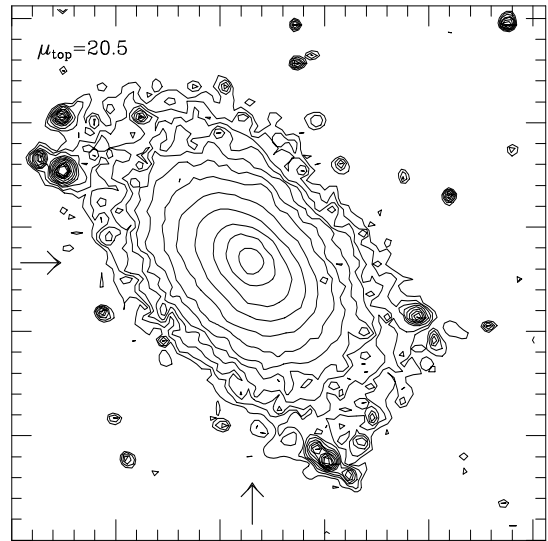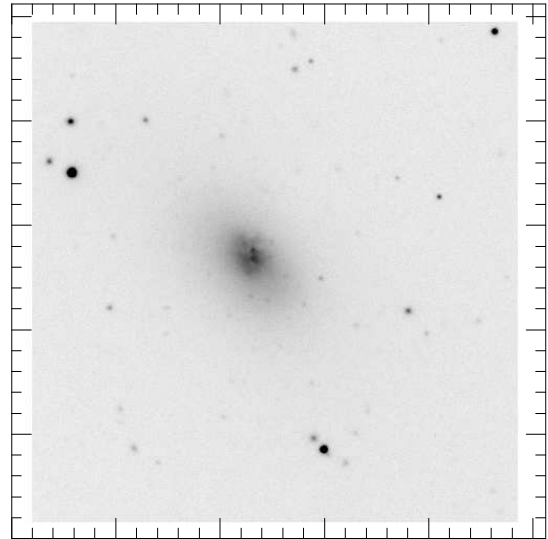
Figure 41: UGC 07684
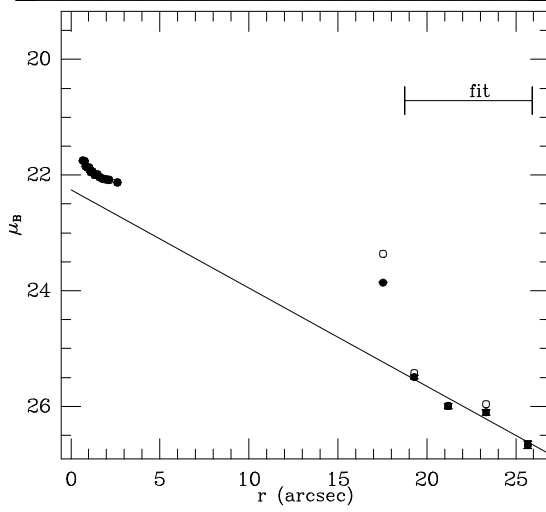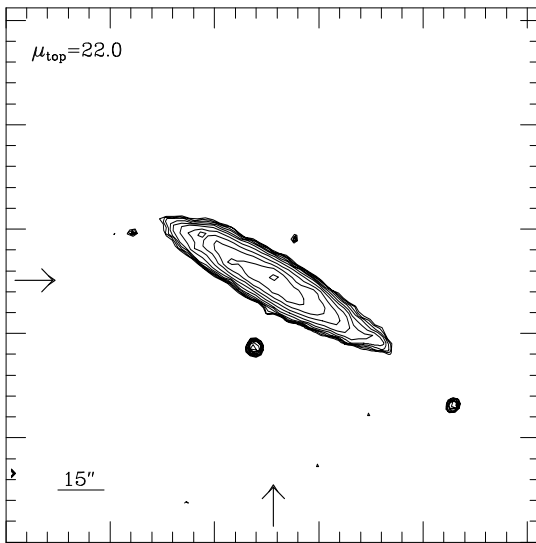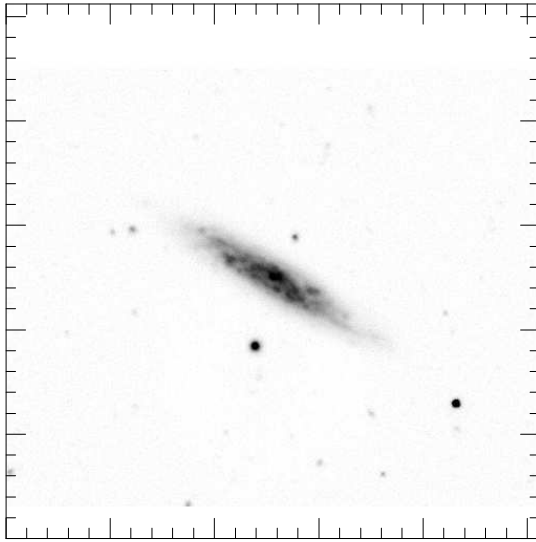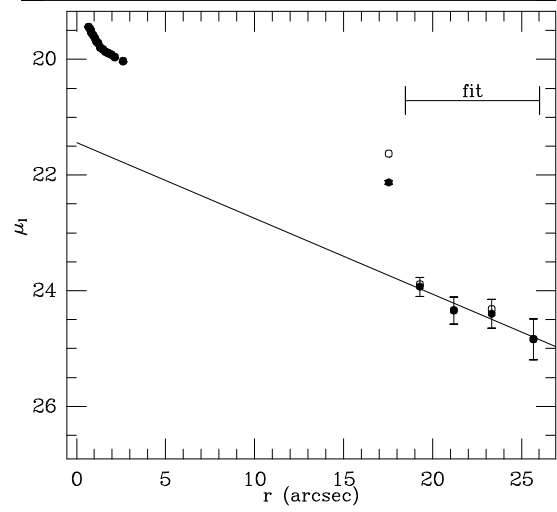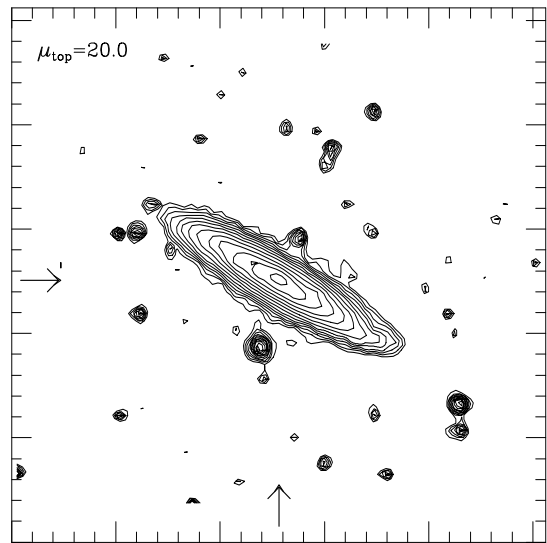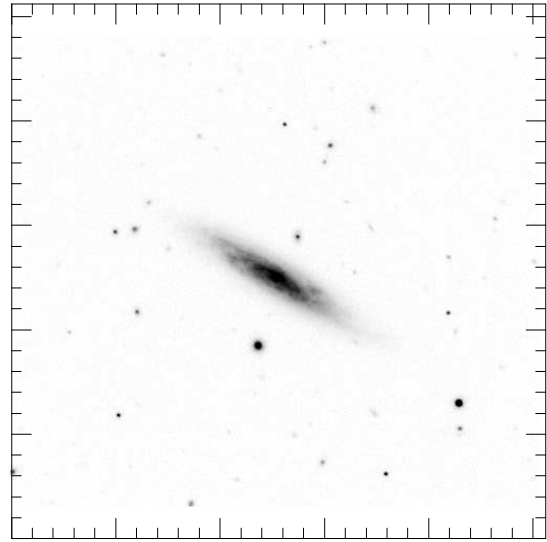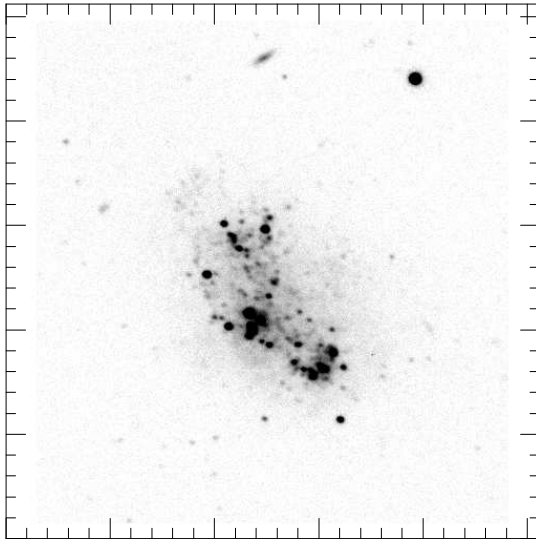
Figure 42: UGC 07882
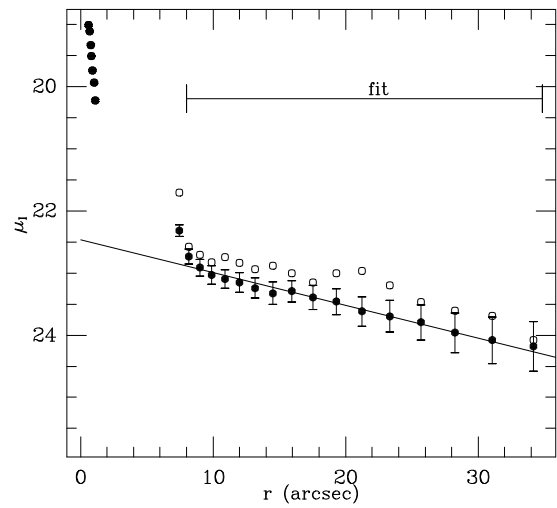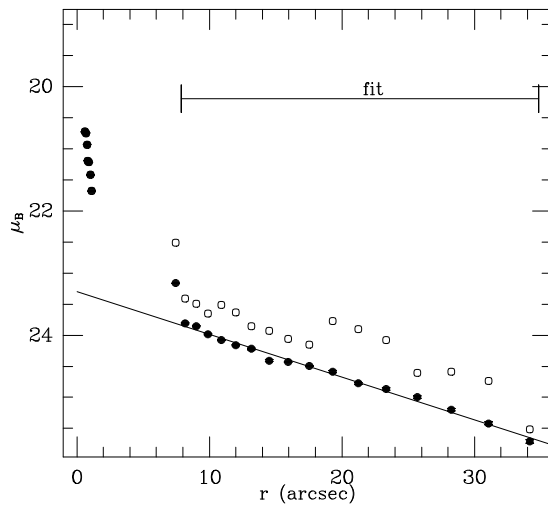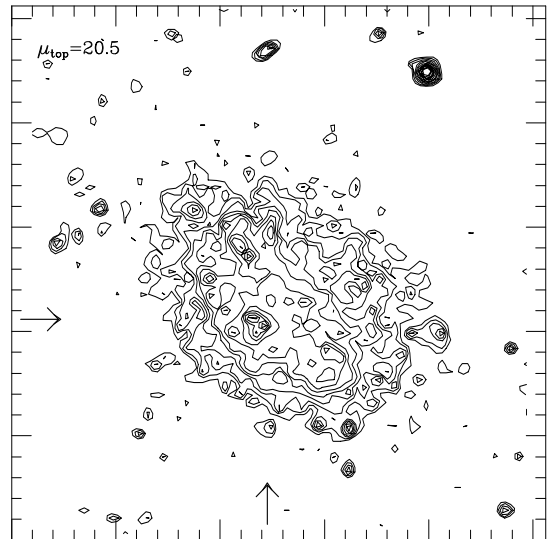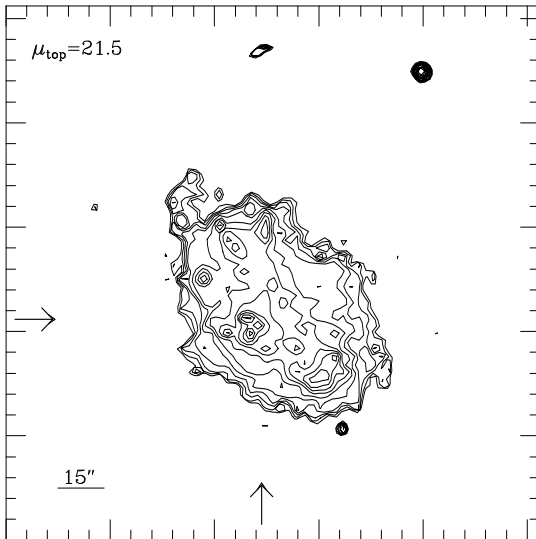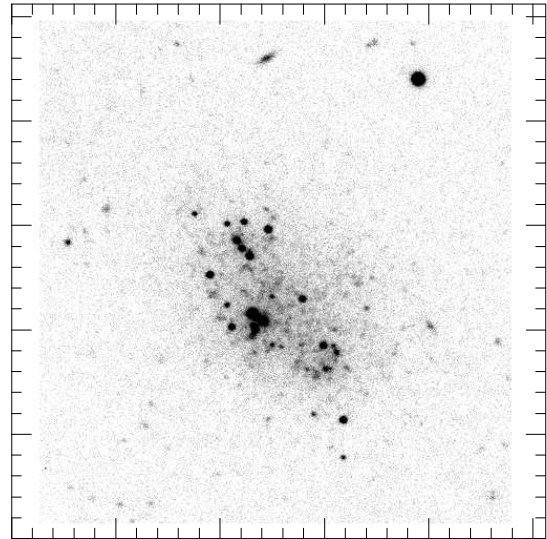
Figure 43: UGC 08091 (GR8)
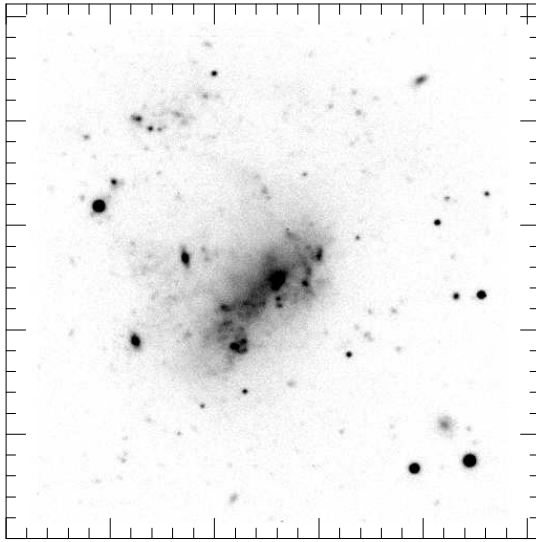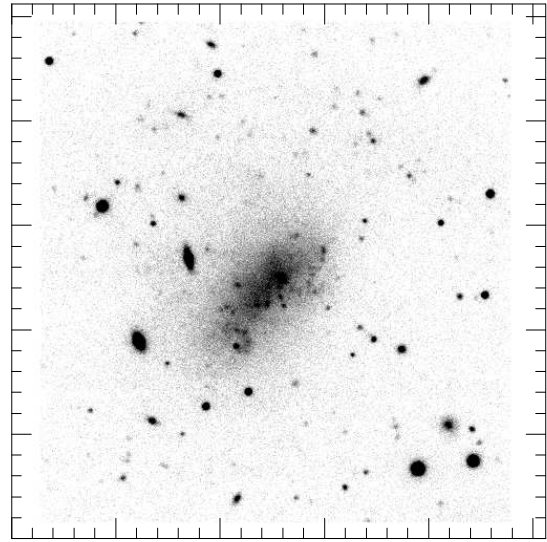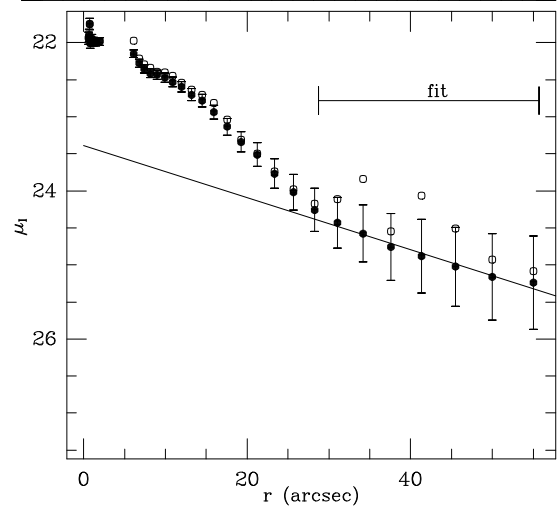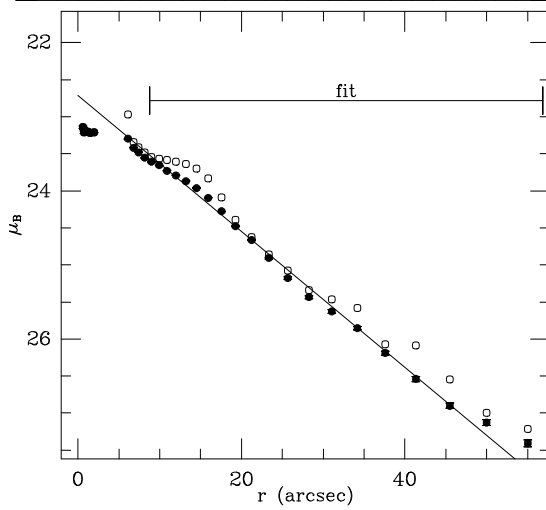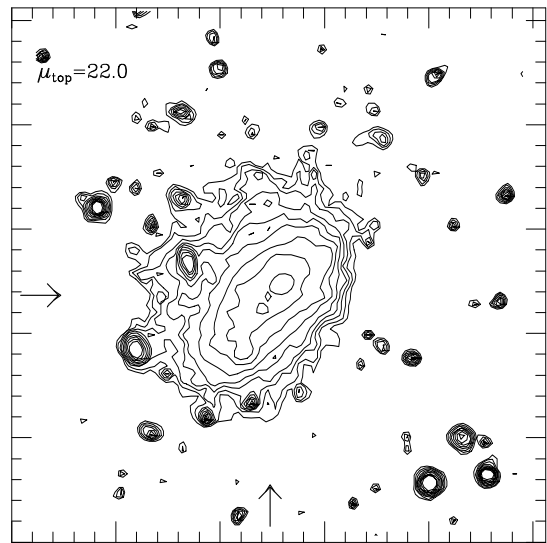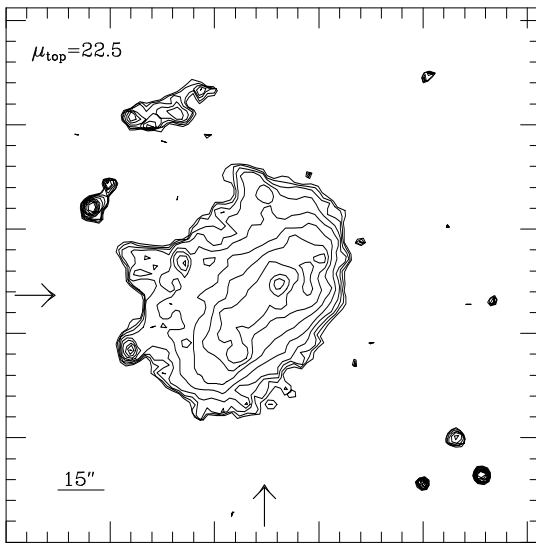
Figure 44: UGC 08683
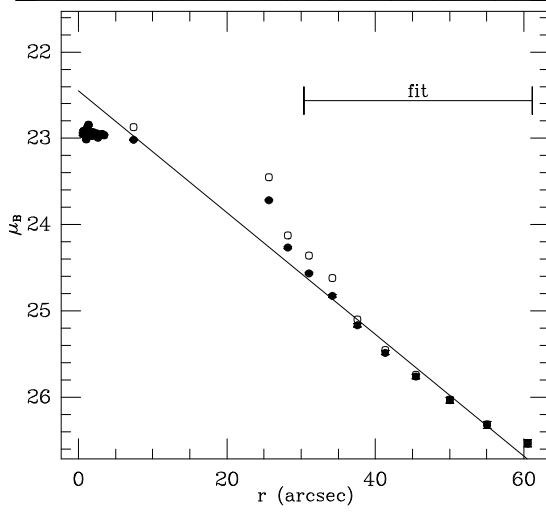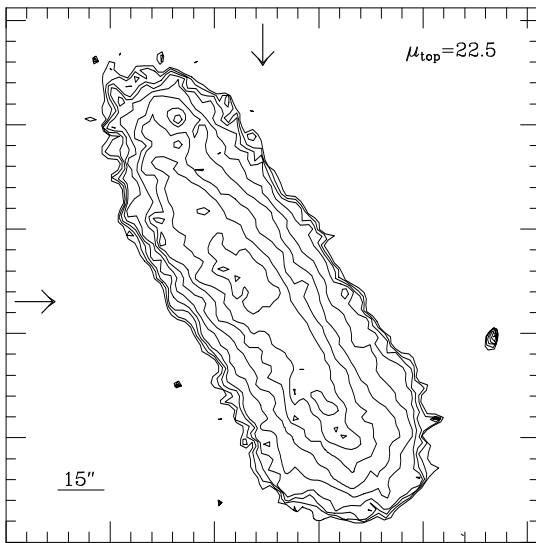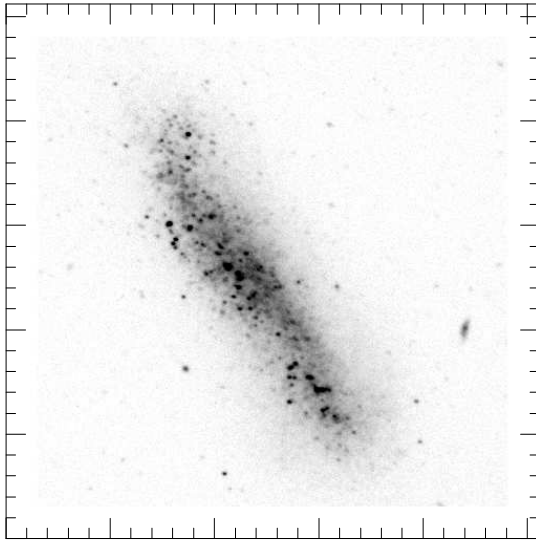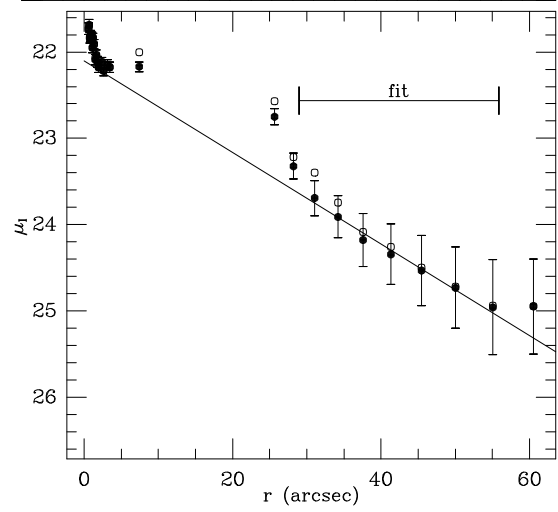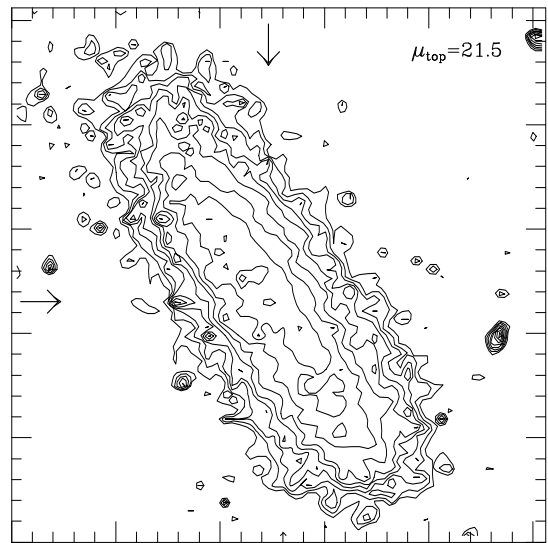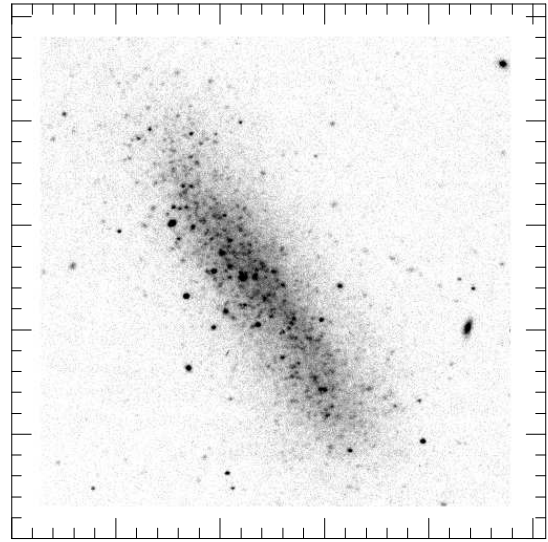
Figure 45: UGC 08760
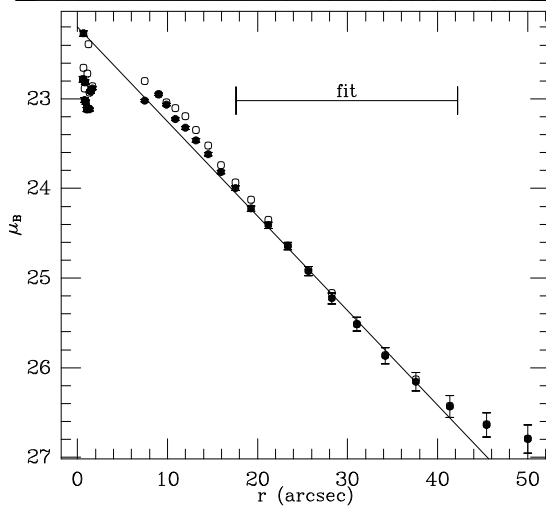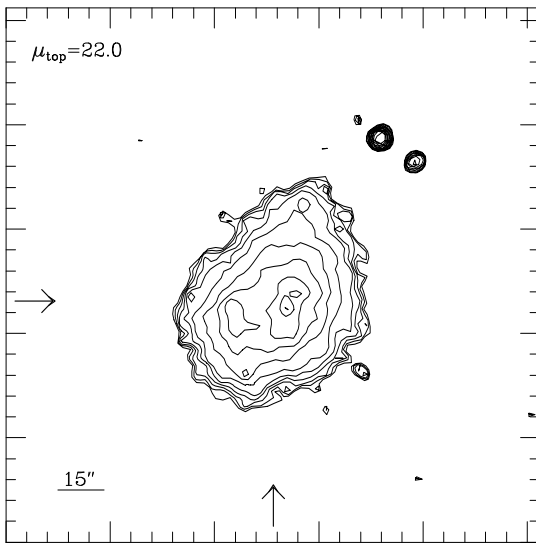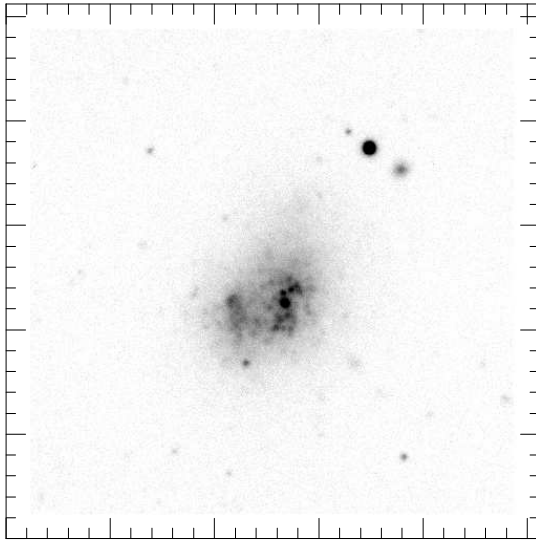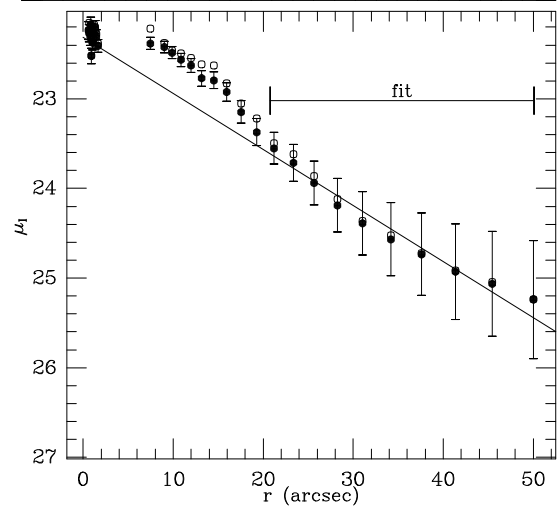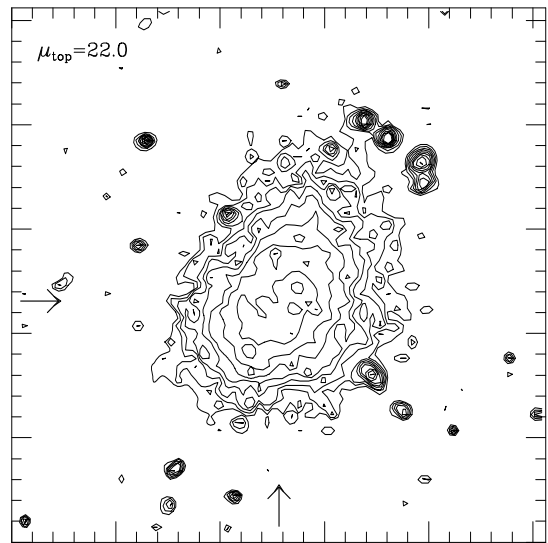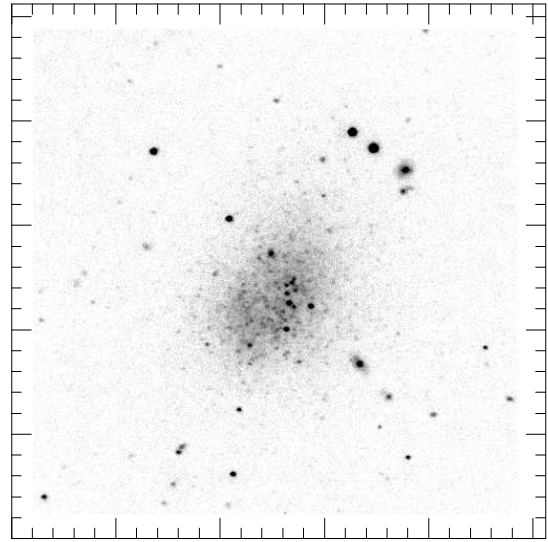
Figure 46: UGC 08833
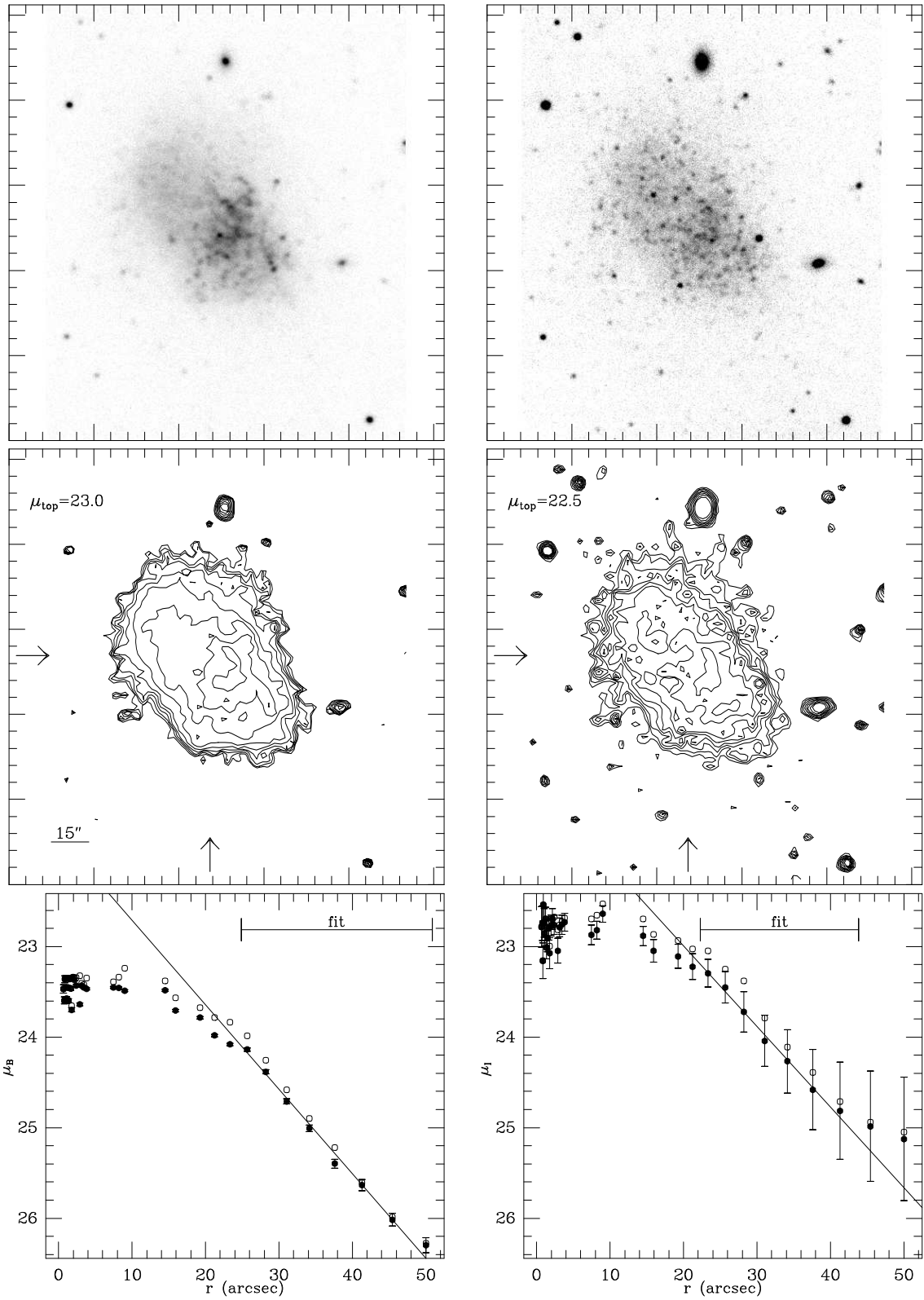
Figure 47: UGC 09128
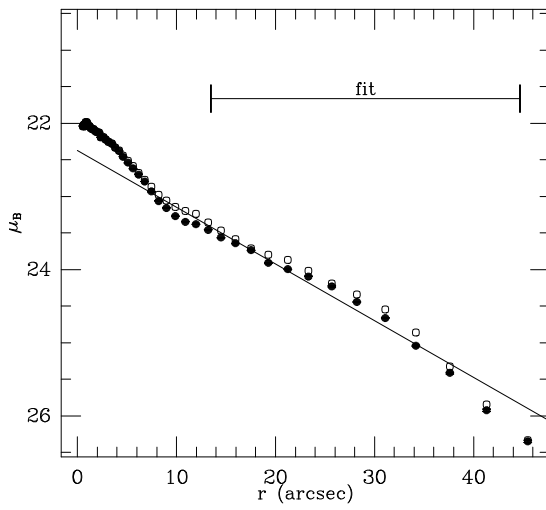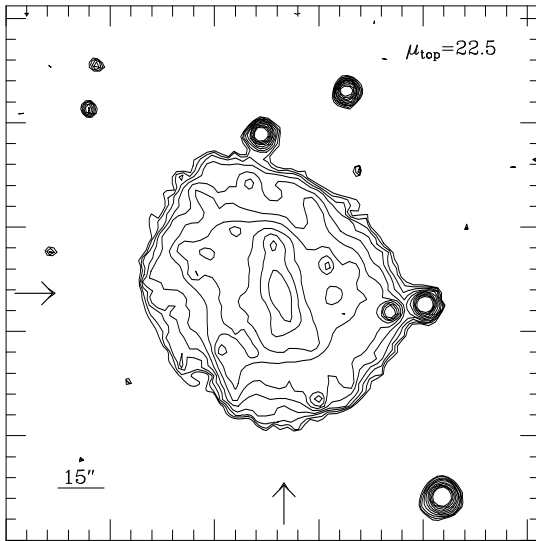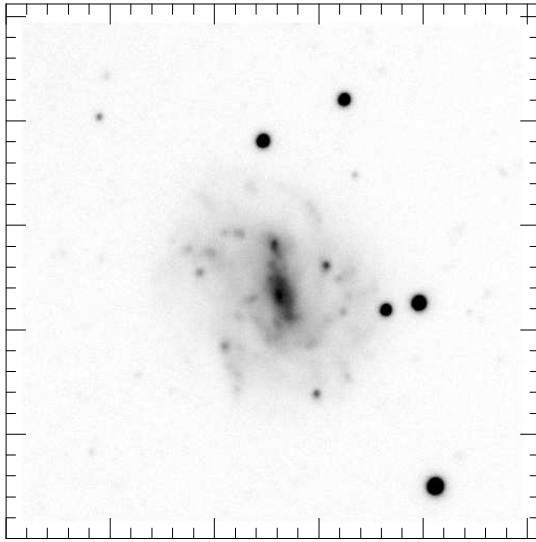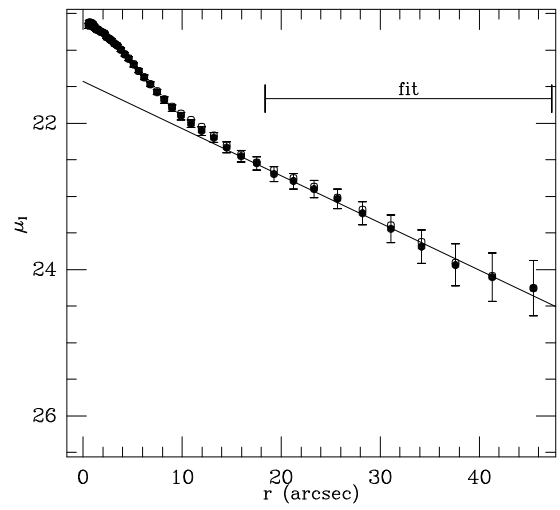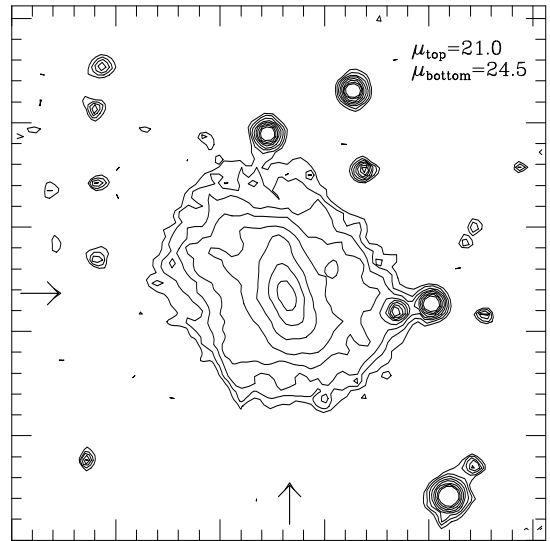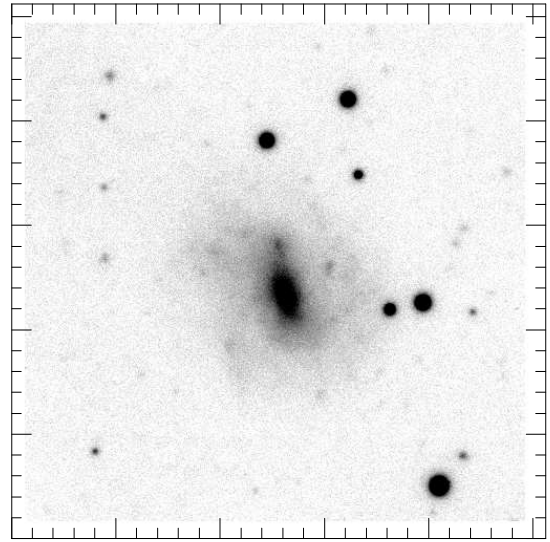
Figure 48: UGC 09391
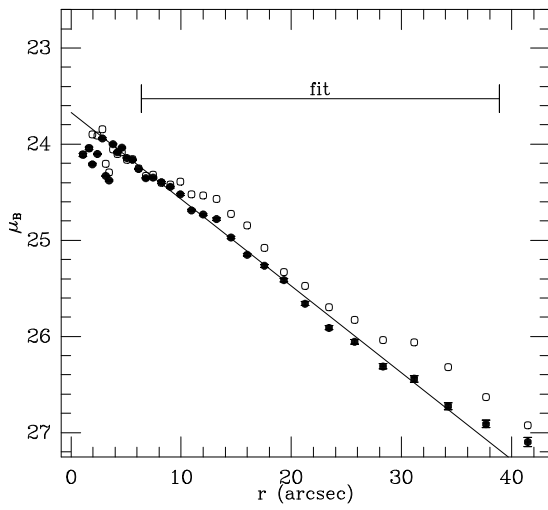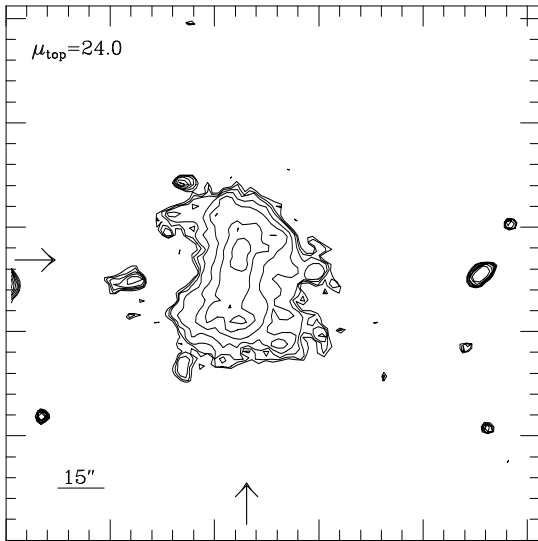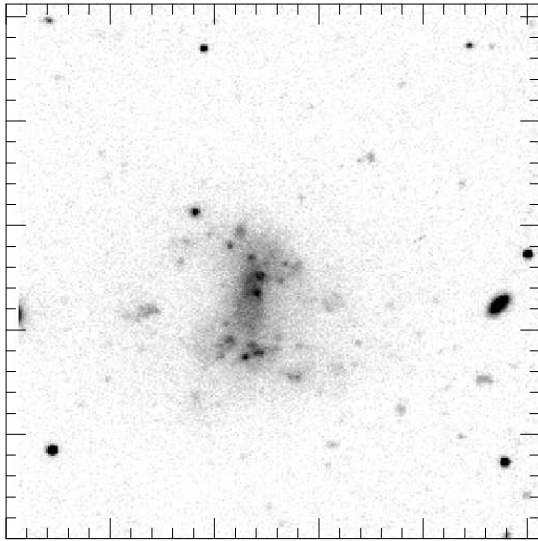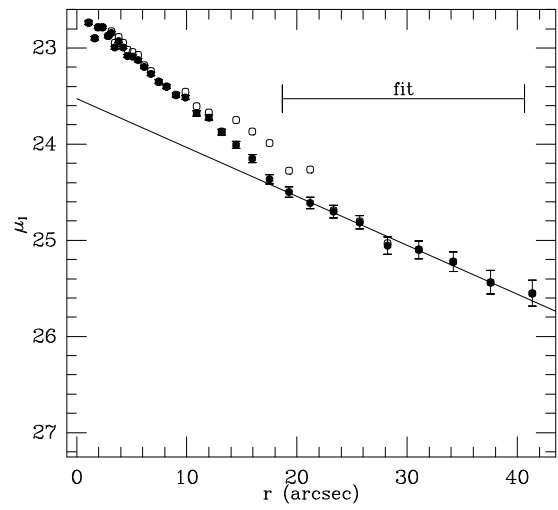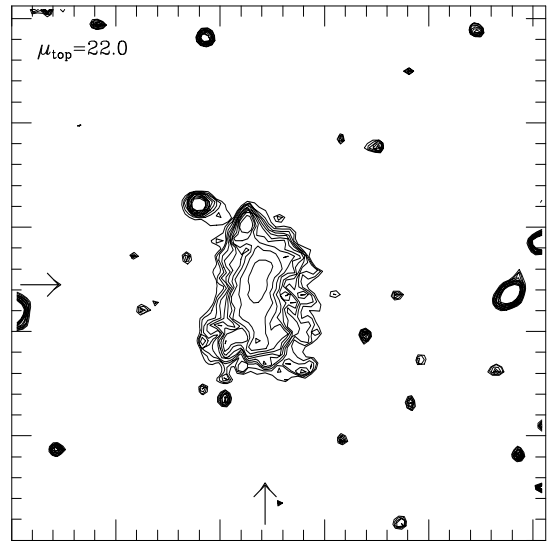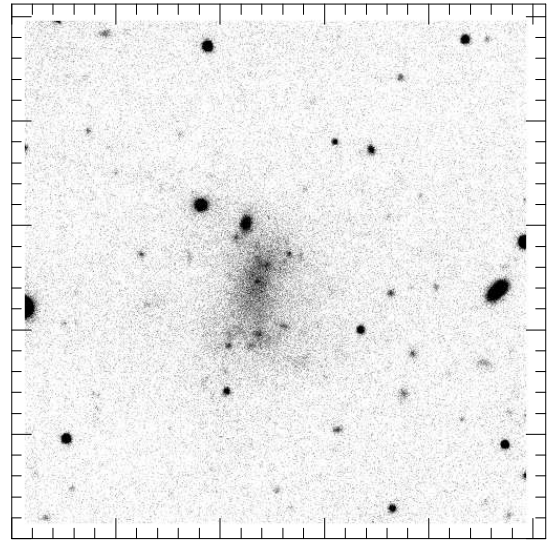
Figure 49: UGC 10031 (**B–May85**)

$\mu_{top}=23.5$

$\mu_{top}=22.0$

$15''$

fit

fit

μ_B

μ_I

r (arcsec)

r (arcsec)
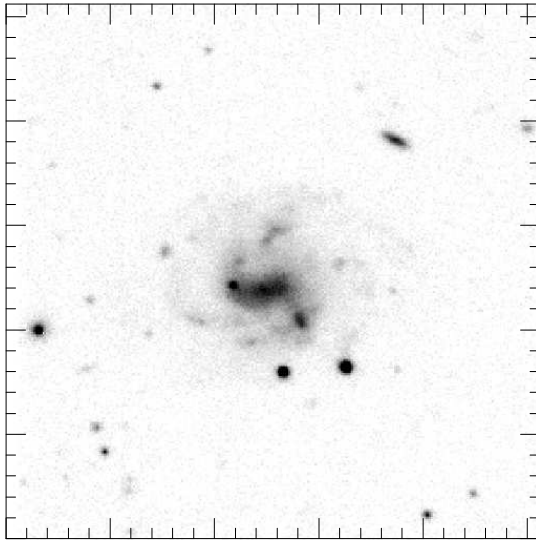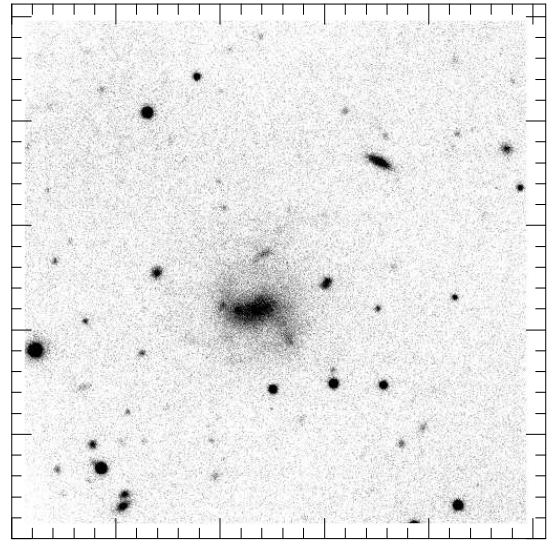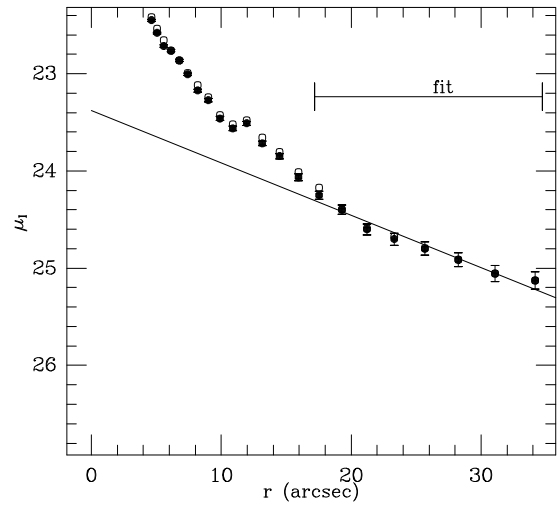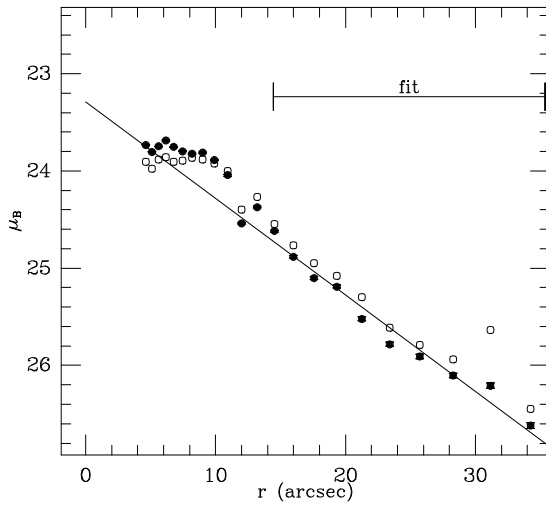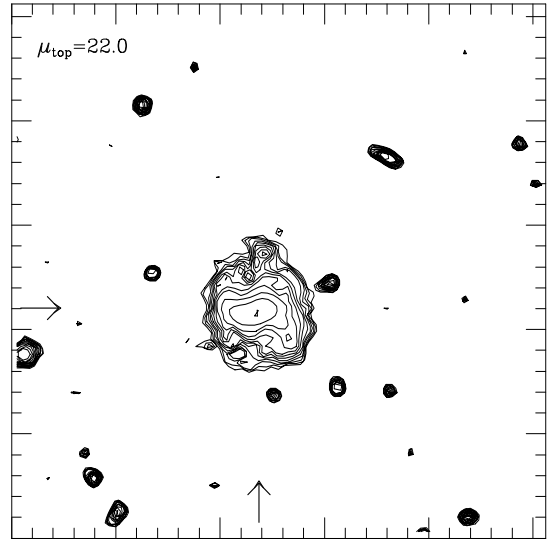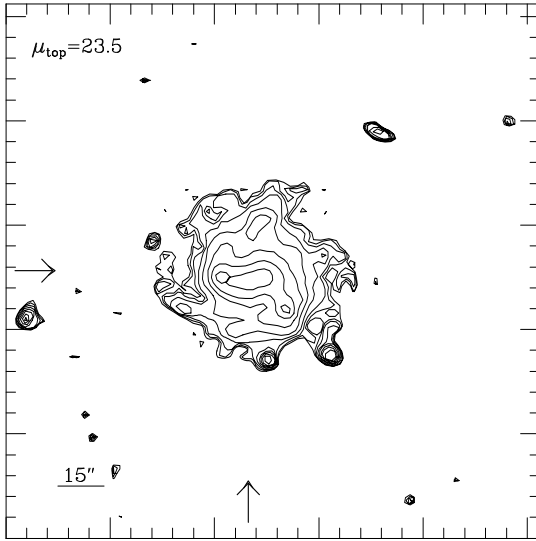
Figure 50: UGC 10058 (**B−May85**)
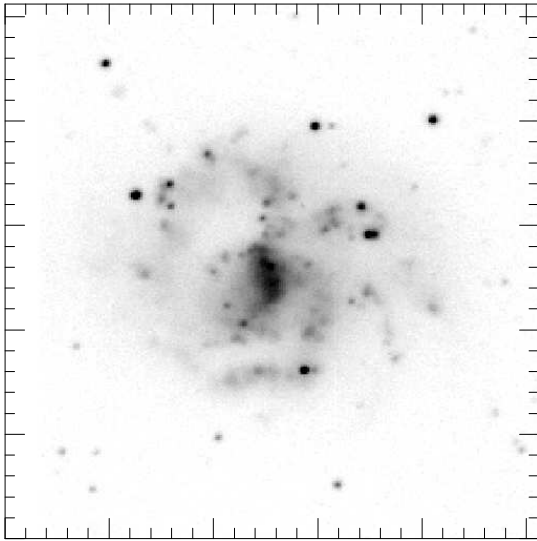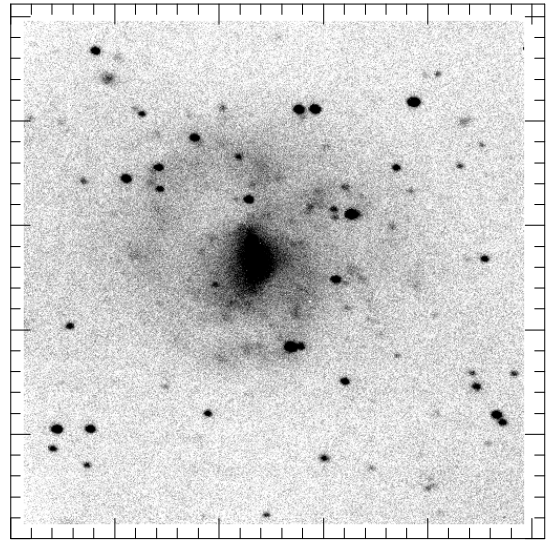
$\mu_{top}=23.0$

$\mu_{top}=21.5$
$\mu_{bottom}=24.0$

15"

fit

fit
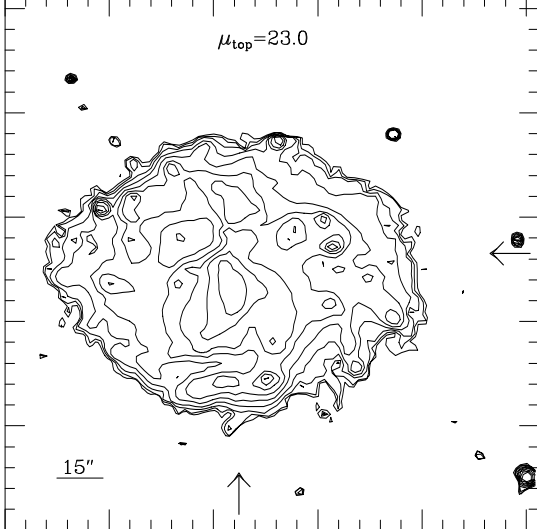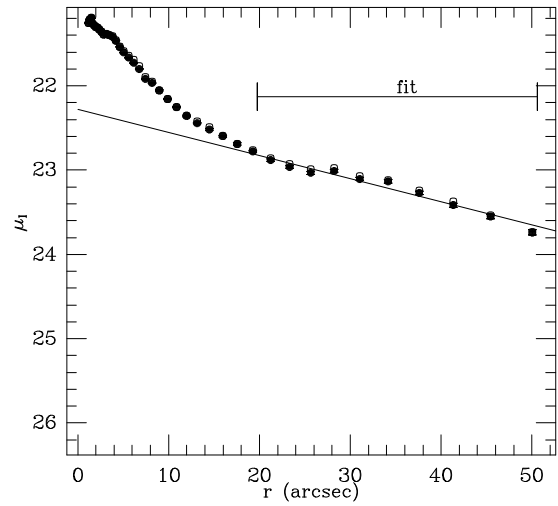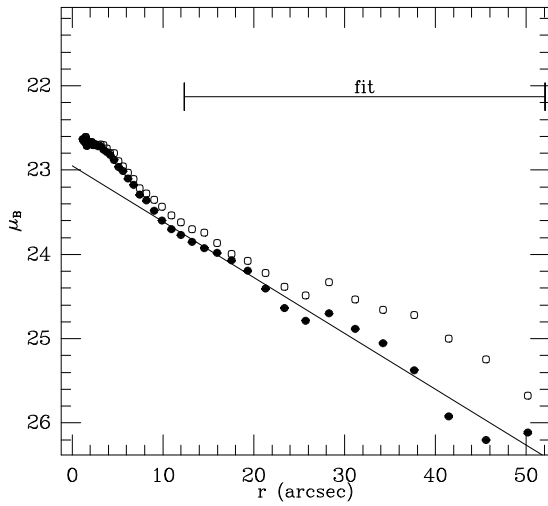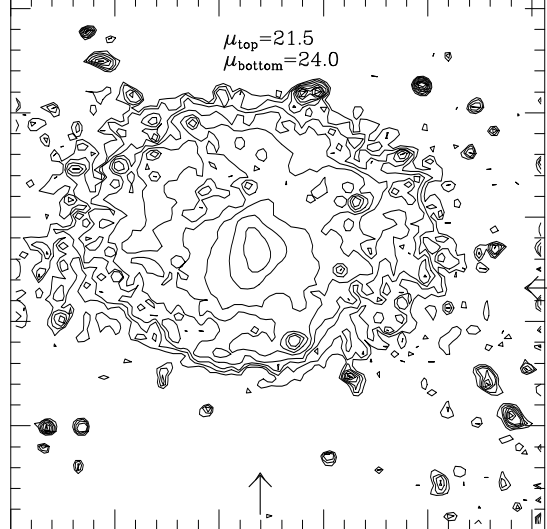
Figure 51: UGC 10290 (**B–May85**)
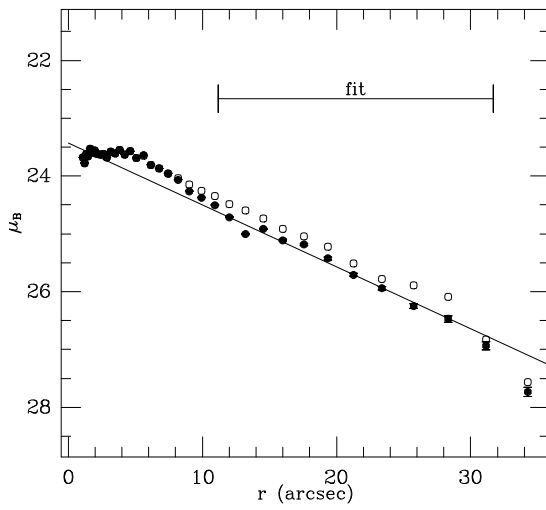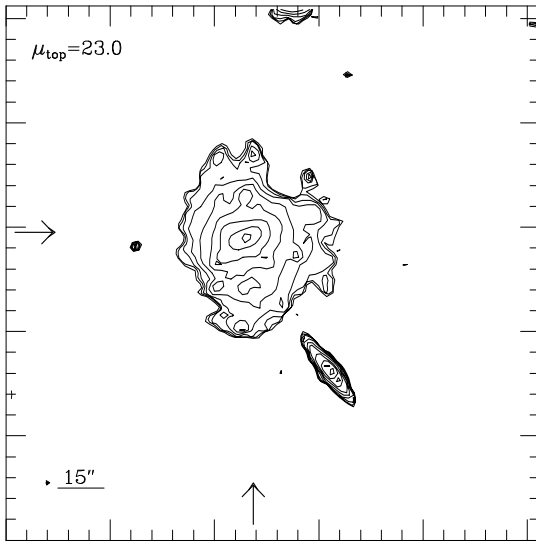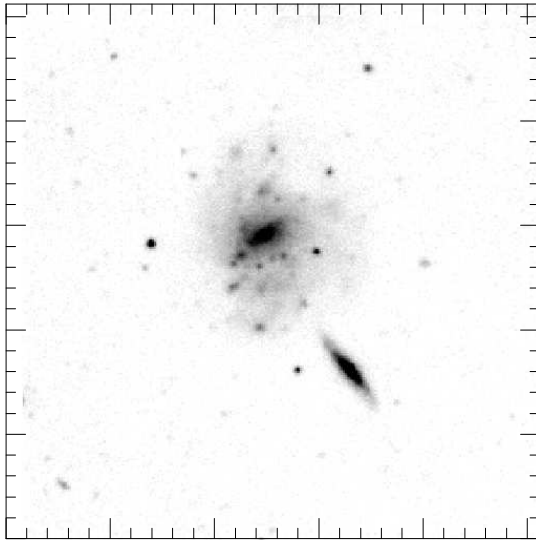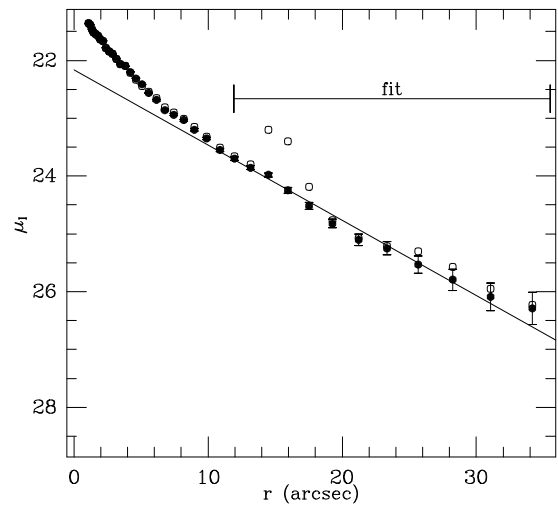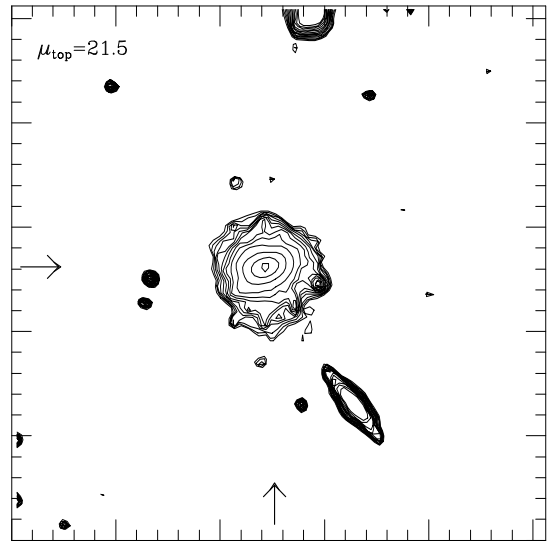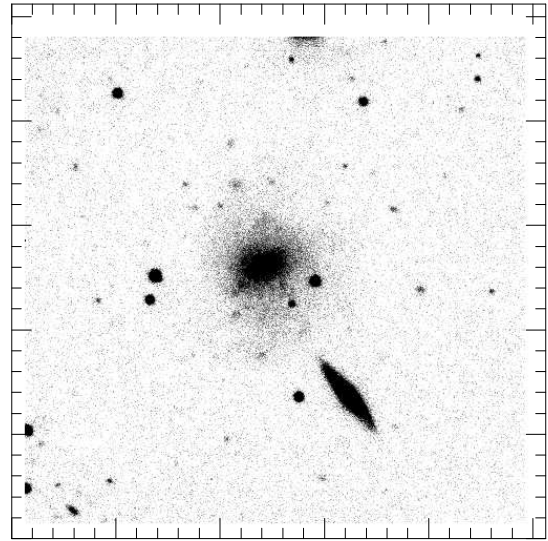
Figure 52: UGC 10376 (**B–May85**)

$\mu_{top}=24.5$

$\mu_{top}=23.0$

15″
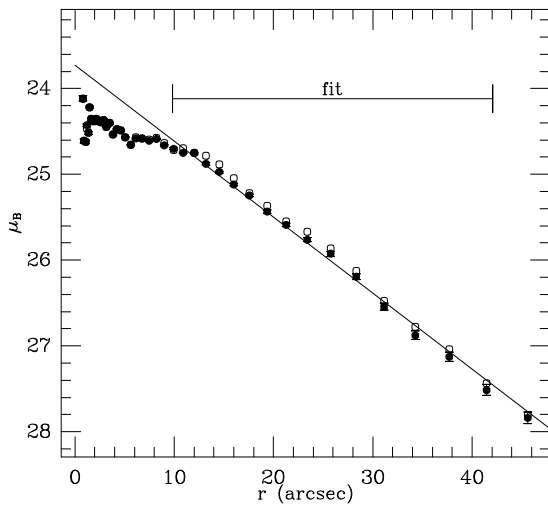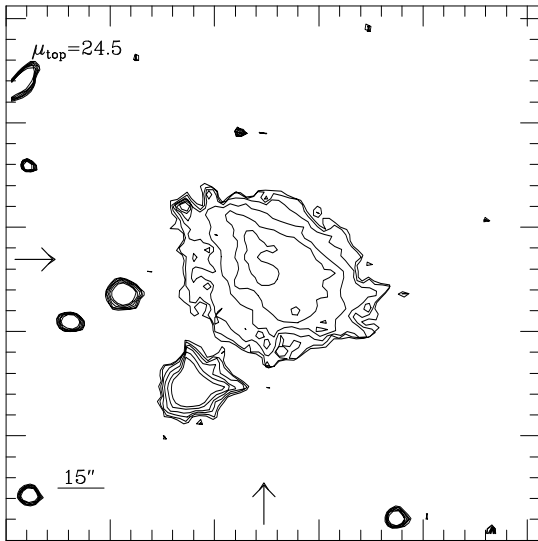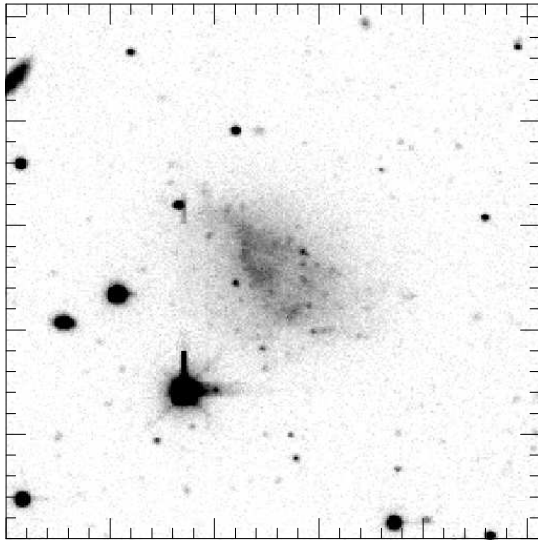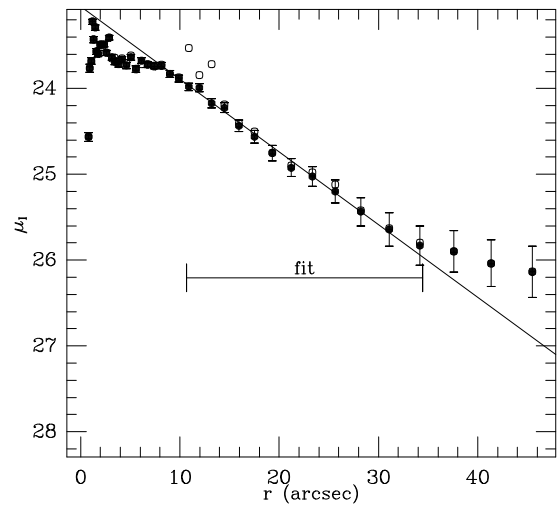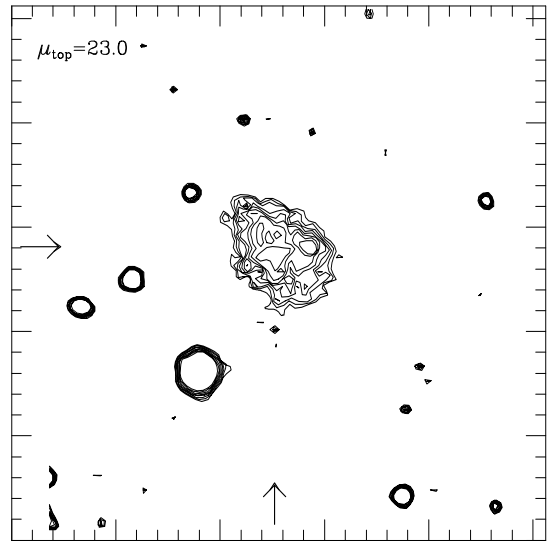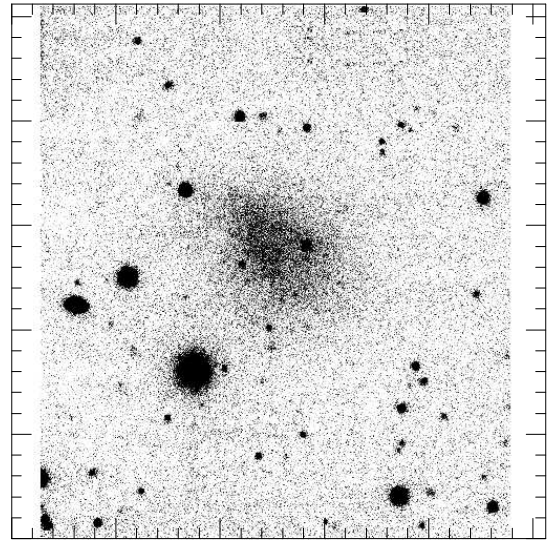
Figure 53: UGC 10669 (**B–May85**)

μ_{top}=23.0

μ_{top}=21.5

15″

fit

fit

μ_B

μ_I

r (arcsec)

r (arcsec)
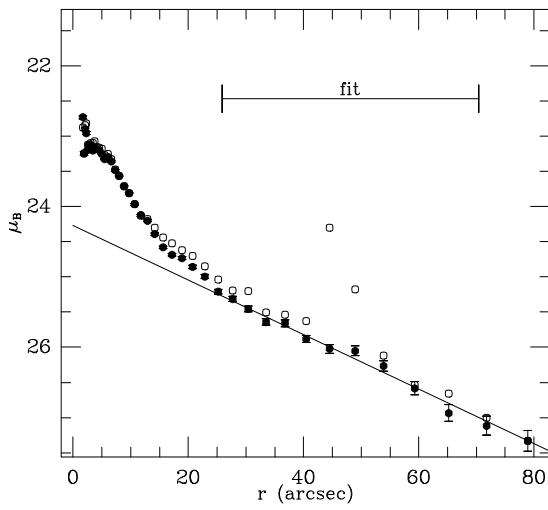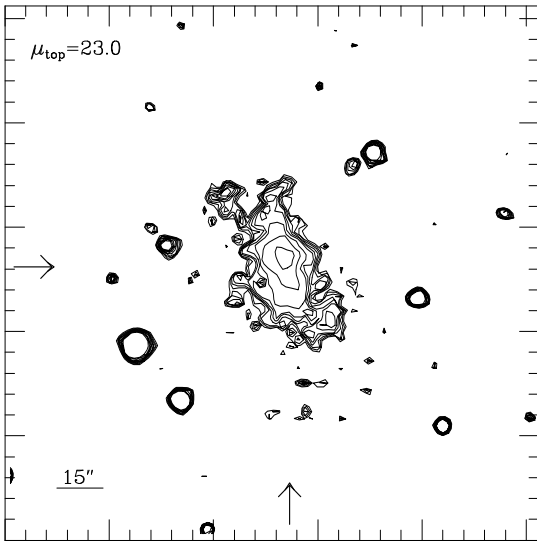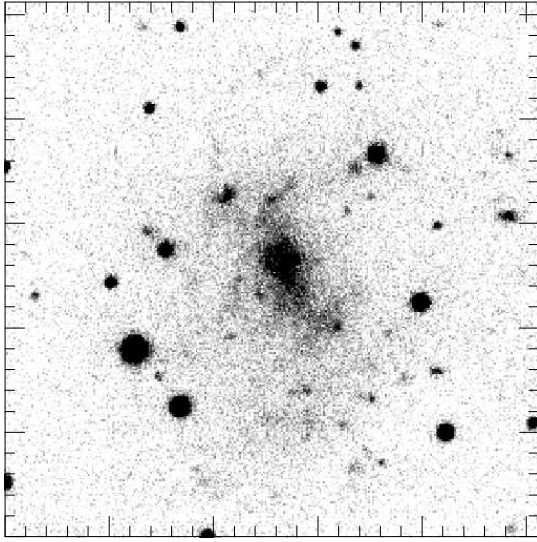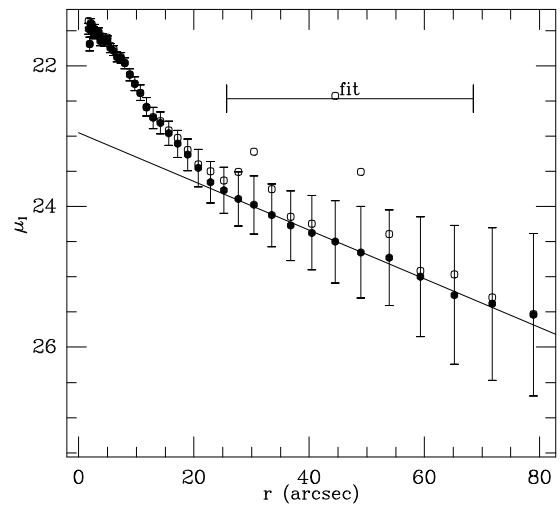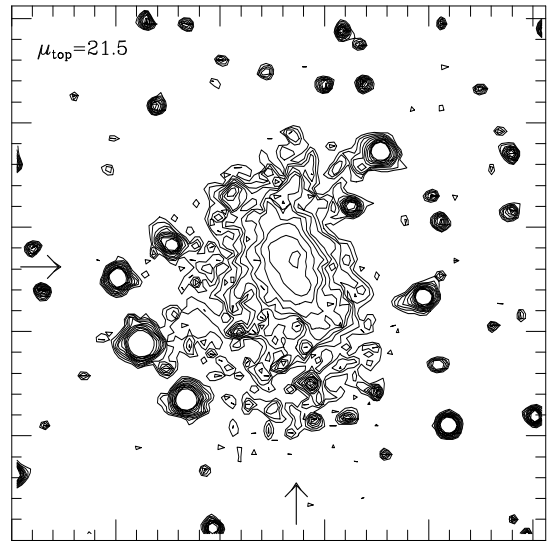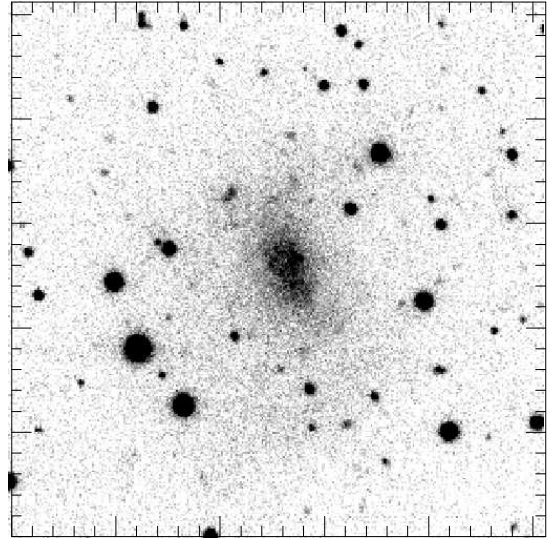
Figure 54: UGC 12082 (Sep91)
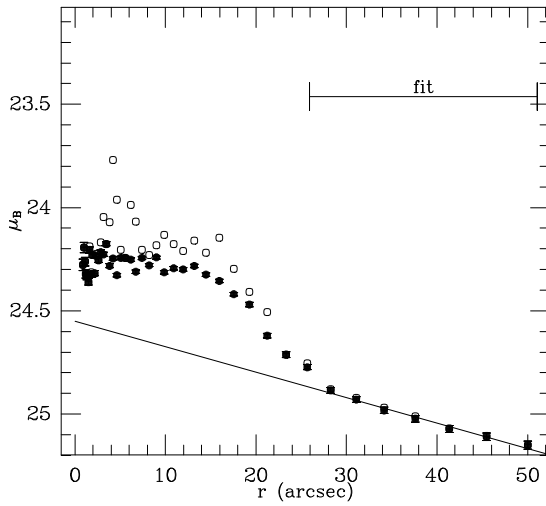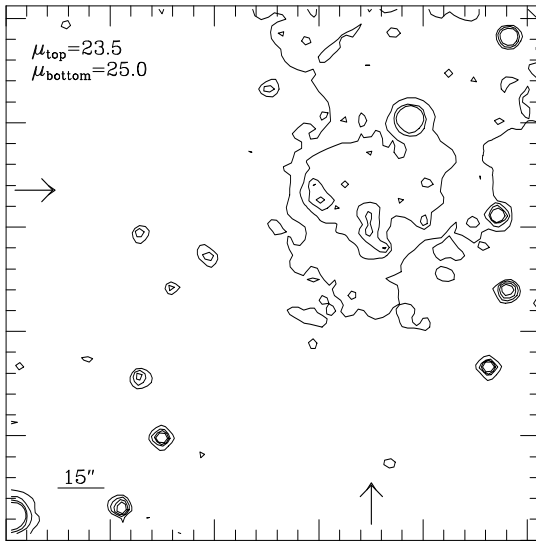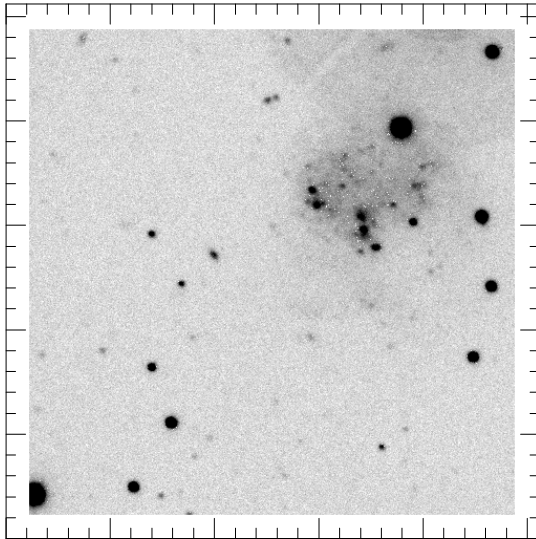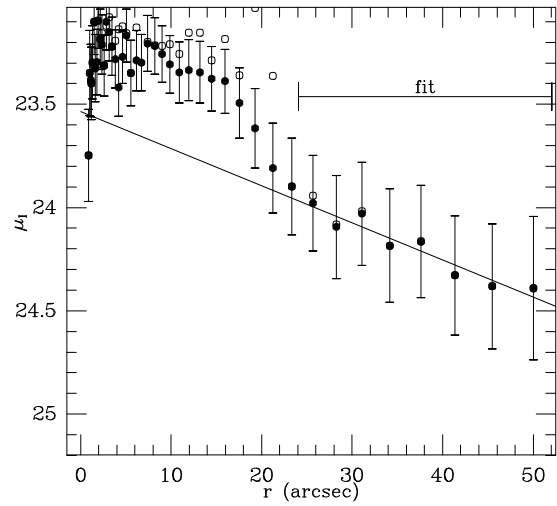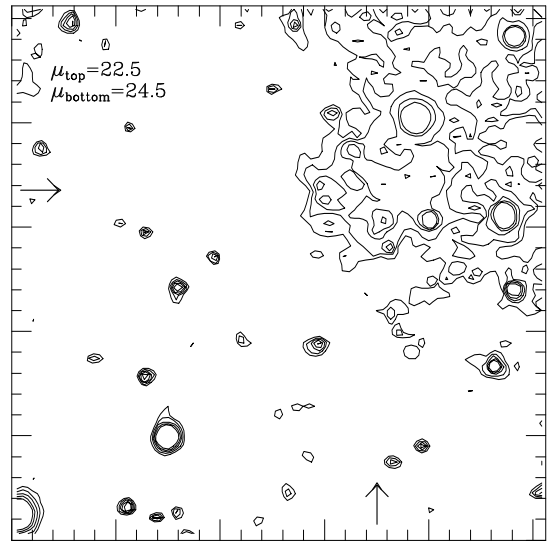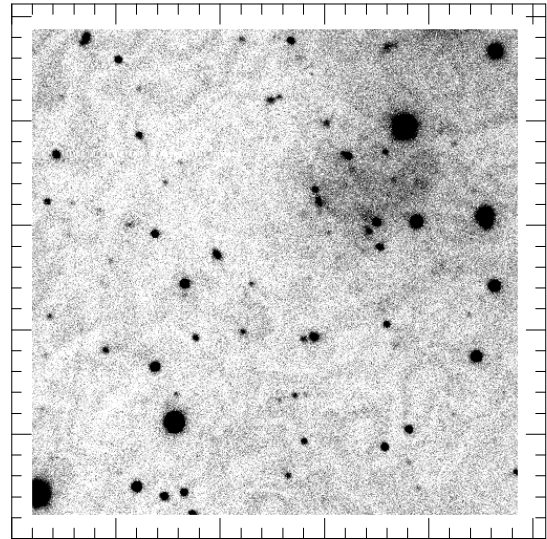
Figure 55: UGC 12894
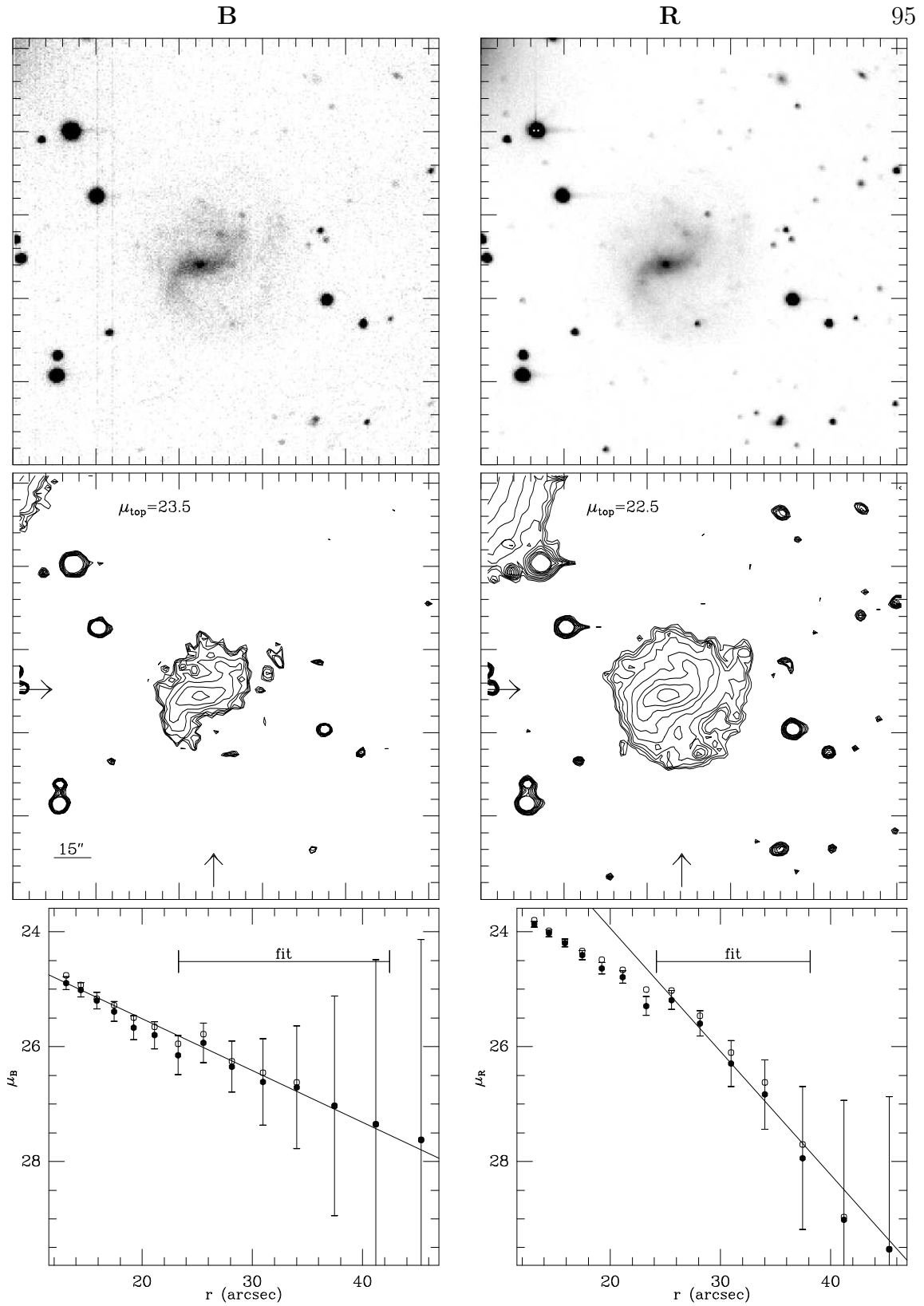
Figure 56: UGC 11764 (May85)

$\mu_{top}=22.5$

15″

$\mu_{top}=21.5$
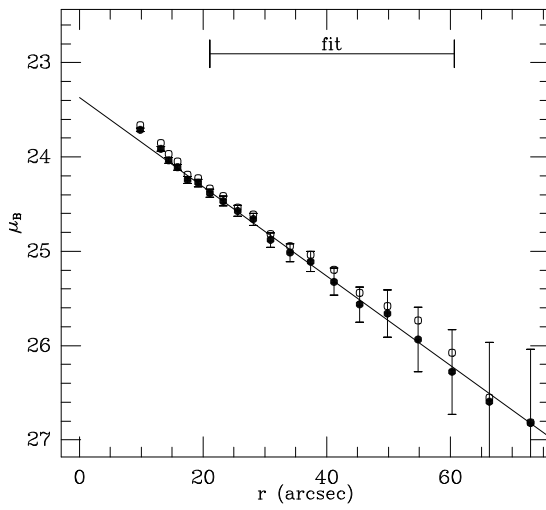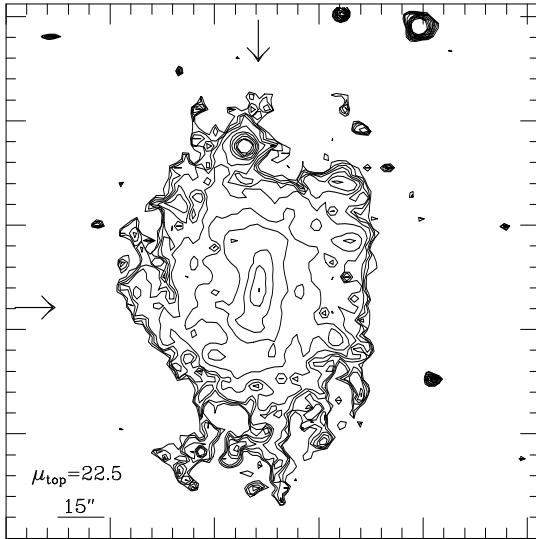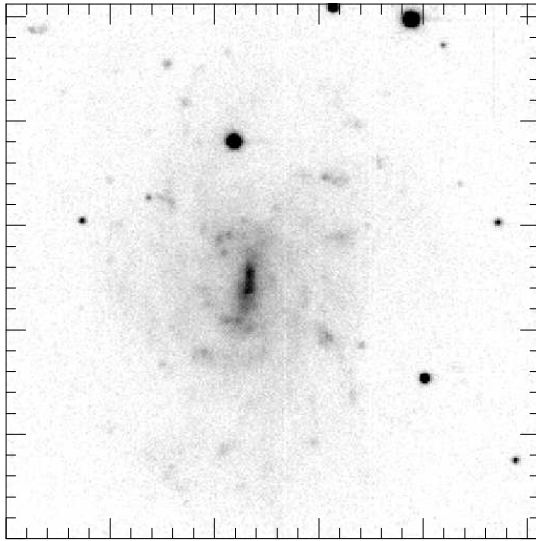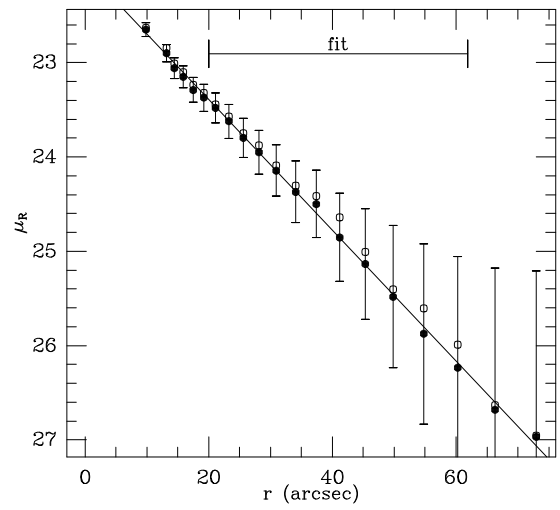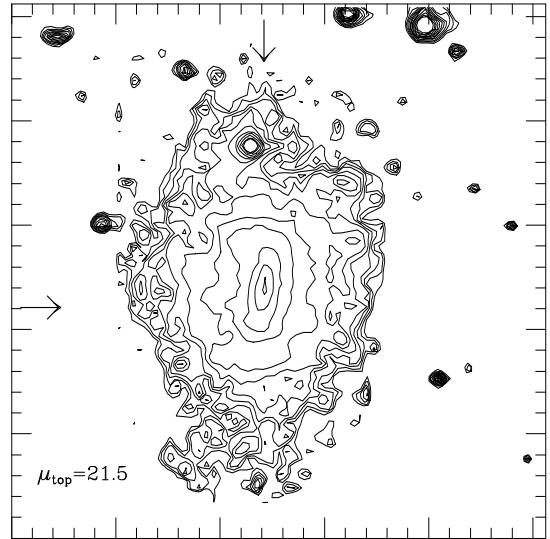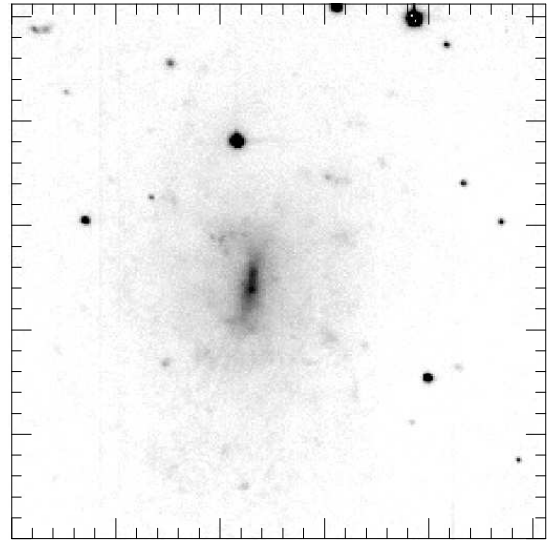
Figure 57: UGC 12151 (May85)

$\mu_{top}=21.0$

$\mu_{top}=21.0$

40″

fit

fit

μ_B

μ_B

r (arcsec)

r (arcsec)
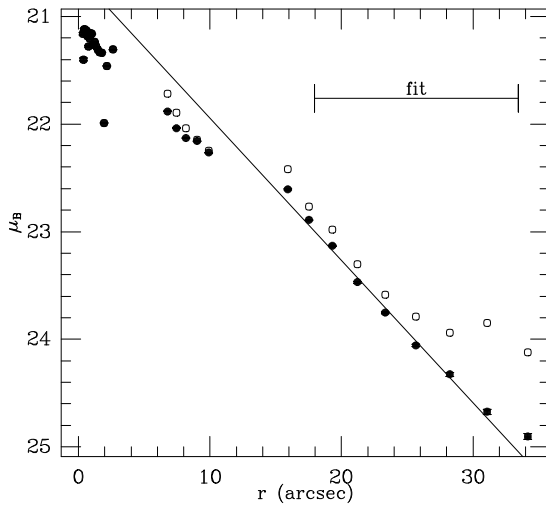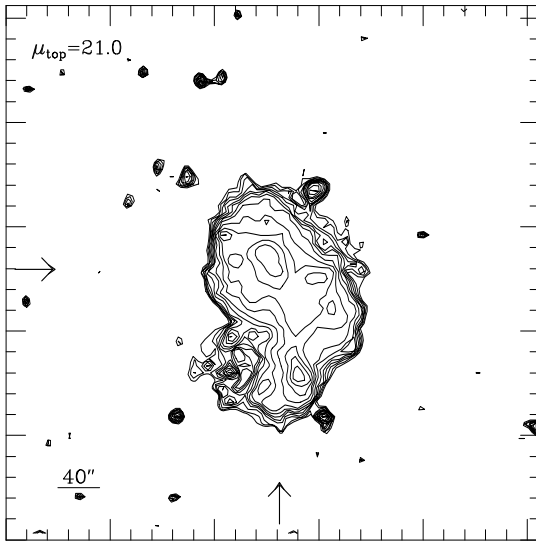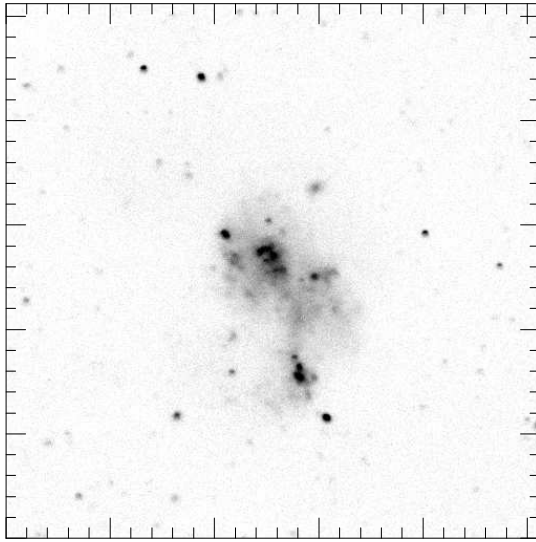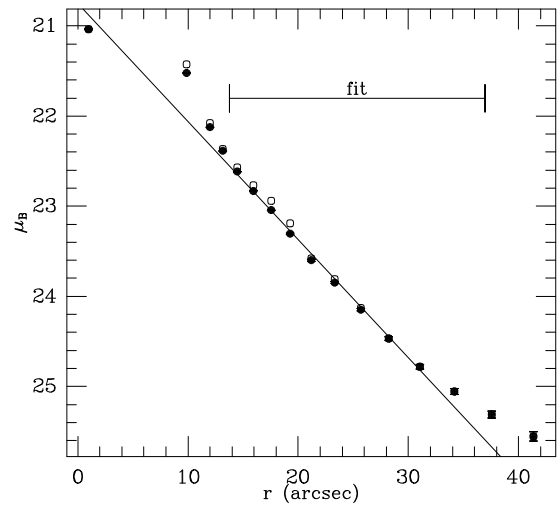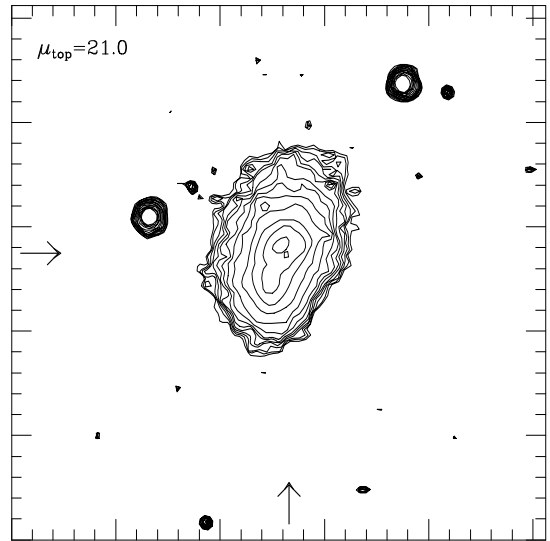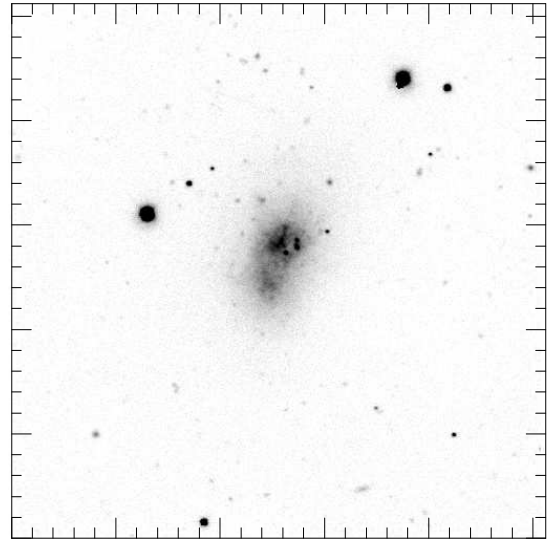
Figure 58: UGC 00772 and UGC 01171
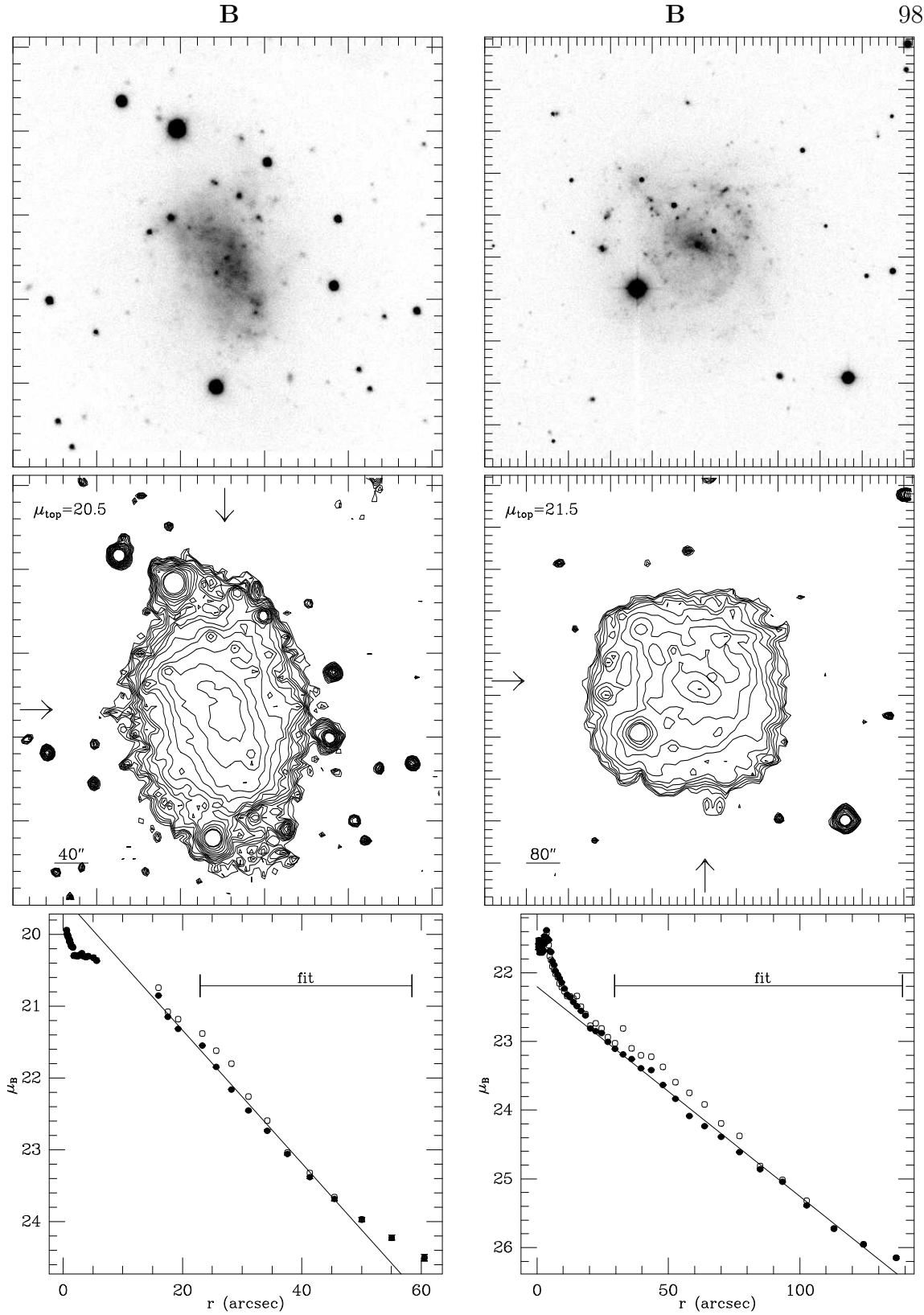
Figure 59: UGC 03860 (Oct90) and UGC 06628 (Apr93)

$\mu_{top}=22.5$

80″

$\mu_{top}=22.0$

μ_B

fit

μ_B

fit

r (arcsec)

r (arcsec)
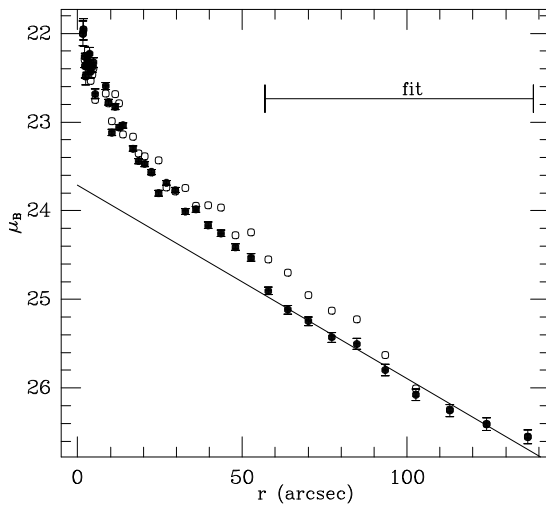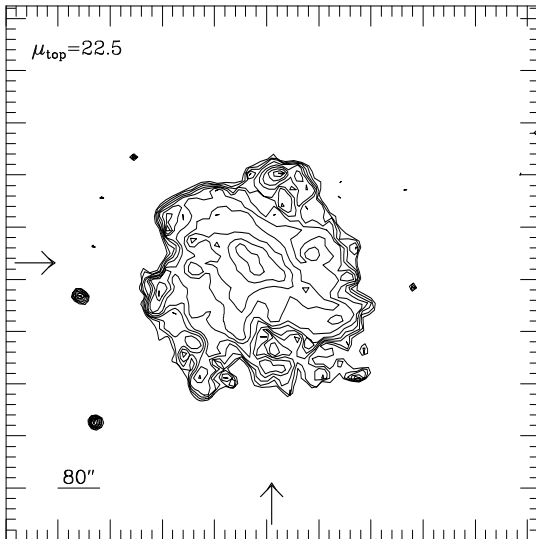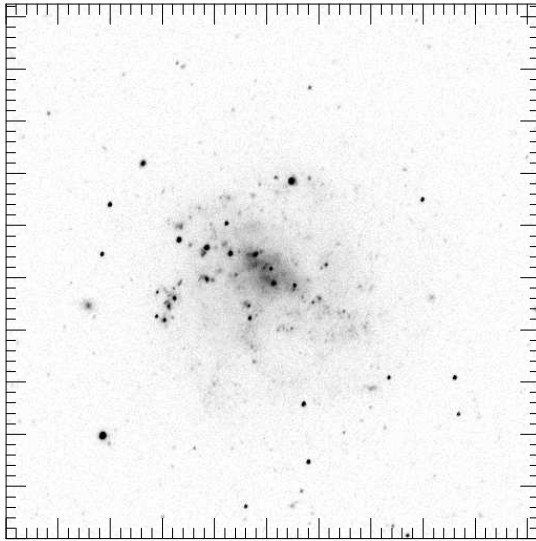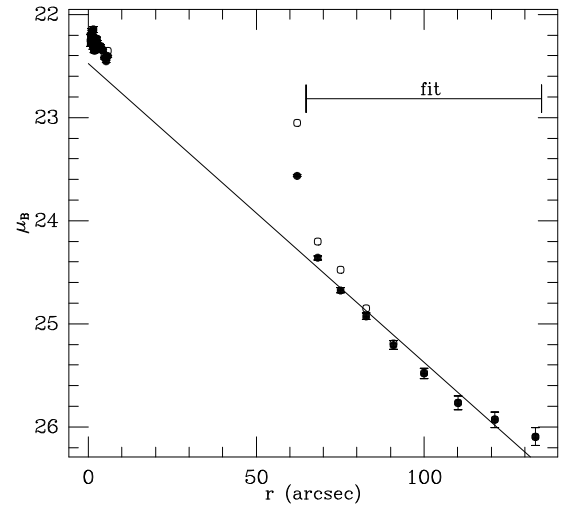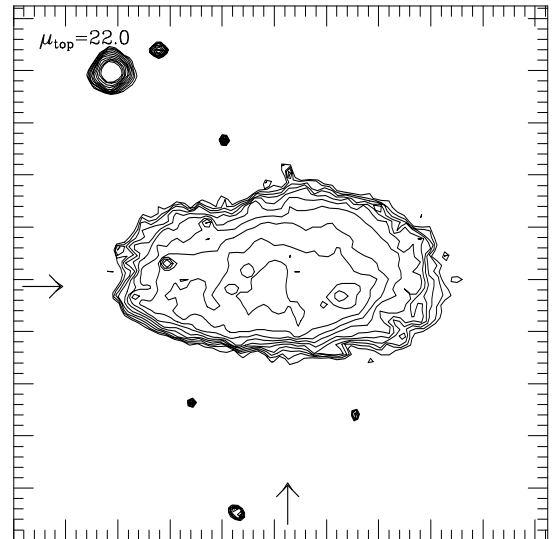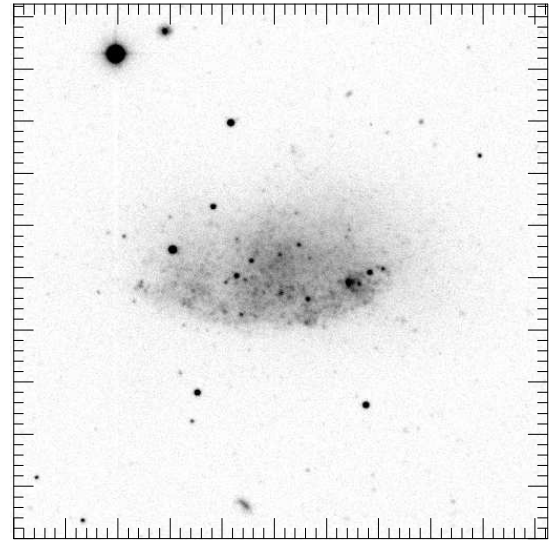
Figure 60: UGC 07608 and UGC 08201 (both Apr93)

$\mu_{top}=23.0$

$\mu_{top}=22.5$

15''

fit

fit

μ_R

μ_R

r (arcsec)

r (arcsec)
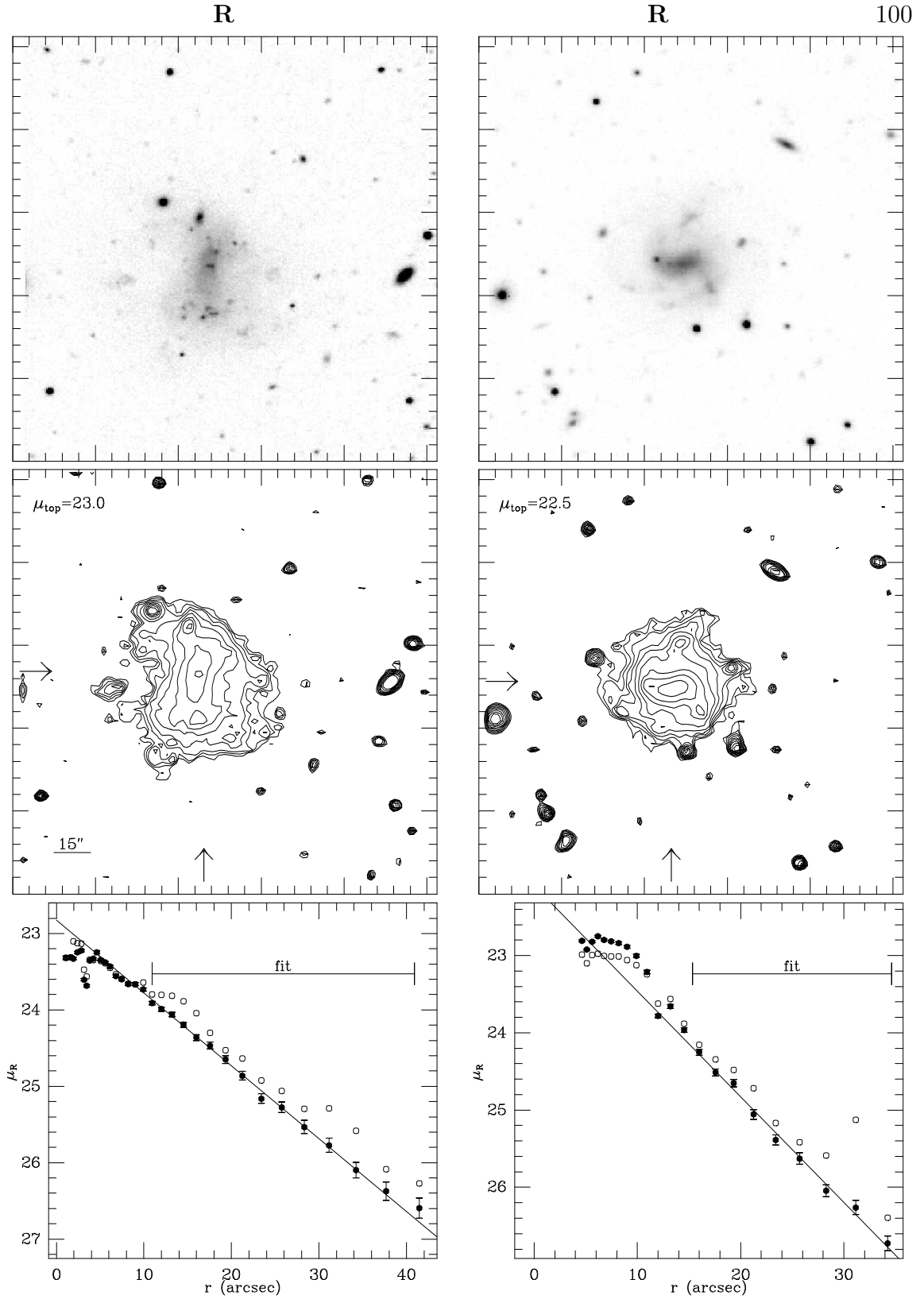
Figure 61: UGC 10031 and UGC 10058 (both May85)
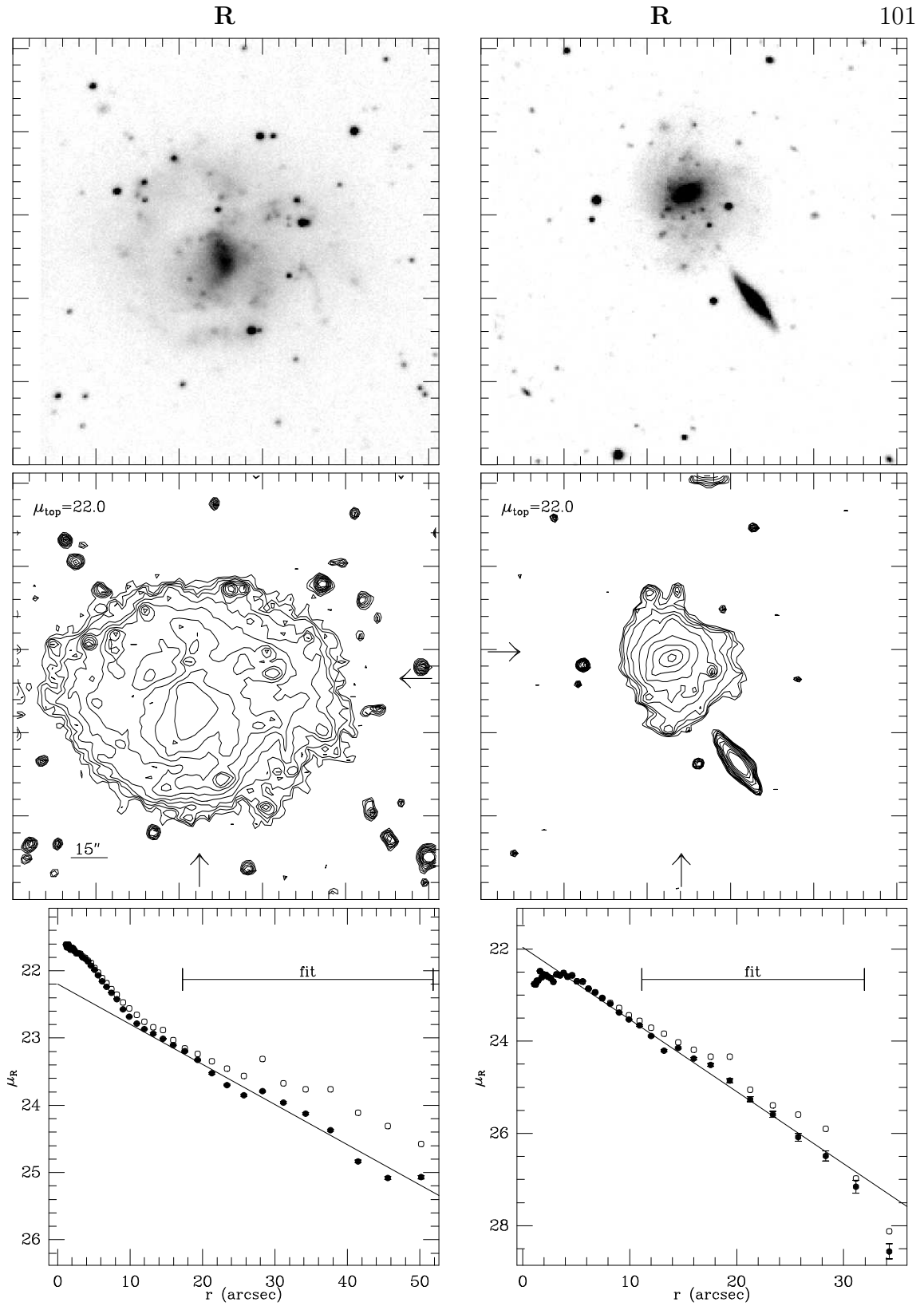
Figure 62: UGC 10290 and UGC 10376 (both May85)

$\mu_{top}=24.0$

15″

fit

μ_R

r (arcsec)
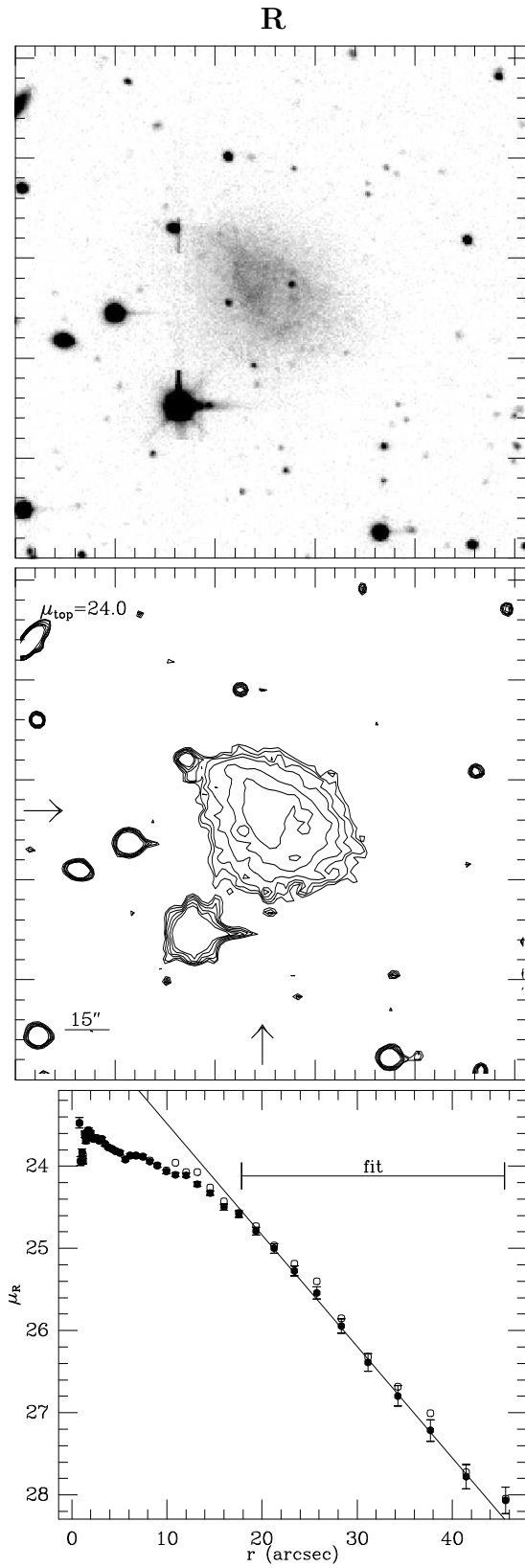
Figure 63: UGC 10669 (May85)

Figures 64–71:   Ellipticity, Cos(4θ) coefficient, and Color Profiles of all Galaxies in the Sample.

In the upper panel, the ellipticity, ϵ is plotted as a function of effective radius for each galaxy. Here $\epsilon = 1 - (b/a)$, where b/a is the ratio of the semi–minor to semi major axis found from the I–band image (except when not available) using the GALPHOT routines. The ellipticity tends to converge to a stable value as r increases. This is the value that was adopted in order to obtain the inclination, as described in Chapter 3.

The middle panel contains plots of the cos(4θ) term (or A_4 parameter) as a function of effective radius. This parameter is commonly used in studies of elliptical galaxies to measure the deviation from ellipticity of the isophotes. In this case, we use the parameter to obtain a measure of the applicability of elliptical fitting. Large deviations from 0 of the A_4 parameter indicate that the isophotes were poorly fit by ellipses.

The $B - I$ color profiles are plotted as a function of effective radius in the lower panel. The color profiles were obtained from the difference of the surface brightness measured within each elliptical annulus (again, with the ellipses determined from the I–band image). The surface brightness used here is the surface brightness *excluding* the HII regions and any stars present. For the seven galaxies for which R–band data also exist, the $B - R$ profiles are plotted with open circles. In the case of the 5 galaxies for which subsequent I–band data was obtained, the $B - I$ color appears to be anomalously red. This was thought to be caused by poorly determined transformation coefficients for the May85 observing run.
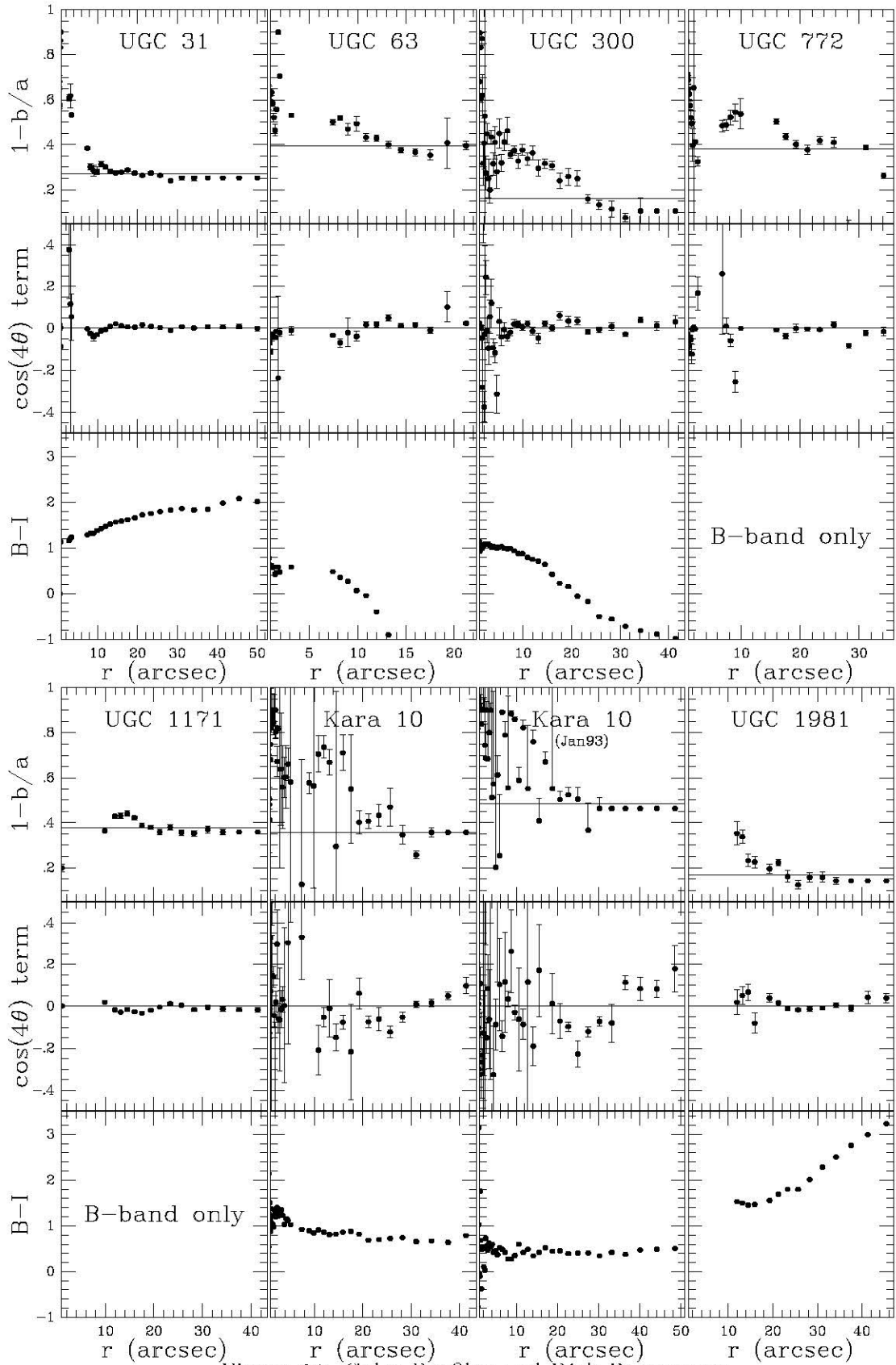
Figure 64: Color Profiles and Disk Parameters
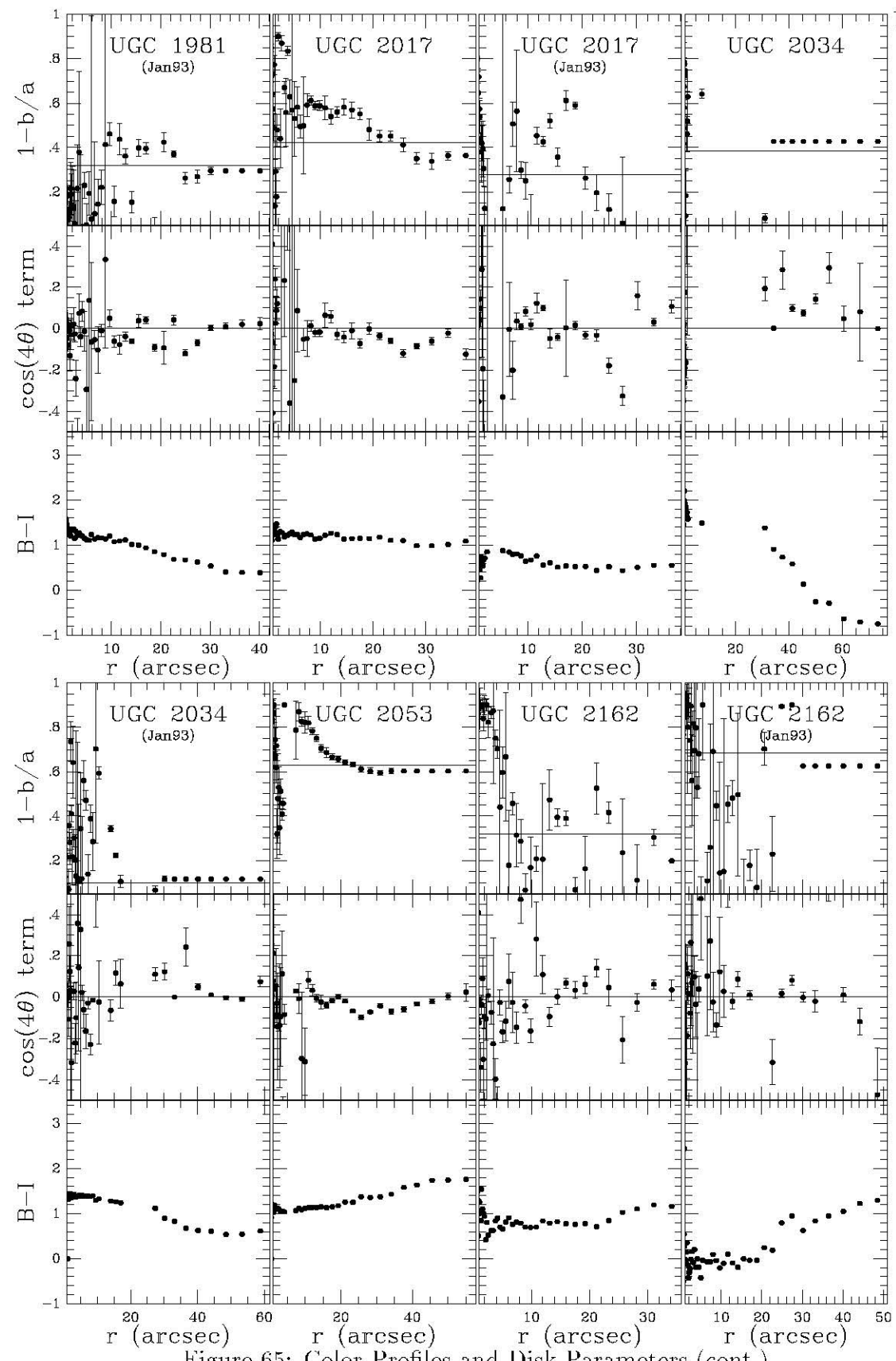
Figure 65: Color Profiles and Disk Parameters (cont.)
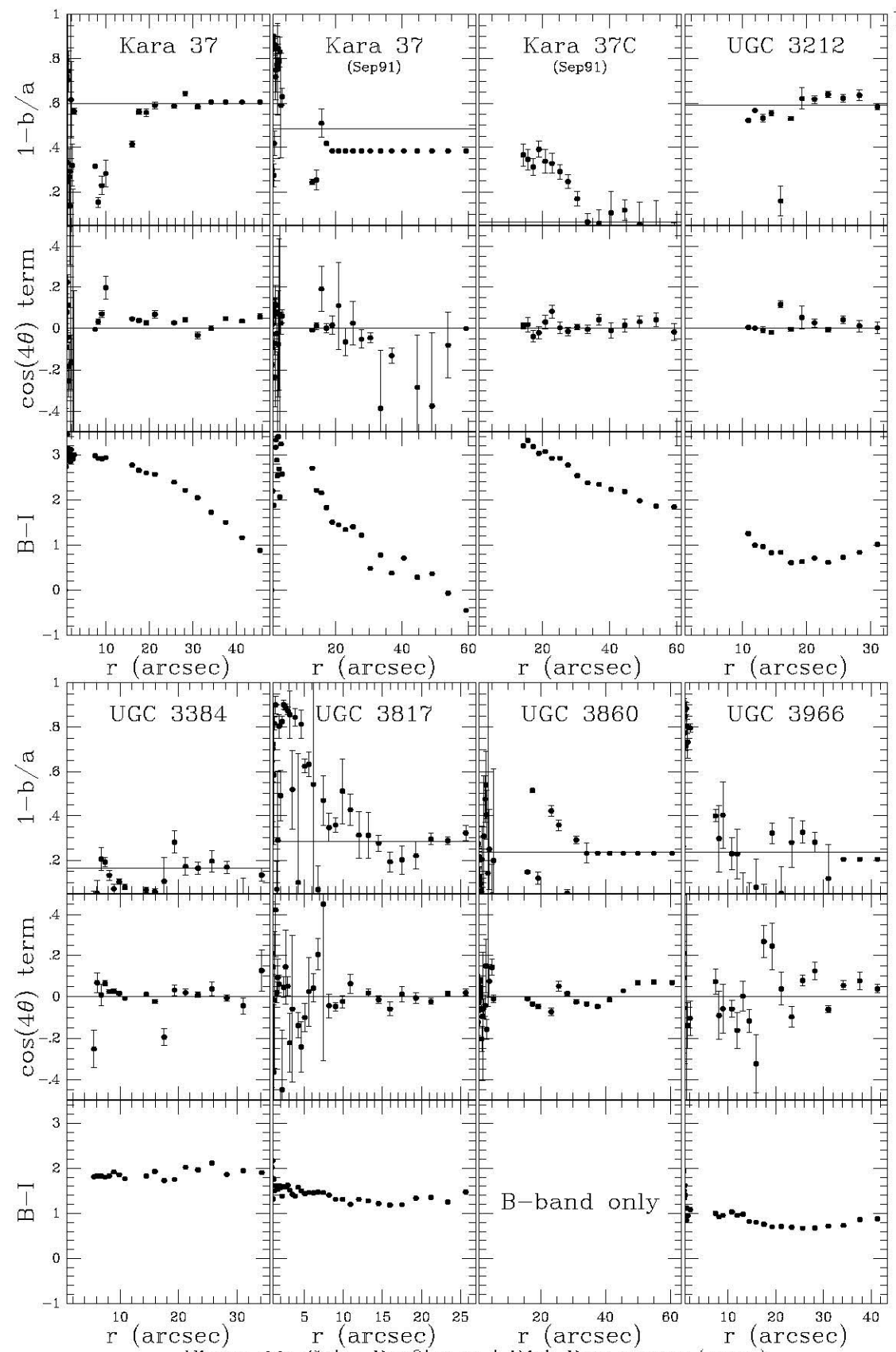
Figure 66: Color Profiles and Disk Parameters (cont.)
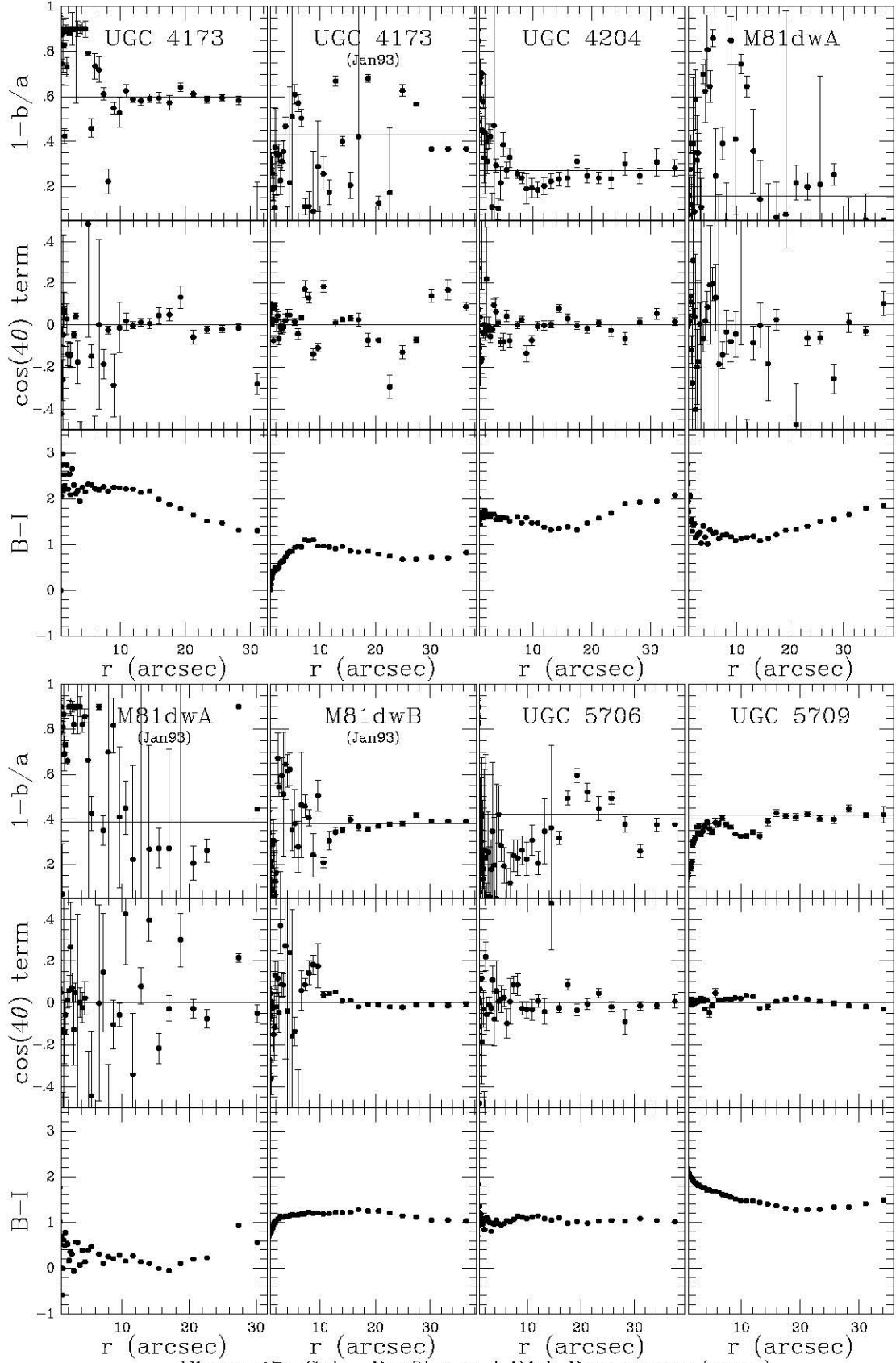
Figure 67: Color Profiles and Disk Parameters (cont.)
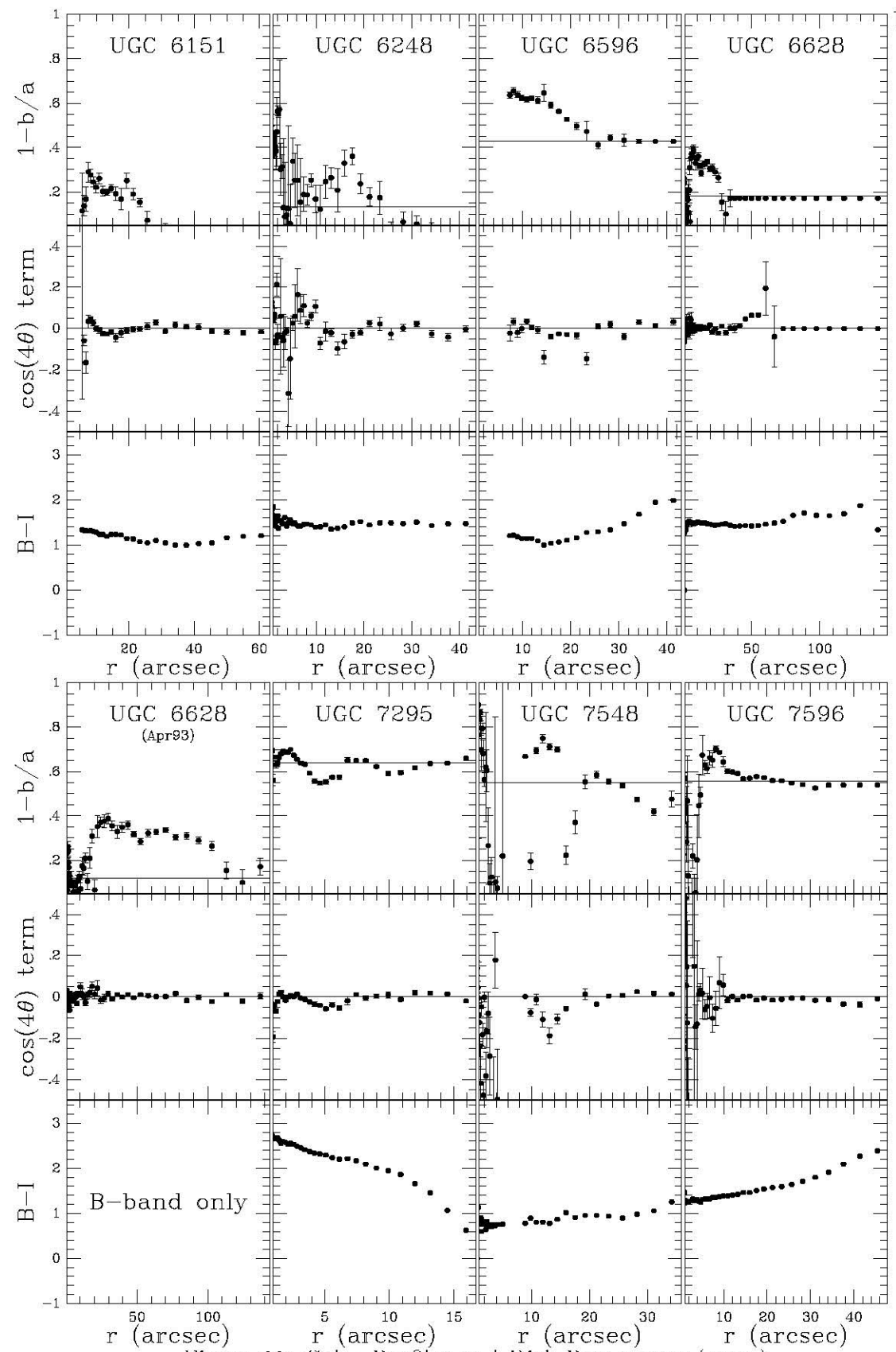
Figure 68: Color Profiles and Disk Parameters (cont.)
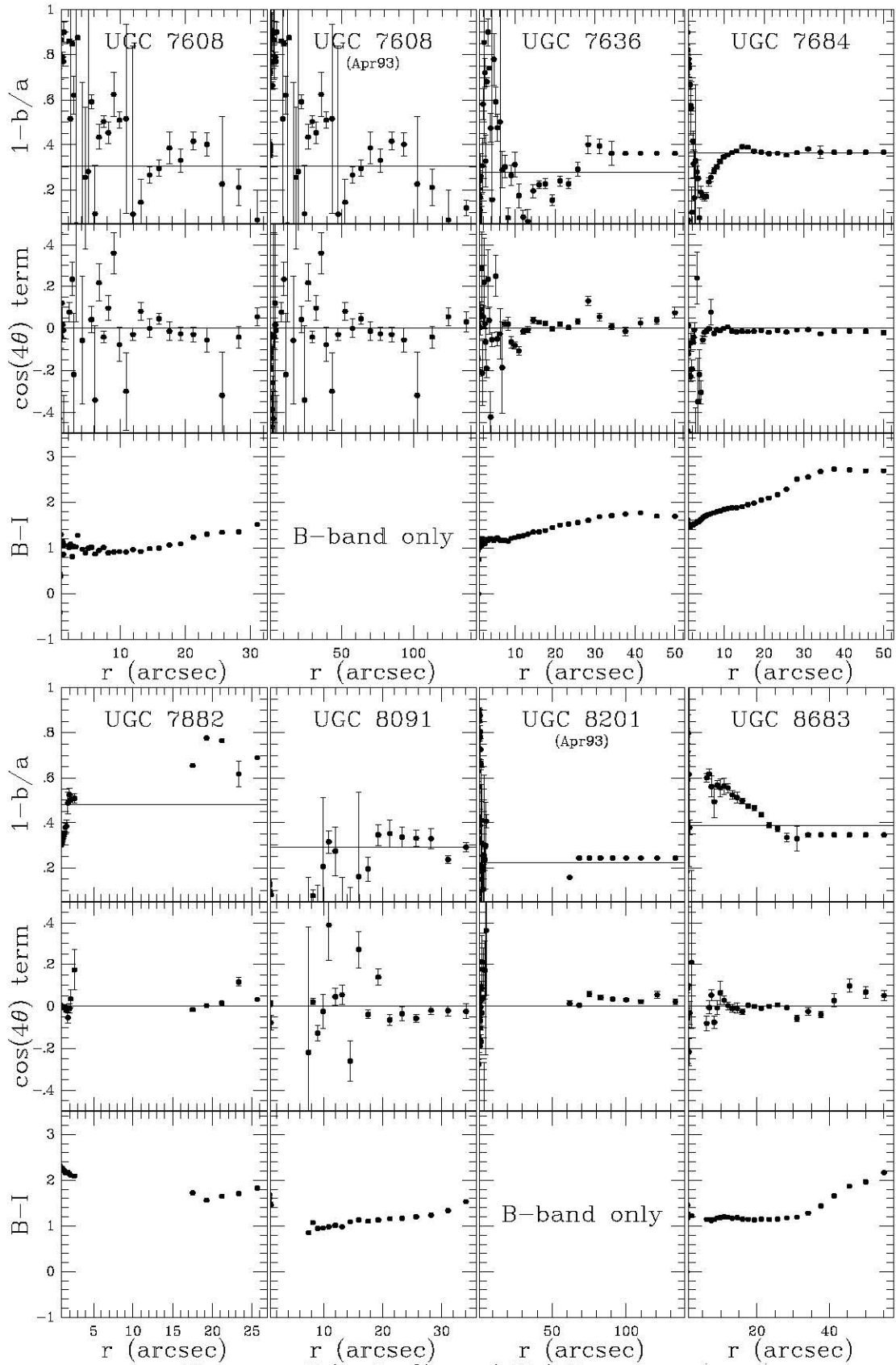
Figure 69: Color Profiles and Disk Parameters (cont.)
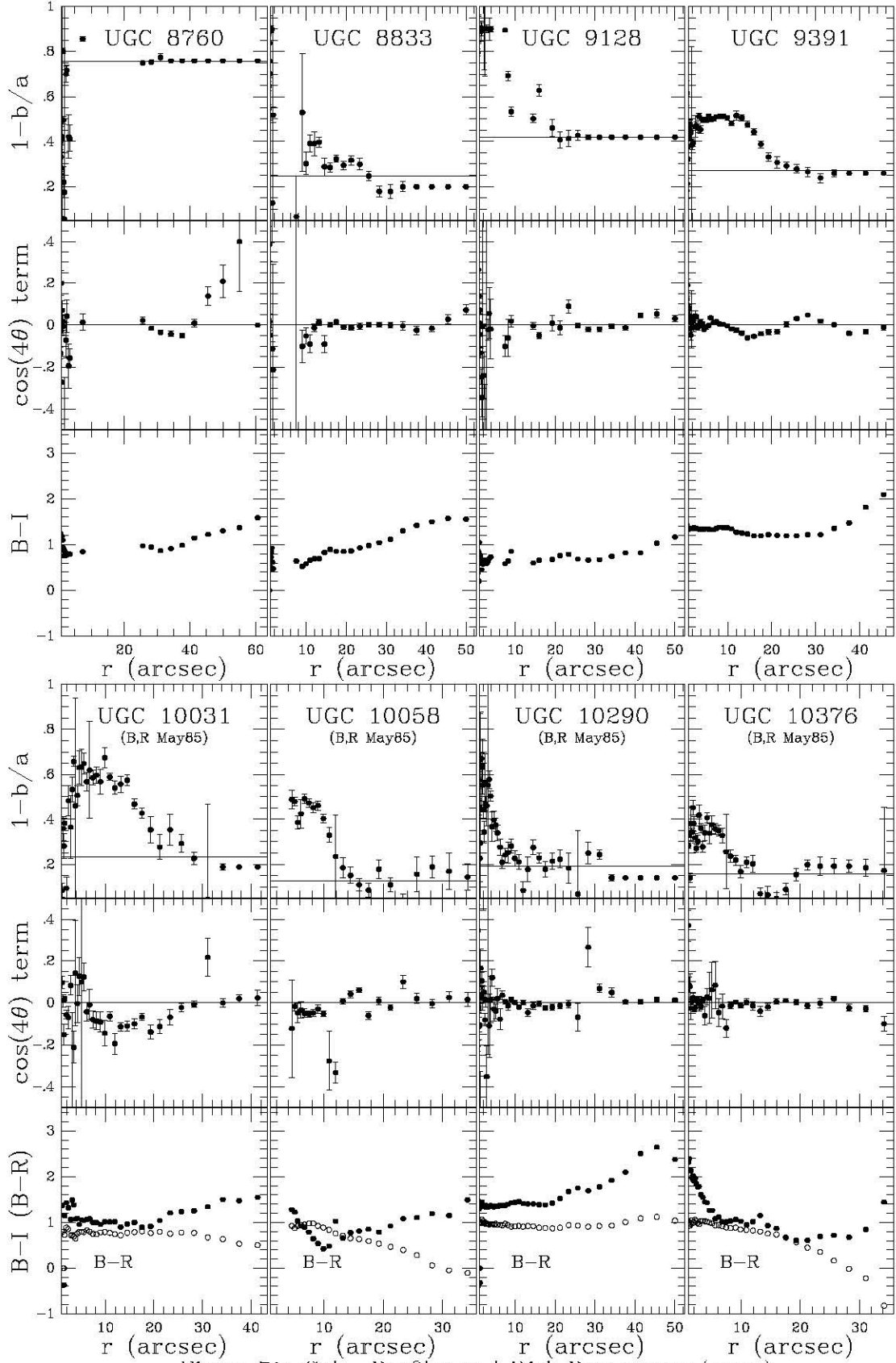
Figure 70: Color Profiles and Disk Parameters (cont.)
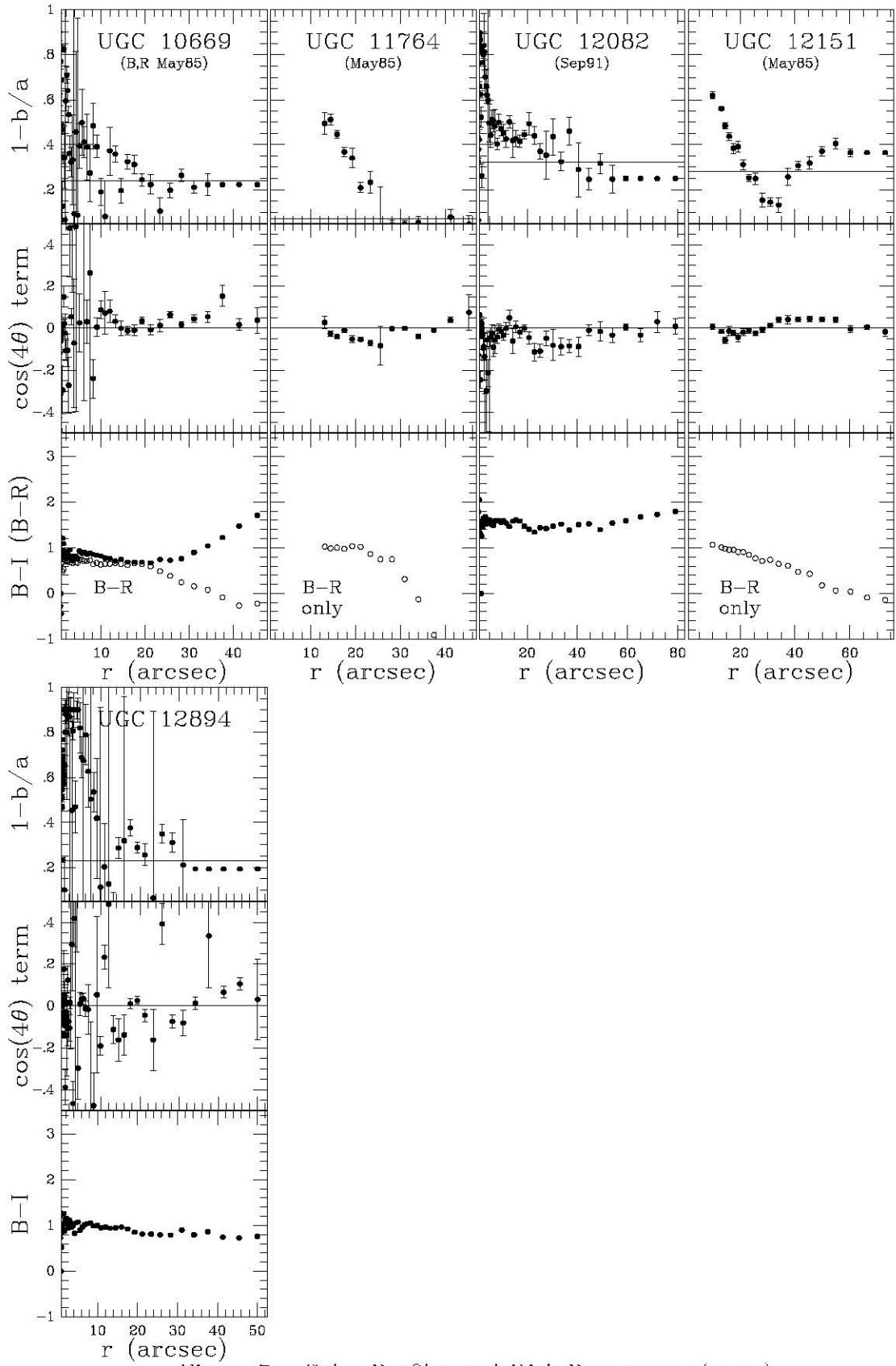
Figure 71: Color Profiles and Disk Parameters (cont.)

Figures 72–80:   Histograms of the Size, Radial, and Azimuthal Distribution of "HII Regions" and Stars for the Galaxies in the Sample.

Histograms showing the size of the regions excluded from the ellipse fitting (as either HII regions, or stars within the galaxy) are given in Figures 72–74 for each galaxy. The size is in parsecs, based on the distance for each galaxy listed in Table 7 (Chapter 3). For histograms which extend past the maximum shown in the figure, the actual number is given in parentheses next to the peak. The discrete, "spikey", nature of the distribution is due to the finite pixel size. The radius smallest, and often largest, peak usually translates to one pixel on the detector. A histogram showing the distribution for all the galaxies taken as a whole is shown in at the bottom of Figure 74.

Histograms showing the logarithmic radial distribution of regions from the center of the galaxy are shown in Figures 75–77. Similar histograms presenting the azimuthal distribution (measured counterclockwise from the West) of the regions are given in Figures 78 80. Most galaxies have a fairly smooth azimuthal distribution, though some display peaks which correlate to ridges of star formation. Again, at the end of each set of histograms, there is a figure showing the distribution for all the galaxies taken as a whole (bottom of Figure 77 and Figure 80).
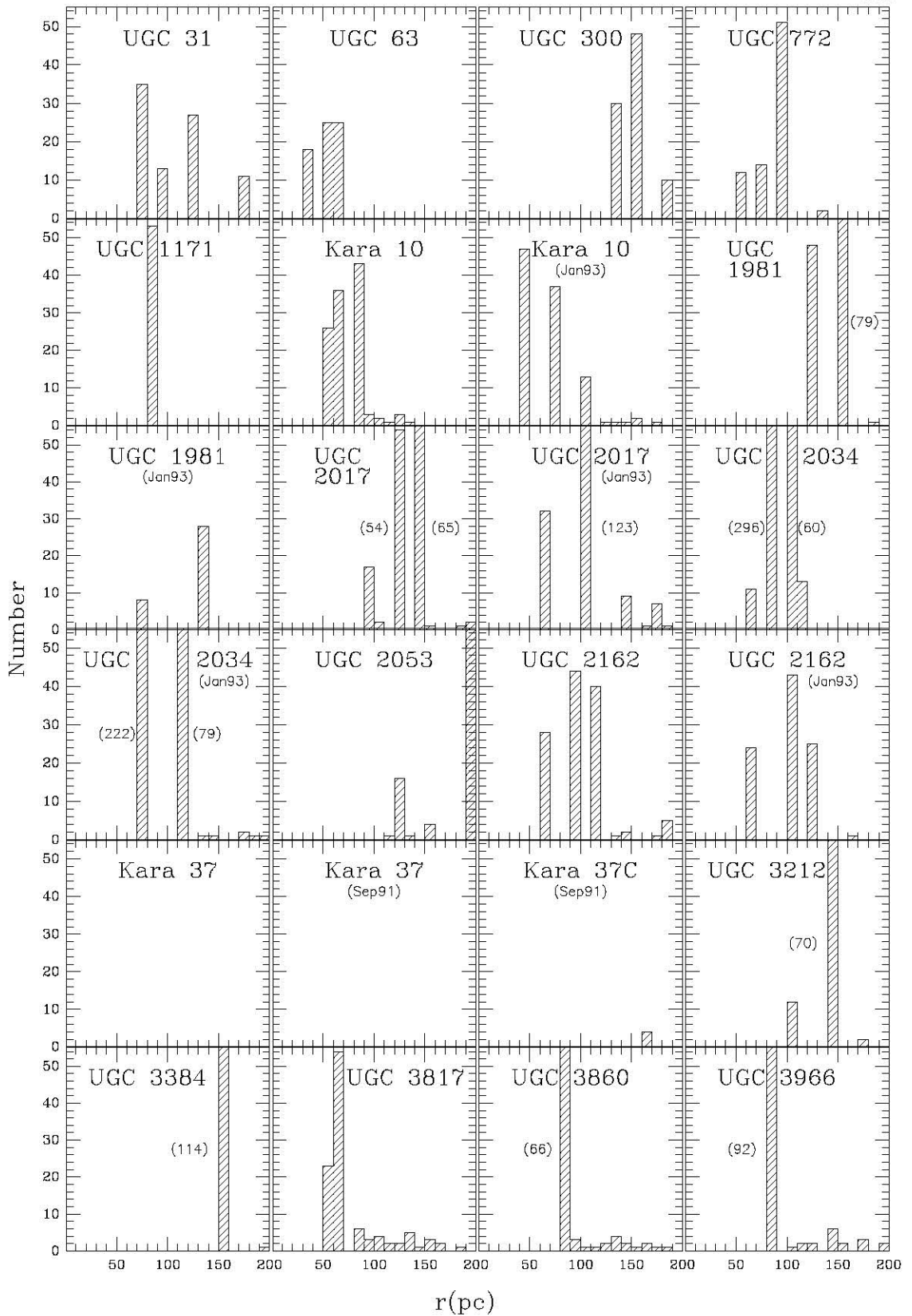
Figure 72: HII Region Size Distribution
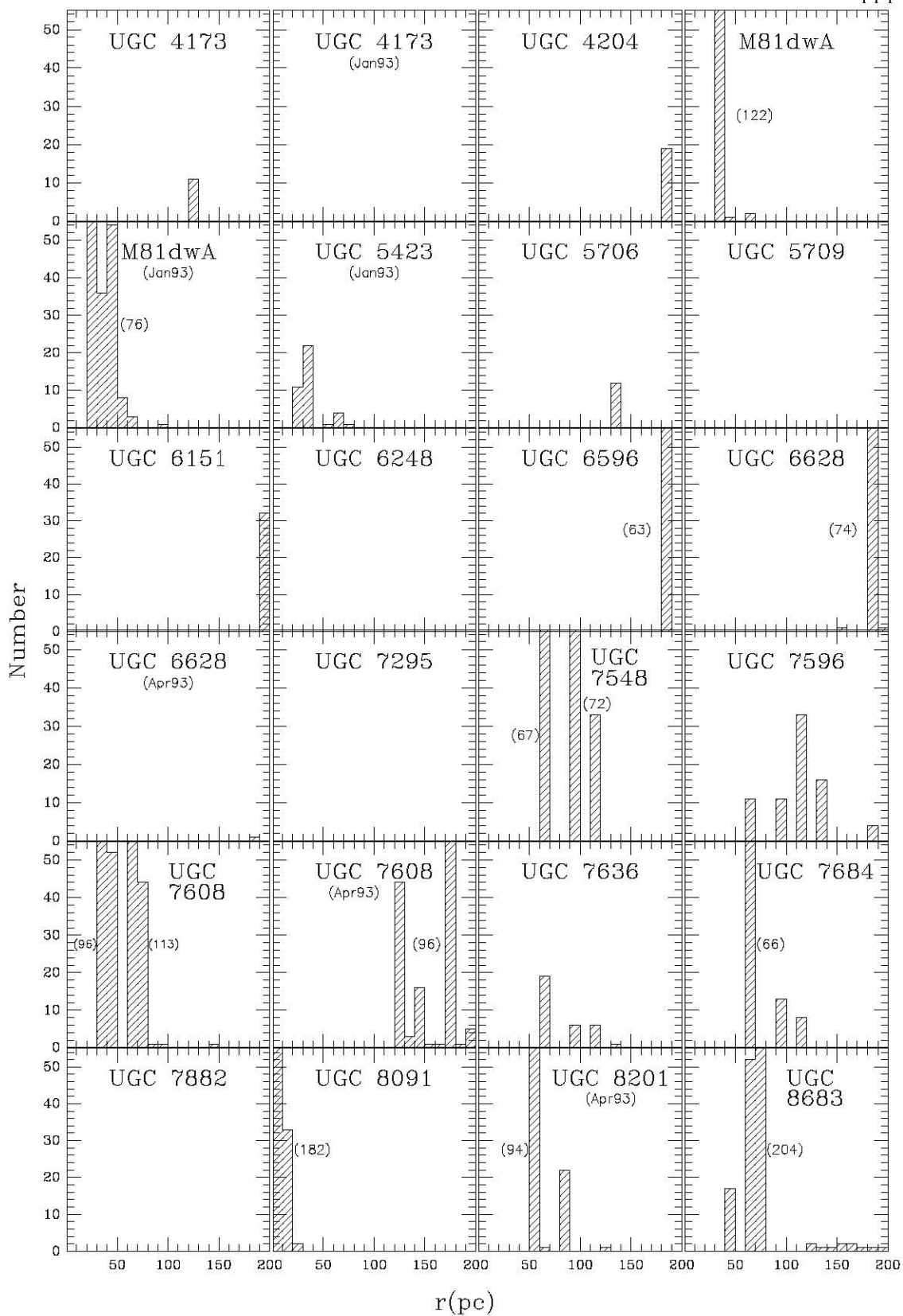
Figure 73: HII Region Size Distribution (cont.)
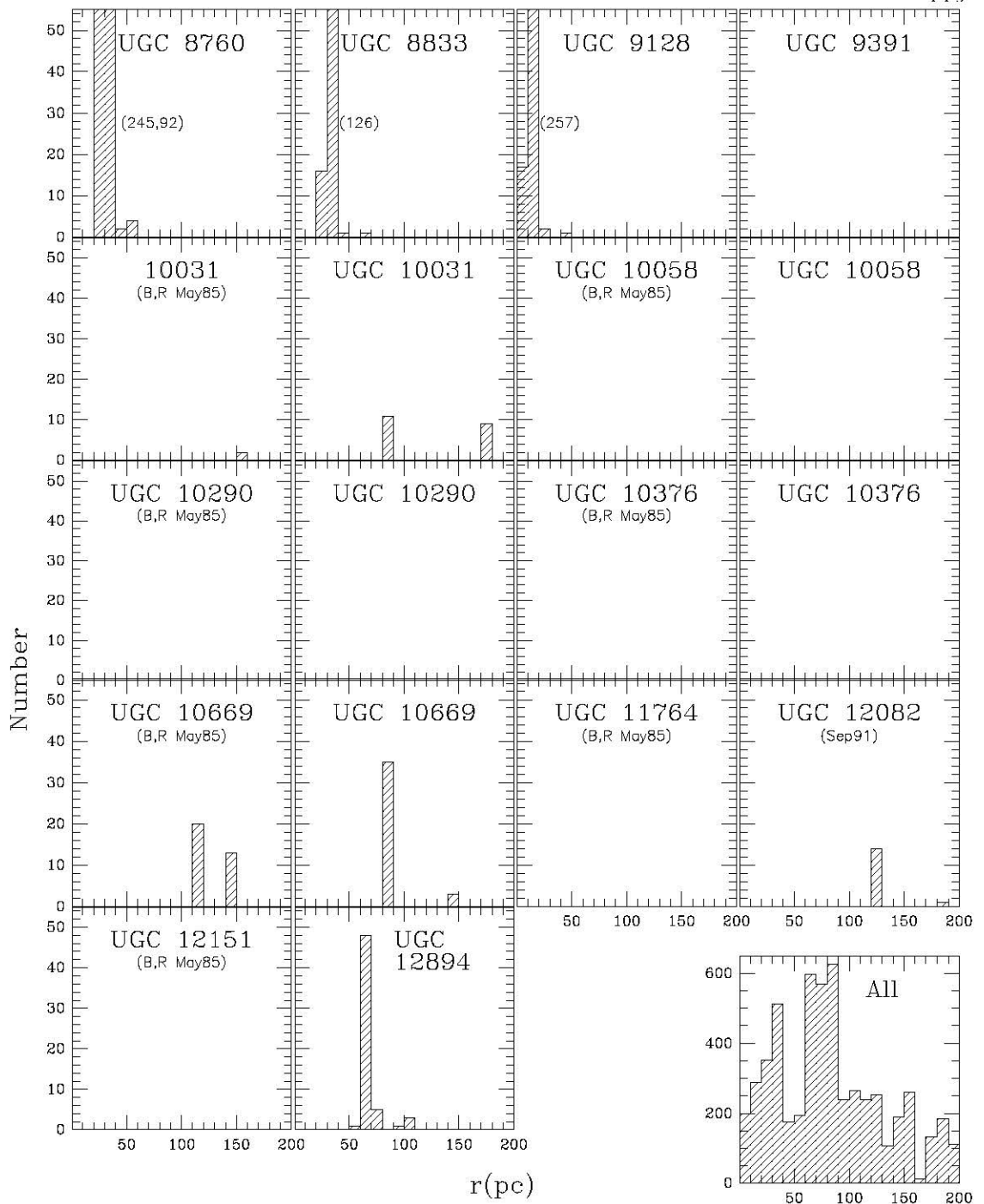
Figure 74: HII Region Size Distribution (cont.)
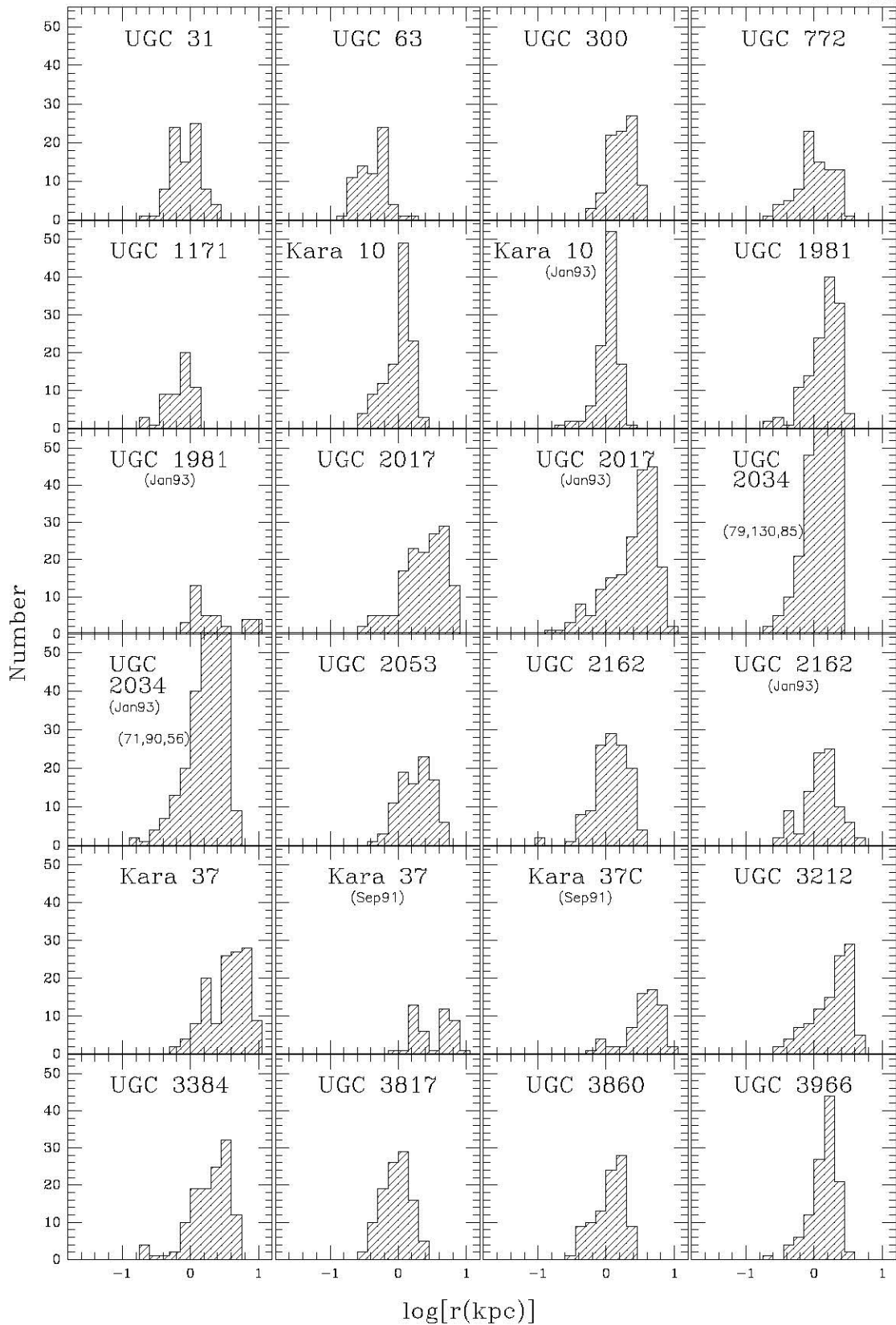
Figure 75: HII Region Radial Distribution
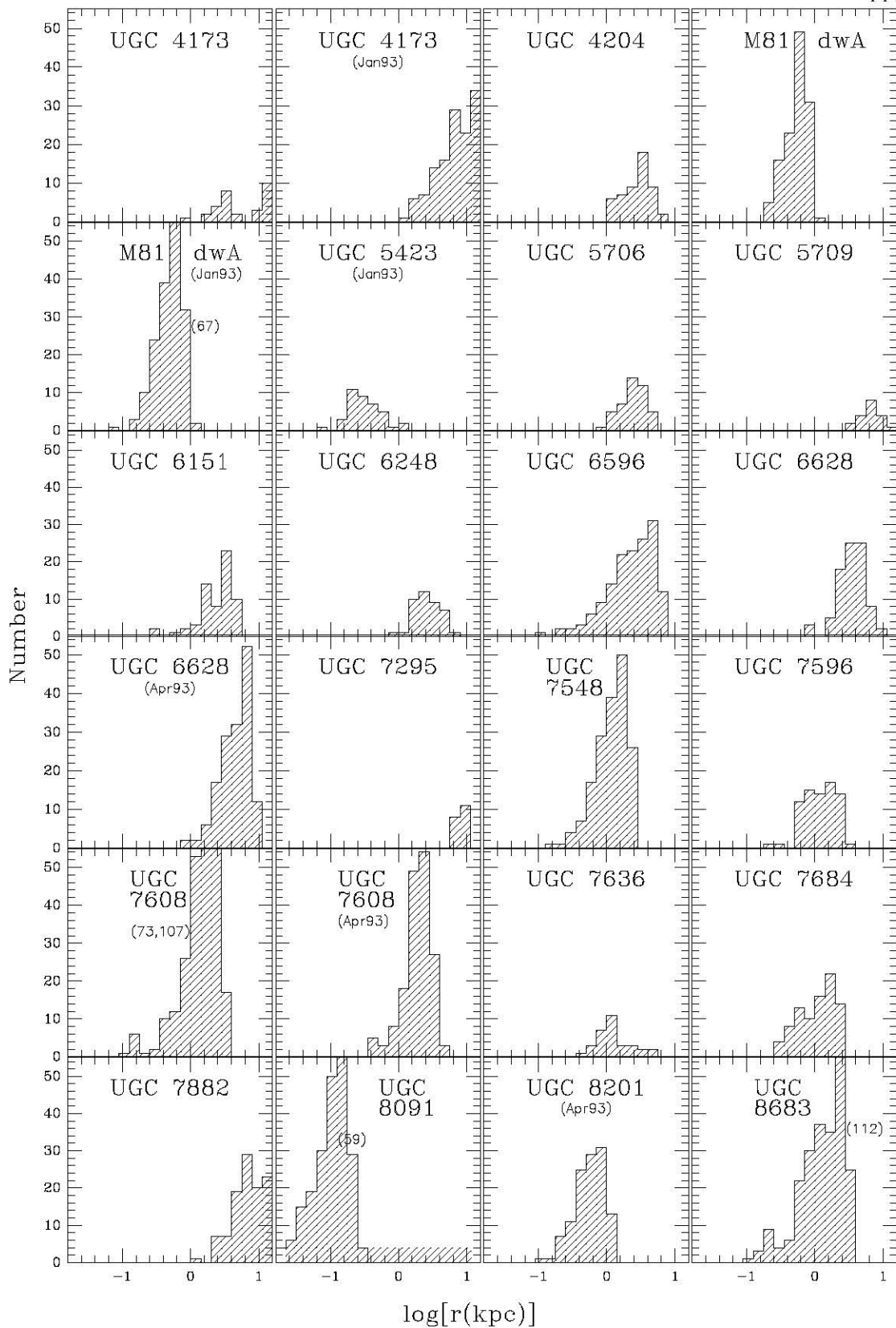
Figure 76: HII Region Radial Distribution (cont.)
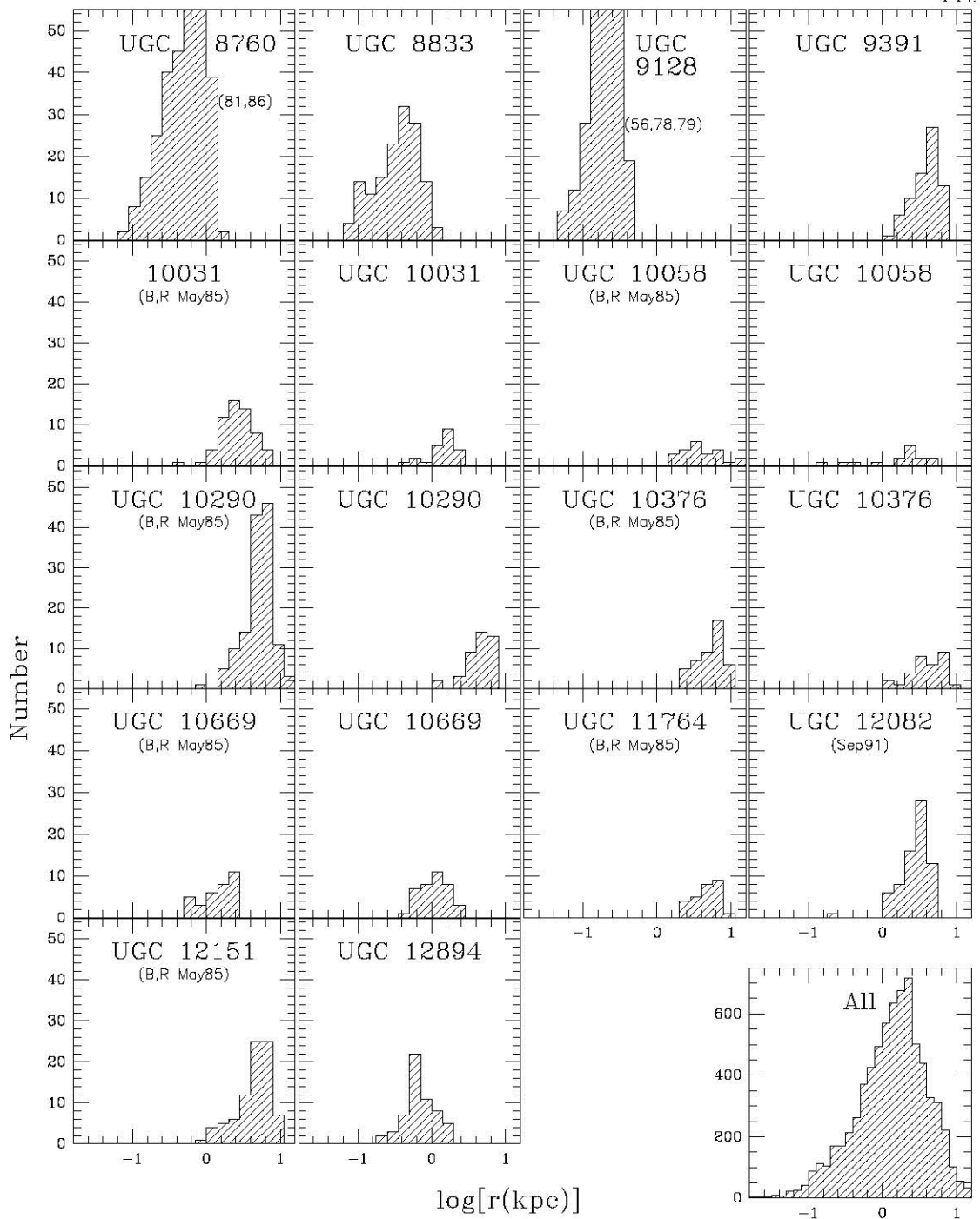
Figure 77: HII Region Radial Distribution (cont.)

119
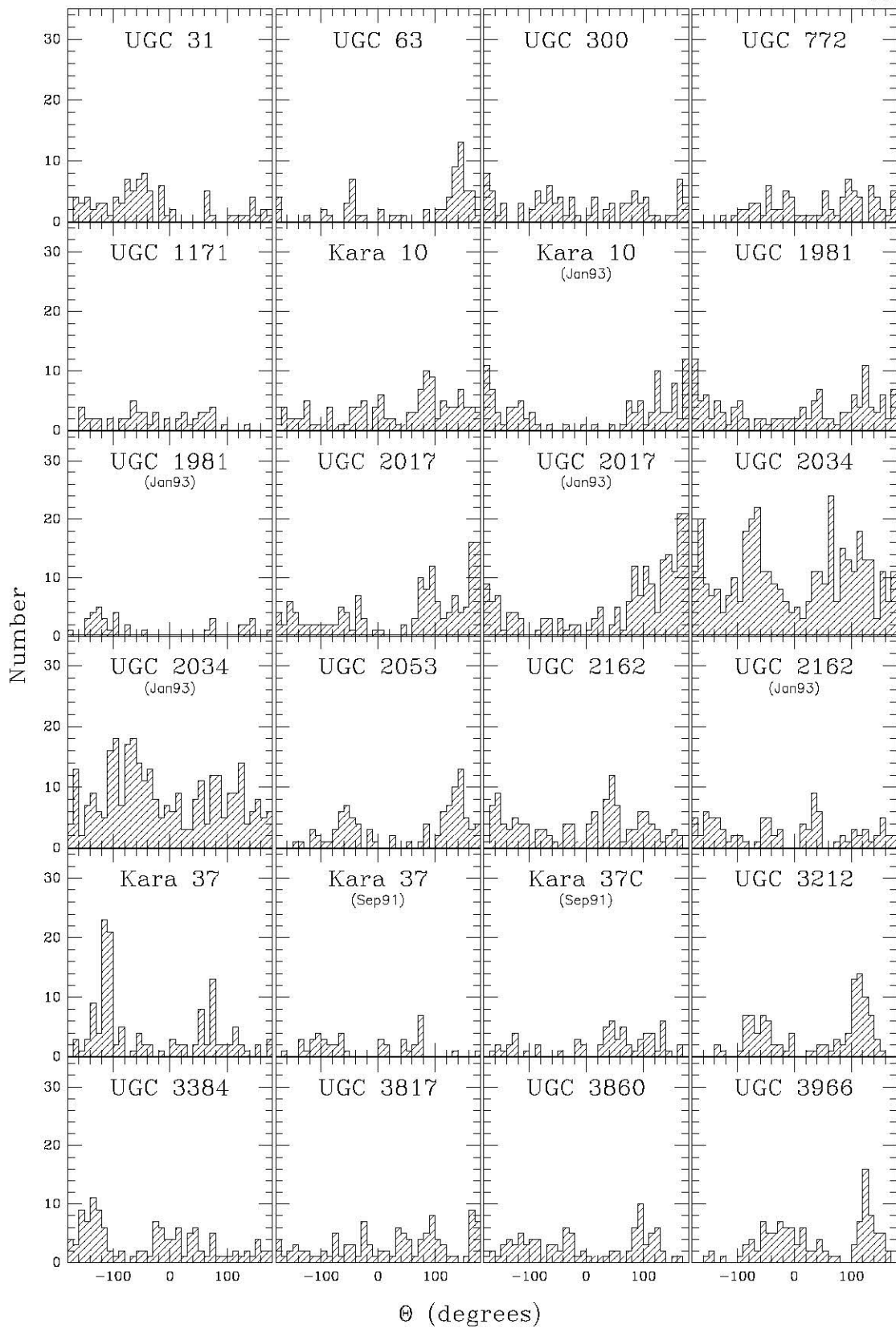
Figure 78: HII Region Azimuthal Distribution
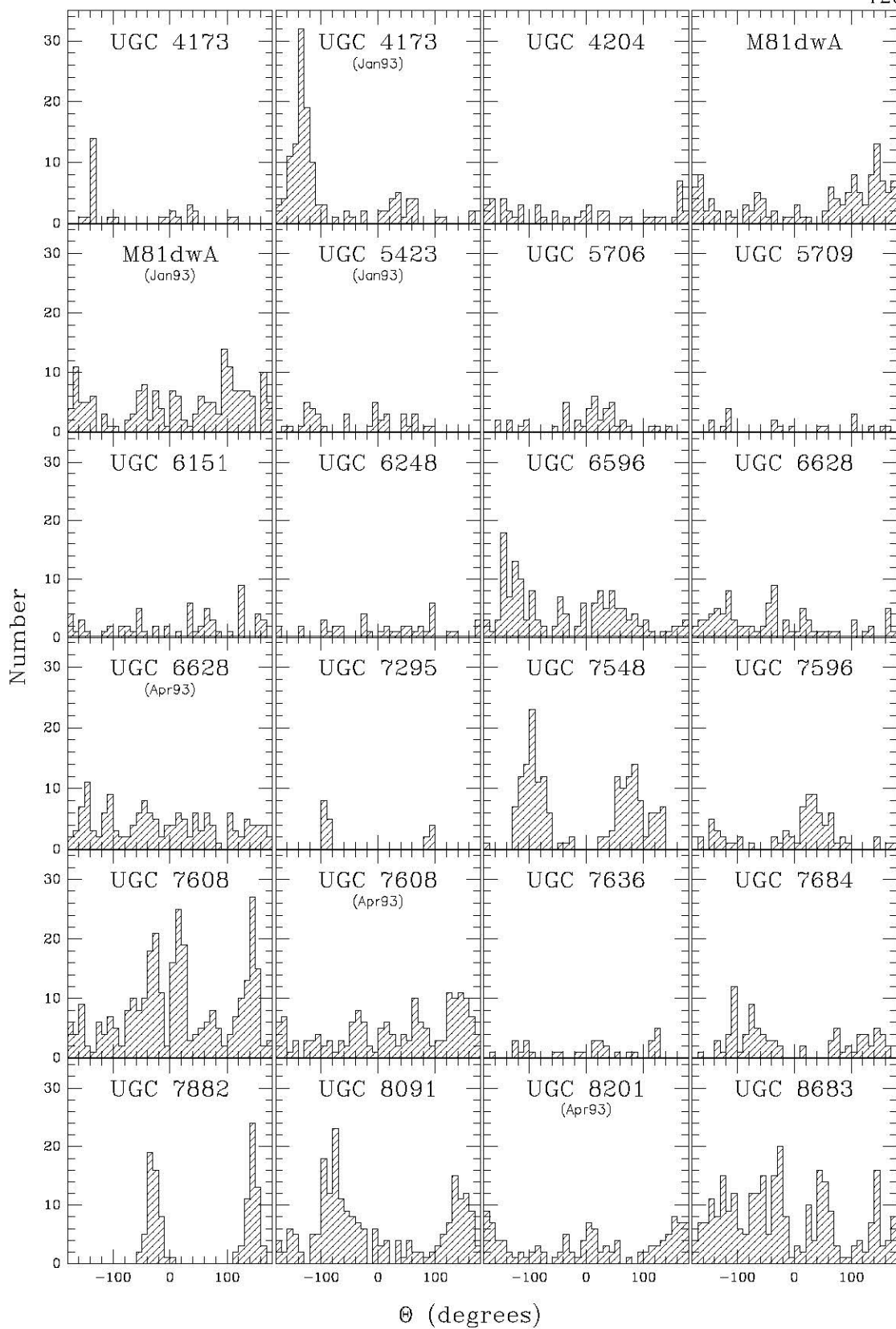
Figure 79: HII Region Azimuthal Distribution (cont.)
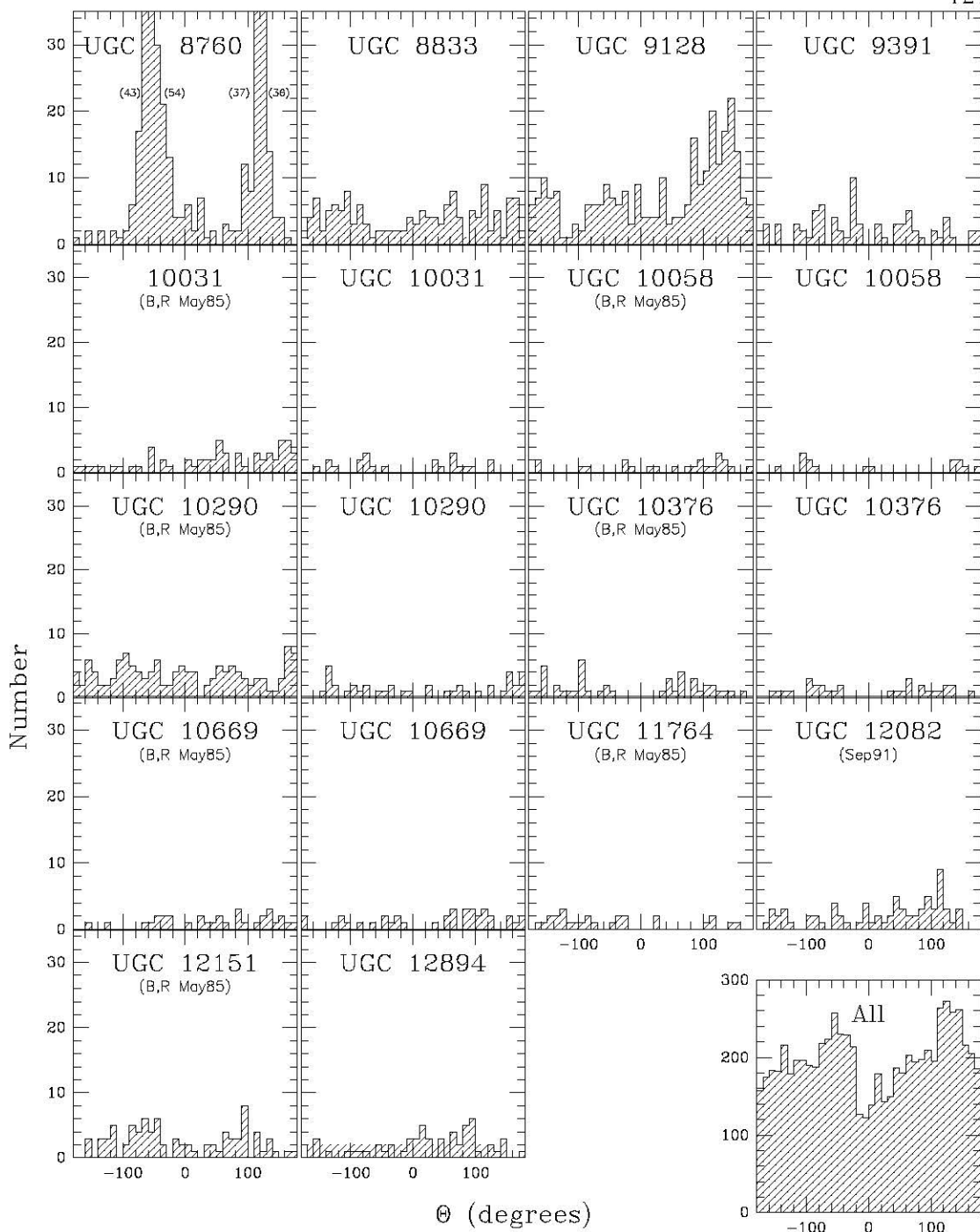
Figure 80: HII Region Azimuthal Distribution (cont.)

Chapter 3

Corrections to Magnitude and HI Linewidth

3.1 Structural Parameters

In order to derive physically meaningful information about the (3–dimensional) structure of the galaxies from the measured (2–dimensional) radial profile, it is necessary to adopt a model for the distribution of the luminous material within the galaxy. These models fall into two categories; a spheroidal bulge, or an exponential disk. There are three major parameterizations of the spheroidal bulge, the empirical Hubble law (Reynolds 1913, Hubble 1930), the theoretical models of King (1966), and the empirical de Vaucouleurs (1948) $r^{1/4}$ law. These three models fit elliptical galaxies almost equally well over a limited range of radii. It is necessary to have surface brightness profiles extending over a large range of radii in order to differentiate between the models.

The exponential disk model (de Vaucouleurs 1959) turns out to be a good fit to most disk like systems, such as the outer parts of spiral galaxies (Freeman 1970) and irregular galaxies (Impey, Bothun & Malin 1988).

However, in the case of low surface brightness galaxies, the range of radii over which the profiles extend is often so limited that it is extremely difficult to distinguish between models. Note that the apparently dE galaxy UGC 31 (Figure 3) appears to be fairly well fit by an exponential disk, although a spheroidal model (such as an $r^{1/4}$ law) does provide a marginally better fit. In most other cases in the present sample, the profiles are much more irregular, making it difficult to decide, even on a case by case basis, which model provides a better fit.

Therefore, it was decided to adopt the exponential disk model described below; both because previous work has confirmed the validity of this model in the low surface brightness and dI regime, and because no significant deviation from this model was found in the present work.

It should be noted, however, that a further complication arises because the disk–like region may only lie in the outer region of the galaxy. This combination of bulge and disk components is well understood in larger disk galaxies, but the faintness of dwarfs makes the profile decomposition into bulge and disk components more difficult. While nuclear regions of enhanced star formation are not similar to bulge components, they do contribute to pronounced deviations from exponentials in the surface brightness profiles in the region dominated by star formation (e.g. UGC 2017, Figure 11; UGC 8091, Figure 43).

3.1.1 Extinction and Orientation Corrections to Surface Brightness

The observed surface brightness and magnitude must be corrected for extinction, both from dust in our own Galaxy (A_{gal}), and from that in the galaxy being observed (A_{int}). In addition, a line–of–sight term must be included to correct the surface brightness to a face–on orientation, since it depends on the area over which the luminous matter appears to be distributed. This is simply $A_{los} = 2.5 \log \cos i$, depending only on the derived inclination i. The corrected surface brightness, μ^C, is therefore given by the following equation:

$$\mu^C = \mu^{obs} - A_{gal} - A_{int} - A_{los}. \tag{3.1}$$

The $A_{gal}(B)$ term for the UGC galaxies is taken from the RC3 (de Vaucouleurs, et al. 1991), and is based on the HI observations of Burstein and Heiles (1984). For the remaining galaxies, the value was simply interpolated from that for nearby galaxies. A relationship between the extinction in B, R and I,

$$A(R) = 0.62 A(B); \qquad A(I) = 0.44 A(B), \tag{3.2}$$

was obtained from a tabulation of interstellar extinction as a function of wavelength (Scheffler & Elsässer 1988), and from Lu et al. (1992).

The value of A_{int} depends on the inclination, i, of the galaxy (assuming it is a disk, as discussed above). This is obtained from the following formula:

$$\cos^2 i = \frac{(b/a)^2 - q_0^2}{1 - q_0^2}. \tag{3.3}$$

The value of q_0, the intrinsic axial ratio, is often taken to be 0.20 for spiral galaxies, based originally on the work of Holmberg (1958) (Bottinelli et al. 1983). A recent

study of a large sample of dwarf galaxies by Staveley–Smith, Davies & Kinman (1992) lead them to determine the most likely value for q_0 given b/a. Using the relationship between $\phi(b/a)$, the observed axial ratio distribution function, and $f(q_0)$, the intrinsic axial ratio distribution function for an oblate ellipsoidal figure (Sandage, Freeman, & Stokes, 1970; Mihalas & Binney, 1981):

$$phi(b/a) = b/a \int_0^{b/a} \frac{f(q_0)dq_0}{\sqrt{(1 - q_0^2)(b/a - q_0^2)}}, \tag{3.4}$$

they found

$$q_0 = 0.65(b/a) - 0.072(b/a)^{3.9} \tag{3.5}$$

provided a good fit to the observational data. This tends to yield values for q_0 which are greater than 0.20, which is perhaps to be expected since the disk in these smaller systems are likely to be less flattened. As noted by McGaugh & Bothun (1994), the actual value adopted for q_0 is not crucial since its effect on the value of i is small compared to the uncertainty in b/a. We adopt the formulation of Staveley–Smith et al. (equation 3.5) for the intrinsic axial ratio for the remainder of this work.

The actual relation for $A_{int}(i)$ adopted is that of Tully & Fouqué (1985):

$$A_{int} = -2.5 \log \left[f(1 + e^{-\tau \sec i}) + (1 - 2f) \left(\frac{1 - e^{-\tau \sec i}}{\tau \sec i} \right) \right], \tag{3.6}$$

where f is the fraction of light which is in front of the absorbing disk, and is taken to be 0.25. The optical depth, τ, is taken to be 0.55 in the $B-$band, while it is only 0.34 in the $R-$band and 0.24 in the $I-$band, from the relation between $A(B)$, $A(R)$ and $A(I)$ given above. This correction is the one adopted for spirals by Pierce & Tully (1992) and Lu et al. (1992) among others.

The Tully & Fouqué formulation for internal extinction is applicable to normal spiral galaxies. However, it is questionable whether this, or any other "simple"

extinction law is suitable for dwarf galaxies with their extremely low metallicities, and irregular distribution of gas and light. The value for A_{int} derived from equation (3.6) turns out to be large (> 0.4mag) for most of the sample.

It was therefore decided not to include the A_{int} term in the surface brightness or magnitudes which are calculated. No correction for internal extinction was applied by Carignan *et al.* (1990) when calculating the optical characteristics for GR8, since they felt the value of the term was too uncertain. Staveley–Smith *et al.* (1992) also apply no correction for internal extinction, stating that in dwarf galaxies (which are interpreted as having fat, inflated disks) any such term is small. This agrees with the early work of Holmberg (1958), who found no indication of an inclination dependent internal extinction in the 10 irregular galaxies in his sample.

The value of the corrections A_{gal} and A_{int} (this correction is not applied, and only listed for reference) for the $B-$band, as well as the line–of–sight correction term (for surface brightness only), are listed in Table 5 for each galaxy.

3.1.2 Exponential Disk Profiles

If the underlying light distribution of the galaxy is in the form of an exponential disk of radius r,

$$\Sigma(r) = \Sigma_0 e^{-r/\alpha}, \tag{3.7}$$

then the surface brightness profile will be well fit by a straight line characterized by the following equation:

$$\mu(r) = \mu_0 + 1.086r/\alpha \tag{3.8}$$

where $\mu_0 = -2.5 \log \Sigma_0$ is the central surface brightness of the disk and α is the scale length of the disk.

The total magnitude can be calculated for the galaxy by combining an isophotal flux (within a reasonably bright isophote) with an extrapolated flux from the outer exponential regions of the galaxy,

$$\Sigma_{total} = \Sigma_{<R} + \Sigma_{>R}, \tag{3.9}$$

where R is the effective radius of the isophote for which the isophotal flux ($\Sigma_{<R}$) was measured. Clearly,

$$\Sigma_{<R} = 10^{-0.4 m_R}, \tag{3.10}$$

where m_R is the isophotal magnitude at radius $r = R$ and the remaining flux is

$$\Sigma_{>R} = \int_R^\infty 2\pi r \, 10^{-0.4\mu_0} \, e^{-r/\alpha} dr. \tag{3.11}$$

This reduces to

$$\Sigma_{>R} = 2\pi\alpha^2 10^{-0.4\mu_0} e^{-R/\alpha} \left(R/\alpha + 1 \right). \tag{3.12}$$

If we adopt the notation used by Lu *et al.* (1993) (see also Lu 1993) and define $\Phi(x) = (1 + x)e^{-x}$, and $m_\infty = -2.5 \log 2\pi\alpha^2 10^{-0.4\mu_0}$ (the total magnitude of a galaxy which is a purely exponential disk), the total magnitude m_T is then given by

$$m_T = m_R - 2.5 \log \left[1 + 10^{-\left(\frac{m_\infty - m_R}{2.5}\right)} \Phi(R/\alpha) \right]. \tag{3.13}$$

This value for the total magnitude must then be corrected for galactic extinction (yielding a m_T^0), in the same manner as the surface brightness in the previous section. However, in the case of magnitudes, no correction for the line of sight is necessary (the A_{los} term), and once again in this case, no correction for internal extinction is applied.

When the outermost contour level in the surface brightness profile is brighter than the standard isophotal level (*e.g.* B_{25}) it was necessary to obtain the isophotal magnitude by extrapolation. This is done as above:

$$m_{25} = m_R - 2.5 \log \left\{ 1 + 10^{-\left(\frac{m_\infty - m_R}{2.5}\right)} \left[\Phi(R/\alpha) - \Phi(r_{25}/\alpha) \right] \right\}, \qquad (3.14)$$

where r_{25} is the effective radius at a corrected surface brightness level, μ^C, of 25 mag arcsec^{-2}.

The uncorrected disk parameters and magnitudes are listed for each galaxy in Table 5. The inclination and position angle were obtained from the outer isophotes of the $I-$band image (or R or B if no I was available). The uncorrected central surface brightness (μ_B^0, μ_I^0) and scale length (α_B, α_I) are listed, followed by the total magnitude in B and I that would result from a purely exponential disk with the given α and μ^0. Finally, the galactic and internal (not applied) extinction in the $B-$band and the line–of–sight correction for the surface brightness are listed.

The results of the exponential fitting, corrected as described above, are listed in Table 6. The B and I central surface brightness ($\mu_B^{(0,c)}, \mu_I^{(0,c)}$) are listed as well as the effective radius at which the corrected surface brightness is equal to 25 mag arcsec^{-2} (r_{25}^B) along with the Holmberg radius ($r_{26.5}^B$). Next the aperture magnitudes at the 25th and 26.5 isophote for B and 22.5 and 24.5 for I are given. Finally the total corrected magnitude with (B_T^0, I_T^0) and without (B_T^{0-}, I_T^{0-}) the identified HII regions and stars within the galaxy are listed.

For the galaxies with previous CCD photometry (Figure 2), we can compare their total corrected magnitudes with ours. For UGC 8091 (GR8) Carignan *et al.* (1990) list $B_T^0 = 14.63$, while we find 14.53 (with some cirrus present). This would appear to be satisfactory, especially since the brightest star "in" GR8 is a foreground

Table 5:   Uncorrected Disk Parameters and Magnitudes

Galaxy	i	PA	μ_B^0	α_B	μ_I^0	α_I	B_∞	I_∞	A_{gal}^B	A_{int}^B	A_{los}
	(°)	(°)	$\left(\frac{\text{mag}}{\text{arcsec}^2}\right)$	(")	$\left(\frac{\text{mag}}{\text{arcsec}^2}\right)$	(")	(mag)	(mag)	(mag)	(mag)	$\left(\frac{\text{mag}}{\text{arcsec}^2}\right)$
31	50	52	21.42	7.6	20.23	9.0	15.31	13.78	0.08	0.40	−0.48
63	60	61	22.03	8.5	17.71	2.0	15.72	14.65	0.22	0.48	−0.74
300	39	43	23.66	16.4	21.86	7.1	15.75	15.78	0.04	0.34	−0.27
772	59	39	20.62	8.2	...	...	14.56	...	0.04	0.47	−0.71
1171	58	163	20.75	8.3	...	...	14.54	...	0.16	0.47	−0.70
K10	57	129	24.10	18.5	23.82	24.4	16.14	15.33	0.13	0.46	−0.65
K10^2	65	122	24.96	52.2	24.77	65.6	14.99	14.37	0.13	0.56	−0.95
1981	40	173	21.34	5.7	21.24	9.0	15.79	14.70	0.00	0.34	−0.29
1981^2	54	2	23.35	16.6	21.86	10.9	15.70	15.12	0.00	0.43	−0.58
2017	61	40	23.93	15.3	22.60	13.5	16.31	15.44	0.31	0.51	−0.80
2017^2	51	7	24.12	20.7	23.53	19.3	15.61	15.35	0.31	0.40	−0.50
2034	59	94	24.02	22.4	21.15	10.2	15.62	14.56	0.20	0.48	−0.71
2034^2	31	124	22.93	25.5	21.13	15.3	13.83	13.24	0.20	0.31	−0.16
2053	73	38	22.61	11.8	21.80	15.1	15.95	14.83	0.39	0.73	−1.34
2162	54	142	24.09	14.2	23.34	14.6	16.71	15.93	0.06	0.43	−0.58
2162^2	76	116	23.93	14.3	24.50	32.7	17.37	16.17	0.06	0.80	−1.52
K37	72	160	25.20	30.0	21.50	11.7	13.83	13.85	3.00	0.69	−1.25
K37^2	65	137	25.64	48.0	23.77	20.3	12.78	14.46	3.00	0.56	−0.95
K37C^2	25	76	25.56	119.1	22.54	37.1	10.27	11.46	3.00	0.30	−0.11
3212	71	23	22.58	6.2	21.51	5.8	17.08	16.46	0.53	0.68	−1.23
3384	40	83	22.63	5.1	21.13	5.6	16.76	15.34	0.57	0.34	−0.28
3817	51	140	23.33	9.4	22.12	9.6	16.49	15.43	0.36	0.41	−0.51
3860	47	15	19.48	11.7	...	...	12.23	...	0.23	0.38	−0.42
3966	47	28	23.80	19.5	23.36	23.8	15.45	14.70	0.22	0.38	−0.41
4173	71	137	24.45	9.6	22.50	11.3	18.44	16.19	0.10	0.68	−1.24
4173^2	62	131	23.45	19.0	22.69	18.9	15.59	14.89	0.10	0.51	−0.81
4204	50	102	23.30	9.5	21.74	8.9	16.66	15.30	0.13	0.40	−0.48
M81dwA	39	9	24.20	20.9	23.57	57.5	15.72	12.94	0.09	0.34	−0.27
M81dwA^2	59	82	23.68	12.3	24.72	38.7	16.71	15.30	0.09	0.48	−0.72
5423^2	59	138	22.07	10.0	20.80	9.6	15.42	14.34	0.20	0.47	−0.71
5706	61	103	24.62	27.6	23.58	27.5	16.02	14.99	0.02	0.51	−0.80
5709	61	117	22.58	11.0	21.30	11.4	15.95	14.61	0.04	0.50	−0.79
6151	18	175	23.46	20.7	22.60	23.2	14.92	13.82	0.00	0.28	−0.05
6248	36	28	24.14	20.4	22.81	22.6	15.73	14.20	0.03	0.33	−0.22
6596	62	123	22.87	10.7	22.85	20.8	16.36	14.89	0.00	0.51	−0.82
6628	41	60	22.45	30.7	21.17	33.8	13.24	11.76	0.01	0.35	−0.31
6628^2	34	48	22.20	35.6	...	...	12.60	...	0.01	0.32	−0.21
7295	74	1	22.50	5.4	19.67	3.7	17.97	15.94	0.00	0.74	−1.37
7548	69	174	22.38	10.5	21.60	11.4	16.02	15.13	0.13	0.63	−1.10
7596	69	134	22.05	9.4	21.13	12.7	16.08	14.51	0.00	0.63	−1.12
7608	53	64	24.26	15.6	23.98	37.9	16.72	14.51	0.00	0.42	−0.55
7608^2	53	38	23.71	49.7	...	...	13.38	...	0.00	0.42	−0.55
7636	51	1	24.07	31.8	22.62	38.9	14.94	13.05	0.00	0.40	−0.50
7684	58	42	21.80	8.1	20.37	10.9	15.71	13.69	0.07	0.46	−0.67
7882	65	59	22.26	6.4	21.44	8.3	17.82	16.45	0.01	0.56	−0.94
8091	52	44	23.30	15.8	22.47	20.6	15.67	14.28	0.04	0.41	−0.52
8201^2	46	88	22.48	37.5	...	...	12.87	...	0.04	0.37	−0.39
8683	59	141	22.71	11.8	23.39	30.9	15.91	14.50	0.00	0.48	−0.72
8760	79	33	22.45	15.4	22.10	20.5	16.05	15.08	0.00	0.92	−1.81
8833	48	150	22.20	10.3	22.31	17.3	15.47	14.45	0.00	0.39	−0.44
9128	61	41	21.78	11.7	21.21	12.2	15.06	14.39	0.00	0.50	−0.79
9391	50	52	22.37	14.0	21.42	16.8	15.01	13.66	0.00	0.40	−0.48
10031	47	17	23.67	12.0	23.53	21.4	16.57	15.19	0.01	0.38	−0.41
10058	35	20	23.29	10.9	23.38	20.1	16.08	14.95	0.18	0.32	−0.21
10290	43	177	22.95	16.4	22.28	39.7	14.77	12.38	0.36	0.36	−0.33
10376	39	22	23.43	10.2	22.17	8.3	16.57	15.75	0.04	0.34	−0.27
10669	47	55	23.73	12.3	23.04	12.8	16.46	15.76	0.15	0.38	−0.42
11764	27	12	23.71	12.0	...	...	16.24	...	0.16	0.30	−0.12
12082^2	54	175	24.27	28.0	22.95	31.4	15.15	13.77	0.33	0.43	−0.39
12151	51	179	23.37	23.0	...	...	14.74	...	0.21	0.41	−0.50
12894	46	148	24.55	88.2	23.53	60.4	12.66	12.73	0.47	0.37	−0.40

Table 6:   Corrected Magnitudes

galaxy	$\mu_B^{(0,c)}$	$\mu_I^{(0,c)}$	r_{25}^B	$r_{26.5}^B$	$B_{25}^c/B_{26.5}^c$	$I_{22.5}^c/I_{24.5}^c$	B_T^0	B_T^{0-}	I_T^0	I_T^{0-}
	$\left(\frac{mag}{arcsec^2}\right)$		(″)	(″)	(mag)	(mag)	(mag)		(mag)	
31	21.82	20.67	25.6	37.5	14.62/14.56	13.59/13.37	14.54	14.97	13.29	13.64
63	22.54	18.35	23.6	34.8	14.87/...	.../15.30	14.76	15.12	15.28	15.96
300	23.90	22.11	24.0	41.3	15.90/...	.../15.71	15.37	15.61	15.46	15.82
772	21.29	...	...	87.1	.../...	.../...	13.69	14.14	...	...
1171	21.28	...	34.2	54.0	13.40/...	.../...	13.37	13.75	...	...
K10	24.62	24.42	...	41.6	.../15.65	.../15.70	15.44	15.66	14.85	15.06
K10^2	25.78	25.66	...	55.1	.../15.13	.../...	14.51	14.60	14.14	14.22
1981	21.63	21.53	20.4	27.7	16.25/16.13	15.45/14.75	16.07	16.60	14.55	14.99
1981^2	23.93	22.43	24.1	55.0	15.67/...	.../15.02	15.23	15.29	14.76	14.85
2017	24.41	23.26	17.9	38.6	15.52/15.31	.../14.95	15.18	15.47	14.64	14.92
2017^2	24.31	23.89	22.6	55.2	15.36/...	.../15.29	14.81	15.00	14.70	15.00
2034	24.54	21.78	34.8	60.2	14.24/14.15	13.78/13.63	14.08	14.81	13.57	14.30
2034^2	22.90	21.20	53.8	76.3	13.85/...	13.86/13.25	13.45	13.72	13.09	13.45
2053	23.56	22.97	27.0	42.8	14.09/14.05	.../13.64	14.02	14.62	13.51	13.99
2162	24.61	23.89	14.0	33.6	16.65/16.30	.../16.37	16.10	16.42	15.61	15.87
2162^2	25.39	25.99	...	26.4	.../15.81	.../...	15.72	15.99	15.50	15.70
K37	23.45	21.43	...	110.8	.../...	11.36/11.26	9.84	10.16	11.22	11.81
K37^2	23.58	23.39	...	251.9	.../...	12.42/12.30	9.71	9.78	12.14	12.51
K37C^2	22.67	21.33	...	308.3	.../...	10.48/...	7.25	7.29	9.81	10.08
3212	23.28	22.50	15.0	23.8	15.06/15.02	.../14.89	14.99	15.78	14.82	15.67
3384	22.35	21.16	15.5	24.4	15.60/15.52	.../14.64	15.49	16.17	14.53	15.15
3817	23.48	22.47	19.4	31.3	15.77/15.62	.../...	15.53	15.98	14.48	15.20
3860	19.67	...	...	95.6	.../...	.../...	11.41	11.88	...	...
3966	24.00	23.68	30.7	47.1	15.04/14.86	.../14.56	14.67	15.06	14.04	14.52
4173	25.59	23.69	...	24.0	.../17.42	.../15.23	17.31	17.70	15.01	15.36
4173^2	24.16	23.45	30.2	68.8	14.77/...	.../14.39	14.54	14.78	14.08	14.28
4204	23.65	22.16	16.7	30.3	16.42/16.18	.../14.89	16.07	16.28	14.73	15.13
M81dwA	24.38	23.80	23.0	45.4	16.04/15.63	.../14.44	15.31	15.56	12.89	12.94
M81dwA^2	24.31	25.40	...	30.2	.../16.07	.../...	15.91	16.40	15.02	15.30
5423^2	22.57	21.42	27.8	44.3	14.42/14.35	13.95/13.70	14.32	14.57	13.61	13.83
5706	25.40	24.37	10.6	42.4	16.10/15.76	.../15.32	15.41	15.53	14.56	14.66
5709	23.33	22.07	23.4	39.7	15.14/15.03	14.17/13.89	14.98	15.05	13.77	13.83
6151	23.51	22.65	37.2	63.2	15.13/14.82	15.05/14.08	14.65	14.83	13.59	13.75
6248	24.34	23.03	19.6	52.1	16.14/...	.../14.58	15.35	15.45	13.98	14.06
6596	23.69	23.67	22.4	34.2	15.16/15.09	.../14.26	15.05	15.78	13.97	14.43
6628	22.75	21.48	73.3	125.8	13.37/13.14	12.87/11.97	13.06	13.18	11.75	11.84
6628^2	22.40	...	97.3	155.4	12.17/...	.../...	12.01	12.43	...	...
7295	23.87	21.04	10.2	16.5	16.52/16.47	.../14.75	16.43	16.52	14.71	14.77
7548	23.36	22.64	24.5	35.7	14.54/14.50	.../14.15	14.46	15.03	14.02	14.48
7596	23.17	22.25	22.7	36.0	14.77/14.72	13.68/13.47	14.69	14.95	13.39	13.62
7608	24.81	24.53	12.7	46.8	16.66/...	.../15.90	16.10	16.33	14.40	14.47
7608^2	24.26	...	78.9	141.5	12.89/12.75	.../...	12.66	13.18	...	...
7636	24.56	23.11	28.1	84.5	15.05/...	14.19/...	14.43	14.45	12.83	12.85
7684	22.41	21.02	23.6	35.0	14.82/14.76	13.28/...	14.73	14.88	12.99	13.12
7882	23.18	22.37	18.3	20.4	14.87/14.87	13.50/13.48	14.84	15.79	13.44	14.33
8091	23.78	22.97	31.4	44.9	14.68/...	.../13.93	14.53	15.43	13.64	14.21
8201^2	22.83	...	90.3	157.3	12.00/...	.../...	11.87	12.54	...	...
8683	23.43	24.11	23.7	42.9	14.98/14.88	.../...	14.83	15.34	13.53	13.95
8760	24.26	23.91	30.8	46.2	13.72/13.70	.../13.18	13.68	14.21	13.10	13.61
8833	22.64	22.75	26.8	44.3	14.93/14.82	14.28/14.16	14.78	15.22	13.86	14.20
9128	22.57	22.00	33.6	50.4	14.39/14.32	.../13.93	14.29	14.87	13.80	14.44
9391	22.85	21.91	35.0	46.5	14.48/14.40	13.79/13.32	14.32	14.56	13.16	13.33
10031	24.07	23.93	17.5	36.9	16.20/15.96	15.56/...	15.86	16.37	14.78	13.59
10058	23.32	23.51	21.3	45.2	15.69/...	15.40/...	15.38	15.88	14.54	13.37
10290	22.92	22.46	47.7	71.7	13.68/...	.../...	13.58	14.41	12.06	11.06
10376	23.66	22.42	18.4	30.6	16.12/15.95	15.41/15.20	15.84	16.35	15.15	13.82
10669	24.00	23.40	17.4	33.8	16.16/15.90	15.96/15.44	15.75	15.95	15.31	13.99
11764	23.67	...	18.0	36.2	16.16/15.81	.../...	15.66	16.03	...	...
12082^2	24.52	23.39	30.0	66.1	14.08/13.91	13.10/12.86	13.78	14.25	12.65	13.21
12151	23.67	...	40.6	70.2	14.17/13.99	.../...	13.88	14.22	...	...
12894	24.49	23.73	...	170.0	.../...	.../13.80	12.21	12.24	12.50	12.57

star (Moss & de Vaucouleurs 1986) and must be excluded from the fitting. GR8 can be considered the most extreme example of an dwarf irregular with numerous IIII regions and stars "disturbing" the underlying profile. Note the very irregular deviation between the surface brightness profiles of Carignan *et al.* and ourselves in Figure 2. The close agreement between our *total* magnitude and that of Carignan *et al.* is gratifying and gives us confidence in the results we find in Chapters 4 and 5 using the total magnitudes listed in Table 6 (and 8).

UGC 12151 was observed by de Jong & van der Kruit (1994), who find $m_B = 14.43 \pm 0.69$ and $m_R = 13.75 \pm 0.55$, compared to our $B_T^0 = 13.88$ and $R_T^0 = 13.52$. They did not correct for galactic extinction ($A_B = 0.21$) so the magnitudes compare even more favorably. McGaugh (1992) (see also McGaugh & Bothun 1994) observed UGC 5709 and UGC 6151 but list magnitudes from the disk component alone. Since both of these galaxies appear to have rather smooth $B-$band profiles (see Figures 31 and 32), these disk magnitudes can be seen as lower limits and compared with our results. McGaugh lists $B_T = 14.92$ for UGC 5709 and $B_T = 14.30$ for UGC 6151, which are very close to our own total magnitudes of 14.98 and 14.65 respectively. The discrepancy would be expected to increase if McGaugh had measured actual magnitudes, but the extreme regularity of the profiles of these two LSB galaxies would tend to minimize this.

The average difference and the deviation are both ~ 0.2 magnitudes. Given the differences in technique of the different authors and the irregularity of the galaxies, we feel satisfied with our results. Again, the comparison of the GR8 data is especially reassuring.

3.2 Adopted Distances

A distance for each galaxy in the sample is listed in Table 7. Three important effects must be considered in addition to the basic Hubble expansion when using the heliocentric HI velocities to obtain distances. First, the correction for the motion of the sun with respect to centroid of the Local Group from Yahil, Tammann & Sandage (1977),

$$\Delta v_{LG} = -79 \cos l \cos b + 296 \sin l \cos b - 36 \sin b, \qquad (3.15)$$

was applied, where l and b are the galactic longitude and latitude of the galaxy. Second, the correction for the Virgocentric infall of nearby galaxies based on the formulation of Schechter (1980) (see also Aaronson et al. 1982) was applied. A Virgocentric infall velocity of 300 km s^{-1} for the Local Group and a heliocentric velocity of 1026 km s^{-1} for Virgo were adopted. The corrections were calculated with the aid of a program provided by Mark Whittle.

Finally, the Nearby Galaxy Atlas and Catalog (Tully & Fisher 1987; Tully 1988) were used to determine group membership for each galaxy in the sample, and a mass or luminosity weighted average redshift for all the galaxies in the group was adopted as the velocity of the galaxy. Because these dwarfs are so much less massive than normal galaxies which dominate the groups, the dwarf velocity can include peculiar motions of hundreds of kilometers per second; the weighted average for the group should therefore provide a much more distance–indicative velocity for the dwarf. This corrected velocity is listed in Table 7.

In the case of galaxies which are not listed in Tully, the Atlas was examined in order to determine likely group membership, based on galactic latitude and longitude

and systemic velocity, v_0. This systemic velocity, used by Tully & Fisher, is simply the heliocentric velocity corrected for the solar motion with respect to the Galaxy, neglecting the Local Group dynamics, and is

$$\Delta v_0 = 300 \sin l \cos b. \tag{3.16}$$

This is similar to the Δv_{LG}, and varies from it by at most $\sim 90 \mathrm{km\ s}^{-1}$ in certain directions. After the group v_0 was obtained, a correction for the Virgocentric infall was made.

A Hubble constant of $H_0 = 75 \mathrm{km\ s}^{-1}$ was adopted and the distances obtained from the group velocities are listed in Table 5. Two galaxies, UGC 8091 and UGC 9128 (DDO 155 and DDO 187) are extremely nearby, possible members of the Local Group (van den Bergh 1994). Many authors have used various independent distance estimators, including brightest blue and red supergiants and size of the largest HII region to obtain distances to these galaxies. For UGC 8091 these estimates include those from Hoessel & Danielson 1983; de Vaucouleurs & Moss 1983; Moss & de Vaucouleurs 1986; and Aparicio, García Pelayo & Moles 1988b; for UGC 9128, we adopt the distance estimate of 1.1 Mpc from Aparicio, García–Pelayo & Moles 1988a.

For the several higher redshift, LSB galaxies, the velocity was corrected for the motion of the local group and the Virgocentric infall, and the distance was obtained in a straightforward way from this velocity.

The distances, listed in Table 7, were then used to calculate the remaining parameters in the table. These include the distance modulus, the disk scale lengths in the B and I from Table 5, converted to kiloparsecs and the absolute magnitudes in B and I, with (M^T) and without (M^{T-}) the identified HII regions and stars present in the galaxy.

Table 7: Distance Dependent Quantities

Galaxy	v_{corr}	D	$m-M$	α_B	α_I	M_B^T	M_B^{T-}	M_I^T	M_I^{T-}
	(km s^{-1})	(Mpc)	(mag)	(kpc)		(mag)		(mag)	
31	1109.1	14.8	30.85	0.54	0.65	−16.31	−15.88	−17.56	−17.21
63	584.8	7.8	29.46	0.32	0.08	−14.70	−14.34	−14.18	−13.50
300	1183.8	15.8	30.99	1.26	0.55	−15.62	−15.38	−15.53	−15.17
772	876.7	11.7	30.34	0.47	...	−16.65	−16.20	...	...
1171	792.1	10.6	30.12	0.43	...	−16.75	−16.37	...	...
K10	792.9	10.6	30.12	0.95	1.25	−14.68	−14.46	−15.27	−15.06
K10^2	792.9	10.6	30.12	2.68	3.37	−15.61	−15.52	−15.98	−15.90
1981	1374.5	18.3	31.32	0.50	0.79	−15.25	−14.72	−16.77	−16.33
1981^2	1374.5	18.3	31.32	1.47	0.96	−16.09	−16.03	−16.56	−16.47
2017	1101.1	14.7	30.83	1.09	0.96	−15.65	−15.36	−16.19	−15.91
2017^2	1101.1	14.7	30.83	1.47	1.37	−16.02	−15.83	−16.13	−15.83
2034	765.5	10.2	30.04	1.11	0.51	−15.96	−15.23	−16.47	−15.74
2034^2	765.5	10.2	30.04	1.26	0.76	−16.59	−16.32	−16.95	−16.59
2053	1104.6	14.7	30.84	0.84	1.08	−16.82	−16.22	−17.33	−16.85
2162	1039.9	13.9	30.71	0.96	0.98	−14.61	−14.29	−15.10	−14.84
2162^2	1039.9	13.9	30.71	0.96	2.20	−14.99	−14.72	−15.21	−15.01
K37	2127.1	28.4	32.26	4.12	1.61	−22.42	−22.10	−21.04	−20.45
K37^2	2127.1	28.4	32.26	6.60	2.79	−22.55	−22.48	−20.12	−19.75
K37C^2	2127.1	28.4	32.26	16.40	5.10	−25.01	−24.97	−22.45	−22.18
3212	1609.1	21.5	31.66	0.65	0.60	−16.67	−15.88	−16.84	−15.99
3384	1395.1	18.6	31.35	0.46	0.51	−15.86	−15.18	−16.82	−16.20
3817	609.4	8.1	29.55	0.37	0.38	−14.02	−13.57	−15.07	−14.35
3860	797.9	10.6	30.13	0.60	...	−18.72	−18.25	...	...
3966	802.4	10.7	30.15	1.01	1.23	−15.48	−15.09	−16.11	−15.63
4173	1881.8	25.1	32.00	1.17	1.38	−14.69	−14.30	−16.99	−16.64
4173^2	1881.8	25.1	32.00	2.31	2.30	−17.46	−17.22	−17.92	−17.72
4204	2851.5	38.0	32.90	1.75	1.64	−16.83	−16.62	−18.17	−17.77
M81dwA	344.2	4.6	28.31	0.47	1.28	−13.00	−12.75	−15.42	−15.37
M81dwA^2	344.2	4.6	28.31	0.27	0.86	−12.40	−11.91	−13.29	−13.01
5423^2	331.7	4.4	28.23	0.21	0.21	−13.91	−13.66	−14.62	−14.40
5706	1970.4	26.3	32.10	3.52	3.51	−16.69	−16.57	−17.54	−17.44
5709	6438.2	85.8	34.67	4.57	4.75	−19.69	−19.62	−20.90	−20.84
6151	1767.2	23.6	31.86	2.37	2.65	−17.21	−17.03	−18.27	−18.11
6248	2041.9	27.2	32.17	2.69	2.98	−16.82	−16.72	−18.19	−18.11
6596	2874.9	38.3	32.92	1.99	3.87	−17.87	−17.14	−18.95	−18.49
6628	1393.2	18.6	31.34	2.77	3.05	−18.28	−18.16	−19.59	−19.50
6628^2	1393.2	18.6	31.34	3.21	...	−19.33	−18.91	...	...
7295	7034.7	93.8	34.86	2.45	1.69	−18.43	−18.34	−20.15	−20.09
7548	1326.0	13.7	30.68	0.70	0.76	−16.22	−15.65	−16.66	−16.20
7596	1326.0	13.7	30.68	0.62	0.84	−15.99	−15.73	−17.29	−17.06
7608	565.1	7.5	29.39	0.57	1.38	−13.29	−13.06	−14.99	−14.92
7608^2	565.1	7.5	29.39	1.81	...	−16.73	−16.21	...	...
7636	1326.0	13.7	30.68	2.11	2.59	−16.25	−16.23	−17.85	−17.83
7684	1326.0	13.7	30.68	0.54	0.72	−15.95	−15.80	−17.69	−17.56
7882	7180.0	95.7	34.91	2.96	3.84	−20.07	−19.12	−21.47	−20.58
8091	1326.0	1.1	25.21	0.08	0.11	−10.68	−9.78	−11.57	−11.00
8201^2	187.9	2.5	26.99	0.45	...	−15.12	−14.45	...	...
8683	558.0	7.4	29.36	0.42	1.11	−14.53	−14.02	−15.83	−15.41
8760	260.3	3.5	27.70	0.26	0.35	−14.02	−13.46	−14.60	−14.09
8833	350.4	4.7	28.35	0.23	0.40	−13.57	−13.13	−14.49	−14.15
9128	173.6	1.7	26.15	0.10	0.10	−11.86	−11.28	−12.35	−11.71
9391	2653.6	35.4	32.74	2.40	2.89	−18.42	−18.18	−19.58	−19.41
10031	1351.4	18.0	31.28	1.05	1.87	−15.42	−14.91	−16.50	−17.69
10058	2478.9	33.1	32.60	1.75	3.23	−17.22	−16.72	−18.06	−19.23
10290	2397.7	31.0	32.52	2.46	5.96	−18.94	−18.11	−20.46	−21.46
10376	3706.9	49.4	33.47	2.43	2.00	−17.63	−17.12	−18.32	−19.65
10669	952.6	12.7	30.52	0.75	0.79	−14.77	−14.57	−15.21	−16.53
11764	3603.4	48.0	33.41	2.80	...	−17.75	−17.38	...	...
12082^2	1091.2	14.5	30.81	1.97	2.20	−17.03	−16.56	−18.16	−17.60
12151	1798.6	24.0	31.90	2.67	...	−18.02	−17.68	...	...
12894	595.5	7.9	29.50	3.38	2.31	−17.29	−17.26	−17.00	−16.93

Table 8 contains the $R-$band disk and magnitude information which can not be found in the three previous tables.

Table 8: $R-$**band Photometric Results**

Galaxy	μ_R^0 $(\frac{mag}{arcsec^2})$	α_R $('')$	R_∞ (mag)	$\mu_R^{(0,c)}$ $(\frac{mag}{arcsec^2})$	$R_{25}/R_{26.5}$ (mag)	R_T^0	R_T^{0-} (mag)	α_R (kpc)	M_R^T	M_R^{T-} (mag)
10031	22.82	11.4	15.85	23.23	15.42/15.25	15.19	15.75	0.99	-16.09	-15.53
10058	22.09	7.9	15.65	22.19	15.16/15.04	15.02	15.60	1.27	-17.58	-17.00
10290	22.20	18.2	13.93	22.31	$\ldots/\ldots$	13.01	13.78	2.73	-19.51	-18.74
10376	21.96	6.9	15.94	22.20	15.44/15.37	15.32	15.86	1.66	-18.15	-17.61
10669	22.12	8.0	15.83	22.45	15.73/15.58	15.51	15.75	0.49	-15.01	-14.77
11764	19.63	5.0	14.11	19.65	15.21/15.14	15.11	15.59	1.18	-18.30	-17.82
12151	22.00	15.7	14.29	22.38	13.64/13.56	13.52	13.91	1.82	-18.38	-17.99

3.3 HI Linewidth Corrections

The galaxies in this sample have been chosen to lie in the turbulence dominated regime, and are therefore distinct from previous Tully–Fisher samples. As a first attempt to correct for turbulence, and in order to be consistent with previous work, however, we calculate a turbulence corrected HI linewidth, following Tully & Fouqué (1985). This formulation yields a smooth transition between the case of *linear* summation of the rotational and dispersional motions found for giant galaxies and *quadratic* summation of the terms, which is observed to apply for dwarf galaxies (Tully *et al.*, 1978):

$$W_r^2 = W_{20}^2 + W_{turb}^2 - 2W_{20}W_{turb}\left[1 - e^{-(W_{20}/W_{crit})^2}\right] - 2W_{turb}^2 e^{-(W_{20}/W_{crit})^2}. \quad (3.17)$$

Here W_{20} is the observed line width at 20% of maximum (Δv_{20} in Table 1), W_{turb} is a turbulent width which is equal to $2k\sigma_z$, which is equal to 38 km s^{-1}, with $k = 1.89$ (the factor which yields the 20% width of a Gaussian profile) and with

$\sigma_z = 10$ km s^{-1}, based on observations of face–on spirals (*e.g.,* van der Kruit & Shostak, 1982). This value for the magnitude of the turbulent component agrees with aperture synthesis observations of dwarf galaxies (Tully *et al.,* 1978; Lo *et al.* 1993). W_{crit} defines the transition region between Gaussian profiles and double–horned profiles, and is taken to be 120 km s^{-1}. The rotational line width, W_r must still be corrected for inclination, therefore

$$W_r^i(\text{TFq}) = W_r/\sin i, \tag{3.18}$$

where we indicate that we have adopted the corrections of Tully & Fouqué by the designation (TFq).

When W_{20} becomes smaller than W_{turb}, $W_{Rot} = 0$. This is simply the point where rotation becomes unimportant and the observed linewidth becomes dominated by turbulence (the exact transition point is of course defined by the choice of W_{turb}). Tully & Fouqué therefore define a dynamical line width:

$$W_D^{i2} = W_r^{i2}(\text{TFq}) + 4\sigma^2, \tag{3.19}$$

where the 4 σ^2 term is a pressure term. In this way, in the case of spherical symmetry and uniform density, the mass interior to R is $W_D^{i2} R/4G$ in the case of either pure circular motion or pure random motion. Here we adopt $\sigma = 17$ km s^{-1}, by assuming $\sigma_x = \sigma_y = \sigma_z = 10$ km s^{-1} (de Vaucouleurs, de Vaucouleurs & Buta 1983). This dynamical linewidth should serve as a better indicator of the total mass of the galaxy and should therefore be better suited for use in the Tully–Fisher relation.

We will find these rather simple corrections for turbulence to be inadequate for the interpretation of our data in the next chapter. The linewidth correction which we finally adopt is further modified, to model more realistically in individual dwarf galaxies the ratio of turbulent to rotational motion.

Chapter 4

Tully–Fisher Relation for Dwarfs with Narrow HI linewidths

4.1 Tully–Fisher Relation for Normal Galaxies

4.1.1 Historical Background and Theoretical Basis

The observed relationship between the 21 cm HI linewidth and the absolute magnitude of a galaxy, known as the Tully Fisher or luminosity linewidth relation, is one of the most widely used distance indicators for galaxies (see Jacoby *et al.* 1992, for a recent review). The relative ease of measuring global HI profiles and obtaining total magnitudes of gas–rich spiral galaxies make this a particularly straightforward distance indicator. This can be seen when the method is contrasted with the primary distance indicator for ellipticals, the Fundamental Plane relationship (Dressler *et al.*

1987) between velocity dispersion, effective surface brightness and effective radius which arose as an extension of the Faber–Jackson (1976) relation.

As far back as the early 1960's (Dieter 1962; Roberts 1962a, 1962b), it was realized that the relationship between the total mass and the III properties (III flux, HI mass fraction, angular size, and HI linewidth) of a galaxy could be used to obtain the distance. Brosche (1971) pointed out a Hubble type dependence on the mean observed V_{max}, while Rogstad & Shostak (1972) noted a tight correlation between V_{max} and the optical radius for a sample of Scd galaxies, and suggested that the global properties of galaxies could be completely described by the Hubble type and V_{max}, but did not propose this as a method of obtaining the distance.

Balkowski *et al.* (1974) were the first to clearly state that "within a given morphological type, W_t [the linewidth corrected for inclination] is correlated to the luminosity". They also noted an extension to dwarf galaxies of the diameter–luminosity relation found for spiral galaxies by Heidmann (1969).

It was not until the work of Tully & Fisher (1977); however, that the usefulness of the HI linewidth as a distance indicator was fully realized. They pointed out the extreme importance of having calibrators with well determined distances to reduce the scatter in order to make the relationship useful (or indeed even recognizable, in the first instance) as a distance indicator. They found a relationship of the form:

$$L \propto \Delta V_0^{2.5\pm0.3}, \tag{4.1}$$

which corresponds to

$$M_{pg} \propto -a \log \Delta V_0 - b . \tag{4.2}$$

Tully & Fisher give a simple physical argument to justify this relation; namely, the

total mass of the galaxy (from the virial theorem) is given by

$$M_T \propto R\Delta V_0^2 \tag{4.3}$$

and if the M/L ratio is assumed to be constant and the empirical relation of $L \propto R^{2.8}$ from Heidmann (1969) for Virgo cluster spirals is adopted, then

$$L \propto \Delta V_0^{3.1}. \tag{4.4}$$

The work of Tully & Fisher was done using photographic magnitudes, corrected for galactic extinction and inclination of the galaxy; and HI line widths, also corrected for inclination (but in the opposite sense: magnitudes are corrected to "face–on", while inclinations are corrected to "edge–on"). This method was immediately seized upon by Sandage & Tammann (1976) as way to test other methods of distance determination.

The first major improvement in this technique came about with the use of infrared $H-$band magnitudes (instead of photographic or photoelectric visual magnitudes) by Aaronson, Huchra & Mould (1979), who found a tighter relationship (further improved in Aaronson et $al.$ 1982). This improvement was possible because the (uncertain) correction for extinction is much smaller in the infrared (Aaronson et $al.$ apply no correction), and the luminosity is dominated by late–type giants in the infrared. This presumably would make the assumption of $M/L =$ constant valid for all galaxies, regardless of type. The dispersion in the $H-$band relation is ~ 0.25 mag (Pierce & Tully 1988).

Despite the hope of Tully & Fisher (1977) that there should be "modest, if any, type dependence" in the relation, Roberts (1978) found a strong type dependence for the linewidth at a constant absolute magnitude. This result was systematically confirmed by Rubin et $al.$ (1985) in both B and H. This type dependence manifests

itself as a zeropoint shift in the TF relation for different types. This would cause a smaller value for the slope to be measured, because of the type dependence of ΔV. Rubin *et al.* found a slope for the TF relation of -10 for each type (Sa, Sb, Sc) considered separately.

Aaronson *et al.* (1979) outlined the physical basis upon which one would expect a slope of -10 for the TF relation (although they found a slope of ~ -9.5 in the $H-$band, a discrepancy which is attributed by Rubin *et al.* to the dependence on type). This slope implies

$$L \propto V_{max}^4 \tag{4.5}$$

which is also found to hold for ellipticals through the Faber Jackson relation when V_{max} is replaced with the velocity dispersion σ (Faber & Jackson 1976). Aaronson *et al.* state that such a power law will naturally arise, from the virial theorem if three conditions are true: "(a) all galaxies have the same mass profiles and rotation curves as a function of some dimensionless scale length, (b) all galaxies have the same central mass surface density, and (c) all galaxies have the same mean M/L."

Conditions (b) and (c) imply constant central surface brightness μ_0 (Burstein 1982), which is not observed over a wide range in galaxies (Binggeli 1994, Ferguson & Binggeli 1994). This is in marked contrast to the earlier work of Freeman (1970), who found a constant μ_0 for spiral galaxies (but see Bosma & Freeman 1993). However, a requirement of constant surface brightness averaged over the disk can also be seen to imply the power law result. If surface brightness is constant ($L \propto R^2$) then the virial theorem becomes:

$$M_{vir} \propto L^{0.5} V_{max}^2 \tag{4.6}$$

which yields the $L \propto V_{max}^4$ power law result if M/L is constant.

It is interesting to note that if $M/L \propto L^\gamma$ and is not constant, then the relation becomes:

$$L \propto V^{4/(2\gamma+1)}_{max}. \qquad (4.7)$$

In addition, if $L \propto R^{(2+\epsilon)}$ so that neither surface brightness nor the mass to light ratio are constant, then

$$L \propto V_{max}^{\frac{4+\epsilon}{2\gamma+\epsilon\gamma+\epsilon+1}}. \qquad (4.8)$$

The slope for this modified TF relation would then be $(-\frac{10+5\epsilon}{2\gamma+\gamma\epsilon+\epsilon+1})$, as opposed to -10.

4.1.2   Nonlinearity of the Tully–Fisher relation

We have already noted the effect that the dependence of M/L on Hubble type has on the zeropoint of the TF relation, which is actually observed as a shallower slope when the sample is not sorted by type. More recently authors have noted that the relation appears to exhibit curvature, in the sense that galaxies at both extremes in luminosity appear to be underluminous at a given linewidth, when compared to the linear TF relation (Aaronson *et al.* 1982; Aaronson *et al.* 1986). The departure at the faint end was attributed at least in part to nonrotational (or turbulent) motion broadening the HI linewidth (Hoffman, Helou, & Salpeter 1988). However applying a simple turbulent width correction as given by Bottinelli *et al.* (1983) or Tully & Fouqué (1985) does not entirely remove this deviation. For the brightest spirals, a relationship of decreasing metallicity with luminosity (Bothun *et al.* 1984) would cause these objects to appear underluminous for a given mass.

The possibility that observational sources of error have given rise to this nonlinearity has been investigated in depth (Aaronson & Mould 1986; Bothun & Mould

1987; Pierce 1988; Kraan–Korteweg, Cameron, & Tammann 1988; Burstein & Ray-chaudhury 1989), and while there is still a lively debate over the impact of Malmquist bias on samples used to determine the Hubble Constant (Pierce & Tully 1992; Sandage 1994a & 1994b and references therein), this seems unlikely.

Theoretical interpretations of the nonlinearity have pointed to dependence on the environment (and therefore the formation) of the galaxies (Djorgovski, de Carvalho, & Han 1988), as well as a luminosity dependence of the dark matter content of disk galaxies (Persic & Salucci 1988, 1990; Mould, Han, & Bothun 1989; Pierce 1991). The use of the TF relation to measure the dark matter content of galaxies is potentially one of the most powerful applications of this relation, aside from its primary utility as a distance indicator.

4.2   Motivation for this Work

Why should we examine the Tully–Fisher relation in dwarf galaxies? There are three main reasons, in light of the preceding discussion of the TF relation, for examining it in detail for dwarf galaxies.

First, is the curvature at the faint end real, and can it be attributed entirely to turbulence? If so, is there a way to still use a modified line width as an indicator of the mass? That is, is there a correction of the form used by Bottinelli *et al.* (1983) or Tully & Fouqué (1985), which will allow the raw HI linewidth to be converted to a parameter which measures the mass, even in dwarf galaxies?

Second, we wish to determine the usefulness of the TF relation as a distance indi-cator for dwarfs. If the curvature can be removed, what is the remaining dispersion

at the faint end? If it is small enough, the TF relation applied to dwarfs would be useful for determining the distances to nearby clusters because of the overwhelming numbers of dwarfs. Measurements of the III linewidths already exist for a large number of dwarf galaxies (Fisher & Tully 1981; Schneider *et al.* 1990, 1992), which can be potentially useful for mapping bulk flow velocities. The Hubble type dependence for the TF relation among spirals (Rubin *et al.* 1985) limits the number of galaxies in a cluster which can be used to obtain a distance.

Finally, what can be determined about the dark matter content of dwarfs using the TF relation (Pierce 1991)? Is there an indication of increased dark matter content in dwarfs as compared to more luminous galaxies? If so, this would be a clue to possibly different formative processes for dwarf and normal galaxies.

In order to address these questions, we must first select a sample of galaxies which are appropriate for an investigation of the TF relation.

4.3 Tully–Fisher Relation for the Sample

4.3.1 The Basic Relation

As a first attempt at examining the relationship, we will simply plot the linewidth versus the absolute magnitude for all of the galaxies for which we have photometric data. We will exclude the galaxies observed under non–photometric conditions, and those which were too large to fit entirely on the CCD chip. Also excluded are UGC 7636, since the HI detected has been stripped from the dwarf (Patterson & Thuan 1992; McNamara *et al.* 1994), and therefore the linewidth will not be indicative

of the mass. Finally, we exclude Karachentseva 37 and 37C (IC342dw6), since the detected III profile is expected to be the sum of the contribution from each of the galaxies, and not to either one alone.

In Figure 81(a), the linewidth, W_{20}, without any corrections for inclination or turbulence is used; while in Figure 81(b), W_r^i(TFq), the linewidth corrected as described in Chapter 3 (equation 3.18) following the method of Tully & Fouqué (1985), is plotted.

The LSB galaxies from our sample are plotted as filled squares, while the data for the "narrow–lined dwarf" sample are plotted as filled triangles. Galaxies from the May85 observing run, marked with an r in Table 1 (Chapter 1), are assigned to the LSB category if they have large linewidths (UGC 10058, 10290 and 12151), and into the narrow–lined dwarf category if they have narrow line widths and a small redshift (UGC 10031 and 10669). The two intermediate cases, UGC 10376 and 11764 (intermediate because while they have fairly narrow linewidths, $\Delta V_{20} = 69$ and 107 km s^{-1} respectively, they are at $v_0 > 3000$ km s^{-1}) are marked by open circles.

The Pierce & Tully (1992) spiral galaxies are plotted as open squares. In Figure 81(b) the TF relation from Pierce & Tully (1992) (which included galaxies in the Local, Sculptor, and M81 groups using 6 local calibrator galaxies with independently determined distances) is shown as a solid line and the relation from Pierce & Tully (1988) (using Virgo and Ursa Major cluster galaxies and 3 local calibrator galaxies) as a dotted line for comparison, in order to show some of the observed range in the TF relation. The $I-$band relations are shown in Figures 82(a) and (b), with the data from the same sources and plotted with the same symbols.
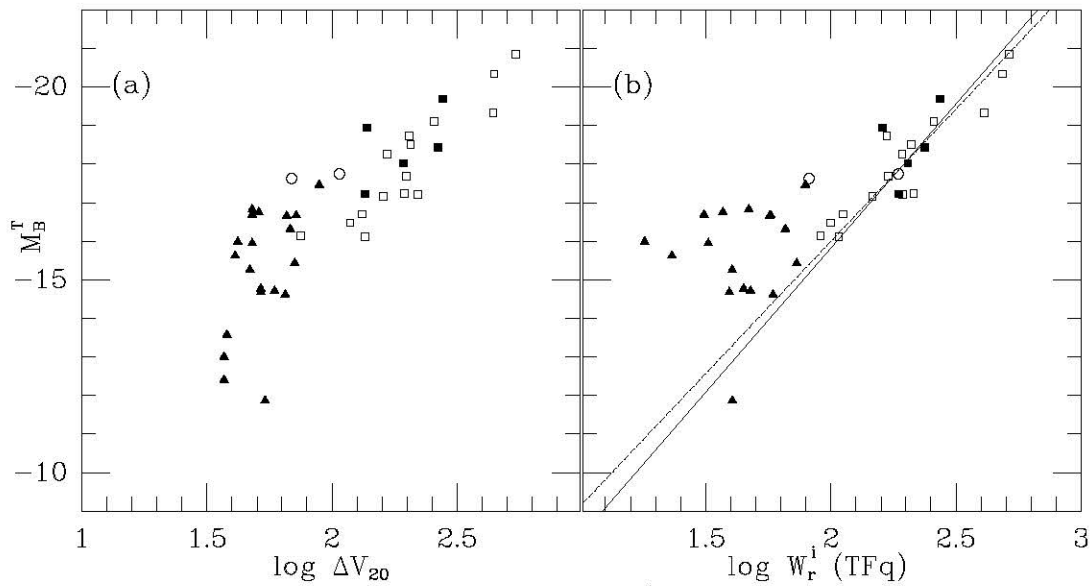
Figure 81: $B-$band Tully–Fisher Relation. (a) is a plot of the observed linewidth versus the absolute magnitude, while (b) shows the corrected line width (equation 3.18). The open squares are the galaxies from Pierce & Tully (1992), the filled squares are the LSB galaxies from this work, the filled triangles are the narrow–lined dwarfs from this sample, and the two open circles are intermediate cases. The solid line in (b) is the empirical Tully–Fisher relation from Pierce & Tully (1992) and the dashed line is from Pierce & Tully (1988). The 3 galaxies plotted at the extreme lower left in (a) have a raw linewidth of less than 38 km s^{-1} and therefore a corrected linewidth of 0. They are not plotted in (b).
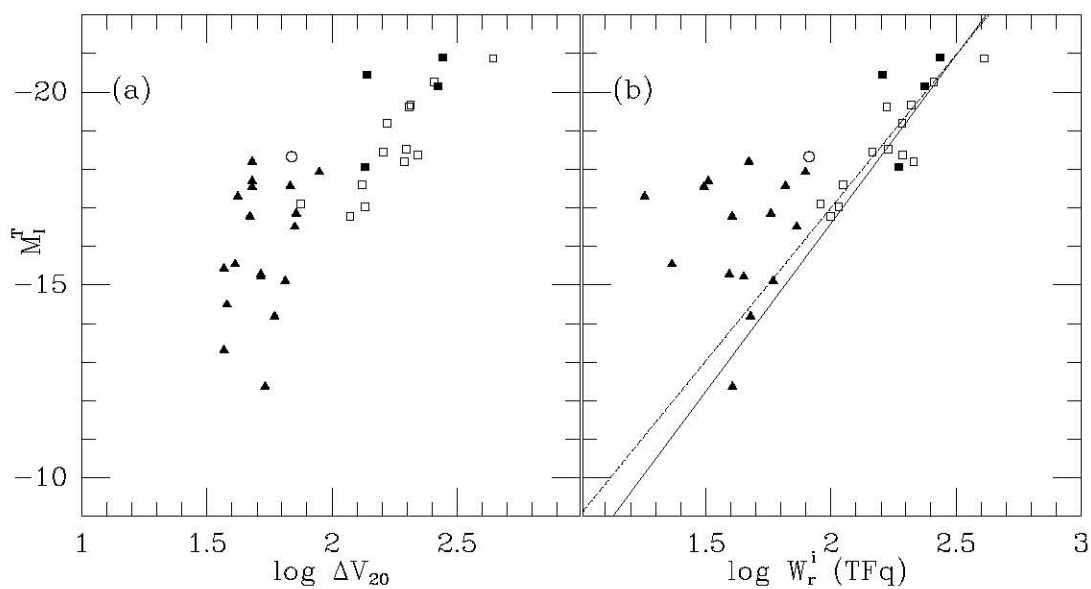
Figure 82: $I-$band Tully–Fisher Relation. Same as Figure 81 for the I data.

It is clear that the LSB galaxies from the sample fit the TF relation very well, while the narrow–linewidth dwarfs do not, either before or after correction for the inclination and turbulence. It appears possible that the dwarf linewidths have been "overcorrected", which is possible if either the inclination correction is too large or the simple correction applied for the turbulence is inappropriate.

It should be stressed that the turbulent correction could be wrong for *all* the galaxies; however, a slight error would be easily visible only in the narrow–lined dwarfs with $\log \Delta V_{20}$ close to 1.58 ($\log 38$ km s^{-1}). The abrupt falloff of the relation shown in Figure 81(a) very close to this value indicates that there is indeed a turbulent limit near 38 km s^{-1}), but does not indicate that the Tully–Fouqué correction is necessarily of the correct *form*.

4.3.2   Correlations with dispersion

In order to investigate possible causes of the dispersion in the TF relation at the faint end, we examined the correlation of the residual from the Pierce & Tully (1992) relation with various observables.

In Figure 83, the TF residual,

$$\text{TF res} = M_B^{T-} - 7.48 \log W_r^i(\text{TFq}) + 0.85, \tag{4.9}$$

is plotted against the derived inclination, the "HII ratio", the color, the measured Holmberg radius, the absolute magnitude, the HI mass, and the profile shape. If the deviation from the relation is due to observational error, one would expect the inclination to be the most likely source of this error, because the correction of the linewidth to edge–on depends critically on the inclination. No correlation is apparent
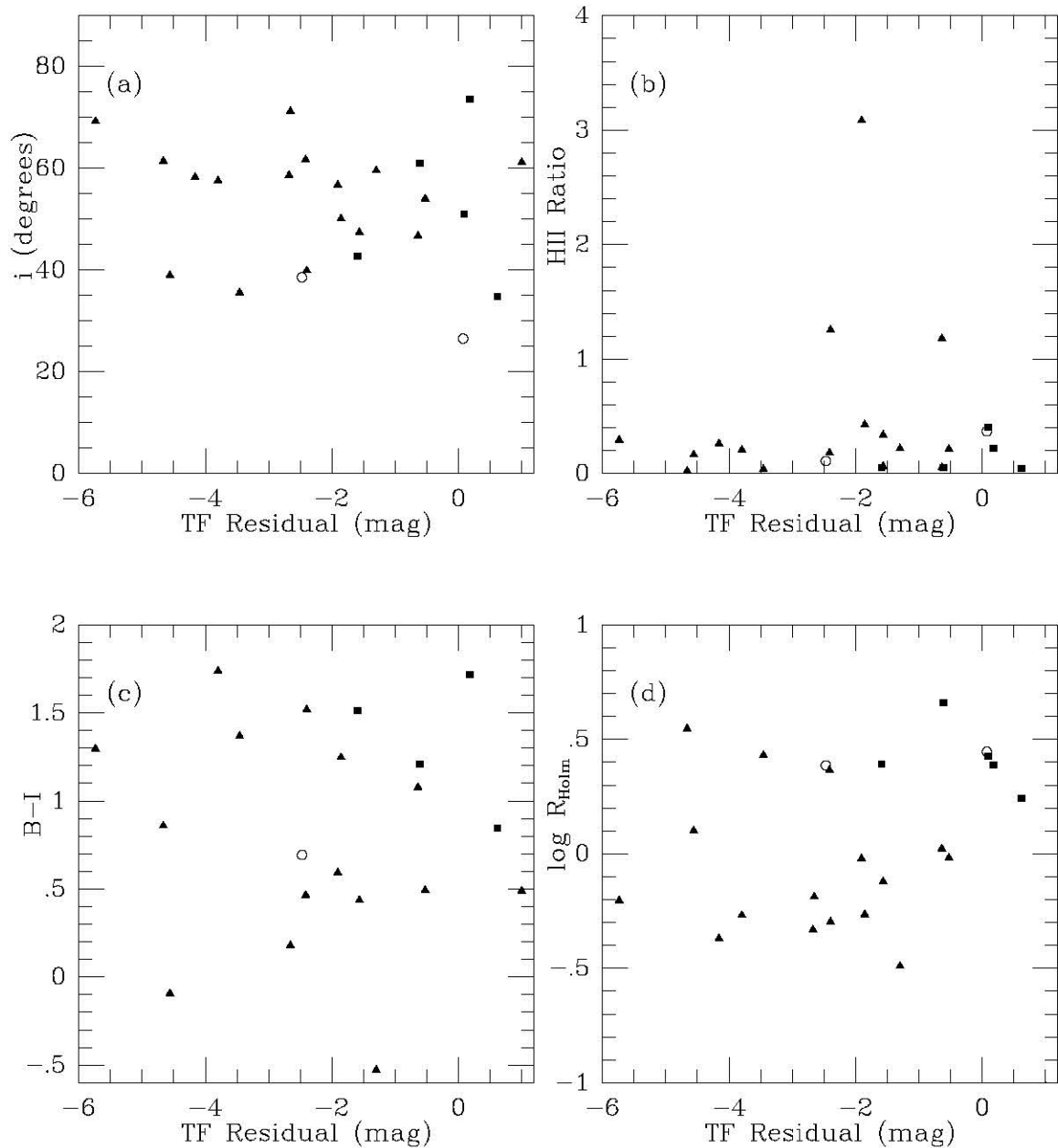
Figure 83: Plots of the Residual from the TF relation (equation 4.9) versus various observables. Symbols are the same as in Figure 81. (a) TF Residual versus inclination. A correlation would be expected if there was a systematic error in the inclination, which would effect the linewidth through equation (3.18). (b) Residual versus HII Ratio (see text). (c) Residual versus color and (d) Residual versus the optical (Holmberg) radius of the galaxy. No correlation is apparent with any of these parameters.
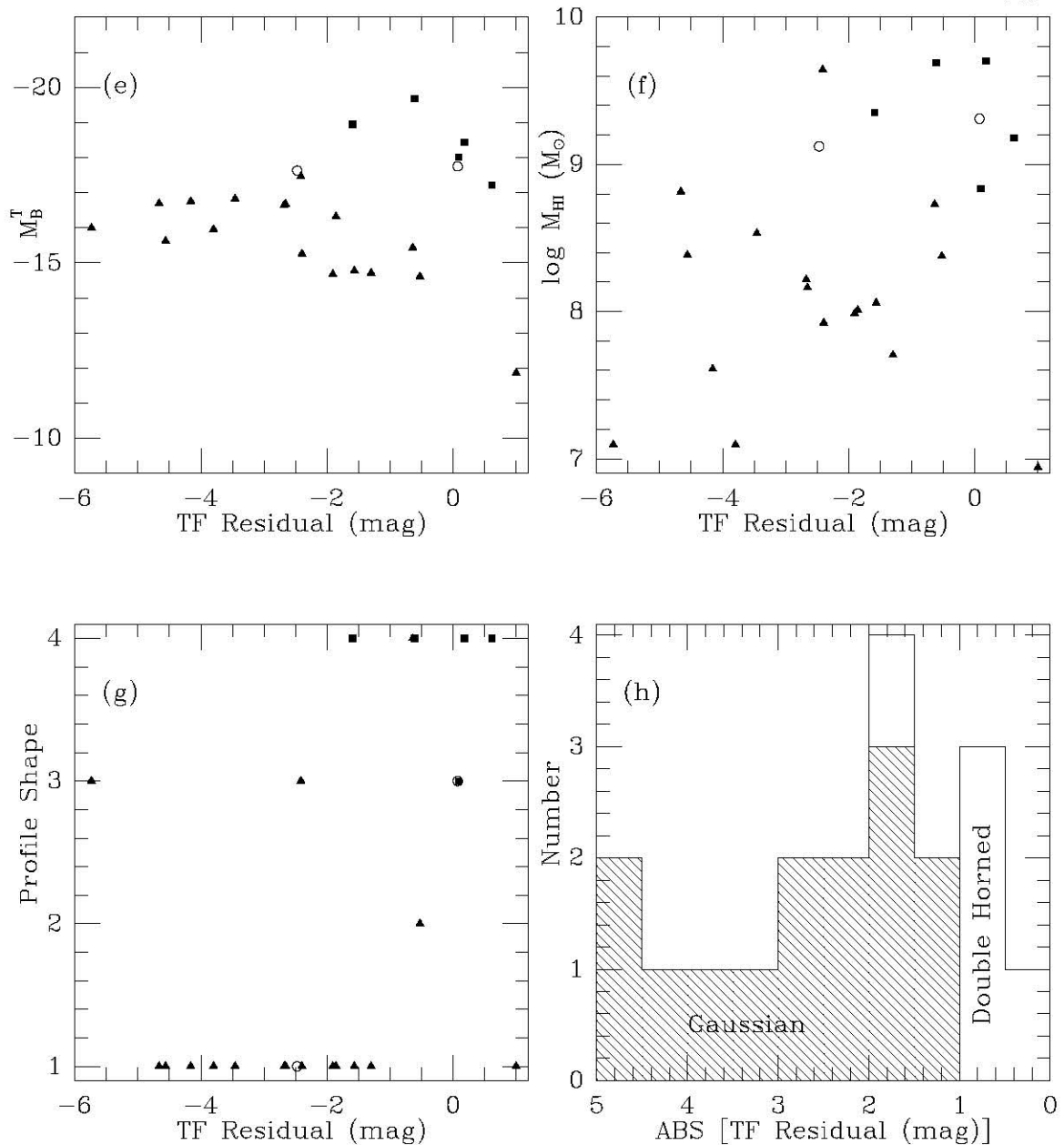
Figure 83: (cont) Plots of the Residual from the TF relation versus various observables. (e) Residual versus absolute magnitude: compare with Figure 81(b). (f) Residual versus HI mass; a weak correlation is present, indicating that the deviation from the TF relation is related to the HI, rather than optical, properties of the galaxy. (g) Residual versus HI Profile Shape. 1 indicates a definite Gaussian profile; 4 a definite Double Horned profile, while 2 and 3 indicate profiles which are intermediate or uncertain. A clear difference between the residual for 1 and 4 is present. (h) Histogram for the *absolute value* of the TF residual for Gaussian (hatched) and Double Horned Profiles.

(Figure 83(a)).

The "HII index" which is a measure of the area of the galaxy excluded from the total magnitude (because of HII regions or stars), normalized by the total area of the galaxy, might be expected to correlate with the residual if there is some systematic problem with the total magnitudes we are using which is caused by the exclusion of the HII regions and stars. It would also indicate a dependence of the TF residual on increased star formation in a galaxy, which would be expected if the star formation rate was high enough to disturb the global HI profile, through the effects of supernovae (Westpfahl & Puche 1994). The $B - I$ color might be expected to correlate for a similar reason. In neither case does a correlation appear to be present (Figure 83(b),(c)).

The Holmberg radius is plotted versus the residual in Figure 83(d). The absolute magnitude is plotted in Figure 83(e). As can also be seen in Figure 83(b), the effect is not linear with magnitude, though the dispersion does increase at lower luminosities. This is merely a consequence of the increased scatter at the faint end.

The trend with $\log M_{HI}$ which can be seen in Figure 83(f) indicates at least that the dispersion is related to the HI properties of the sample, and *not* to the optical properties (or any errors in the measurement of these properties).

Finally, the most dramatic relation is that between the TF residual and the HI profile shape (Figure 83(g)). The profiles have been classified in Table 1, as Gaussian (=1), probably Gaussian (=2), probably Double Horned (=3), and Double Horned (=4). If the uncertain classifications are excluded, the dichotomy of the two classes of profiles can be clearly seen (Figure 83(h)). Since the Gaussian profiles are expected when the motion is largely (but not exclusively) turbulent, while the Double Horned

(DH) profiles are found when rotation dominates, the linewidth is at the very least measuring the mass in a different way in the two cases.

This correlation, then, is what one would expect even in the absence of any observational errors. The fact that the galaxies with Gaussian profiles exhibit such large residuals even after they have been corrected for turbulent motion, confirms the suspicion that the Tully–Fouqué correction for turbulence is not adequate.

4.4 Modified Version of the Line Width

In place of the assumption that all galaxies have a turbulent component of 38 km s^{-1}, we follow Staveley–Smith *et al.* (1992), and assume that the ratio of rotation to dispersion, β, in a dwarf galaxy is given by the intrinsic axial ratio, q_0 (equation 3.5) in the following manner (Binney, 1978; Fall & Frenk 1983):

$$\beta = \left(\frac{V_{rot}}{\sigma}\right)^2 = \frac{(1 + 2q_o^2)\cos^{-1} q_0 - 3q_0(1 - q_0^2)^{1/2}}{q_0(1 - q_o^2)^{1/2} - q_0^2 \cos^{-1} q_0}, \tag{4.10}$$

which follows from the tensor virial theorem (Binney, 1978) and holds for an oblate ellipsoidal disk with a negligible contribution to the apparent axial ratio from a bulge component. Here V_{rot} is the maximum rotational velocity and σ is the velocity dispersion. We can then replace W_t in equation (3.17) with 3.5882σ (the factor of 3.5882 converts from σ to full width at 20% of the peak for a Gaussian) to obtain:

$$
\begin{aligned}
W_r^{i2}(\text{quad})\sin^2 i \; = \; & W_{20}^2 + (3.5882\sigma)^2 - \\
& 2W_{20}(3.5882\sigma)\left[1 - e^{-(W_{20}/120)^2}\right] - \\
& 2(3.5882\sigma)^2 e^{-(W_{20}/120)^2},
\end{aligned}
\tag{4.11}
$$

which is simply equation (3.17) with a factor of $\sin^2 i$ included to remove the effects of inclination, and $W_{crit} = 120$ km s^{-1}. Since $W_r^i = 2V_{rot}$ (even for dwarf galaxies; Tully *et al.* 1978), we find after substituting $\sigma = W_r^i(\text{quad})/(2\sqrt{\beta})$ that,

$$
\begin{aligned}
0 &= W_r^{i2}(\text{quad})\left[\sin^2 i + \left(\frac{3.5882}{2\sqrt{\beta}}\right)^2 (2e^{-(W_{20}/120)^2} - 1)\right] + \\
&\quad W_r^i(\text{quad})\left[\frac{3.5882 W_{20}}{\sqrt{\beta}}[1 - e^{-(W_{20}/120)^2}]\right] - W_{20}^2,
\end{aligned}
\tag{4.12}
$$

which is a simple quadratic in $W_r^i(\text{quad})$.

A further assumption is introduced when we consider that the corrected linewidth is correlated with the absolute magnitude presumably because the mass is correlated with the luminosity, and the linewidth is related to the mass through the virial theorem (see discussion in §4.1.1). The virial theorem in solar units is

$$
M_{vir}^{rot} = 2.33 \times 10^5 r_{vir} V_{rot}^2,
\tag{4.13}
$$

or

$$
M_{vir}^{rot} = 2.33 \times 10^5 r_{vir} \left(\frac{W_r^i(\text{TFq})}{2}\right)^2,
\tag{4.14}
$$

with r_{vir} the virial radius (usually taken to be the Holmberg radius for dwarfs and R_{25} for spirals) in kiloparsecs, and V_{rot} and $W_r^i(\text{TFq})$ are given in km/s. The *rot* indicates that this mass is calculated assuming rotation alone (except for the constant additive factor of 38 km s^{-1}).

However, if there is a significant contribution from random motions then this must be generalized to (Staveley–Smith *et al.* 1992):

$$
M_{vir}^{rot+turb} = 2.33 \times 10^5 r_{vir}(3\sigma^2 + V_{rot}^2)
\tag{4.15}
$$

or

$$
M_{vir}^{rot+turb} = 2.33 \times 10^5 r_{vir} \left(\frac{W_r^i(\text{quad})}{2}\right)^2 (1 + 3/\beta).
\tag{4.16}
$$

It would be equivalent to substitute

$$W_r^{i\,2}(\text{mod}) = W_r^{i\,2}(\text{quad})\,(1 + 3/\beta) \tag{4.17}$$

for $W_r^{i\,2}$ in the Tully Fisher relation (with $W_r^{i\,2}(\text{quad})$ obtained from solving the quadratic in equation (4.12)), if we still wish to plot the luminosity versus a "linewidth". We plot the modified linewidth versus the absolute magnitude in Figure 84, with the Pierce & Tully galaxies again represented by open squares. In this case we plot only the galaxies from our sample which are have profiles which are either clearly Gaussian (filled triangles) or clearly Double Horned (DH; filled squares).

The most striking feature of this plot is the dichotomy between the Gaussian and DH galaxies. The overall appearance of the relation is much closer to that for the raw linewidths (Figure 81(a)) than for the Tully–Fouqué modified line widths (Figure 81(b)). There is clearly a difference in the M/L dependence on L between the Gaussian and the DH galaxies. The transition occurs at $M_B^T \sim -16$.

At this point it might be more informative to plot the luminosity versus the virial mass (from equation 4.16) directly, instead of "hiding" the mass inside this modified linewidth, $W_r^i(\text{mod})$. This is shown in Figure 85(a) for the same points as in Figure 84.

4.5 Turbulence Alone?

Is it really necessary to include both turbulence and rotation in the formula for the linewidth in such narrow lined dwarfs? In this section we look at the effects of ignoring rotation entirely.
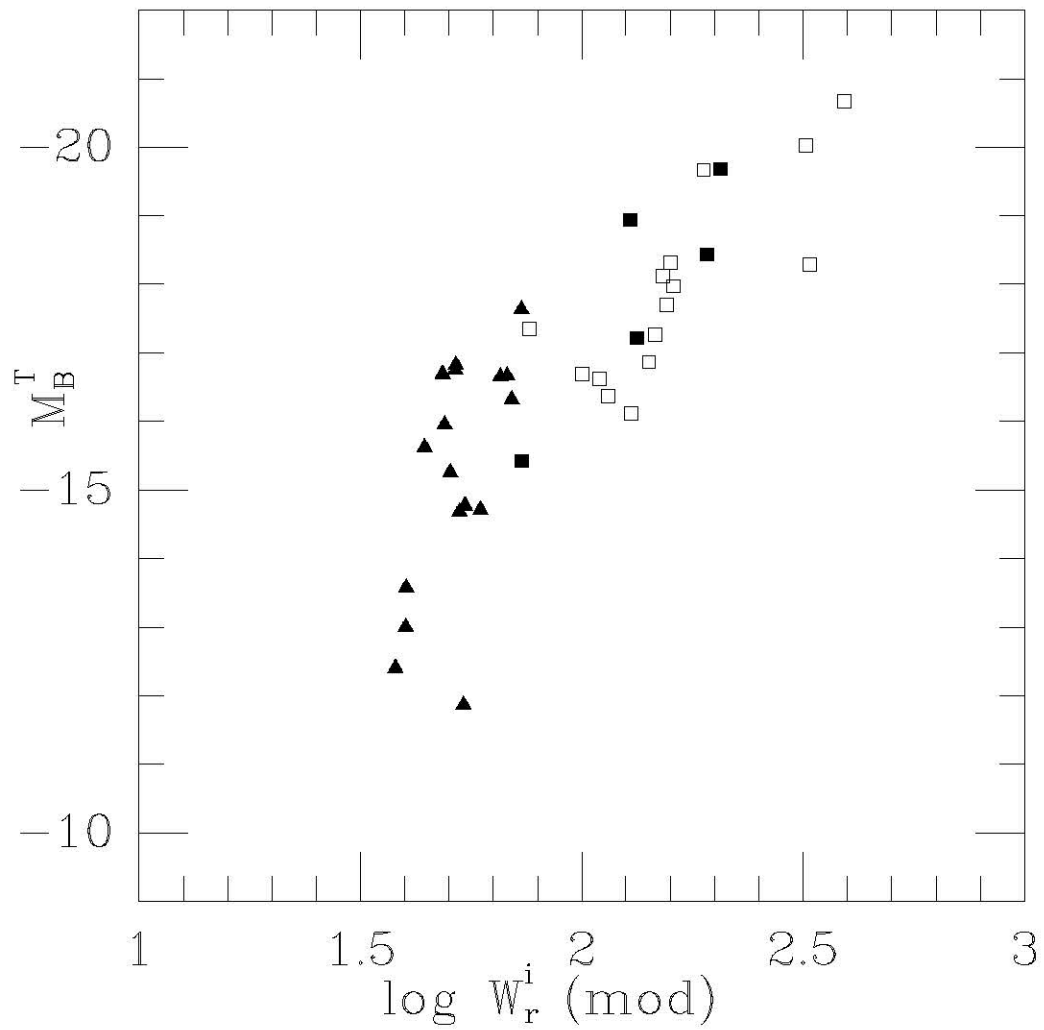
Figure 84: Modified Tully–Fisher Relation. Modified linewidth calculated from equation (4.17) (See text). Open squares are from Pierce & Tully (1992); Filled squares are galaxies from this sample that have Double Horned III profiles; Filled triangles are Gaussian profiled galaxies.
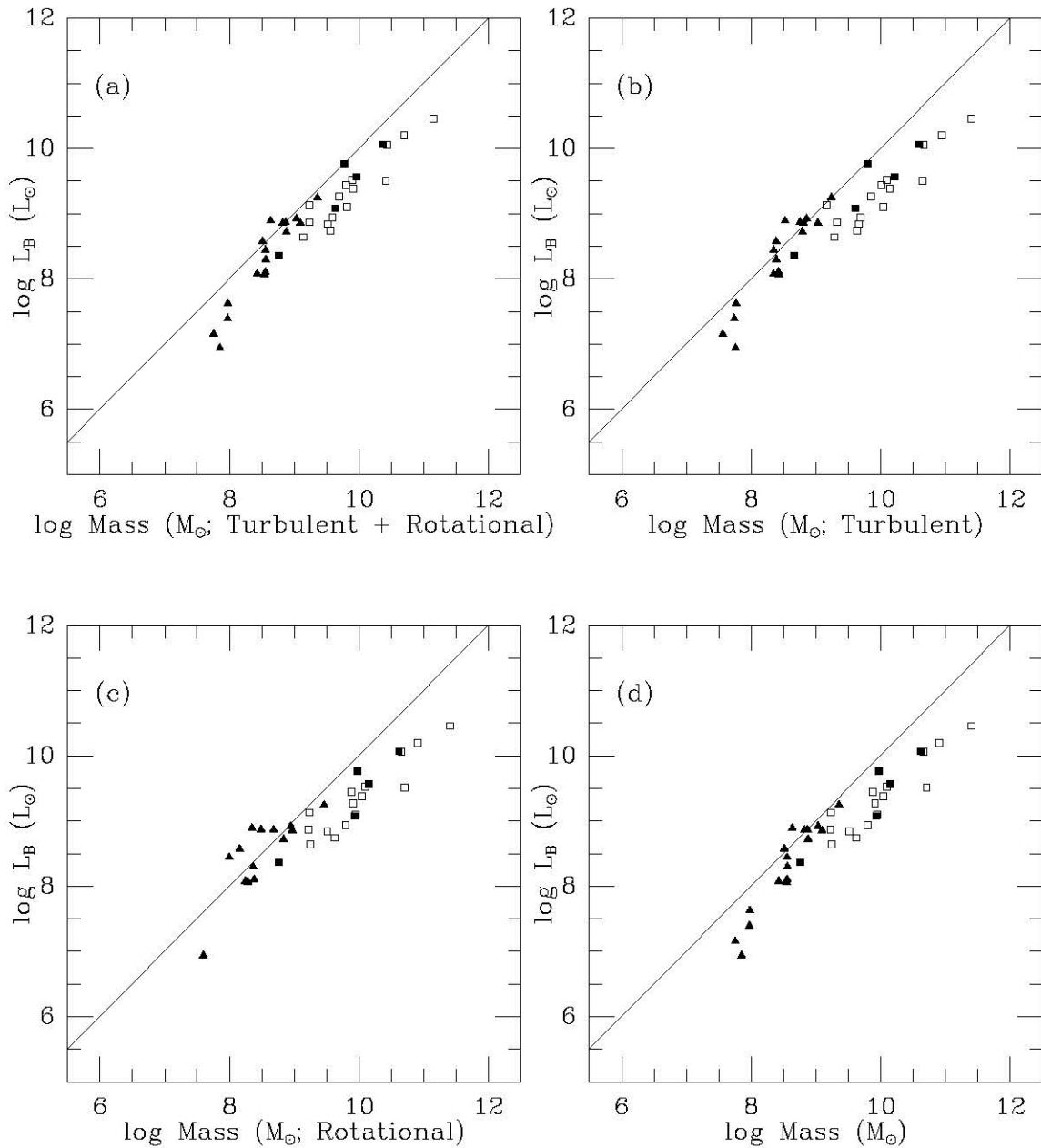
Figure 85: Virial Mass/Luminosity Diagrams. Symbols are as in Figure 84. (a) Mass calculated from equation 4.16 (See text). (b) Mass calculated from (4.18) assuming that the linewidth arises from turbulence alone. (c) Mass calculated from (4.14) assuming that the Tully–Fouqué formulation for the linewidth is correct (constant turbulence of 38 km s^{-1}). (d) Mass as in (a) for Gaussian profiled galaxies and as in (c) for Double Horned profiles. In each panel, the solid line represents $M/L = 1$.

If the Gaussian HI linewidth is assumed to be solely due to turbulent motions in the galaxy, then this width can be divided into two different components (Lo *et al.* 1993): dispersion *within* a cloud ($< \sigma_v >$), due to the temperature of the cloud; and dispersion *between* clouds (σ_{c-c}), due to random motions of individual clouds in the potential well of the galaxy. The *observed* single–dish velocity dispersion ($\sigma_T = W_{20}/(3.5882)$) is then just the quadratic sum of the two components.

VLA observations of nine dwarf galaxies by Lo *et al.* find a range for $< \sigma_v >$ (averaged over the entire galaxy) of between 4.0 to 8.5 km s^{-1}, with an average of 5.4 km s^{-1}. Adopting this value, and setting $V_{rot} = 0$ in equation (4.14), we have

$$M_{vir}^{turb} = 2.33 \times 10^5 r_{vir} 3 \left[(W_{20}/3.5882)^2 - (5.4)^2 \right]. \tag{4.18}$$

The virial mass from turbulence alone is plotted versus the luminosity in Figure 85(b) and, for comparison, in Figure 85(c) we plot the virial mass due to rotation alone (equation 4.14).

The linewidth for spiral galaxies, which are dominated by rotation (double horned), are described adequately by the Tully–Fouqué approximation. In fact, it is misleading to apply the modified linewidth developed in §4.4 to spirals, because the observed axial ratio for a spiral is not an indication of the intrinsic axial ratio, and hence the velocity anisotropy (Staveley–Smith *et al.* 1992); but rather is merely an indication of the inclination of a disk which is *assumed* to be intrinsically circular (Holmberg 1958; Bottinelli *et al.* 1983). Therefore, in Figure 85(d) we plot the $M_{vir}^{turb+rot}$ from equation (4.16) for the galaxies which exhibit Gaussian profiles (turbulence dominated) and the M_{vir}^{rot} from equation (4.13) for the DH (rotationally dominated) galaxies. Again, in this sample, it is clear that there is a difference in the M/L for the two classes of galaxies.

4.6   Is the Effect Real?

In order to see if the dichotomy between turbulent– and rotationally–supported galaxies is observed to occur for all galaxies in the manner we have seen above, we expanded the sample by including data from the literature. It is necessary for each additional galaxy to have an accurate: absolute magnitude (which requires an accurate distance); axial ratio (in order to calculate either the inclination or β, the velocity anisotropy); and III linewidth, as well as a III profile with high signal–to–noise in order to classify it as either Gaussian or Double Horned.

In Figure 86, we plot the virial mass versus the luminosity for galaxies from our own sample as well as additional points from the literature. As in Figure 85(d), the $M_{vir}^{turb+rot}$ from equation (4.16) is used for the galaxies which exhibit Gaussian profiles (turbulence–dominated) and the M_{vir}^{rot} from equation (4.13) for the DII (rotationally–dominated) galaxies. The additional points are from Staveley–Smith, Davies, & Kinman (1992), from their observations of dwarf and LSB galaxies; McGaugh (1992) (also McGaugh & Bothun 1994), from his observations of mostly LSB galaxies; Lo, Sargent, & Young (1993), from their VLA observations of extremely faint dwarf galaxies; Pierce & Tully (1992), the Tully–Fisher calibrator galaxies from the previous figures; Romanishin, Strom, & Strom (1983), from their sample of LSB spirals; Tully (1988) (NBG); from which we selected all galaxies with $M_B^T > -16$ for which there was an accurate ΔV_{20}; and Carignan, Demers, & Côté (1991), for data on the Phoenix dwarf galaxy, which appears to be an intermediate type between dwarf spheroidal and dwarf irregular (see also van de Rydt, Demers, & Kunkel 1991).

The solid line represents the relation $M/L = 1$, and any locus of constant mass to light ratio must be parallel to this line. The two dotted lines are *not* fits to the data.
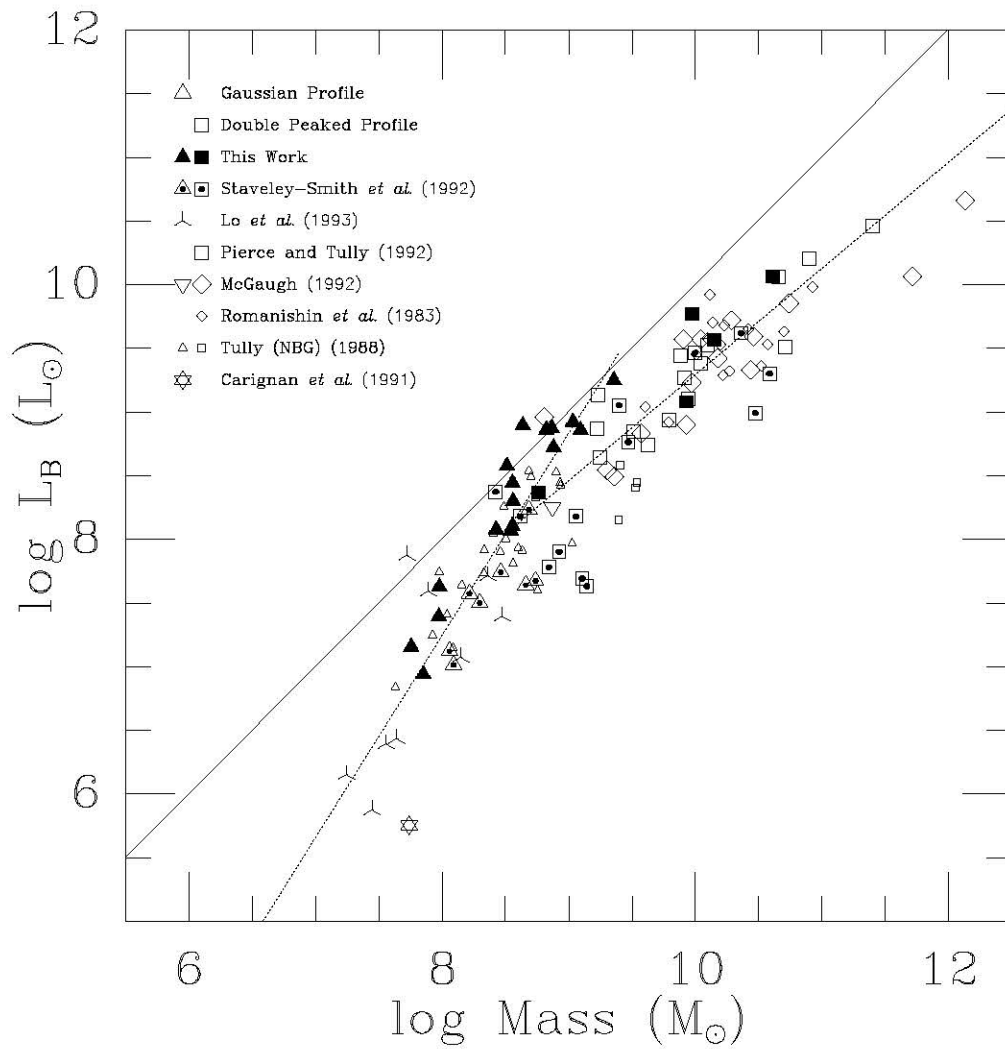
Figure 86: Virial Mass/Luminosity Diagram. Same as Figure 85(d) with additional points from the literature. The solid line is the line for $M/L = 1$. The two dotted lines are $M/L \propto L^{-0.37}$ (for the Gaussian profiles; see §4.8) and $M/L \propto L^{0.2}$ (for the rotating galaxies; see §4.9). They do *not* indicate fits to the data.

The dotted line through the Gaussian dwarfs is the relation $M/L \propto L^{-0.37}$, with the zeropoint adjusted to fit the data. This relation arises from the theoretical model of Dekel & Silk (1986) for supernovae driven mass–loss in dwarf galaxies embedded in a massive dark halo (see also Blumenthal *et al.* 1984). In this scenario, the supernovae drive most of the ISM out of the galaxy, which remains bound, due to the dark halo. This model was advanced for the formation of dwarf spheroidals, but Dekel & Silk speculate that incomplete mass loss may result in the formation of a dwarf irregular. This relation, which is seen to represent a good fit to the data, will be discussed further in §4.8.

The dotted line through the "normal" galaxies is the relation $M/L \propto L^{0.2}$, which is implied by the Fundamental Plane relations between velocity dispersion, surface brightness, and effective radius for elliptical galaxies (Dressler *et al.* 1987; Ferguson & Binggeli 1994). The relation also appears to represent a good fit to the spiral data, and is briefly discussed in §4.9. The transition occurs at $\log L_B/L_\odot \sim 8.3$ or $\log M/M_\odot \sim 8.6$, which is discussed in §4.8.1.

In Figure 87 the Gaussian dwarfs are plotted alone. A formal least–squares fit to the points yields a relation of $M/L \propto L^{-0.30\pm0.16}$ (shown as the dashed line) with a dispersion about the fit of 0.94 mag. Similarly, in Figure 88 we have plotted only the DII galaxies. A least–squares fit yields $M/L \propto L^{0.25\pm0.37}$ (the dashed line) with a dispersion of 0.83 magnitudes.

The actual relation indicated by the dotted line in Figure 87 is given by $\log L_B = 1.435 \log M - 4.23$ in solar units. The luminosity of these Gaussian dwarfs can therefore be calculated from the mass from equation (4.16), which depends on the observed line width and the axial ratio. The results of the fits for the data in all the
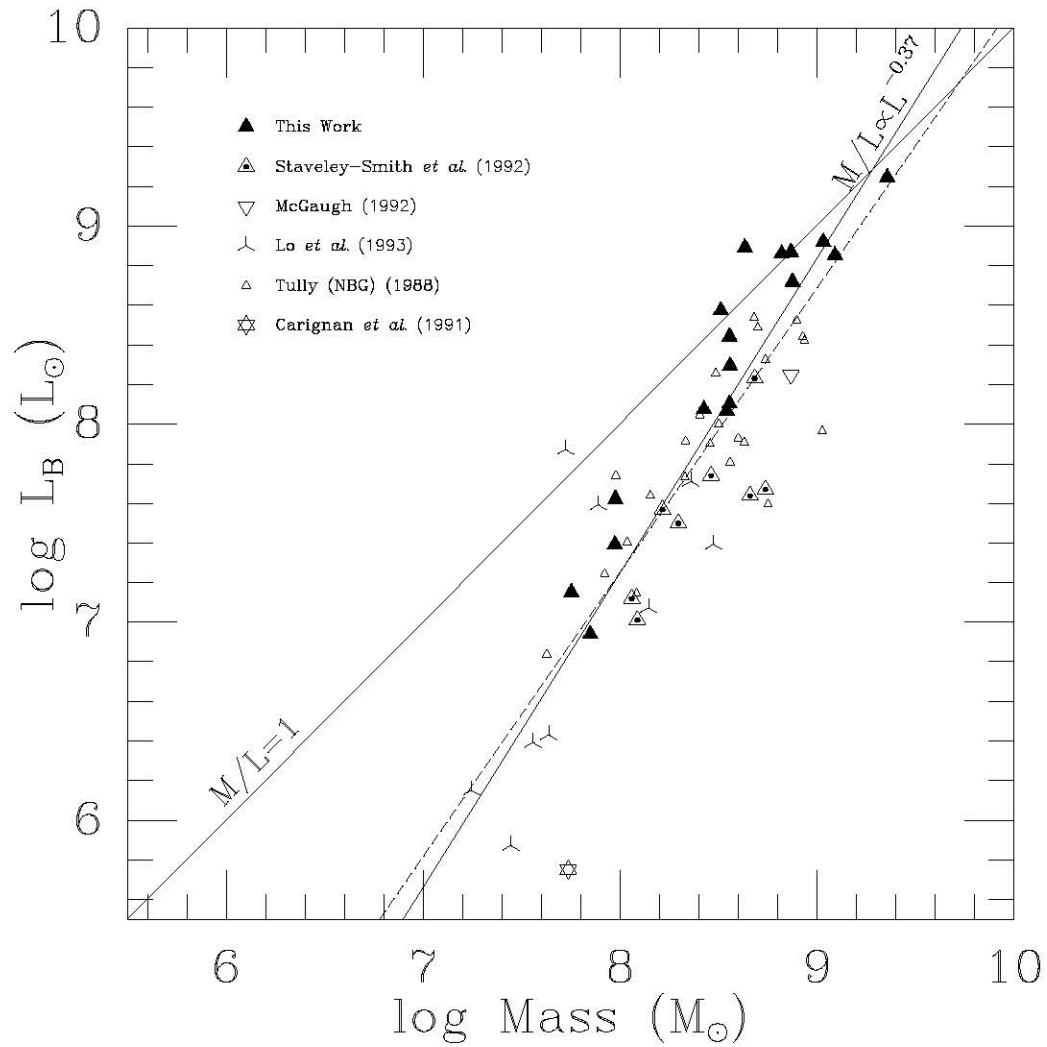
Figure 87: Virial Mass/Luminosity Diagram for Gaussian Profile Galaxies. The solid lines represent the relations $M/L = 1$ and $M/L \propto L^{-0.37}$ (Dekel & Silk 1986; see §4.8). The dashed line is the least–squares fit to the data.
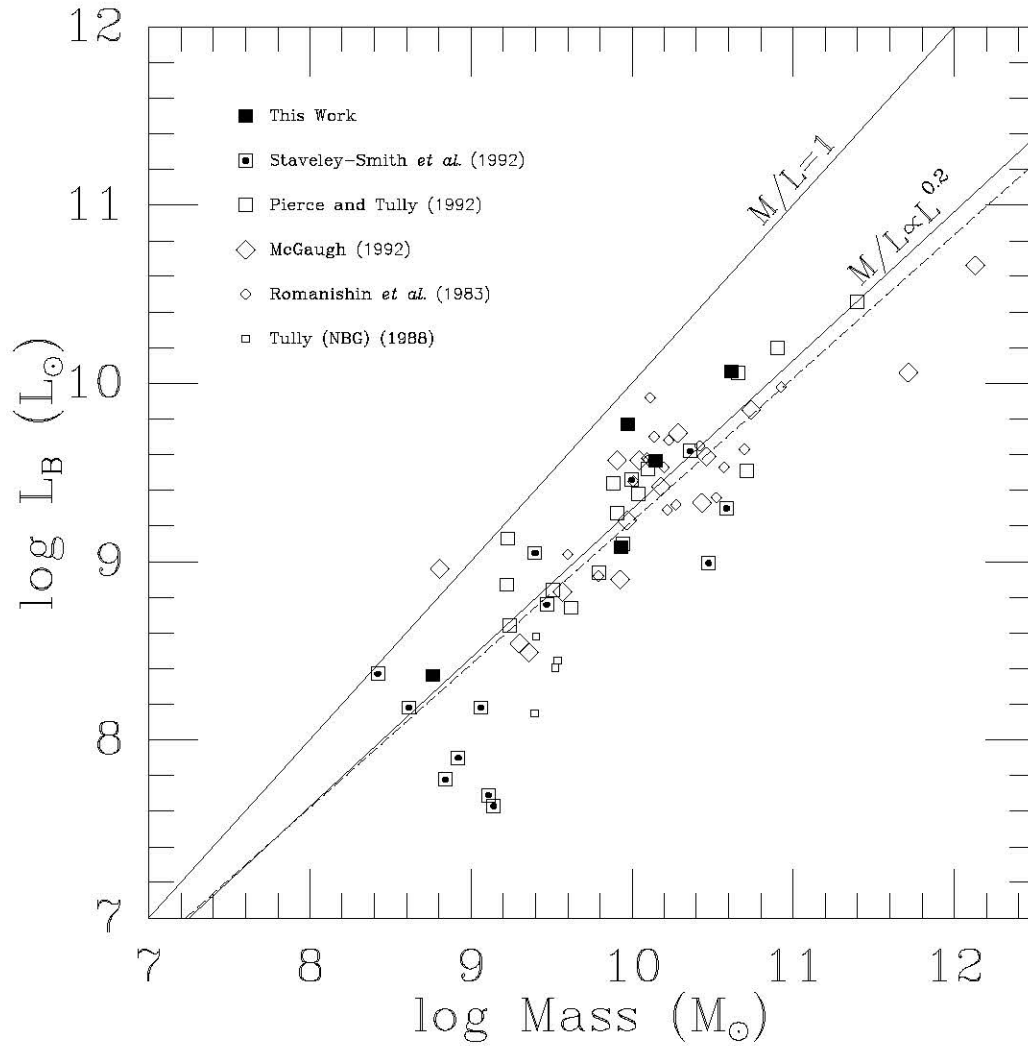
Figure 88: Virial Mass/Luminosity Diagram for DII Sample. The solid lines represent the relations $M/L = 1$ and $M/L \propto L^{0.2}$. The dashed line is the least-squares fit to the data.

figures are listed in Table 9 (§4.6.1).

In Figure 89, we replot the points from Figure 88, after removing the extreme low surface brightness galaxies from the sample (the data of McGaugh 1992; and Staveley–Smith *et al.* 1992). What remains are normal spirals (from Pierce & Tully 1992; Romanishin *et al.* 1982; and from this sample), usually used to define the Tully–Fisher relation in the first place. Also shown are the LSB spirals from Romanishin, Strom, & Strom (1982); these are not galaxies of extremely low surface brightness in contrast to the McGaugh sample. The correlation is much improved, and the relation for elliptical galaxies discussed in §4.9, from Dressler *et al.* (1987) is a good fit to the data. The formal least squares fit leads to a relation of $M/L \propto L^{0.35 \pm 0.49}$ (the dashed line) with a dispersion of 0.57 magnitudes. For comparison, the internal rms dispersion for the blue Tully–Fisher relations is on the order of 0.35 mag (Jacoby *et al.* 1992), the larger dispersion can be attributed to the fact that a sample specifically selected for use in determination of the Tully-Fisher relation has strict criteria for inclination, and the distance is determined independently (and is not simply determined using a redshift with virgocentric correction)

The inclusion of the LSB galaxies would be expected to worsen the fit (as is seen in Figure 88), since the M/L for these giant disk galaxies, with a very different history of star formation, must be different from that for normal spirals.

4.6.1 The relation for the $I-$band

Although the number of suitable galaxies for which $I-$band data is available is small when compared to the data available in the $B-$band, it is desirable to at least check the relation in the longest wavelength available. If the effects seen in B are
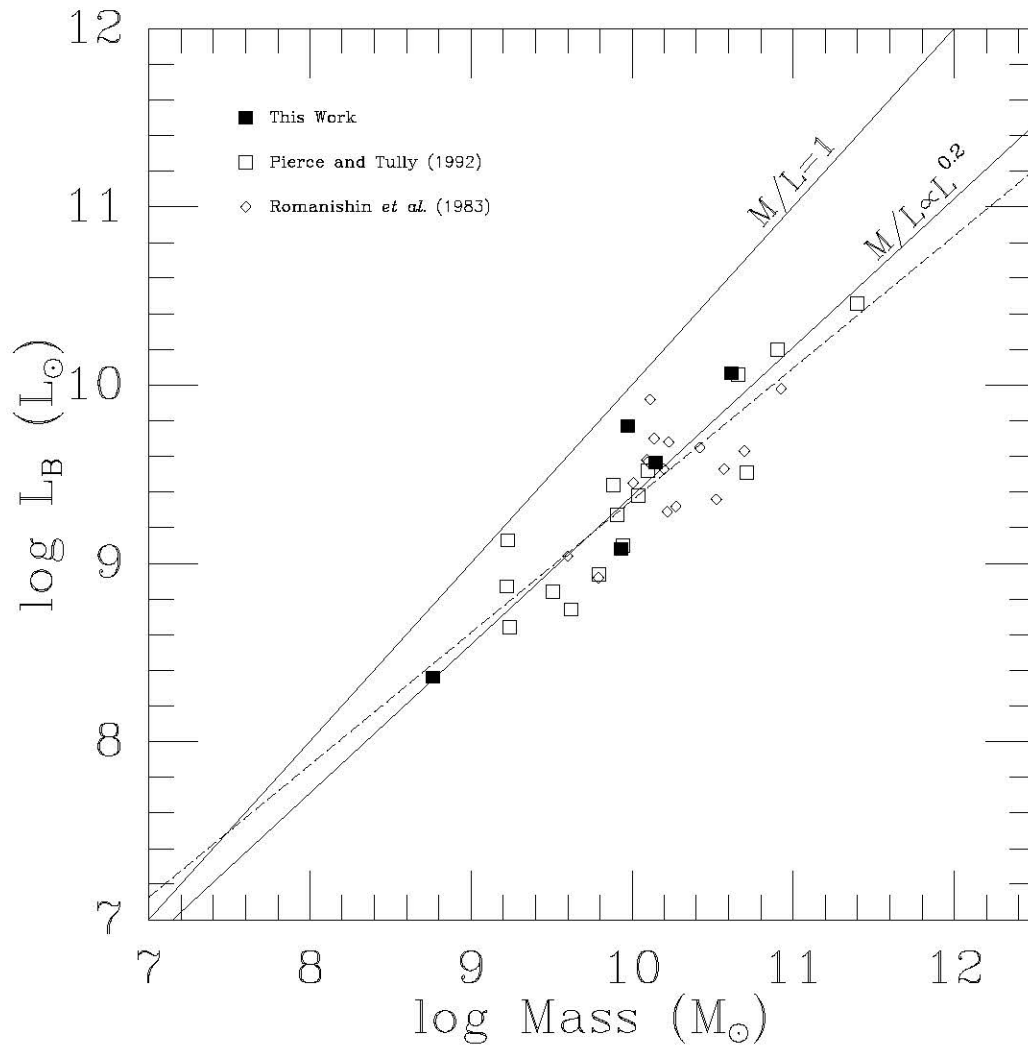
Figure 89: Virial Mass/Luminosity Diagram for DH sample (LSBs excluded). Same as Figure 88, with the LSB galaxies from McGaugh (1992) and Staveley–Smith *et al.* (1992) excluded. The dashed line is the least–squares fit to the points in the figure. The close fit of the spiral data to the $M/L \propto L^{0.2}$ relation found for ellipticals (Dressler *et al.*) indicates that the formative processes are similar.

purely due to internal extinction corrections, we should be able to discern this from examining the I relation, for which this would be significantly smaller. This was what originally prompted us to obtain data in two widely separated bands. Because the effect seen in Figure 87 is such that it could be (and has been) attributed to increased scatter at the faint end (in Figure 86, for example), we have thus far concentrated on the B relation, for which there was a substantial amount of reliable data available (especially Staveley–Smith *et al.* 1992; for the luminosity range of interest). In this section we plot the I data and compare the results with the B relation.

In Figure 90 we plot the the Gaussian (a) and DH (b) galaxies for which there is I data (again we exclude the LSB galaxies of McGaugh in (b)). The variation of M/L with L for the Gaussian sample is still pronounced, and appears to have the same slope as seen in Figure 87 for the B data. However the DH galaxies appear to have a nearly constant M/L when observed in I. This tendency for the slope of the relation to steepen to nearly 10 when observing in longer wavelengths is well documented (Aaronson, Huchra, & Mould 1979; Jacoby *et al.* 1992). It is most likely due to both metallicity effects and the larger (and therefore less accurate) correction for internal extinction in B (see §4.9). The formal least–squares fit to the points in (a) yields an exponent of -0.26 ± 0.25 (shown as a dashed line; compare to the solid line with an exponent of -0.37) with a dispersion of 0.90 mag. The fit to (b) gives an exponent of about 0.02 ± 0.34 with a dispersion of 0.75 magnitudes (the dashed line). These fits are summarized in Table 9. In the table the sample, corresponding figure number, and band in which the observations were made are listed. This is followed by the slope (a) and zeropoint (b) (with errors) of the relation $\log L = a \, \log M \, + \, b$ in solar units. The exponent α of the luminosity dependence of $M/L (\propto L^{\alpha})$ is listed next, along with its error. Finally the r.m.s. of the fit in dex is listed along with the
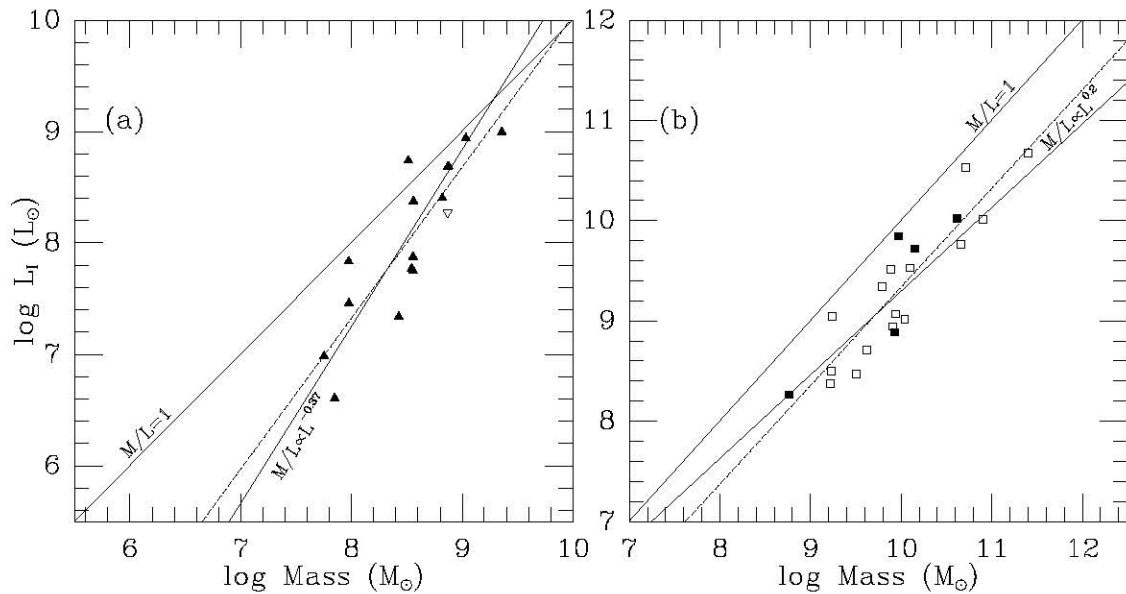
Figure 90: $I-$band Virial Mass/Luminosity Diagrams. (a) is the same is Figure 87, for the I data (our Gaussian sample, and one point from McGaugh). The points still seem to follow the $M/L \propto L^{-0.37}$ relation from Dekel & Silk (see §4.8). In (b) the relation is plotted for the I data with DH profiles (LSB galaxies excluded, as in Figure 89). The data fall along a relation with a steeper slope than in Figure 89, which would be expected if the $M/L \propto L^{0.2}$ trend in Figure 89 is due to metallicity effects. The trend in the $I-$band is one of nearly constant M/L. See §4.9.

dispersion in magnitudes (σ_{mag}).

The important point in the context of this work is that the slope for the Gaussian sample is not dependent on the wavelength of the observation. This again points to the fact that this is not an observational effect, but is an intrinsic difference present between the Gaussian (dwarf) sample and the DH (spiral) sample.

Table 9:
Mass/Luminosity Fitting Results for Samples

Sample	Figure	Band	#	a	b	α	r.m.s.	σ_{mag}
Gaussian	87	B	60	1.44±0.33	−4.23±0.96	−0.30±0.16	0.377	0.94
DH (spirals)	88	B	68	0.80±0.24	1.20±0.76	0.25±0.37	0.330	0.83
"good" DH	89	B	36	0.74±0.27	1.93±0.85	0.35±0.49	0.227	0.57
Gaussian	90a	I	16	1.36±0.46	−3.52±1.35	−0.26±0.25	0.359	0.90
DH	90b	I	20	0.98±0.33	−0.49±1.05	0.02±0.34	0.300	0.75

4.7 Surface Brightness and Color: Distance Independent Tests

In examining the physical meaning of the IR Tully–Fisher relation (Aaronson *et al.* 1982), Burstein (1982, 1988) found that the observed relation did not imply a constant M/L, since the M/L was found to depend on the luminosity. In order to investigate the relation in a distance independent manner, he formed a hybrid surface brightness from the $H-$band aperture magnitudes.

We will adopt this surface brightness for the DH sample of galaxies:

$$SB^i = B_T^0 + 5\log R_{vir} + 2.5\log(b/a), \qquad (4.19)$$

where the total apparent magnitude, B_T^0, is from Table 6 or the literature; R_{vir} is the virial radius used in equation (4.13) but expressed in arcseconds, and b/a is the axial ratio. For the Gaussian sample, we use the same expression, without the correction for inclination, as discussed in §3.1.1,

$$SB = B_T^0 + 5\log R_{vir}. \tag{4.20}$$

In Figure 91, we plot the line width versus the surface brightness. In (a) the linewidth with corrections from Tully & Fouqué (1985) (equation 3.18) is plotted for all the points, while in (b) the modified line width (equation 4.17) is used for the Gaussian dwarfs. While there is more scatter, it is clear that the diagram is showing the same effect seen in Figure 85 (c) and (d). As pointed out by Pierce & Tully (1992), this surface brightness relation (Figure 91) should be insensitive to effects of star formation and extinction in the sample, but sensitive to changes in the HI properties. In neither case do the Gaussian dwarfs fall on the same relation as the normal (DH) spirals. The significantly smaller dispersion for the relationship seen in Figure 91 (b) gives us confidence that our procedure for correcting the linewidth for turbulence is correct. Again, this relation seems to indicate that there is not only a tight relationship between the mass and light within the Gaussian dwarf sample, but also that it is distinct from the relationship found for the sample of spirals. Again, the LSB points in the DH sample are excluded (see above), as well as the LSB spirals from Romanishin *et al.* and McGaugh.

The color/linewidth relation is shown in Figure 92, with the linewidths calculated in the same way as in the previous figure. All of the data for which $B - I$ colors exist are plotted. This includes most of the galaxies in this sample, as well as the LSB galaxies of McGaugh and the normal spirals from Pierce & Tully. Pierce &
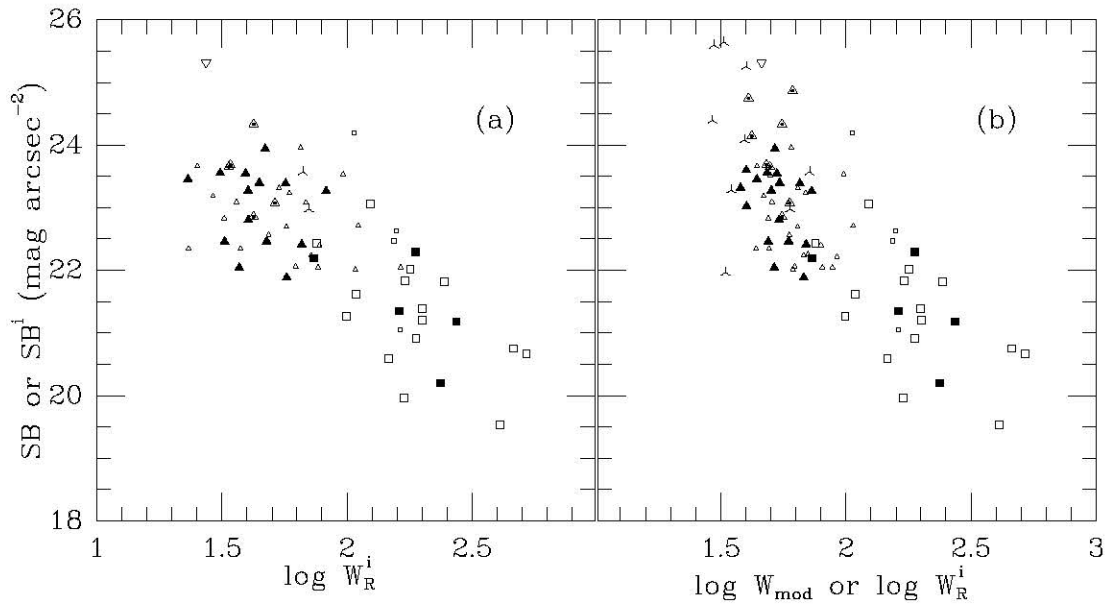
Figure 91: Surface–Brightness/Linewidth relation. (a) is a plot of the observed linewidth, corrected as in equation (3.18) versus the B surface brightness either from equation (4.19) for the DH sample or from equation (4.20) for the Gaussian sample. In (b), the modified form of the linewidth (equation 4.17) is used for the Gaussian sample. All symbols are the same as in Figure 86. Compare the lack of correlation for the Gaussian dwarfs in (a) with Figures 81(a) and 85 (c). The relation seen in (b) for the Gaussian dwarfs, different from that for the DH sample, should be compared to Figures 84 and 85(d). The presence of the effect in the surface–brightness/linewidth indicates that the correlation seen in the earlier figures is *not* a distance effect (Burstein 1982).The the different behaviours of the Gaussian sample and the DH sample in either figure suggests that the dichotomy discussed in §4.8 is real.

Tully note that this diagram is sensitive to recent differences in star formation. The Pierce & Tully spirals (open squares) form a continuum along with the DII galaxies from our sample, while the LSB disks lie to the red side of this, implying less star formation, which is obviously the case in these "crouching giants". In contrast to this, the Gaussian sample is distributed over a large range in color, with hardly any spread in the linewidth.

The color/linewidth relation is also sensitive to the internal extinction, and since we have chosen not to apply any such correction to our sample (§3.1.1), we should perhaps be concerned that the scatter in Figure 92 is largely due to uncorrected internal extinction. However, the range in color observed (~ 2.5mag) is much greater than would be expected from *any* model for internal extinction. In addition, we have already seen (§4.3.2, Figure 83(a)) that there is no correlation of the Tully–Fisher residual with inclination.

4.8 Evidence for Mass–Loss within a Dominant Dark Halo

4.8.1 Theoretical Basis

The precipitous drop in the luminosity with mass below an apparent threshold of $\sim 10^{8.5} M_\odot$, which is close to the minimum mass for a stable, rotating disk (Toomre 1964; Fall & Efstathiou 1980; Ashman 1990), can be understood naturally within the framework of supernovae driven mass–loss within a dark halo, according to Dekel & Silk. Because the energy from the supernovae will drive much of the ISM out of the
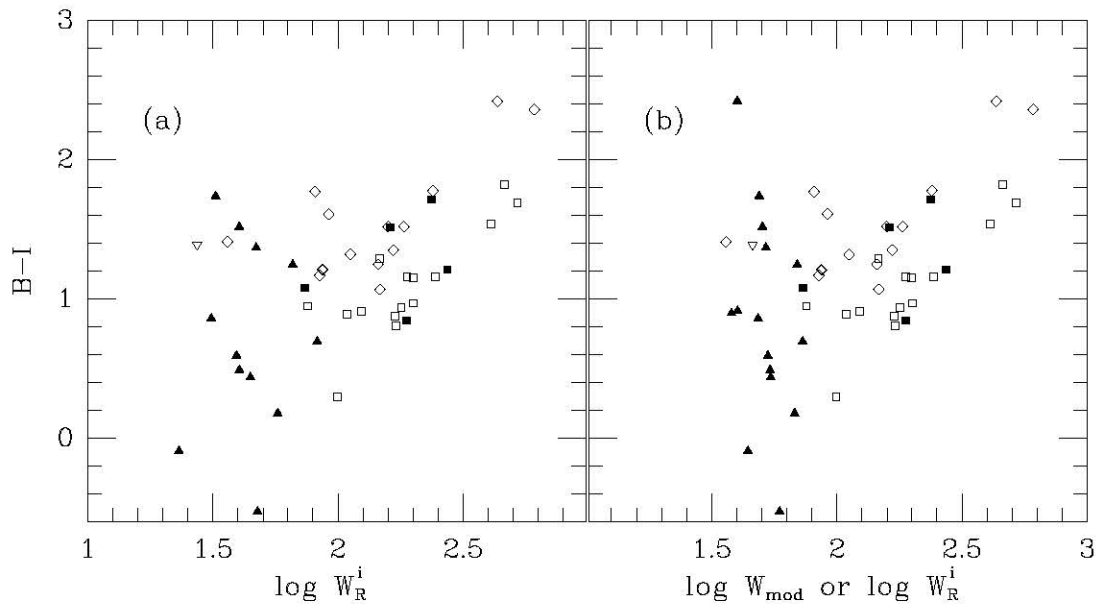
Figure 92: Color/Linewidth relation. (a) is a plot of the observed linewidth, corrected as in equation (3.18) versus the $B - I$ color for all the galaxies with I data. In (b), the modified form of the linewidth (equation 4.17) is used for the Gaussian sample. All symbols are the same as in Figure 86. Again, the Gaussian dwarfs do not follow the relation seen for the DII sample, with the DII galaxies getting bluer as the linewidth gets smaller (also seen in Pierce & Tully 1992). The dispersion increases dramatically with the Gaussian sample, and the color and linewidth appear uncorrelated, suggesting different star formation histories for the two samples.

galaxy, if the galaxy's mass (including the dark halo) is low enough, star formation will drop dramatically (in the case of dIs) or cease (in the case of dEs, where the entire ISM has been removed). The dark matter halo is crucial in order to keep the dwarf bound after much (or all) of its gas has been removed.

The supernovae driven mass loss scenario also will rid the galaxy preferentially of high metallicity gas (in the form of the supernova ejecta itself) (Vader 1986; 1988). This would explain naturally the extremely low–metallicity of dwarfs, while still allowing more than one generation of star formation to have occurred. It has long been realized that simple chemical evolution models of BCDs which do not take into account mass loss cannot reproduce the heavy element abundances and gas mass fractions observed (Matteucci & Chiosi 1983).

This model is also attractive because of its possible explanation of the existence of faint blue galaxies in deep CCD frames (Tyson 1988). Babul & Rees (1992) propose that these objects are dwarf ellipticals undergoing there first burst of star formation, which drives away the remaining ISM in this scenario. They identify present–day dwarf ellipticals as the surviving members of this population, preserved in high pressure environments, while those formed in low pressure regions would fade away. It is not clear if this can fully explain the discrepancy between the number of faint blue galaxies inferred to exist from observations and the local galaxy luminosity function.

Dekel & Silk determine the critical velocity, V_{crit}, below which substantial gas loss is possible. This velocity is dependent on the density and temperature of the interstellar medium, given reasonable assumptions for the amount of energy generated by supernovae. They find V_{crit} to be only very weakly dependent on the gas

number density, with a value ~ 100 km s^{-1}.

Therefore, in this scenario, dwarfs are simply galaxies with virial velocities below about 100 km s^{-1} which have experienced substantial (or complete, in the case of dEs) mass loss after a primary burst of star formation. This velocity corresponds to a mass of $\sim 10^{8.5} - 10^{9.5} M_\odot$. The range is masses is due to the fact that the critical mass depends not only on V_{crit} but also the luminosity of the galaxy (see Figure 6 of Dekel & Silk).

4.8.2 Observational Evidence

Although this model was the theoretically favored explanation for the striking differences between dwarf and massive galaxies (cf. Silk, Wyse, & Shields 1987; De Young & Gallagher 1990; Sandage & Hoffman 1991; Wyse 1993; and De Young & Heckman 1994), little observational evidence existed for such outflows of supernovae driven gas until Meurer et al. (1992) found dramatic evidence for an expanding superbubble of ionized gas in the BCD, or "post–starburst" galaxy, NGC 1705. Subsequent work by Hunter, Hawley, & Gallagher (1993) and Marlowe et al. (1994) provide evidence that this phenomenon is occurring in a number of low luminosity starburst galaxies. In addition, Papaderos et al. (1994) find evidence from ROSAT data for hot gas outflow in the BCD VII Zw 403 and Thuan et al. (1994) find very broad line components in Hα profiles in a number of BCDs. The III holes observed by Puche et al. (1992) in Holmberg II also support this picture.

Much effort has been devoted to determining M/L for the local dE galaxies (e.g. Aaronson & Olszewski 1987; Bender & Nieto 1990; Bender, Paquet, & Nieto 1991; Carter & Sadler 1990). The results seem to support the Dekel & Silk model

$(M/L \propto L^{-0.37})$, although the difficulties in measuring radial velocities for faint, weak lined stars are considerable (Peterson & Caldwell 1993; Ferguson & Binggeli 1994).

Because the model was mainly conceived as a way of explaining the observed properties of gas depleted dEs, with the inclusion of dIs nearly as an afterthought, little attention has been paid to dIs in the light of this model. Pierce (1991) does note that the M/L for disk galaxies below $\log L_I/L_\odot \sim 9.8$ appears to change abruptly (compared to a transition seen in Figure 90 at $\log L_I/L_\odot \sim 8.5 - 9.0$), and suggests the Dekel & Silk scenario as a possible explanation. However, it seems unlikely that the Dekel & Silk dwarfs could remain disk systems. The quantity and global nature of the predicted mass–loss, while not completely disrupting the galaxy due to the dark matter halo, seems likely to disrupt any disk, leaving a chaotic dwarf behind. The lack of dwarf spirals, as well as the high anisotropy of dEs supports this. The disk galaxies in Pierce's (1991) sample could have undergone at best a very mild form of mass loss in the Dekel & Silk scenario, more dramatic effects would only be observable in less massive, "true" dwarfs, where the escape velocity is sufficiently low to allow substantial mass loss.

At this point a "critical mass" of accurate CCD data (along with the III data) for Gaussian profiled dwarfs has accumulated from various authors, notably Staveley–Smith et $al.$ (1992) and those cited by Lo et $al.$ (1993) for their extreme sample of VLA dwarfs, as well as the observations presented here. These observations, in conjunction with those of dEs, as well as the observations of outflows in starbursting dwarfs (Meurer et $al.$ 1992; Marlowe et $al.$ 1994; Papaderos et $al.$ 1994), finally bring a quantity of evidence to support Dekel & Silk's original suggestion that the formation of both dE and dI galaxies could be understood in terms of supernovae

driven mass–loss in a dominant dark halo.

4.9 Mass to Light Dependence in Massive Galaxies: Implications for Spirals from the Tully–Fisher Relation

We now put our results for low–luminosity systems in the context of more luminous systems. We examine the M/L versus L dependence in massive galaxies, in light of the similarity of our Figure 86 to Figure 4 (for ellipticals) of Ferguson & Binggeli (1994), not only at the dwarf end, but also in the regime of normal spirals and ellipticals. It appears from both of these figures that the M/L depends on L in the same way over the same range, which suggests a similarity in the formative processes for ellipticals and spirals, as well as dEs and dIs (as discussed above).

The relation between the central velocity dispersion (σ_0), the effective surface brightness (I_e), and effective radius (r_e) for elliptical galaxies, is well described by the scaling law which restricts ellipticals to the Fundamental Plane of this parameter space (Dressler $et\ al.$ 1987; Djorgovski & Davis 1987):

$$r_e \propto \sigma_0{}^A I_e{}^B, \tag{4.21}$$

where $A \sim 1.4$ and $B \sim -0.9$ (Kormendy & Djorgovski 1989; Bender, Burstein, & Faber 1992). Dressler $et\ al.$ show that in conjunction with the virial theorem, the above scaling relation implies a relation approximately of the form $M/L \propto L^{0.2}$ (Ferguson & Binggeli 1994). They also note that much of this dependence on luminosity is due to the bolometric correction, since the brighter ellipticals are

systematically redder, due to metallicity effects (Faber & Jackson 1976; Smith & Tinsley 1976)). (For discussions on the deviation of the dEs from the Fundamental Plane, see Wirth & Gallagher 1984; Kormendy 1985, 1987; Nieto *et al.* 1990)

If the M/L for spirals was also taken to be proportional to $L^{0.2}$, due to metallicity effects (Bothun *et al.* 1984), or for some other reason, then (from equation 4.8) the slope of the Tully–Fisher Relation is expected to be 7.14 rather than 10. This assumes that $L \propto R^2$, which is at least a reasonable assumption (see Figure 93 in chapter 5). The fact that this slope comes out so close to the observed slope for the $B-$band relation (7.48; Pierce & Tully 1992) suggests a connection. The slightly steeper slope found in the redder relations appears consistent with this idea (Figure 90(b)). It seems likely that the dependence of M/L on L seen for spirals in B is due to the effects of metallicity, with some increased scatter due to the large and uncertain correction for internal extinction.

4.10 A Distance Indicator for Dwarfs?

The usefulness of the modified TF (MTF) relation as a distance indicator for dwarf galaxies is discussed in this section. We have seen that a wavelength independent relationship between mass (calculated from the HI linewidth) and luminosity exists for dwarf galaxies with Gaussian HI profiles (Figures 87 and 90a), and that this is well fitted by the Dekel–Silk model ($M/L \propto L^{-0.37}$).

This relationship exists despite the uncertain photometry (from various sources) for the Lo *et al.* (1993) sample of extremely faint dwarfs. The uncertainty in the actual distance for many of the dwarfs has also increased the scatter along the log L

axis. However, the steep slope of the relation means that the dispersion from the fit will be small even for large changes (errors) in $\log L$.

The standard deviation of the residuals to the fit along the $\log L$ axis in Figure 87 is 0.94 mag, compared with 0.57 mag for the "good" DII galaxy fit shown in Figure 89 and 0.83 mag for the entire DH sample (Figure 88). While the MTF relation seems to be a less accurate distance indicator for dwarfs than the Tully–Fisher relation is for larger galaxies, it would appear that it could prove to be useful.

In order to realize the full potential of this relation accurate distances need to be established for local calibrator dwarfs. Because of the unknown star formation histories and lack of other standard candles in these dwarfs, this is a difficult task (see §3.2 for a discussion and references regarding the distance to GR8). Another approach would be to obtain accurate photometry for a large number of dwarfs in the Virgo cluster and establish an accurate slope for the relation. An accurate distance for the Virgo Cluster from other means, such as Cepheid variables (Pierce *et al.* 1994) would also allow the zeropoint to be fixed. Dwarfs that are faint enough to fix the low end of the relation would be difficult to discover optically over an area as large as that subtended by the Virgo cluster (Sandage & Binggeli 1984), so a systematic deep III survey would be necessary, with deep followup CCD photometry (for a discussion of the detection of dwarfs in III, systematically or serendipitously, see Hoffman, Helou & Salpeter 1988; Briggs 1990; Weinberg *et al.* 1991; and Taylor, Brinks, & Skillman 1993).

At this stage, the MTF relation is most useful as a confirmation of a theoretical model for galaxy formation, and further work should emphasize determining the slope of the relation. In addition, the MTF relation can also be used to check the

distances of dwarfs determined by other methods, but the accuracy of this method as a distance estimator is limited by the uncertainty of the calibration. One potentially useful sample of dwarfs with independently determined distances are those observed by Tikhonov & Karachentsev (1993) and Karachentsev & Tikhonov (1994) for which photometric distances have been determined from the mean apparent magnitude of the 3 brightest stars in the galaxy.

If the MTF should prove to be a *reliable* distance indicator for dwarfs, the numerous III observations of dwarfs (Fisher & Tully 1981; Schneider *et al.* 1990; 1992) could, in conjunction with followup CCD observations, be used to to examine bulk flow motions (e.g., Lynden Bell *et al.* 1988). In addition, dwarfs with accurate peculiar velocities can be used as test particles to probe the dark matter content of groups and clusters of galaxies (Zaritsky & White 1994.)

Chapter 5

Global Properties and Comparative Structure of Dwarfs

In this chapter, we compare the various global quantities and derived structural parameters for the galaxies in our sample. By comparing the location of our sample in these various parameter spaces with the location of other types of galaxies, we gain some insight into the relationship between these types.

5.1   Surface Brightness

In Figure 93(a), the relationship between the virial radius (R_{vir}) and the luminosity is plotted for all the galaxies from this sample and the sources in the literature cited in §4.6. The solid line represents a relation of constant surface brightness. The data show a great deal of scatter, but do follow the relation. In Figure 93(b), only the
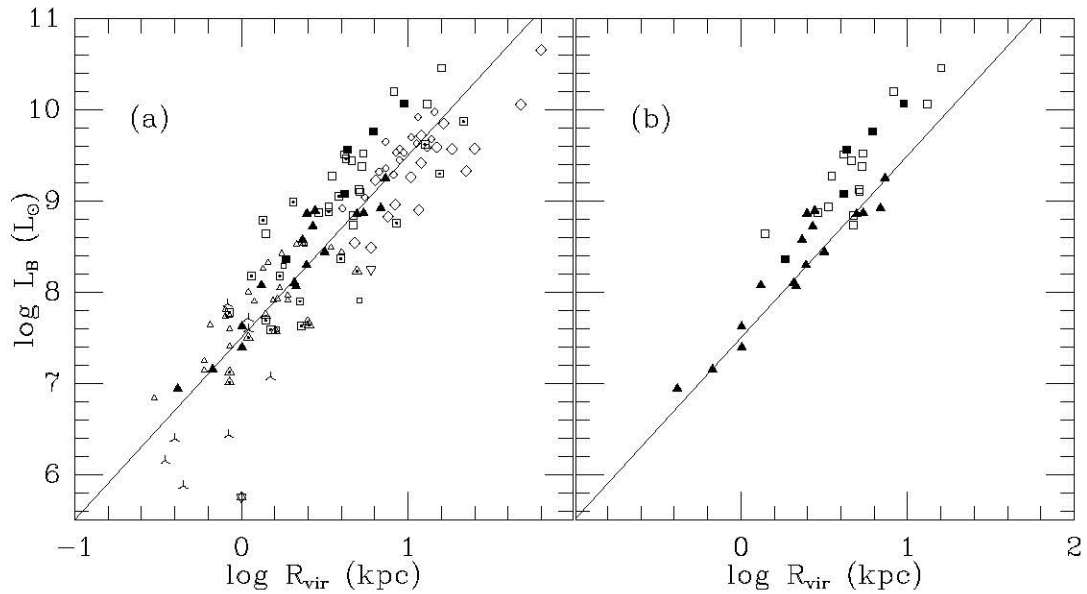
Figure 93: Radius/Luminosity Relation. In (a) the relation is shown for all of the galaxy samples discussed in §4.6. A relation parallel to the solid line is one of constant surface brightness. Symbols are the same as in Figure 86. In (b) just the Pierce & Tully (1992) and the galaxies from this sample are plotted. The galaxies in our DII sample have the same surface brightness as the Pierce & Tully galaxies, while in general the Gaussian dwarfs have a lower surface brightness. *Within* each sample the assumption of constant surface brightness appears reasonable.

galaxies from this sample and from the Pierce & Tully (1992) sample of "normal" spirals are plotted. Here it is obvious that most of the dwarfs follow their own relationship of roughly constant surface brightness ($< \mu >_{max} \sim 22.0$ mag arcsec^{-2}), slightly fainter than the spirals ($< \mu >_{max} \sim 21.0$ mag arcsec^{-2}) (see Figure 94).

Interestingly, the five Gaussians which appear to lie close to the relation for normal spirals (UGC 31, UGC 63, UGC 1171, UGC 3212, and UGC 7684), appear to have fairly smooth surface brightness profiles. They do *not* appear to be undergoing a widespread burst of star formation, which would be expected to cause a corresponding increase in the surface brightness. Any star formation seems confined to in or near the nucleus.

The average surface brightness, calculated from equations (4.19) and (4.20) is plotted in Figure 94. The two extreme points to the lower left are Malin 1–type objects from McGaugh (1992). These are giant disk galaxies with extremely low surface brightness. The dwarf galaxies have a slightly fainter peak surface brightness in this diagram. However they do seem to overlap with both the spiral and LSB distributions.

The surface brightness of the sky ($\mu_B \sim 22.7$ mag arcsec^{-2}) is indicated by the dashed line in Figure 94. It has long been realized (cf., Disney 1976) that the surface brightness of the night sky seriously restricts our knowledge of the true galaxy luminosity function. Irwin *et al.* (1990) find no decrease in the number density of LSBs at lower surface brightness levels ($\mu_B \sim 27.3$ mag arcsec^{-2}) using the APM machine to perform an automated search of deep plates covering a large area of the sky. Bothun, Impey, & Malin (1991) also find evidence for an increase in the slope of the luminosity function at the faint end. McGaugh (1994) postulates that there could
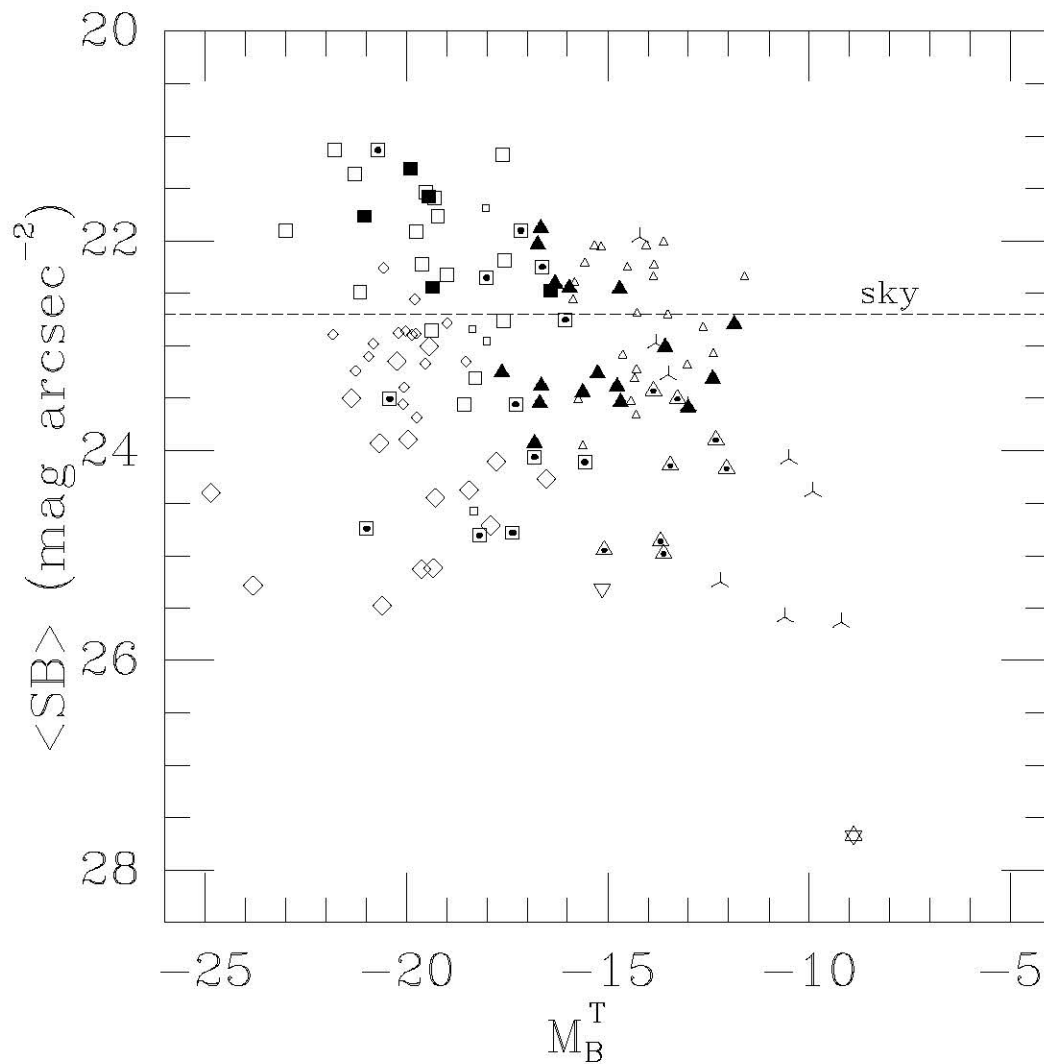
Figure 94: Average Surface Brightness versus Absolute Magnitude. Symbols are the same as Figure 86. The dashed line indicates the sky brightness in B at Kitt Peak. The average surface brightness is computed as in §4.7. The Gaussian and DH sample exhibit a similar range in surface brightness, with a slightly lower maximum value observed for dwarfs. This is consistent with the idea of mass–loss in dwarfs (as in the Dekel & Silk model or any other stripping scenario). The two LSB galaxies at the extreme left are Malin 1–type giant disk galaxies. Phoenix is at the extreme lower right; it was only discovered because of its proximity and hence the ability to detect individual stars.

be enough LSB "crouching giants" to account for a local population corresponding to the faint blue galaxies at intermediate redshift (Tyson 1988; Broadhurst *et al.* 1988). Obviously, we cannot determine this population through optical surveys. However, evidence from HI surveys, as well as statistics from "blind" offsets, do not seem to support the existence of a large population of local LSB disk galaxies (cf., Briggs 1990)

A similar distribution can be seen in the central surface brightness (μ_0^B) versus absolute magnitude diagram (Figure 95), adopted from Kormendy (1987) and Ferguson & Binggeli (1994). This diagram is often used to demonstrate the three distinct classes of stellar systems. To the upper left lie the ellipticals (filled circles) and the bulges of spirals (crosses), making a tight relationship which marks the intersection of the Fundamental Plane (see §4.9) with this parameter space. The M32–like compact ellipticals also fall on this continuum. Globular clusters populate a distinct section of the diagram.

Spiral disks (plus signs; from Freeman 1970; Boroson 1981; and Bothun *et al.* 1985) form a comparatively tight group near $M_B^T \sim -20$ and $\mu_0^B \sim 21$. This is partly an observational selection effect due to the surface brightness of the sky, indicated by the dashed line; the more recently discovered LSB galaxies including Malin 1 (Sprayberry *et al.* 1993), can be seen as part of a continuum extending down from the spirals. The dwarf Irregular and the Local Group dwarf Spheroidal (dSph) galaxies appear to fall along an overlapping relation which bends over and extends to extremely faint absolute magnitudes.

There is the potential for much confusion in the literature between the terms dwarf Spheroidal, dwarf Elliptical and compact Ellipticals. Binggeli (1994) and
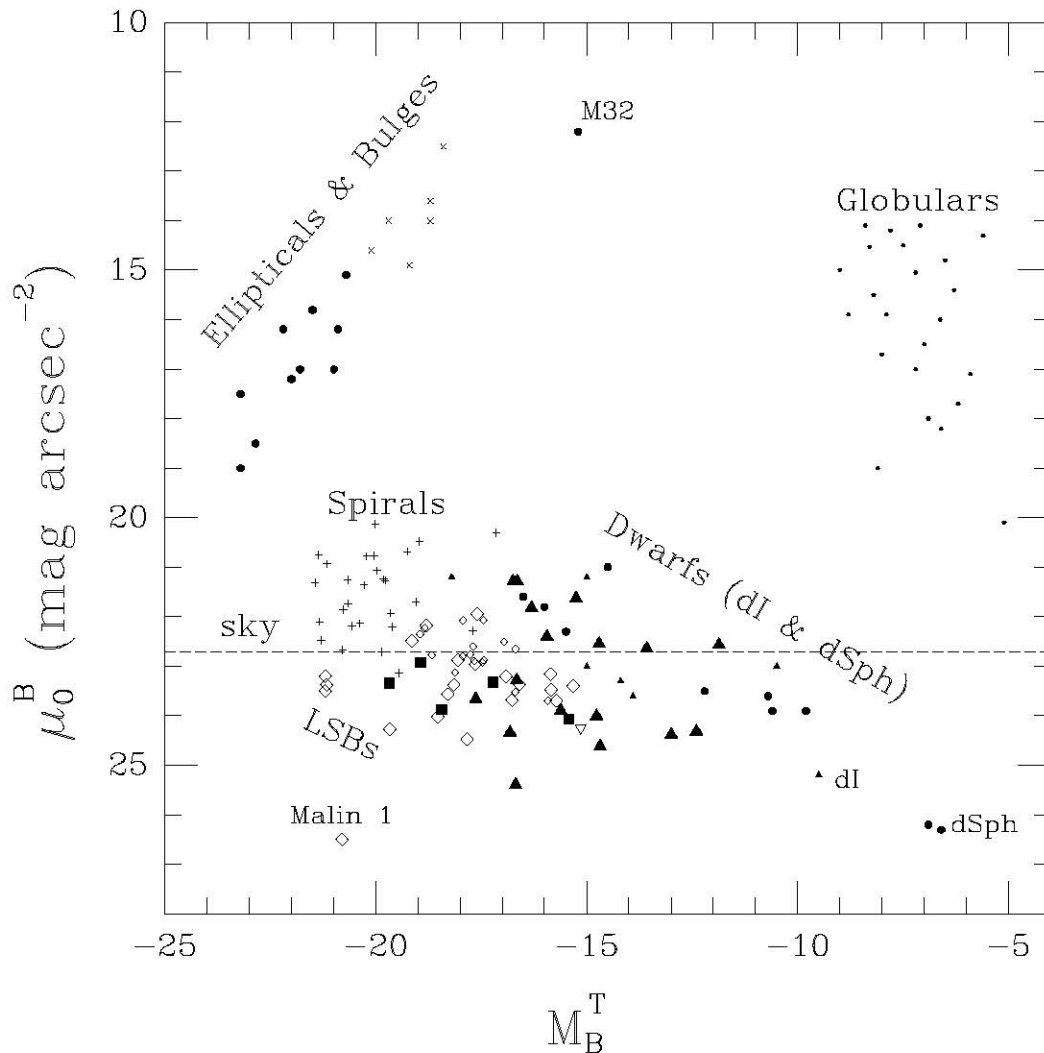
Figure 95: Central Surface Brightness versus Absolute Magnitude. Adapted from figures in Kormendy (1987) and Binggeli (1994). The intersection of the Fundamental Plane for ellipticals ($\bullet$) and bulges ($\times$) is at the upper left. A separate area of the plane is populated by globular clusters. Spirals (+; and the DH sample; filled squares) and LSBs (from McGaugh, large $\diamond$; and from Romanishin *et al.* small $\diamond$) form a continuum extending down to Malin 1. Dwarf galaxies, both dI (including the Gaussian sample, filled triangles; and the McGaugh Gaussian dwarf, inverted triangle) and dSph ($\bullet$) form an extension of this relationship to faint magnitudes and low surface brightness. Note that the relation bends down; there is an upper envelope for the surface brightness of dwarfs which is less than that observed in spirals. Also, some dSphs have a brighter surface brightness than the dIs at a given magnitude; this appears to rule out simple models of stripping (see text). The lower envelope to the spiral and dwarf sequence is a selection effect; it is difficult to find galaxies with surface brightnesses so far below the sky surface brightness (dashed line).

others refer to the faintest spheroidal systems as dEs or dSphs, while the compact elliptical systems such as M32 are merely ellipticals (or compact ellipticals). Other authors (e.g., Kormendy 1985) make a clearer distinction between the ellipticals and the true dwarf systems, which they refer to as dwarf spheroidals. The term dwarf elliptical, if used at all, refers to M32–type ellipticals (Kormendy & Bender 1994).

The Binggeli (1994) terminology is rooted in the morphological similarity between the dwarf and normal early–type systems, as well as the preliminary conclusion that they formed a continuous surface brightness sequence (based on photographic photometry with poor dynamic range; Binggeli, Sandage, & Tarenghi 1984). It was the subsequent work of Kormendy (1985) which first showed that these two classes were distinct. It would seem to be best to not use the term dwarf elliptical at all, and stick with the clearer divisions of ellipticals (and compact ellipticals if some distinction needs to be made for the M32–type systems), and dwarf spheroidal. This terminology makes the division in the observational properties of these systems clearer; dwarf spheroidals are no more "elliptical" than globular clusters are. Their origin is more closely tied to dwarf irregular galaxies than giant ellipticals, and the morphological similarity should not be mistaken for any more than that.

In this section, then, we refer to the faint and diffuse early–type galaxies as dSphs.

Although neither the dI nor dSph galaxies are apparently composed of an actual disk, they are nonetheless well fit by an exponential profile (see §3). The proximity of the dwarf sequences in Figure 95 has lead some authors to propose that stripping of faint spirals and dIs will give rise to dSphs (Kormendy 1987). However, the fact that some of the brighter dSphs have a central surface brightness which is brighter than that for similar dIs (e.g. Bothun *et al.* 1986), in addition to other problems
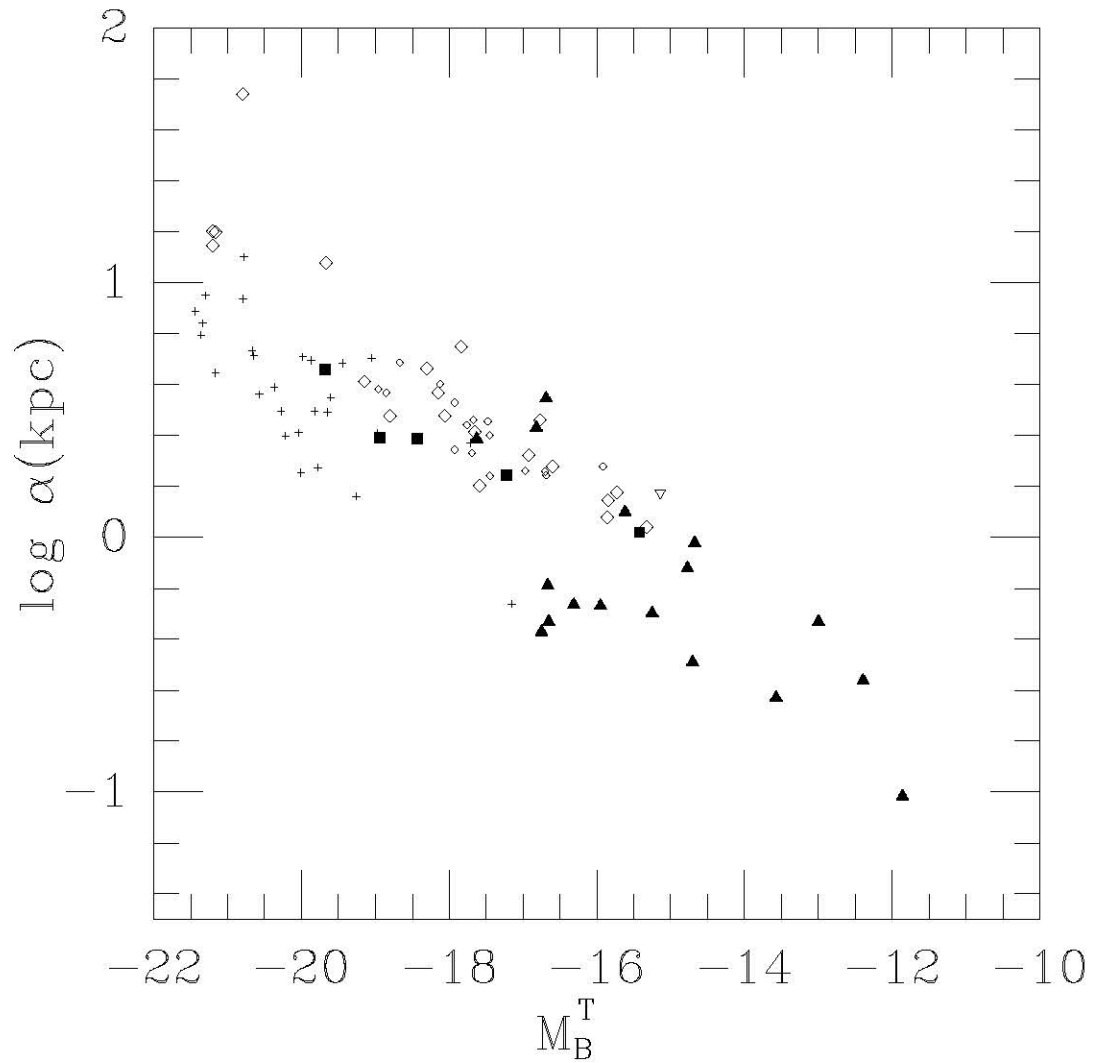
Figure 96: Disk Scale Length versus Absolute Magnitude. Symbols are as in Figure 95. There exists a tight relationship between disk scale length and magnitude. This is similar to the relation seen in Figure 93. Note that the massive LSB galaxy Malin 1 at the extreme upper left deviates markedly from this relationship

including differences in the infrared colors (e.g. James, 1991), present difficulties for the stripping model.

The luminosity/surface brightness relation implies that there is a common preferred scale length for dIs and dSphs. This implies a common formation scenario for these two classes of galaxies. A common formation scenario also is implied by the fact that the Dekel–Silk relation (§4.8) holds for both dSph and dI galaxies.

Figure 96 shows the scale length versus magnitude for the dwarf and spiral samples. Again, we see a rather tight relation for the entire sequence, excluding the Malin 1–type galaxies at the extreme upper left. These giant disk galaxies have a larger scale length for a given luminosity than do the normal spirals.

Conclusions

We have presented CCD surface photometry for 51 dwarf and LSB galaxies in B and I. The magnitudes obtained are used in conjunction with existing HI data to investigate the Tully–Fisher relation in the regime of narrow linewidth. The dwarfs do not follow the original Tully–Fisher relation because the HI linewidth arises from turbulent as well as rotational motion. If the intrinsic axial ratio of the galaxy is used to determine the degree of anisotropy in the galaxy, a modified linewidth can be determined, which is an indicator of the total mass.

The dwarfs are found to follow a mass/luminosity relation which is quite distinct from that of normal spirals. While normal spirals have values of M/L which increase slightly with L (which results in an observed slope for the Tully–Fisher relation (~ 7) that is slightly less than 10, which is predicted for a constant M/L), the dwarfs display a definite trend of increasing M/L as L *decreases*.

The exact form of the relation was found to be well fit by the model of Dekel & Silk (1986): $M/L \propto L^{-0.37}$. The Dekel–Silk relation arises in low mass systems with massive dark halos which undergo extensive mass loss due to supernova driven winds. The dark halo allows the galaxy to remain bound even as most (or all) of the gas is removed, drastically reducing the rate of star formation. The trend towards higher M/L at lower L is the result of the lower escape velocity of the less massive systems, allowing the gas to be removed more efficiently. The Dekel–Silk relation also appears to be present in the dwarf Spheroidal systems, indicating a common evolutionary history for these dwarfs, distinct from normal ellipticals and spirals.

The similar central surface brightness of dIs and dSphs support this conclusion. However, a simple evolutionary sequence dSph $\Rightarrow$ dI through environmentally–

induced stripping seems to be ruled out by the infrared colors. Rather, the Dekel–Silk model of mass loss is envisioned as a process which occurs during the formation of the galaxy, upon the death of the very first stars formed.

Deep CCD imaging of galaxies at the extreme low–luminosity end (with independent distances) is needed to supplement the detailed HI observations which already exist, in order to constrain the slope of the modified Tully–Fisher relation for dwarfs. This could then provide a useful distance indicator for gas–rich dwarfs, which would enable them to be used as test particles to examine bulk flows as well as peculiar velocities within clusters.

References

Aaronson, M., Bothun, G., Mould, J., Huchra, J., Schommer, R. A., & Cornell, M. E. 1986, ApJ, 302, 536

Aaronson, M., Huchra, J., & Mould, J. 1979, ApJ, 229, 1

Aaronson, M., Huchra, J., Mould, J., Schecter, P. L., & Tully, R. B. 1982, ApJ, 258, 64

Aaronson, M., & Mould, J. 1986, ApJ, 303, 1

Aaronson, M., & Olszewski, E. W. 1987, in *Dark Matter in the Universe,* IAU Symp 117, eds. J. Kormendy & G. R. Knapp, (Dordrecht: Reidel), p. 153

Aparicio, A., García–Pelayo, J. M. & Moles, M. 1988a, A&AS, 74, 367

Aparicio, A., García–Pelayo, J. M. & Moles, M. 1988b, A&AS, 74, 375

Ashman, K. M. 1990, ApJ, 359, 15

Babul, A., & Rees, M. J. 1992, MNRAS, 255, 346

Balkowski, C., Bottinelli, L., Chamaraux, P., Gouguenheim, L., & Heidmann, J. 1974, A&A, 34, 43

Bender, R., Burstein, D., & Faber, S. M. 1992, ApJ, 399, 462

Bender, R., & Nieto, J.–L. 1990, A&A, 239, 97

Bender, R., Paquet, A., & Nieto, J. L. 1991, A&A, 246, 349

Binggeli, B. 1994, in *ESO/OHP Workshop on Dwarf Galaxies,* ed. G. Meylan & P.

Prugniel (Garching: ESO), p. 13

Binggeli, B., & Cameron, L. M. 1993, A&AS, 98, 297

Binggeli, B., Sandage, A., & Tarenghi, M. 1984, AJ, 89, 64

Binggeli, B., Tarenghi, M., & Sandage, A. 1990, A&A, 228, 42

Binney, J. 1978, MNRAS, 183, 501

Blumenthal, G. R., Faber, S. M., Primack, J. R., & Rees, M. J. 1984, Nature, 311, 517

Börngen, F., & Karachentseva, V. E. 1985, AN, 306, 301

Boroson, T. A. 1981, ApJS, 46, 177

Bosma, A., & Freeman, K. C. 1993, AJ, 106, 1394

Bothun, G. D., Romanishin, W., Strom, S. E., & Strom, K. M. 1984, AJ, 89, 1300

Bothun, G. D., Impey, C. D., & Malin, D. F. 1991, ApJ, 376, 404

Bothun, G. D., & Mould, J. R. 1987, ApJ, 313, 643

Bothun, G. D., Mould, J. R., Caldwell, N., & MacGillivray, H. T. 1986, AJ, 92, 1007

Bothun, G. D., Schommer, R. A., Aaronson, M., Mould, J., Huchra, J., & Sullivan, W. 1985, ApJS, 57, 423

Bottinelli, L., Gouguenheim, L., Paturel, G., & de Vaucouleurs, G. 1983, A&A, 118, 4

Briggs, F. H. 1990, AJ, 100, 999

Broadhurst, T. J., Ellis, R. S. & Shanks, T. 1988, MNRAS, 235, 827

Brosche, P. 1971, A&A, 13, 293

Bruzual A., G., & Charlot, S. 1993, ApJ, 405, 538

Burstein, D. 1982, ApJ, 253, 539

Burstein, D. 1988, in *Towards Understanding Galaxies at Large Redshift*, ed R. G. Kron & A. Renzini (Dordrecht: Kluwer), p. 93

Burstein, D., & Heiles, C. 1984, ApJS, 54, 33

Burstein, D., & Raychaudhury, S. 1989, ApJ, 343, 18

Carignan, C. 1983, Ph. D. Thesis, ANU

Carignan, C. 1985, ApJS, 58, 107

Carignan, C., Beaulieu, S., & Freeman, K. C. 1990, AJ, 99, 178

Carignan, C., Demers, S., & Côté, S. 1991, ApJL, 381, L13

Carter, D. 1978, MNRAS, 182, 797

Carter, D., & Sadler, E. 1990, MNRAS, 245, 12

Christian, C. A., Adams, M., Barnes, J. V., Butcher, H., Hayes, D. S., Mould, J. R., & Siegel, M. 1985, PASP, 97, 363

Davis, L. E. 1991, private communication

Davis, L. E., Cawson, M., Davies, R. L., & Illingworth, G. 1985, AJ, 90, 169

Dekel, A., & Silk, J. 1986, ApJ, 303, 39

De Young, D., & Gallagher, J. 1990, ApJL, 356, L15

De Young, D., & Heckman, T. M. 1994, ApJ, 431, 598

Dieter, N. H. 1962, AJ, 67, 313

Djorgovski, S., de Carvalho, R., & Han, M.-S. 1988, in *The Extragalactic Distance Scale*, PASPC, Vol. 4, ed S. van den Bergh & C. J. Pritchet, (Provo: ASP), p. 329

Djorgovski, S. & Davis, M. 1987, ApJ, 313, 59

Dressler, A., Lynden Bell, D., Burstein, D., Davies, R. L., Faber, S. M., Terlevich, R. J., & Wegner, G. 1987, ApJ, 313, 42

Faber, S. M., & Jackson, R. E. 1976, ApJ, 204,668

Fall, S. M., & Efstathiou, G. 1980, MNRAS, 193, 189

Fall, S. M., & Frenk, C. S. 1983, AJ, 88, 1626

Fanelli, M. N., O'Connell, R. W., & Thuan, T. X. 1988, ApJ, 334, 665

Ferguson, H. C. 1992, in *Physics of Nearby Galaxies: Nature or Nurture?* ed. T. X. Thuan, C. Balkowski, & J. T. T. Van (Gif-sur-Yvette: Editions Frontières), p. 443

Ferguson, H. C., & Binggeli, B. 1994, A&ARev, in press

Fisher, J. R., & Tully, R. B. 1981, ApJS, 47, 139

Freeman, K. C. 1970, ApJ, 160, 811

Freeman, K. C. 1987, in *Nearly Normal Galaxies*, ed. S. Faber (New York: Springer

Verlag), p. 317

Franx, M., Illingworth, G., & Heckman, T. 1989, AJ, 98, 538

Freudling, W. 1992, GALPHOT User's Manual, ESO

Gelderman, R. 1994, Ph. D. Thesis, U. Virginia

Gerola, H., Seiden, P. E., & Schulman, L. S. 1980, ApJ, 242, 517

Heidmann, J. 1969, AstrLett, 3, 19

Hoessel, J. G., & Danielson, G. E. 1983, ApJ, 271, 65

Hoffman, G. L., Helou, G., & Salpeter, E. E. 1988, ApJ, 324, 75

Holmberg, E. 1958, Medd. Lunds astr. Obs. 2, 136

Hubble, E. P. 1930, ApJ, 71, 231

Huchtmeier, W. K., & Richter, O.–G. 1989 *A General Catalog of HI Observations of Galaxies* (New York: Springer Verlag)

Hunter, D. A., & Gallagher, J. S. 1985, ApJS, 58, 533

Hunter, D. A., & Gallagher, J. S. 1986, PASP, 98, 5

Hunter, D. A., Hawley, W. N., & Gallagher, J. S. 1993, AJ, 106, 1797

Ichikawa, S., Wakamatsu, K., Okamura, S. 1986, ApJS, 60, 475

Impey, C., Bothun, G., Malin, D. 1988, ApJ, 330, 634

Irwin, M. J., Davies, J. I., Disney, M. J., & Phillipps, S. 1990, MNRAS, 245, 289

Izotov, Yu. I., Thuan, T. X., & Lipovetsky, V. A. 1994, ApJ, in press

Jacoby, G. H., Branch, D., Ciardullo, R., Davies, R. L., Harris, W. E., Pierce, M. J., Pritchet, C. J., Tonry, J. L., & Welch, D. L. 1992, PASP, 104, 599

James, P. A. 1991, MNRAS, 250, 544

Jedrzejewski, R. I. 1987, MNRAS, 226, 747

de Jong, R. S., & van der Kruit, P. C. 1994, A&AS, 106, 451

Jørgensen, I., Franx, M., & Kjærgaard, P. 1992, A&AS, 95, 489

Karachentseva, V. E. 1968, Comm. Byurakan Obs. 39, 61

Karachentsev, I. D., & Tikhonov, N. A. 1994, in *ESO/OHP Workshop on Dwarf Galaxies,* ed. G. Meylan & P. Prugniel (Garching: ESO), p. 109

Kennicutt, R. C. 1989, ApJ, 344, 685

King, I. R. 1966, AJ, 71, 64

Kormendy, J. 1985, ApJ, 295, 73

Kormendy, J. 1987, in *Nearly Normal Galaxies,* ed. S. M. Faber (New York: Springer–Verlag) p. 163

Kormendy, J., & Bender, R. 1994, in *ESO/OHP Workshop on Dwarf Galaxies,* ed. G. Meylan & P. Prugniel (Garching: ESO), p. 161

Kormendy, J., & Djorgovski, S. 1989, ARA&A, 27, 235

Kraan-Korteweg, R. C. 1986, A&AS, 66, 255

Kraan Korteweg, R. C., Cameron, L. M., & Tammann, G. A. 1988, ApJ, 331, 620

Landolt, A. U. 1983, AJ, 88, 439

Landolt, A. U. 1992, AJ, 104, 340

Larson, R. B., & Tinsley, B. M. 1978, ApJ, 219, 46

Lo, K. Y., Sargent, W. L. W., & Young, K. 1993, AJ, 106, 507

Lu, N. Y. 1993, Ph. D. Thesis, Cornell

Lu, N. Y., Hoffman, G. L., Groff, T., Roos, T., & Lamphier, C. 1993, ApJS, 88, 383

Lu, N. Y., Houck, J. R., Salpeter, E. E., & Lewis, B. M. 1992, AJ, 104, 1505

Lynden–Bell, D. Faber, S. M., Burstein, D., Davies, R. L., Dressler, A., Terlevich, R., & Wegner, G. 1988, ApJ, 326, 19

Marlowe, A. T., Heckman, T. M., Wyse, R. F. G., & Shommer, R. 1994, ApJ, in press

Massey, P., & Jacoby, G. H. 1992, in *Astronomical CCD Observing and Reduction Techniques*, PASPC, Vol. 23, ed. S. B. Howell (Provo: ASP), p. 240

Mateo, M. 1993, PASP, 105, 1075

Matteucci, F., & Chiosi, C. 1983, A&A, 123, 121

McGaugh, S. S. 1992, Ph. D. Thesis, Univ. Michigan

McGaugh, S. S. 1994, Nature, 367, 538

McGaugh, S. S., & Bothun, G. D. 1994, AJ, 107, 530

McNamara, B. R., Sancisi, R., Henning, P. A., Junor, W. 1994, AJ, 108, 844

Meurer, G. R., Freeman, K. C., Dopita, M. A., & Cacciari, C. 1992, AJ, 103, 60

Mihalas, D. & Binney, J. 1981 *Galactic Astronomy,* 2nd edn. (San Francisco: Freeman), p. 337

Moss, C., & de Vaucouleurs, G. 1986, PASP, 98, 1282

Mould, J., Han, M.-S., & Bothun, G. 1989, ApJ, 347, 112

Nieto, J.-L., Bender, R., Davoust, E., & Prugniel, P. 1990, A&A, 230, L17

Nilson, P. 1973, Uppsala General Catalogue of Galaxies (Uppsala Astr. Obs. Ann., v6) [UGC]

Pagel, B. E. J., Simonson, E. A., Terlevich, R. J., & Edmunds, M. G. 1992, MNRAS, 255, 325

Papaderos, P., Fricke, K. J., Thuan, T. X., & Loose, H.-H. 1994, A&A, 291, L13

Patterson, R. J., & Thuan, T. X. 1992, ApJ, 400, L55

Peimbert, M. 1986, in *Star-forming Dwarf Galaxies and Related Objects,* ed. D. Kunth, T. X. Thuan, and J. T. T. Van (Gif-sur-Yvette: Editions Frontières), p. 403

Pence, W. D. 1978, U. Texas Publ Astr, 14

Persic, M., & Salucci, P. 1988, MNRAS, 234, 131

Persic, M., & Salucci, P. 1990, ApJ, 355, 44

Peterson, R. C., & Caldwell, N. 1993, AJ, 105, 1411

Pierce, M. J. 1988, Ph. D. Thesis, U. Hawaii

Pierce, M. J. 1991, in *The Evolution of the Universe of Galaxies*, PASPC, Vol. 10, ed. R. G. Kron (Provo: ASP), p. 48

Pierce, M. J., & Tully, R. B. 1988, ApJ, 330, 579

Pierce, M. J., & Tully, R. B. 1992, ApJ, 387, 47

Pierce, M. J., Welch, D. L., McClure, R. D., van den Bergh, S., Racine, R., & Stetson, P. B. 1994, Nature, 371, 385

Puche, D., Westpfahl, D., Brinks, E., & Roy, J. R. 1992, AJ, 103, 1841

Pustil'nik, S. A., Ugryumov, A. V., Lipovetsky, V. A., Thuan, T. X., & Guseva, N. G. 1994a, ApJ, in press

Pustil'nik, S. A., Ugryumov, A. V., Lipovetsky, V. A., Thuan, T. X., & Salzer, J. J. 1994b, in *ESO/OHP Workshop on Dwarf Galaxies*, ed. G. Meylan & P. Prugniel (Garching: ESO), p. 133

Rees, M. J. 1985, MNRAS, 213, 75P

Reynolds, J. H. 1913, MNRAS, 74, 132

Roberts, M. S. 1962a, AJ, 67, 431

Roberts, M. S. 1962b, AJ, 67, 437

Roberts, M. S. 1978, AJ, 83, 1026

Rogstad, D. H., & Shostak, G. S. 1972, ApJ, 176, 315

Romanishin, W., Strom, K., Strom, S. 1983, ApJS, 53, 105

Rubin, V. C., Burstein, D., Ford, Jr., W. K., & Thonnard, N. 1985, ApJ, 289, 91

Salzer. J. J. 1989, ApJ, 347, 152

Salzer. J. J., Hanson, M. M., & Gavazzi, G. 1990, ApJ, 353, 39

Salzer, J. J., & Rosenberg, J. L. 1994, in *ESO/OHP Workshop on Dwarf Galaxies*, ed. G. Meylan & P. Prugniel (Garching: ESO), p. 129

Sancisi, R., & van Albada, T. S. 1987, in *Dark Matter in the Universe*, IAU Symp 117, eds. J. Kormendy & G. R. Knapp (Dordrecht: Reidel), p. 67

Sandage, A. 1985, private communication

Sandage, A. 1986, in *Star forming Dwarf Galaxies and Related Objects*, ed. D. Kunth, T. X. Thuan, and J. T. T. Van (Gif-sur-Yvette: Editions Frontières), p. 31

Sandage, A. 1994a, ApJ, 430, 13

Sandage, A. 1994b, ApJ, 430, 29

Sandage, A., & Binggeli, B. 1984, AJ, 89, 919

Sandage, A., Freeman, K. C., & Stokes, N. R. 1970, ApJ, 160, 831

Sandage, A., & Hoffman, G. L. 1991, ApJL, 379, L45

Sandage, A., & Tammann, G. A. 1976, ApJ, 210, 7

Sargent, W. L. W., Sancisi, R., & Lo, K. Y. 1983, ApJ, 265, 711

Schecter, P. L. 1980, AJ, 85, 801

Scheffler, H., & Elsässer, H. 1988, *Physics of the Galaxy and Interstellar Matter*, (Berlin: Springer Verlag), p. 156

Schild, R. E. 1983, PASP, 95, 1021

Schmidt, K.-H., & Boller, T. 1992, AN, 313, 189

Schmidt, R., Richter, G. M., & Karachentseva, V. E. 1985, AN, 306, 257

Schneider, S. E., & Thuan, T. X. 1989, private communication

Schneider, S. E., Thuan, T. X., Magri, C., & Wadiak, J. E. 1990, ApJS, 72, 245

Schneider, S. E., Thuan, T. X., Mangum, J. G., & Miller, J. 1992, ApJS, 81, 5

Schweizer, F. 1992, in *Physics of Nearby Galaxies: Nature or Nurture?* ed. T. X.
    Thuan, C. Balkowski, & J. T. T. Van (Gif-sur-Yvette: Editions Frontières), p.
    283

Silk, J., Wyse, R. F. G., & Shields, G. A. 1987, ApJL, 322, L59

Smith, H. A., & Tinsley, B. M. 1976, PASP, 88, 370

Sprayberry, D., Impey, C. D., Irwin, M., McMahon, R. G., & Bothun, G. D. 1993,
    ApJ, 417, 114

Staveley–Smith, L., Davies, R. D., & Kinman, T. D. 1992, 258, 334

Stetson, P. B. 1987, PASP, 99, 101

Strobel, N. V., Hodge, P., & Kennicutt, R. C. 1991, ApJ, 383, 148

Tammann, G. A. 1980, in *ESO Report of Workshop on Dwarf Galaxies*, ed. M.
    Tarenghi and K. Khar, p. 3

Taylor, C. L., Brinks, E., & Skillman, E. D. 1993, AJ, 105, 128

Thuan, T. X. 1986, in *Star–forming Dwarf Galaxies and Related Objects*, ed. D. Kunth, T. X. Thuan, & J. T. T. Van (Gif-sur-Yvette: Editions Frontières), p. 129

Thuan, T. X. 1991, in *Massive Stars in Starbursts*, eds C. Leitherer, N. R. Walborn, T. M. Heckman, & C. A. Norman (Cambridge: Cambridge Univ. Press), 183

Thuan, T. X., Alimi, J. M., Gott, J. R., & Schneider, S. E. 1991, ApJ, 370, 25

Thuan, T. X., Izotov, Yu. I., Lipovetsky, V. A., & Pustilnik, S. A. 1994, in *ESO/OHP Workshop on Dwarf Galaxies*, ed. G. Meylan & P. Prugniel (Garching: ESO), p. 421

Thuan, T. X., Patterson, R. J., Condon, J. J., & Mitchell, K. J. 1992, AJ, 104, 1331

Tikhonov, N. A., & Karachentsev, I. D. 1993, A&A, 275, 39

Toomre, A. 1964, ApJ, 139, 1217

Tremaine, S. & Gunn, J. E. 1978, Phys Rev Letters, 42, 407

Tully, R. B. 1988 *Nearby Galaxies Catalog* (Cambridge: Cambridge Univ. Press) [NBG]

Tully, R. B., Bottinelli, L., Fisher, J. R., Gouguenheim, L., Sancisi, R., van Woerden, H. 1978, A&A, 63, 37

Tully, R. B., & Fouqué, P. 1985, ApJS, 58, 67

Tully, R. B., & Fisher, J. R. 1977, A& A, 54, 661

Tully, R. B., & Fisher, J. R. 1987 *Nearby Galaxies Atlas* (Cambridge: Cambridge Univ. Press)

Tyson, J. A. 1988, AJ, 96, 1

Vader, J. P. 1986, ApJ, 305, 669

Vader, J. P. 1987, ApJ, 317, 128

van de Rydt, F., Demers, S., & Kunkel, W. E. 1991, AJ, 102, 130

van den Bergh, S. 1981, AJ, 86, 1464

van den Bergh, S. 1994, AJ, 107, 1328

van der Hulst, J. M., Skillman, E. D., Smith, T. R., Bothun, G. D., McGaugh, S. S., & de Blok, W. J. G. 1993, AJ, 106, 548

van der Kruit, P. C., & Shostak, G. S. 1982, A&A, 105, 351

de Vaucouleurs, G. 1948, AnnAp, 11, 247

de Vaucouleurs, G. 1959, in *Handbuch der Physik*, v 53, ed. S. Flügge (Berlin: Springer–Verlag), p. 275

de Vaucouleurs, G., & Moss, C. 1983, ApJ, 271, 123

de Vaucouleurs, G., de Vaucouleurs, A., & Buta, R. 1983, AJ, 88, 764

de Vaucouleurs, G., de Vaucouleurs, A., Corwin, H. G., Jr., Buta, R. J., Paturel, G., & Fouqué, P. 1991, *The Third Reference Catalogue of Bright Galaxies* (New York: Springer–Verlag) [RC3]

Vennik, J., & Richter, G. M. 1994, AN, 315, 245

Weinberg, D. H., Szomoru, A., Guhathakurta, P., & van Gorkom, J. H. 1991, ApJL, 372, L13

Westpfahl, D., & Puche, D. 1993, AJ, submitted

Wirth, A., & Gallagher, J. S. 1984, ApJ, 282, 85

Wyse, R. F. G. 1993, in *The Environment and Evolution of Galaxies*, ed. J. M. Shull & H. A. Thronson, Jr. (Dordrecht: Kluwer) p. 305

Yahil, A., Tammann, G. A., & Sandage, A. 1977, ApJ, 217, 903

Zaritsky, D. & White, S. D. M. 1994, in *ESO/OHP Workshop on Dwarf Galaxies*, ed. G. Meylan & P. Prugniel (Garching: ESO), p. 355

Zwicky, F. 1933, Helv. Phys. Acta, 6, 110

Zwicky, F., Herzog, E., Will, P., Karpowicz, M., & Kowal, C. 1960–1968, *Catalog of Galaxies and Clusters of Galaxies* (Pasadena: Caltech)